THE JOURNAL OF

PHYSICAL CHEMISTRY

THE JOURNAL OF
PHYSICAL CHEMISTRY

Notice to Authors last printed in the issue of January 16, 1975

ห้องสมุด กรมวิทยาศาสตร์
15.ค.ค.2519

1A

COMMUNICATIONS TO THE EDITOR

■ Supplementary material for this paper is available separately, in photocopy or micro-
fiche form. Ordering information is given in the paper.

* In papers with more than one author, the asterisk indicates the name of the author to
whom inquiries about the paper should be addressed.

AUTHOR INDEX

Reactions of Hydrogen and Deuterium with Silane and Mono-, Di-, and Trimethylsilanes at Room Temperature

J. A. Cowfer, K. P. Lynch, and J. V. Michael*

Department of Chemistry, Carnegie-Mellon University, Pittsburgh, Pennsylvania 15213   (Received October 25, 1974)

Publication costs assisted by the Energy Research and Development Administration

The reactions of H and D with silane and monomethyl-, dimethyl-, and trimethylsilanes have been studied at room temperature and 3 Torr of He in a discharge-flow apparatus. The method of detection is time-of-flight mass spectrometry. Rate constants based on atom depletion in reactant-rich systems or reactant depletion in atom-rich systems have been measured, and stoichiometry factors have been estimated. Also products of the reactions have been identified, and reaction profile experiments have been carried out. Mechanisms are proposed for these eight reactions which are consistent with observations and invoke considerable atomic cracking through chemical activation. The theoretical basis for this result is qualitatively discussed, and the observed isotope effects are also compared to theoretical BEBO estimates.

Introduction

There have been a number of reaction rate studies of H and D with silane and mono-, di-, and trimethylsilanes,[1-6] but the techniques which have been used range from relative-photochemical methods to absolute discharge-flow experiments. Presuming that mechanisms under the conditions of a given experiment are well known, comparisons of results between such divergent techniques should be valid, and such comparisons have been made.[4] Also, important quantities such as Arrhenius A factors and activation energies can be estimated, and comparisons for the series of silane molecules can be made. These can then be interpreted theoretically and compared with isoelectronic alkane systems. Much of this work has been done.[3-5] However it has been done on the theoretically reasonable assumption that H and D react at similar rates for a given silane molecule.

The present room temperature experiments were undertaken in order to measure absolute abstraction rate constants for both H and D with silane and methylated silanes with the same apparatus and technique. Mechanistic information is also obtained for the reactions under consideration, since reactants, products, and some intermediates may be observed during reaction with the present experimental technique. The experiments are carried out under two isolation conditions for each reaction, atom in excess and reactant in excess. Absolute rate constants are measured for both H and D with substrate molecules, and thus, isotope effects are estimated. Where possible the absolute rate constants are compared with other workers.

Experimental Section

The apparatus which was used has been described previously[7,8] so no detailed description will be given. Experiments were carried out at room temperature in excess He in a discharge-flow reactor that was poisoned with Drifilm. Experiments were performed in both excess reactant and excess atom concentrations, and pseudo-first-order decays were measured. Under atom excess conditions, reactant decays were measured at four to six atomic concentrations. The decay constants were found to be linearly proportional to atom concentrations, and the slope of the k_{1st}^R vs. $[H]_0$ or $[D]_0$ graph is the apparent bimolecular rate constant, k_{app}^R. Similarly, experiments in reactant excess were performed and first-order decay constants based on atom attenuations were measured at four to six reactant concentrations. Again the slope of the linear $k_{1st}^{H(D)}$ vs. $[R]_0$ graph is the apparent bimolecular rate constant, $k_{app}^{H(D)}$.

Regardless of which reactant molecule was used, the presence of reactants of the type studied in this paper greatly increased the wall activity for atomic wall recombination. Thus, in the reactant excess cases, the extrapolated zero reactant decay constants ranged from 10 to 50 sec⁻¹ depending on the frequency of the Drifilm poisoning process. In this case the first-order decay constant is k_w +

TABLE I:[a] **Apparent Rate Constants for H and D with Silane and Methylsilanes at Room Temperature**

	k_{app}^{H} [b]	k_{app}^{R} [c]	k_{app}^{D} [b]	k_{app}^{R} [d]
SiH_4	52 ± 5	0.5 ± 0.3	9.0 ± 1.0	3.0 ± 0.7
CH_3SiH_3	46 ± 3	11.5 ± 2.0	12.5 ± 1.8 [e]	3.0 ± 0.8
$(CH_3)_2SiH_2$	25 ± 2	4.1 ± 0.9	11.8 ± 1.8	1.4 ± 0.2
$(CH_3)_3SiH$	9.1 ± 0.8 [f]	0.3 ± 0.2	5.0 ± 0.7 [f]	1.7 ± 0.2

[a] Units are 10^{-13} cc/molecule sec. [b] Obtained in reactant excess. [c] Obtained in H excess. [d] Obtained in D excess. [e] Average of values measured at 1, 3, and 5 Torr. [f] Average of values measured at 3 and 5 Torr.

$k_{app}^{H(D)}$ [R]$_0$, and the nonzero intercept value measures the wall recombination rate constant. The slope of $k_{1st}^{H(D)}$ vs. [R]$_0$ still gives $k_{app}^{H(D)}$, but unless the measurements are made at a variety of [R]$_0$ the inferred values for $k_{app}^{H(D)}$ will be greatly in error. Also in the H or D in excess experiments where attenuation of R is measured, stabilization of atom concentrations is impossible even though atom concentrations exceed reactant concentrations by factors of 30 to 80. This observation might be interpreted as the presence of a very fast homogeneous reaction between atoms and silanes, but the rate of atom removal is not at all dependent on reactant concentration. The time it takes to establish the constant steady-state attenuated atom concentration at a particular dwell time varies with reactant concentration, but the reduction in atom concentration is the same regardless of the reactant concentration. This observation clearly suggests that the walls of the reactor are being treated with reactant and instabilities in atom concentration are caused by increased wall activity.

Reactant decay constants can still be measured in such a system if the decay is observed over a limited change in atom concentration. Thus, the results presented in this paper for k_{app}^{R} are obtained only over a 50% atomic concentration change, and the atom concentration is taken as the average of the initial and final dwell time values. Because of this troublesome wall problem, the rate constants in both atom excess and reactant excess systems are estimated to only be accurate to $\pm 20\%$.

In addition to rate constant measurements, complete mass spectra were obtained as a function of dwell time in both reactant excess and atom excess experiments. Products of the reactions have been identified and followed as a function of time, and thus, reaction profiles in the form of peak height vs. time have been obtained.

For all of the silanes studied in this paper, there are no appreciable parent peaks at m/e equal to the parent molecular mass. This feature of silane mass spectrometry is well known.[1,2,9] The principal mass peak closest to the parent molecular mass is derived from the parent mass less the mass of H (or D in the case of deuterated silanes) where H (or D) is bound to the silicon atom. Another important mass peak occurs at the parent molecular mass less 15 (CH_3) in the case of methylsilanes. If no H (or D) atom is bound to silicon as in the case of tetramethylsilane the closest mass peak is the parent molecular mass less 15.[9] This shows unambiguously that $(CH_3)_{4-n}SiH_n + e^- \rightarrow (CH_3)_{3-n}(CH_2)SiH_n^+ + H + 2e^-$ is a negligible ionization

process in comparison to $(CH_3)_{4-n}SiH_n + e^- \rightarrow (CH_3)_{4-n}SiH_{n-1}^+ + H + 2e^-$. Thus, the major mass peak in $(CH_3)_3SiH$ and $(CH_3)_3SiD$ is the same and appears at $m/e = 73$. Small but measurable silicon isotope peaks of 5 and 3% also occur at 74 and 75, respectively, due to the natural abundances of ^{29}Si and ^{30}Si.

Silane was obtained from Airco Rare and Specialty Gases as electronic grade. Dimethyl and monomethylsilanes were obtained from PCR Inc. and trimethylsilane was obtained from Columbia Organic Chemicals Inc. All silanes were purified by bulb-to-bulb distillation, and the middle third was used. Purity checks were routinely made by mass spectrometry. Research grade H_2 and D_2 (99.7% isotopically pure) were obtained from Air Products and Chemicals Inc. and Isomet Corporation and were used as received.

Results

The room temperature rate constants which were measured are presented in Table I for silane and the three methylsilanes with H and D in both atom excess and reactant excess experiments. For the limited pressure range available (1–5 Torr), no measurable differences in rate constants could be documented within experimental error ($\pm 20\%$) with changes in total pressure. Also the constants obtained with reactant in excess are always larger than those obtained with atoms in excess. This indicates that a large stoichiometric correction is necessary for the reactant in excess experiments. This point is discussed further in connection with each reaction system.

In all cases the initial process is hydrogen abstraction from the reactant silane. It will be shown that the abstracted hydrogen is bound to the silicon atom and not the carbon atom. This is observed as an increase in m/e 3 due to HD formation in the D with silane studies. The subsequent reactions which occur are complicated and will be discussed separately in connection with each reaction system.

H and D with SiH_4. SiH_4 was observed at 19 ± 1 eV as m/e 31 in both H in excess and D in excess experiments. The mass spectrum also consists of small silicon isotope peaks at 32 and 33 of 5 and 3%, respectively. There is also a major mass peak at m/e 30 (intensity 1.2 times m/e 31), and minor mass peaks exist at 29 and 28.

In the H in excess experiments very small if any depletion of m/e 31 was observed and the apparent rate constant (Table I) for SiH_4 removal is $(0.5 \pm 0.3) \times 10^{-13}$ cc/molecule sec. This should be viewed as an upper limit and indicates that almost no overall reaction was occurring. Furthermore, no observable products at higher mass, such as disilane, could be documented under these conditions.

That a reaction does occur can be seen from the results obtained in reactant in excess where H atom attenuation is measured as a function of dwell time. The apparent rate constant (Table I) is $(52 \pm 5) \times 10^{-13}$ cc/molecules sec. Under these atom lean conditions small but measurable concentrations of disilane (Si_2H_6) were detected as a product. These results suggest the following mechanism:

$$H + SiH_4 \longrightarrow H_2 + SiH_3 \tag{1}$$

$$H + SiH_3 + M \longrightarrow SiH_4 + M \tag{2}$$
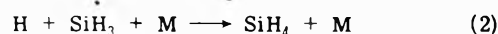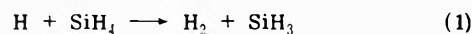
Reaction 2 may be homogeneous, in which case a third body is absolutely necessary, or it may occur heterogeneously on the walls of the reactor. In the H in excess experiments, reactions 1 and 2 predict no SiH_4 removal or product formation. When the H atom concentration is smaller (the reactant in excess experiments), the resulting

TABLE II: Room Temperature Abstraction Rate Constants for H and D with Silane and Methylsilanes

Reaction		$10^{13}\ k_{abs}$, cc/molecule sec[a]
$H + SiH_4$	26 ± 3^c	$2.2,^d\ 2.5^f$
$D + SiH_4$	3.0 ± 0.7^b	$4.7,^e\ 3.0^h$
	4.5 ± 0.5^c	
$H + CH_3SiH_3$	11.5 ± 2.0^b	1.5^f
	11.5 ± 2.0^c	
$D + CH_3SiH_3$	3.0 ± 0.8^b	5.1^e
	3.1 ± 0.5^c	
$H + (CH_3)_2SiH_2$	4.1 ± 0.9^b	2.1^f
	4.2 ± 0.3^c	
$D + (CH_3)_2SiH_2$	1.4 ± 0.2^b	5.0^e
	2.0 ± 0.3^c	
$H + (CH_3)_3SiH$	3.7 ± 1.0^c	1.9^f
$D + (CH_3)_3SiH$	1.7 ± 0.2^b	$4.9,^e\ 1.8^g$

[a] This work unless noted. [b] Measured. [c] Inferred (see text). [d] Reference 1. [e] Reference 4. [f] Reference 3. [g] Reference 2. [h] Reference 5.

Figure 1. Product profile for the reaction $D + SiH_4$; $[D]_0 = 1.9 \times 10^{13}$ atoms/cc, $[SiH_4]_0 = 9.5 \times 10^{13}$ molecules/cc; $P = 3$ Torr, linear flow velocity $v = 1261$ cm/sec; (◯) D, (□) HD, (◇) Si_2H_6, (△) SiD_4.

silyl radicals can either homogeneously or heterogeneously recombine to give disilane

$$SiH_3 + SiH_3(+M) \longrightarrow Si_2H_6(+M) \qquad (3)$$
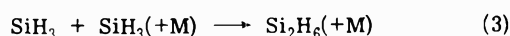
or they may disproportionate as suggested by Pollock, Sandhu, Jodhan, and Strausz[10] to give silylene which subsequently reacts with the large SiH_4 concentration in an insertion reaction to give disilane. The present results do not agree with the proposal[1] that silylene is formed by disproportionation of H and silyl because little or no SiH_4 was removed from the system in the H in excess experiments. The predominant reaction between H and silyl under the present conditions is reaction 2. Reaction 2 is the major reaction even under reactant in excess conditions since the disilane yield is minor. Thus, the rate constant which is based on H depletion in this system will be twice the abstraction rate if the steady-state approximation is valid for silyl. The rate constant for abstraction of hydrogen by H in SiH_4 is then $(26 \pm 3) \times 10^{-13}$ cc/molecule sec, and this value is tabulated in Table II.

The reaction of D with SiH_4 was then studied with D in excess. The predominant products are HD and SiD_4. No partially deuterated silanes could be documented in the D in excess system. No disilanes were observed as products. SiD_4 was observed as m/e 34, and SiH_4 depletion was observed as m/e 31. No gradual relaxation from low to high mass as a function of distance occurred in the silane peaks; i.e., m/e 34 increased proportionately to the m/e 31 decrease and no change in m/e 33 occurred at all as a function of distance. This observation clearly suggests that a fast sequential exchange between silyl and D occurs in the D in excess system, and the final product, SiD_4, will result from the reaction between D and SiD_3. By analogy with the H in excess experiments, the detailed mechanism for the reaction can be written:
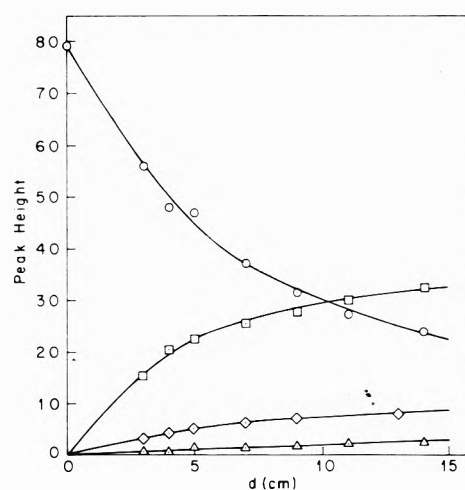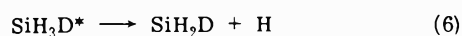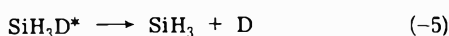
$$D + SiH_4 \longrightarrow HD + SiH_3 \qquad (4)$$

$$D + SiH_3 \longrightarrow SiH_3D^* \qquad (5)$$

$$SiH_3D^* \longrightarrow SiH_3 + D \qquad (-5)$$

$$SiH_3D^* \longrightarrow SiH_2D + H \qquad (6)$$

$$SiH_3D^* \longrightarrow SiH_3D \qquad (\omega)$$

where SiH_3D^* is vibrationally hot. Dissociation reaction -5 is the reverse of reaction 5 and will likely be negligible in comparison to reaction 6 because the chemical activation function for SiH_3D^* will originate at the critical energy for reaction -5 while reaction 6 will be lower lying by approximately the difference between Si–H and Si–D bond energies. Reaction ω represents collisional stabilization and will be small in comparison to reaction 6 for a species with so few degrees of freedom. Thus, in the present D in excess system the silyl-d_1 radicals which are a product of reaction 6 will rapidly exchange through reactions analogous to (5) and (6) to give silyl-d_2. Silyl-d_2 will subsequently exchange to give silyl-d_3, and silyl-d_3 will ultimately yield SiD_4 through reaction with D either on the wall or through stabilization (reaction ω). The overall process in the D in excess system is then:

$$5D + SiH_4 = HD + SiD_4 + 3H \qquad (I)$$
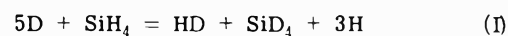
The silyl radicals which are produced are always in steady state in the detailed mechanism since the m/e 31 decrease is nearly equal to the m/e 34 increase. Since SiH_4 is only removed by reaction 4, apparent rate constants based on SiH_4 depletion in the D in excess experiments have unit stoichiometry and refer to reaction 4. The measured value (Table I) is $(3.0 \pm 0.7) \times 10^{-13}$ cc/molecule sec and is tabulated in Table II.

The reaction was then studied with reactant in excess, and D depletion was measured. A typical profile experiment is shown in Figure 1 where D depletion results primarily in HD formation. Two other products, Si_2H_6 and SiD_4, were identified but both were found to be present in minor amounts. Due to the small concentration of D in these experiments it is apparent that the fast sequential exchange of SiH_3 with D which results in overall process I is not going to completion. Since disilane is completely protonated, and it is derived from silyl radicals as described previously, and since only small amounts of SiD_4 are being formed, the predominant fate of the silyl radicals from reaction 4 in the reactant in excess (atom lean) system is likely to be reaction with D followed by stabilization or heterogeneous reaction to form SiH_3D. Due to mass peak interferences from the large concentration of SiH_4, this presumed product, SiH_3D, will not be observable in small con-
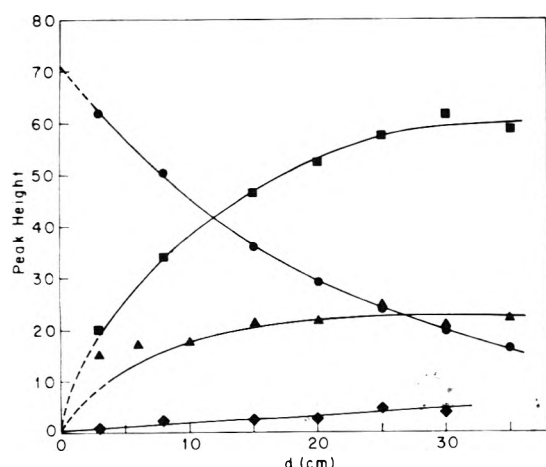
Figure 2. Product profile for the reaction D + $(CH_3)_3SiH$: $[D]_0 = 5.9 \times 10^{14}$ atoms/cc, $[(CH_3)_3SiH]_0 = 6.2 \times 10^{12}$ molecules/cc; $P = 3$ Torr, linear flow velocity $v = 1251$ cm/sec; (●) m/e 59, (■) m/e 60, (▲) CD_4, (♦) SiD_4.

centrations. Thus, the following overall process is inferred in the reactant in excess experiments:

$$2D + SiH_4 = HD + SiH_3D \qquad (II)$$
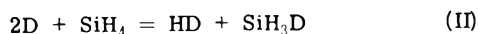
Process II predicts a stoichiometry factor of 2. The measured rate constant (Table I) is $(9.0 \pm 1.0) \times 10^{-13}$ cc/molecule sec. Thus, a value of $(4.5 \pm 0.5) \times 10^{-13}$ cc/molecule sec is inferred for the intial abstraction reaction 4, and this value is tabulated in Table II. The D in excess value of $(3.0 \pm 0.7) \times 10^{-13}$ cc/molecule sec is in moderate agreement with this reactant in excess value.

H and D with $(CH_3)_3SiH$. Experiments on $(CH_3)_3SiH$ depletion were carried out in the presence of excess D concentration. The mass spectrum of $(CH_3)_3SiH$ at 19 ± 1 eV consists of m/e 73 with silicon isotope peaks of 5 and 3% at 74 and 75. The mass spectrum at 19 ± 1 eV also consists of major mass peaks at 59 and 58 (intensities of 1.1 and 0.53 of m/e 73, respectively). These fragmentation peaks are derived from the parent mass less CH_3 and CH_4 (or CH_3 + H). In the D in excess experiments the m/e 73 (the parent mass less 1) peak was chosen as a measure of reactant concentration. Also higher masses up to m/e 78 were monitored as a function of dwell time and $58 \leq m/e \leq 60$ was observed. Very small but measurable concentrations of masses up to m/e 78 were observed, but there was no appreciable relaxation from lower to the higher masses as a function of dwell time. That is m/e 74–78 increased proportionately to one another. These peaks are undoubtedly due to deuteration of $(CH_3)_3SiH$ and must include deuteration in the methyl groups. Depletion of reactant $(CH_3)_3SiH$ was observed at m/e 73, and, based on equal sensitivities for trimethylsilanes, the conversions to the deuterated compounds only amount to ~3% of the total loss of m/e 73. Thus, the process which forms these compounds is minor in this system. Small but measurable amounts of CD_4 (m/e 20) were observed as a product. The rate constant based on m/e 73 depletion was found to be $0.3 \pm 0.2 \times 10^{-13}$ cc/molecule sec which indicates almost no reaction. The major process was observed in the m/e 58 to 60 fragmentation peaks. For the same minor decrease in m/e 73, the m/e 59 peak decreases while the m/e 60 increases substantially as shown in Figure 2. Such behavior has previously been observed.[2] No higher mass products were observed, but H atoms as m/e 1 were observed as a product of the reaction.

Reaction studies in excess H concentration were carried out where m/e 73 was again taken as a measure of reactant concentration. Again only small depletion rates were observed, and the estimated rate constant is $(0.3 \pm 0.2) \times 10^{-13}$ molecules/cc sec as shown in Table I. Also small but measurable CH_4 was observed as a product at m/e 16. On the basis of the above observations two alternative detailed mechanisms can be proposed for the reaction.

Mechanism A

$$D + (CH_3)_3SiH \longrightarrow HD + (CH_3)_3Si \qquad (7)$$

$$D + (CH_3)_3Si \longrightarrow (CH_3)_3SiD^* \qquad (8)$$

$$(CH_3)_3SiD^* \longrightarrow (CH_3)_3SiD \qquad (\omega')$$

$$(CH_3)_3SiD^* \longrightarrow D + (CH_3)_3Si \qquad (-8)$$

$$(CH_3)_3SiD^* \longrightarrow CH_3 + (CH_3)_2SiD \qquad (9)$$

Mechanism B

$$D + (CH_3)_3SiH \longrightarrow HD + (CH_3)_2SiH(CH_2) \qquad (10)$$

$$D + (CH_3)_2SiH(CH_2) \longrightarrow (CH_3)_2(CH_2D)SiH^* \qquad (11)$$

$$(CH_3)_2(CH_2D)SiH^* \longrightarrow (CH_3)_2(CH_2D)SiH \qquad (\omega'')$$

$$(CH_3)_2(CH_2D)SiH^* \longrightarrow CH_3 + (CH_3)(CH_2D)SiH \qquad (12)$$

$$\text{or } CH_2D + (CH_3)_2SiH$$
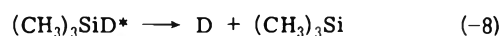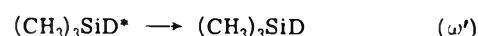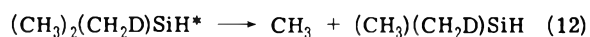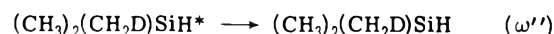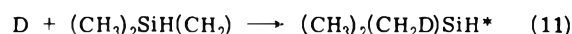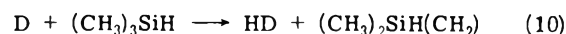
As in the case of H and D with SiH_4 the species marked with an asterisk are vibrationally excited and have to be considered as possibilities in the present low pressure work. In mechanism A, reaction -8 likely is negligible in comparison to reaction 9 since the Si–D bond is believed to be stronger by ~4 kcal/mol than the Si–C bond. The chemical activation function will then originate at the critical energy for reaction -8 while the critical energy for reaction 9 will be lower lying by ~4 kcal/mol. Processes similar to reaction -8 have then been neglected in mechanism B for the same reasons.

The observation of little depletion in both excess D and excess H in m/e 73 while mixing in m/e 59 and 60 is substantial in the D reaction suggests that most of the reaction in this case is due to reactions 8 or 11 followed by stabilization ((ω') or (ω'')). If these processes were the only important processes then re-formation of parent compound would occur exclusively in the H in excess system and no reactant depletion would be observed. The rate constant for depletion is, however, $(0.3 \pm 0.2) \times 10^{-13}$ cc/molecule sec, and this can be attributed to decomposition through methyl cracking (reactions 9 or 12 in the D system). The presence of methane as products in these atom excess systems confirms this observation as will be discussed below.

Stabilization is the major process for removal of vibrationally excited species and results in the production of either $(CH_3)_3SiD$ or $(CH_3)_2SiH(CH_2D)$ in the D system depending on whether mechanism A or B is invoked. If $(CH_3)_2SiH(CH_2D)$ is formed, the parent less 1 value for m/e (i.e., 73) should decrease for the reactant molecule and m/e 74 should increase substantially. As discussed above only small conversions to highly deuterated trimethylsilanes are observed. This would indicate that mechanism B is unimportant. On the other hand, the assertion that m/e 73 in the reactant molecule is due only to $(CH_3)_3Si^+$ ions leads to the conclusion that this same molecular mass will result if $(CH_3)_3SiD$ is ionized. Also the observation of large changes in m/e 59 and 60 is understandable since these are derived from parents less CH_3. Thus, a good measure of reactant trimethylsilane and product trimethylsilane-d_1

are m/e 59 and 60, respectively, as shown in Figure 2. Other workers have come to the same conclusion.[2]

Decay constants can then be obtained for m/e 59 depletion in the D in excess system, and these yield a value for reactant depletion of $(1.7 \pm 0.2) \times 10^{-13}$ cc/molecule sec as indicated in Table I. As discussed above the total trimethylsilane concentration (m/e 73) depletes with a rate constant of $(0.3 \pm 0.2) \times 10^{-13}$ cc/molecule sec due to methyl cracking.

Mechanism A with the back reaction -8 neglected then explains the observations. As will be discussed later in conjunction with the other methylsilane systems, the dimethylsilyl radicals which are produced in reaction 9 then react rapidly with D, and another methyl is cracked out. This scheme is analogous to reaction 8 followed by reaction 9 for trimethylsilyl (i.e., it goes through a chemically activated vibrationally hot species), but there is no evidence that stabilization (i.e., reaction ω') can take place at the low pressure of these studies for vibrationally excited dimethylsilane. The overall process is then

$$D + (CH_3)_2SiD \longrightarrow CH_3 + (CH_3)SiD_2 \qquad (13)$$
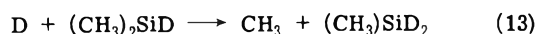
As will be discussed below there is also no evidence for monomethylsilyl reaction with D with subsequent stabilization of the excited methylsilane. Instead the excited species always decomposes to give methyl and silyl. The overall process following reaction 13 is then

$$D + (CH_3)SiD_2 \longrightarrow CH_3 + SiD_3 \qquad (14)$$

In the D in excess system the methyl radicals from reactions 9, 13, and 14 rapidly exchange, again through a chemical activation scheme which is analogous to that of silyl (reactions 5 and 6). The overall processes are

$$CH_3 + D \longrightarrow CH_2D + H \qquad (15)$$

$$CH_2D + D \longrightarrow CHD_2 + H \qquad (16)$$

$$CHD_2 + D \longrightarrow CD_3 + H \qquad (17)$$
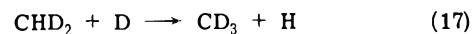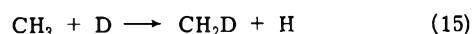
Thus, a distribution of deuterated methyl radicals is formed which depends on the D atom concentration, and H atoms are formed as a product which agrees with observation. The deuterated methyl and silyl radicals will react with D and stabilize again through a chemical activation scheme (overall processes)

$$CH_{3-n}D_n + D + M \longrightarrow CH_{3-n}D_{n+1} + M \qquad 0 \le n \le 3 \qquad (18)$$

$$SiD_3 + D + M \longrightarrow SiD_4 + M \qquad (19)$$
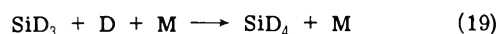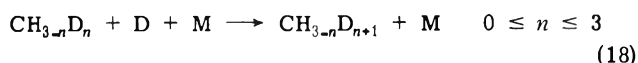
and recombination of methyl and any methylated silyl radical, which is highly favored from a chemical activation viewpoint, will likely be partially competitive with the D plus radical recombinations (reactions 18 and 19) even with high D concentrations. Reactions 18 and 19 are not highly favored from a chemical activation viewpoint due to the relatively small number of degrees of freedom in the vibrationally excited methane and silane molecules. Thus, the overall process for methylated silane production can be viewed as

$$CH_{3-n}D_n + (CH_3)_{3-m}SiD_m + M \longrightarrow$$
$$(CH_3)_{3-m}CH_{3-n}D_nSiD_m + M \qquad 0 \le n, m \le 3 \qquad (20)$$
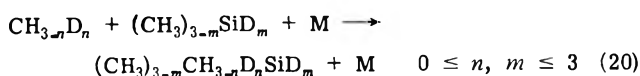
Reaction 18 predicts CD_4, and this is observed as a product (Figure 2); reaction 19 predicts SiD_4, and this is observed as a product (Figure 2); and reaction 20 predicts mono-, di-, tri-, and tetradeuteriomethylsilanes as products. Of these

possibilities deuterated trimethylsilanes are observed as minor products. Mono- and dimethylsilanes are impossible to observe in small concentrations due to m/e peak interferences. Tetramethylsilane is impossible to observe since it has no m/e peak near 88. Its major mass peak is 73 also.

Even though reactions 18 and 19 are not favored from a chemical activation viewpoint because of the small number of degrees of freedom in the excited methanes and silane, these reactions are the major removal processes for methyl and silyl radicals at the conditions of these experiments (high [D]). The negligible concentrations of methylated silanes confirm this view. Thus, we conclude that the system in excess D can be explained by mechanism A with reaction -8 considered to be negligible. The sequence of reactions following mechanism A is reactions 13 through 19. Reaction 20 is not included since only minor products attributable to it are observed.

If m/e 59 is taken as a measure of $(CH_3)_3SiH$, then the rate constant, $(1.7 \pm 0.2) \times 10^{-13}$ cc/molecule sec, will refer to the abstraction process, reaction 7, because this process precedes both stabilization and decomposition of $(CH_3)_3SiD^*$. This value is listed in Table II. The rate constant based on m/e 73 attenuation, $(0.3 \pm 0.2) \times 10^{-13}$ cc/molecule sec, is derived from the difference between the depletion rate of $(CH_3)_3SiH$ and the formation rate of $(CH_3)_3SiD$. Under the steady-state assumption for $(CH_3)_3Si$ and $(CH_3)_3SiD^*$, this rate constant refers to k_7F where F is the ratio of decomposition to decomposition plus stabilization of $(CH_3)_3SiD^*$ and is $\langle k_9/k_9 + \omega' \rangle$. The average is taken over the chemical activation function for $(CH_3)_3SiD^*$. For the present conditions F is 0.3/1.7 or 0.18.

In the reactant in excess experiments the measured rate constants based on D and H atom depletion are $(5.0 \pm 0.7) \times 10^{-13}$ and $(9.1 \pm 0.8) \times 10^{-13}$ cc/molecule sec, respectively (Table I). In all experiments the D and H atom concentrations ranged from 2 to 6 $\times 10^{12}$ atoms/cc. It is likely that the fast sequential atomic cracking scheme which gives CH_3 (reactions 8 and 9, 13, and 14) is occurring. The resulting CH_3 and SiD_3 radicals do not appreciably recombine as discussed previously, and by analogy with the D with SiH_4 system we envision these radicals as simply stabilizing with D atoms perhaps homogeneously or on the walls of the reactor. Thus, the decomposition channel terminates with reaction 18 with $n = 0$ and reaction 19. No firm evidence from product analysis could be obtained due to mass peak interference except that HD was definitely a product of the reaction. With mechanism A, reactions 13, 14, 18, with $n = 0$, and 19 and the assumption of steady state for all vibrationally excited species and intermediate radicals, the rate constant for D depletion is $2k_7(1 + 3F)$. As discussed previously in the D in excess experiments, $k_7 = (1.7 \pm 0.2) \times 10^{-13}$ cc/molecule sec, and $k_7F = (0.3 \pm 0.2) \times 10^{-13}$ cc/molecule sec. Thus, a value for the D depletion rate constant of $(5.2 \pm 2.0) \times 10^{-13}$ cc/molecule sec is inferred, and the measured value is $(5.0 \pm 0.7) \times 10^{-13}$ cc/molecule sec. This is in adequate agreement and further justifies the stoichiometry arguments.

The same procedure is followed in the H atom depletion experiments (reactant in excess). The measured rate constant in the H in excess experiments is $(0.3 \pm 0.2) \times 10^{-13}$ cc/molecule sec, and this is k_7F. $2k_7(1 + 3F) = (9.1 \pm 0.8) \times 10^{-13}$ cc/molecule sec. Thus, k_7, the abstraction rate constant for H with $(CH_3)_3SiH$, is $(3.7 \pm 1.0) \times 10^{-13}$ cc/molecule sec. F is then 0.08. The abstraction rate constant is entered in Table II.

H and D with $(CH_3)_2SiH_2$. $(CH_3)_2SiH_2$ depletion was observed in the presence of excess D concentrations. The 19 ± 1 eV mass spectrum of $(CH_3)_2SiH_2$ consists of major mass peaks at m/e 59, 58, 45, and 44 (relative intensities of 1.0, 1.0, 0.42, and 0.98, respectively). Small but observable deuterated dimethylsilanes were observed as products. As in the trimethylsilane case, however, the process which form these compounds is minor. HD (m/e = 3), CD_4 (m/e = 20), and SiD_4 (m/e = 34) were observed as products. All of the major mass peaks (59, 58, 45, and 44) decreased with an increase in dwell time, and first-order decay constants based on attenuation of any of these peaks gave the same value within experimental error. Particular attention was given to the growth of m/e 46 with m/e 45 decay. This observation, by analogy with the trimethylsilane case (m/e 59 and 60), would indicate whether $(CH_3)_2SiHD^*$ stabilization occurs to an appreciable extent. The increase of m/e 46 was negligible and could be interpreted as fragmentation of the minor deuterated dimethylsilanes. No large decrease in the parent molecular mass less CH_3 accompanied by a large increase in the parent-d_1 less CH_3 was observed. This case is clearly different from trimethylsilane. Thus, there is no evidence for stabilization of dimethylsilane-d_1 after initial abstraction and D addition. Instead the channel for decomposition is clearly favored. The mechanism that agrees with all of the observations is

$$D + (CH_3)_2SiH_2 \longrightarrow HD + (CH_3)_2SiH \qquad (21)$$

$$D + (CH_3)_2SiH \longrightarrow CH_3 + (CH_3)SiHD \qquad (22)$$

$$D + (CH_3)SiHD \longrightarrow CH_3 + SiHD_2 \qquad (23)$$
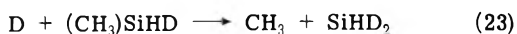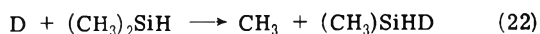
where reactions 22 and 23 are written as overall processes of the chemical activation scheme. In the D in excess experiments the methyl and silyl-d_2 radicals rapidly exchange as in reactions 15, 16, and 17. These partially and totally deuterated radicals can give rise to minor buildup of deuterated tri-, di-, and monomethylsilanes similar to reaction 20, but their predominant fate in excess D is recombination (reactions 18 and 19) to form SiD_4 and CD_4. Both products are observed. Also higher mass observations indicate the formation of deuterated trimethylsilane in minor amounts.

Thus, the only process of importance is decomposition, and the overall process in excess D is 13D + $(CH_3)_2SiH_2$ = HD + $2CD_4$ + SiD_4 + 7H. Rate constants based on reactant depletion (as m/e 59, 58, 45, or 44) refer to the rate-controlling reaction which is reaction 21. The value obtained is (1.4 ± 0.2) × 10^{-13} cc/molecule sec. Similarly, the value obtained in the H in excess experiments is (4.1 ± 0.9) × 10^{-13} cc/molecule sec, and this value refers to the abstraction rate constant. The process in the latter case is similar to the D reaction, but CH_4 and SiH_4 are predicted to be products. Both are observed at m/e 16 and 31, respectively.

Results were also obtained in the reactant in excess systems. Following the conclusions made in connection with the silane and trimethylsilane cases (i.e., D concentrations are sufficiently small that only monodeuteration occurs with free methyl and silyl radicals either homogeneously or on the wall), the reactant in excess overall process is 6D + $(CH_3)_2SiH_2$ = HD + $2CH_3D$ + $SiHD_3$. The rate-controlling reaction is reaction 21, and steady-state analysis gives $k_{app}^D = 6k_{21}$. The measured rate constant based on D depletion is (11.8 ± 1.8) × 10^{-13} cc/molecule sec, and thus, k_{21} = (2.0 ± 0.3) × 10^{-13} cc/molecule sec. As stated previously the value obtained in D excess is (1.4 ± 0.2) × 10^{-13}

cc/molecule sec, and the agreement is adequate. The overall process for the H depletion experiments also shows that six H atoms are used up for one dimethylsilane. The measured value in the reactant in excess experiments with H is (25 ± 2) × 10^{-13} cc/molecule sec, and this gives an inferred value for the H atom abstraction rate of (4.3 ± 0.3) × 10^{-13} cc/molecule sec in good agreement with the previously stated value of (4.1 ± 0.9) × 10^{-13} cc/molecule sec obtained in H excess. These values are listed in Table II.

H and D with CH_3SiH_3. This system is similar to dimethylsilane. No evidence was found for stabilization. The reaction goes entirely through a decomposition channel after the initial abstraction and subsequent D addition. In the D in excess experiments the overall process is 9D + CH_3SiH_3 = HD + CD_4 + SiD_4 + 5H. The rate constant for reactant depletion is measured to be (3.0 ± 0.8) × 10^{-13} cc/molecule sec. The H in excess value is (11.5 ± 2.0) × 10^{-13} cc/molecule sec. By analogy with the other systems the reactant in excess overall process is modified to 4D + CH_3SiH_3 = HD + CH_3D + SiH_2D_2. The value obtained from D depletion experiments is (12.5 ± 1.8) × 10^{-13} cc/molecule sec which yields a value of (3.1 ± 0.5) × 10^{-13} cc/molecule sec in excellent agreement with the value from D in excess. The overall process also suggests a value of 4 for the stoichiometry factor for the H depletion with reactant in excess experiments. The measured value is (46 ± 8) × 10^{-13} cc/molecule sec which, after correction for the stoichiometry factor, gives (11.5 ± 2) × 10^{-13} cc/molecule sec in excellent agreement with the H in excess value previously given. These values are also listed in Table II.

There is further evidence that the stoichiometric relationships which have been suggested between the atom-lean and -rich experiments are reasonable. Small peak heights at m/e 90, 89, 88, 87, and 86 in ratios of 1.0, 0.9, 0.9, 0.4, and 0.6, respectively, were observed in both reactant in excess systems with D and H. The spectrum was identical in both systems and was a product of the reaction. As is the case in the H and D with SiH_4 where disilane-d_0 was observed, we suggest that this spectrum is due to the dimer of methylsilyl radicals, $(CH_3)_2H_4Si_2$. Production rates were minor and do not affect the stoichiometry arguments made above. However the observation does serve as a tracer for the fate of CH_3SiH_2 radicals and shows that D with radical recombinations with subsequent methyl cracking predominates over simple exchange. The free methyl and silyl-d_1 radicals then primarily monodeuterate to give methane-d_1 and silane-d_2. This is a common feature in the stoichiometric arguments which we have used for all eight reactions studied in this paper.

Discussion

One feature of the present study which has not been suggested before in the H with methylated silane systems is the extent of atomic cracking of methyl due to atom with methylated silyl radical reactions. Two things will limit the extent to which these processes are important. One is obviously the relative concentration of the atoms and radicals, and the other is the total pressure. Obi et al.,[4] who are the only workers who have made detailed product analyses, report only minor production of methane and this indicates relatively little atomic cracking. This is not a point of disagreement but should be expected because the photochemical generation of D atoms in the presence of large concentrations of C_2D_4 and methylsilanes (~100–200 Torr) will limit [D] to small values, and even if D with radical interac-

tions do take place the resulting vibrationally excited species should stabilize rather than dissociate at the higher pressures of their experiments.

Under the present low pressure conditions the subsequent cracking, after abstraction and atom addition to the methylated silyl radical, is to be expected. Obi et al.[4] present bond energy estimates of the Si–H bond for silane and for mono-, di-, and trimethylsilanes and these decrease with increasing methyl substitution. Thus, when H is added to trimethylsilyl the minimum vibrational energy of the chemically activated molecule, E^*, is 81.1 kcal/mol. Similarly, when H is added to dimethylsilyl, monomethylsilyl, and silyl the values for E^* are 84.0, 85.9, and 95.2 kcal/mol, respectively.

Simons and coworkers[11–14] have carried out experiments and RRKM calculations with chemically activated methylsilanes. However, the technique of activation is methylene insertion, and their preferred E^* value is very much higher, ~130 kcal/mol, than those in the present cases. A common feature in all methylsilane systems which these workers have used is that the C–Si bond energy is 78 ± 4 kcal/mol. This value is inferred from several sources.[15] Thus, the critical energy, E_0, for methyl dissociation from any chemically activated methylated silane should be approximately 78 kcal/mol. Assuming the same critical energy for methyl decomposition for the present mode of activation (H addition to tri-, di-, and monomethylsilyl), the methyl dissociation channel will be lower lying than the H dissociation channel by 3.1, 6.0, and 7.9 kcal/mol, respectively. Hence methyl rupture from an activated methylated silane is energetically favored over H rupture, and this tendency increases with decreasing methylation. Not only are the methyl dissociation channels progressively lower lying, but the number of degrees of freedom of the vibrationally excited molecules decreases from trimethylated to monomethylated excited silanes. According to RRKM theory, the lifetime with respect to dissociation of an activated molecule decreases with increasing energy E^* and also decreases with a decrease in the number of active degrees of freedom (all other things being equal). These two features combine to make the specific rate constant for methyl dissociation increase by several orders of magnitude as methylation decreases. The effect of a decrease in degrees of freedom can be seen in the RRKM calculated k_E values for di- and trimethylsilanes from Hase, Mazac, and Simons.[14] In their calculation E^* is nearly constant, as is E_0. Their calculated values for k_E are 2.0×10^7 and 9.2×10^8 sec^{-1} for tri- and dimethylsilanes at E^* values of 130 and 129 kcal/mol, respectively.

The effect of decreasing the excess energy of the activated molecule from 130 to 81 kcal/mol for a constant E_0 of 78 kcal/mol will be to substantially decrease the k_E value even more in the trimethylsilane case. This has been partially tested from $E^* = 133$ to 123 kcal/mol,[13] and the decrease in k_E is from 34.8 to 6.8×10^6 sec^{-1} (for assumed RRKM models for the reaction), respectively, where k_E is the specific rate constant for decomposition of the chemically activated species.

The present result of $F = 0.08$ in the H with trimethylsilane case gives k_E an approximate value of 9×10^5 sec^{-1} for an assumed effective collision frequency of ~10^7 sec^{-1}. To be sure, this value is lower than the 6.8×10^6 sec^{-1} value quoted above for $E^* = 123$ kcal/mol. However, the difference in k_E does not appear to be large enough for such a large difference in excess energy. For the present mode of

activation, the activation function will arise at $E_{min}^{\pm} = E_{min}^* - E_0 = 3.1$ kcal/mol, whereas in the methylene addition mode $E_{min}^{\pm} = 52$ kcal/mol. With reasonable molecular models of similar complexity, detailed RRKM calculations of k_E generally decrease by ~6 orders of magnitude for such a large change in excitation energy.[16] This can be seen more easily from the simple RRK theory on the basis of only one quarter of the available oscillators being active, i.e., $S = 9$. The ratio of dissociation rate constants at $E^* = 130$ to $E^* = 81.1$ for $E_0 = 78$ is $((52.0 \times 81.1)/(3.1)(130))^8 = 1.4 \times 10^8$. This ratio would be larger for $S > 9$. Also, at $E^* = 130$ kcal/mol the molecular elimination channel to give methane is presumably competitive with methyl dissociation according to Simons and coworkers.[14] In the present trimethylsilane work at $E^* = 81.1$ kcal/mol, there is evidence against such processes since the methane which is observed in the excess D system is always CD_4 rather than CH_3D. Methane elimination will arise from a much different transition state than that for methyl dissociation even though the active molecule is common for both channels. The principal differences in the molecular elimination compared to bond cleavage dissociation channels are the rigidity of the models for the transition states and also the E_0 values. In general, the E_0 values for elimination channels are lower than those of cleavage channels and this would favor elimination over cleavage. However the major effect is the need for rigid transition states, and this seriously decreases the sum of states in the calculation for k_E, and it is markedly lowered.

It is difficult to devise RRKM models for these molecular elimination cases. We suggest from our results and those of Simons and coworkers[11–14] that molecular elimination channels are negligible under the present activation conditions and only become important at higher E^* values. We suggest that the methyl dissociation channel accounts for the present results in which case the lifetime for the excited state in the trimethylsilane case is ~10^{-6} sec and stabilization is competitive at 3 Torr of He. We suggest on the basis of the above discussion that the lifetimes of excited mono- and dimethylsilanes will be orders of magnitude smaller than trimethylsilane, methyl decomposition will predominate, and stabilization will be negligible for the present conditions. These theoretical considerations agree with the experimental conclusions.

With regard to the H atom dissociation channels which are possible when D is added to any silyl or partially methylated silyl, the rate constants for these channels should also be much larger than molecular elimination and should be nearly competitive with methyl dissociation. H dissociation will lie lower than E_{min}^* by approximately the difference in zero point energies of Si–H and Si–D (~1.0 kcal/mol). Since the transition states for H and methyl dissociations should be similar (i.e., loose complexes), the sum of states for the complexes will be similar for a common activated molecule. Since methyl dissociation is lower lying than hydrogen atom dissociation for D with radical activation, methyl dissociation should predominate over exchange, but exchange will still be orders of magnitude more probable than stabiliztion for all silanes except trimethylsilane under the present conditions. This is exactly the view taken to rationalize the data above.

The inferred and measured room temperature abstraction rate constants for H and D with silane and mono-, di-, and trimethylsilanes are given in Table II. There is relatively little work with which to compare the present data,

but the comparisons that can be made are also noted in Table II.

Contineanu, Mihelcic, Schindler, and Potzinger[2] report a room temperature measurement of the abstraction rate constant of 1.8×10^{-13} cc/molecule sec for D + $(CH_3)_3SiH$ in a discharge-flow system with ESR detection. They have also determined an activation energy of 2.3 kcal/mol. The present results, which are also obtained in a discharge-flow system, are in excellent agreement. The present work has also confirmed the details of their reactant profile analysis and most of the conclusions about the mechanism. We have further suggested the presence of atomic cracking in the trimethylsilane reaction which they would not consider since they observed no methane as a product.

Mihelcic, Potzinger, and Schindler[5] in a recent paper have also investigated the D with SiH_4 reaction. These workers have obtained a value of $(3.0 \pm 1.0) \times 10^{-13}$ cc/molecule sec at room temperature in excellent agreement with the present value. Temperature variation studies indicate an activation energy of 2.5 kcal/mol. The present results confirm nearly all of the conclusions drawn by these authors with regard to reaction profiles and product formation. One apparent difference is the magnitude of disilane production inferred by these workers compared to the present reactant in excess with D experiments. The conditions of the present experiments (Figure 1) are such that only initial formation rates are observed since [D] and [SiH_4] are small. Reference to Figure 7 of the previously cited paper[5] shows that SiH_3D builds up initially followed by Si_2H_6, in complete agreement with the view taken here.

Moortgat[1] reports a lower limit for the abstraction rate constant of 2.2×10^{-13} cc/molecule sec for H + SiH_4 determined with a discharge-flow system at room temperature. Under the same conditions, excess atom concentrations, the observed value is $< (0.5 \pm 0.3) \times 10^{-13}$ cc/molecule sec, and these results are not in agreement.

Hong[3] has performed relative experiments in which steady-state H atom changes are observed by Lyman α absorption spectrophotometry as a function of added reactant concentration. The experiment is designed to give rate constants relative to H + C_2H_2.[8] The results at 15 Torr for H with silane and mono-, di-, and trimethylsilanes are also given in Table II. The results for tri- and dimethylsilanes are within 50% of the present results and are therefore in moderate agreement. The results for monomethylsilane and silane are an order of magnitude different and do not agree.

Lastly, the abstraction rate constants for D with all of the reactant silanes have been estimated by Obi, Sandhu, Gunning, and Strausz[4] from results relative to D + C_2D_4 in its high pressure limit. The value which they used for the calibration reaction is in close agreement with that recently estimated from this laboratory[17] and we therefore expect good agreement. These values are also listed in Table II; however, they are generally higher by a factor of 2–3 than the present results. Considering the combined uncertainties in both studies this is moderate agreement.

With regard to the relatively large isotope effects which are observed in the abstraction rate constants (Table II), some theoretical isotope effect calculations were carried out for these systems. Obi et al.[4] have listed the bond parameters for silane and the methylsilanes and have used the BEBO method to extract estimates for the potential energies of activation for the H atom abstraction process. If the approximation is made that the abstraction process can

TABLE III:

Complex	n_1^a	$V'*^{b,c}$	ZPE_R^d	ν^*	ν_{str}	ν_b
SiH_3–H–H	0.25	6.2 (6.2)	3.12	1102i	1336	530 (2)
SiH_3–H–D				832i	1188	496 (2)
CH_3SiH_2–H–H	0.13	3.3 (3.6)	3.10	685i	1693	417 (2)
CH_3SiH_2–H–D				493i	1658	393 (2)
$(CH_3)_2SiH$–H–H	0.11	3.0 (3.3)	3.06	622i	1761	394 (2)
$(CH_3)_2SiH$–H–D				446i	1736	372 (2)
$(CH_3)_3Si$–H–H	0.09	2.5 (2.8)	3.04	554i	1832	365 (2)
$(CH_3)_3Si$–H–D				395i	1817	345 (2)

^{a} n_1 is the bond order for H–H at V^*. ^{b} Values calculated from modified expression for V_{tr} listed in ref 4 with $\alpha = 1.19$. ^{c} Values in parentheses are taken from ref 4 and were calculated in a similar manner. ^{d} $ZPE_R = \omega_e/2$ expressed in kcal mol^{-1} where ω_e is the Si–H stretching frequency for a given silane as listed in ref 4.

TABLE IV:

Reactant	k_H/k_D	Γ_H^*/Γ_D^{*a}
SiH_4	0.98	1.3
CH_3SiH_3	1.26	1.0
$(CH_3)_2SiH_2$	1.33	1.0
$(CH_3)_3SiH$	1.33	1.0

^{a} Computed tunneling corrections for an unsymmetrical Eckart barrier as defined in ref 18.

be treated as an H atom plus diatomic molecule reaction to form a linear activated complex, then the BEBO calculation can be continued as described by Johnston,[18] and estimates of force constants and rate constants can be obtained.

The bond parameters assigned by Obi et al.[4] have been used to calculate the activated complex properties listed in Table III. These properties were used to calculate the isotope effects that would be predicted in each case from the expression[19]

$$\frac{k_H}{k_D} = \frac{\nu_{LH}^{\ddagger}}{\nu_{LD}^{\ddagger}} \prod_{i=1}^{3N-6} \frac{\nu_{iH}^{\ddagger}}{\nu_{iD}^{\ddagger}} \left(\frac{1 - e^{-h\nu_{iD}^{\ddagger}/kT}}{1 - e^{-h\nu_{iH}^{\ddagger}/kT}} \right) e^{-(\epsilon_{0H}^{\ddagger} - \epsilon_{0D}^{\ddagger})/RT}$$

The approximation is made that the ratio of reaction coordinates $\nu_{LH}^{\ddagger}/\nu_{LD}^{\ddagger}$ is given by ν_H^*/ν_D^*, the ratio of imaginary frequencies, and the results are listed in Table IV. The fact that the ratio of k_H/k_D for reaction with SiH_4 is less than unity is not surprising since this can occur in cases of isotopic substitution of an atom reactant.[19] However, the predicted increasing trend in the ratio k_H/k_D through the series of compounds, silane to trimethylsilane, contradicts the observed decreasing trend: $k_H/k_D \approx 6$ for silane to $k_H/k_D \approx 2$ for trimethylsilane.

A possible cause for the observed trend in k_H/k_D is the increasing importance of quantum tunneling of H atoms as the potential energy of activation increases. This effect is shown in Table IV. The ratio of tunneling corrections for an assumed asymmetric Eckart barrier does decrease from the silane to monomethylsilane as does the potential energy of activation. This correlation suggests that the present results could be explained by tunneling. However, the predicted magnitudes of the tunneling ratios are much lower than would be necessary to explain the data.

The discrepancy between experiment and theory could be due to either inaccurate data or an inadequate reaction model. The good agreement between the measured (atom excess) and inferred (reactant excess) abstraction rate constants through consistent stoichiometric arguments for all eight reactions is evidence that the data are accurate. Also the comparison between the present results and other workers, where possible, is adequate and gives confidence in the abstraction rate constants. The kinetic role of certain unobservable species such as vibrationally excited hydrogen cannot explain the discrepancy. If such a species was reacting with silanes, substantial silane depletion rates should have been observed, for example, in the H in excess with SiH_4 and the H and D in excess with $(CH_3)_3SiH$ systems. As already mentioned, no substantial depletion was observed.

On the other hand, there is no question but that the BEBO model, which has been adopted as the reaction model, is too simple. A more sophisticated theoretical treatment at the present time is not called for since there are still ambiguities in the kinetic parameters which are needed for such calculations. For example, the best estimates of kinetic parameters give 6.2 kcal/mol (Table III) for the potential energy of activation for H or D with SiH_4. This value should be nearly equal to the activation energy, but the recently measured value for D + SiH_4 is 2.5 kcal/mol.[5] Also a relative method for H + SiD_4 gives 3.2 kcal/mol.[6] Both of these values are similar to that found in the D + $(CH_3)_3SiH$ case.[2] This observation may be evidence that the linear abstraction complex used in the BEBO formulation is entirely inadequate and that some other more complicated intermediate configuration resulting in abstraction is more appropriate. A five-bonded silicon complex utilizing the d orbitals of silane has been suggested.[20] The present results neither confirm nor deny the possibility of such a five-bonded system. However they suggest that

such a complex is not vibrationally activated and that its lifetime is small in comparison to the collision rate. Thus, it should be considered a nonlinear three-centered transition state. Whether such reaction models can predict the isotope effects presented here is a subject of further research.

References and Notes

(1) G. K. Moortgat, Ph.D. Thesis, University of Detroit, 1970; *Diss. Abstr. B,* **31,** 1879 (1970).
(2) M. A. Contineanu, D. Mihelcic, R. N. Schindler, and P. Potzinger, *Ber. Bunsènges. Phys. Chem.,* **75,** 426 (1971).
(3) J. Hong, Ph.D. Thesis, University cf Detroit, 1972; G. J. Mains, private communication.
(4) K. Obi, H. S. Sandhu, H. E. Gunning, and O. P. Strausz, *J. Phys. Chem.,* **76,** 3911 (1972).
(5) D. Mihelcic, P. Potzinger, and R. N. Schindler, *Ber. Bunsenges Phys. Chem.,* **78,** 82 (1974).
(6) P. Potzinger, L. C. Glasgow, and B. Reimann, *Z. Naturforsch. A,* **29,** 493 (1974).
(7) J. R. Barker, D. G. Keil, J. V. Michael, and D. T. Osborne, *J. Chem. Phys.,* **52,** 2079 (1970).
(8) J. A. Cowfer, D. G. Keil, J. V. Michael, and C. Yeh, *J. Phys. Chem.,* **75,** 1584 (1971).
(9) G. P. van der Kelen, O. Volders, H. van Onckelen, and Z. Eeckhaut, *Z. Anorg. Allg. Chem.,* **338,** 106 (1965).
(10) T. L. Pollack, H. S. Sandhu, A. Jodhan, and O. P. Strausz, *J. Am. Chem. Soc.,* **95,** 1017 (1973).
(11) W. L. Hase and J. W. Simons, *J. Chem. Phys.,* **52,** 4004 (1970).
(12) W. L. Hase and J. W. Simons, *J. Organometal. Chem.,* **32,** 47 (1971).
(13) W. L. Hase, W. G. Brieland, P. W. McGrath, and J. W. Simons, *J. Phys. Chem.,* **76,** 459 (1972).
(14) W. L. Hase, C. J. Mazac, and J. W. Simons, *J. Am. Chem. Soc.,* **95,** 3454 (1973).
(15) For original references, see ref 4 and 14.
(16) B. S. Rabinovitch and D. W. Setser, *Adv. Photochem.,* **3,** 1 (1964).
(17) J. A. Cowfer and J. V. Michael, submitted to *J. Chem. Phys.*
(18) H. S. Johnston, "Gas Phase Reaction Rate Theory", Ronald Press, New York, N.Y., 1966.
(19) J. Bigeleisen and M. Wolfsberg, *Adv. Chem. Phys.,* **1,** 15 (1958).
(20) L. C. Glasgow, G. Olbrich, and P. Potzinger, *Chem. Phys. Lett.,* **14,** 466 (1972).

The Structural Isomerization $CH_2{=}C{=}CH_2 \rightleftarrows CH_3{-}C{\equiv}CH$. Studies with a Single Pulse Shock Tube

Assa Lifshitz,* **Michael Frenklach,**[1]

Department of Physical Chemistry, The Hebrew University, Jerusalem, Israel

and Alexander Burcat

Department of Aeronautical Engineering, Technion, Israel Institute of Technology, Haifa, Israel *(Received November 5, 1974)*

The allene → propyne isomerization highly diluted in an inert gas was studied behind reflected shocks in a single-pulse shock tube. The temperature range covered was 1030–1220°K and pressures (P_5) varied between 1.2 and 6 atm. Under these experimental conditions the isomerization is very "clean". Only 0.17% of the decomposition products was found after 30% of the allene had isomerized. The isomerization is first order with respect to allene and very slightly dependent on the total pressure under the above-mentioned experimental conditions. Around 5 atm the first-order rate constant is $k_{uni} = 10^{13.17 \pm 0.60} \exp\{-(60.4 \pm 3.1) \times 10^3 / RT\}$ sec^{-1}, with an overall power dependence of 0.2 on the total density. All the data points fit an equation $k_{uni} = 10^{\alpha} \exp(-E/RT)\rho^{\beta}$ with $\alpha = 14.17 \pm 0.66$, $E = 61.2 \pm 2.5$ kcal/mol, and $\beta = 0.20 \pm 0.09$ where ρ is the total density in units of mole/cc and 10^{α} is in sec^{-1}. Several shocks run in the propyne → allene direction gave rate constants which were by a factor of ~2.3 smaller than those of the allene → propyne direction. This value of 2.3 is smaller than the equilibrium constant calculated from the difference in $\Delta F_f°$ of the two isomers at 1100°K. Shocks which were run with mixtures of 1% $CD_2{=}C{=}CD_2$ and 1% $CH_2{=}C{=}CH_2$ and the analysis of the isotope distribution in the products proved the reaction to be pure unimolecular.

I. Introduction

The allene → propyne isomerization takes place by the removal of a hydrogen from one carbon atom and the attachment of a hydrogen to another carbon in the molecule. A single bond and a triple bond are thus formed to replace two double bonds. This process can take place by a unimolecular migration of the hydrogen atom from one end of the molecule to the other. It may also proceed via the formation of four-center dimers or by some free-radical mechanism. By the study of the kinetics of the reaction, the decomposition that accompanies the isomerization, and the isotope distribution of the product when labeled reactant is being used, the mechanism of the isomerization can be clarified.

Although this isomerization is rather straightforward, very little attention has been devoted to its study. Only one kinetic investigation has come to our attention.[2] This investigation presents the isomerization as one out of a number of reactions that take place when allene or propyne is heated to high temperatures. Using a flow system, Levush et al.[2] determined the first-order rate constants of the isomerization over the temperature range 900–1150°. With mixtures of 1.23 and 2.26% propyne and 1.10% allene in nitrogen at an overall pressure of 1 atm the following rate constants were obtained $k_{A \to P} = 4.4 \times 10^{11} \exp(-54.7 \times 10^3/RT)$ sec^{-1} and $k_{P \to A} = 2.0 \times 10^{11} \exp(-55.2 \times 10^3/RT)$ sec^{-1}. The fact that the two propyne mixtures gave the same profiles of conversion vs. time led the authors to the conclusion that the reaction was first order with respect to the isomerized molecule. They did not look, however, at the effect of the total pressure on the isomerization nor did they try to study the mechanism of the reaction.

The allene → propyne isomerization was also mentioned in a series of papers by Sakakibara[3,4] who demonstrated that the structural isomerization was considerably faster than the decompositions. He did not, however, calculate rate constants.

In this article we present a detailed investigation of the allene → propyne isomerization behind reflected shocks in a single pulse shock tube. Rate constants, reaction orders, and details on the mechanism are presented.

II. Experimental Section

A. Apparatus. The isomerization reaction was studied in a 2-in. i.d. single-pulse shock tube. The driven section was 13 ft long made of "double tough" Pyrex tubing including an 11-in. stainless steel test section. The driver section was constructed from brass and its length could be adjusted in small steps in order to achieve the best cooling conditions. A 36-l. dump tank was connected to the driven section near the diaphragm area to prevent reheating of the gas by doubly reflected shock waves. The driver section was separated from the driven section by Mylar polyester films of various thickness. A full description of the shock tube and the details of its operation has already been discussed in previous publications.[5]

Before each test run, the tube was pumped down to several hundredths of a micron. The leak and/or degassing rate was approximately 2×10^{-5} Torr/min. The vacuum in the tube was measured with a cold cathode gauge located near the end plate of the driven section.

Incident shock velocities were measured from which the reflected shock parameters were calculated. This was done with two miniature high-frequency pressure transducers (Vibrometer Model 6QP500) the output of which was fed into a home-built period meter, accurate to 0.1 μsec. Dwell times corresponding to the location of one of the transducers were recorded on the oscilloscope and could be determined from the pictures to ±10%. These dwell times were later corrected and averaged as has been discussed in a previous publication.[6]

TABLE I: Test Mixtures and Experimental Conditions of the Seven Groups of Experiments

Group	Composition	p_1 range, Torr	T_5 range, °K	No. of shocks run	Symbol used in figures
1A	0.25% allene	178–224	1060–1200	29	■
2A	1% allene	169–223	1052–1198	20	●
3A	1% allene	46–58	1040–1217	19	●
4D	1% allene-d_4	198–218	1027–1212	15	+
5P	0.25% propyne	190–210	1083–1151	7	▲
6P	1% propyne	194–198	1039–1109	6	●
7P	1% propyne	49–55	1051–1160	9	♦

B. Materials. Seven reaction mixtures, three containing allene, one containing allene-d_4, and three containing propyne (all diluted in argon), were prepared on a high-pressure stainless steel line and were stored in stainless steel cylinders at approximately 100 psi. The cylinders were baked prior to their use and were later pumped down to 2 × 10⁻⁵ Torr. The seven reaction mixtures and some additional information are presented in Table I.

A number of tests were also run with a mixture of 1% allene and 1% perdeuterioallene for isotope distribution studies.

The allene and the propyne used were obtained from the Matheson Gas Co. Before the preparation of the mixtures, a portion of the allene was transferred into a glass bulb for removal of impurities. It was frozen in liquid N_2, pumped on, and then thawed out. This was repeated several times. It was later frozen in a methylcyclohexane–liquid N_2 bath and pumped on for some time. The final analysis of the allene showed 0.00022% CH_4, no traces of C_2H_4 or C_2H_6, 0.001% C_2H_2, and 0.10% propyne. Following the same procedure, the propyne showed in the final analysis 0.0003% CH_4, no traces of C_2H_4 or C_2H_6, 3.9% C_2H_2, and 0.425% allene. The cleaning procedure in the propyne increased slightly the acetylene from 3.6 to 3.9%, but decreased the allene contamination from 2.1 to 0.425%. We could not decrease the percentage of acetylene in the propyne.

The perdeuterioallene was purchased from Merck Sharp and Dohme of Canada, Ltd. A mass spectrometric analysis showed approximately 9% C_3D_3H and 91% C_3D_4. A gas chromatographic analysis showed 0.024% propyne and almost undetectable quantities of the other hydrocarbons mentioned above.

The argon used was Matheson Grade listed as 99.9995% pure. The driver gas was helium prepurified grade.

C. Analysis. Samples were taken from the end block of the driven section in 50-cc glass bulbs and were analyzed for allene and propyne on a Packard 800 series gas chromatograph using a flame ionization detector. A Porapak N column at 85° separated the allene from the propyne. At very low extents of reaction where the ratio [propyne]:[allene] did not exceed 1:100, the analyses were carried out at

65° to increase the separation. Runs at high extent of reaction were analyzed also for decomposition products. This was done at an initial temperature of 40° which was gradually raised to 85° with a Packard Model 846 temperature programmer. At the highest temperature (1217°K) tested, the following decomposition products were observed: CH_4, 0.067%; C_2H_4, 0.071%; and C_2H_2, 0.16%. In this run 27.6% conversion to propyne has occurred.

The mass spectral analysis of the pure C_3D_4 was performed on a Varian-MAT Model 311 mass spectrometer. Mixtures of 1% C_3D_4 + 1% C_3H_4 (allene), shocked and unshocked, were analyzed on the GNOM, Varian—MAT Model 111 GC-MS, using Porapak N column at 85°. The mass spectrum of each substance was recorded photographically when reaching the peak on the gas chromatograph detector (total ionization detector).

III. Computations

A. Reflected Shock Parameters. The reflected shock parameters were calculated from the measured incident shock velocities using the three conservation equations and the ideal gas equation of state. The enthalpies of allene and propyne were taken from the Americal Petroleum Institute Project No. 44,[7] and were presented as six-term polynomials. The polynomial coefficients were calculated by the least-squares method. The calculations were carried out on a C.D.C. 6600.

B. Dwell Times. The reaction dwell times were recorded as the time interval between the arrival of the reflected shock wave and the expansion wave to the transducer located farthest from the end plate. The dwell time at this point is considerably smaller than the average dwell time which must be introduced into the kinetic equations. The measured dwell time must be corrected for its variation along the test section of the driven section and for the change in the location of the gas during the expansion process. These two corrections require the knowledge of the shock parameters and the final pressure in the shock tube, P_7. The equation which relates the corrected dwell time t_c with the measured one t_m is[6]

$$t_c = t_m + \left\{ b_m - \frac{1}{2} d_f (P_7/P_1)/(\rho_5/\rho_1) \right\} \left(\frac{1}{u_5} + \frac{1}{a_5} \right) \quad (1)$$

where b_m is the distance between the transducer which measures t_m and the end plate, d_f is the length of the sampling zone, ρ_5/ρ_1 is the compression ratio behind the reflected shock, u_5 is the reflected shock velocity, and a_5 is the speed of sound at T_5.

IV. Results and Discussion

A. Rate Constants. In order to determine the reaction order, the rate constants and the activation energy of the reaction, seven groups of experiments were carried out. Four started from allene and three started from propyne. The seven groups and their experimental conditions are listed in Table I. In Table II three representative shocks from each one of the seven groups are listed in detail. Owing to the very high purity of the allene used, conversions as low as a few tenths of 1% could be accurately measured and a variation of almost 2 orders of magnitude in the isomerization rate constant could be covered, considerably below equilibrium.

We have chosen the first three groups of experiments in such a way that both the effect of the total pressure and the concentration of the reacting molecule on the first-order

TABLE II: Details of Three Representative Tests from Each of the Seven Groups of Experiments

| Group | Composition | p_1, Torr | T_5, °K | Dwell time, msec | | P_5, atm | Conversion (t) - conversion (0), % | k_{uni}, sec^{-1} |
				t_m	t_c			
1A	0.25% CH_2=C=CH_2	207	1081	1.78	2.46	4.48	2.1	8.5
		204	1126	1.78	2.45	4.74	6.7	28.7
		179	1200	1.67	2.30	4.64	30.4	168
2A	1% CH_2=C=CH_2	217	1052	1.69	2.41	4.70	1.0	4.2
		200	1101	1.72	2.42	4.70	3.4	14.4
		186	1151	1.72	2.39	4.73	11.5	52.4
3A	1% CH_2=C=CH_2	56	1040	1.83	2.54	1.19	0.5	2.0
		52	1111	1.69	2.34	1.24	3.2	13.9
		57	1216	1.56	2.17	1.59	27.1	154
4D	1% CD_2=C=CD_2	198	1027	1.61	2.33	4.11	0.46	2.0
		200	1101	1.44	2.14	4.70	2.4	16.2
		215	1212	1.67	2.32	5.97	33.2	188
5P	0.25% CH_3—C≡CH	195	1083	1.69	2.38	4.24	1.2	5.4
		194	1116	1.68	2.34	4.44	2.0	9.0
		197	1151	1.75	2.41	4.75	4.6	21.5
6P	1% CH_3—C≡CH	197	1039	1.78	2.48	4.17	0.4	1.6
		197	1063	1.69	2.40	4.35	0.6	2.5
		195	1109	1.75	2.43	4.64	2.1	9.3
7P	1% CH_3—C≡CH	55	1051	1.81	2.50	1.19	0.5	1.8
		54	1086	1.89	2.57	1.24	0.7	2.8
		55	1160	1.69	2.32	1.42	4.5	22.0
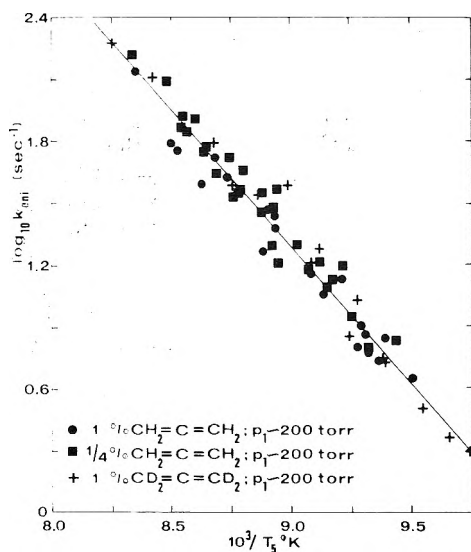
Figure 1. A plot of log k_{uni} vs. $1/T$ for groups of experiments 1A, 2A, and 4D (allene). The points of these three groups scatter along one line indicating first order with respect to allene.

Figure 2. A plot of log k_{uni} vs. $1/T$ for experiments of group 3A (allene). These points are slightly below the ones shown in Figure 1 indicating a weak dependence on the total pressure. The line obtained by Levush et al. is shown for sake of comparison.

rate constant could be independently determined. In Figure 1, log k_A is plotted vs. $1/T$ for groups of experiments 1A, 2A, and 4D. The points of these three groups scatter along one line indicating no effect of the allene concentration on the first-order rate constant and no obvious isotope effects. A least-squares analysis of the 1A, 2A, and 4D data points yields $k_A = 10^{13.17\pm0.6} \exp\{-(60.4 \pm 3.1) \times 10^3/RT\}$ sec^{-1}.

The data points of group 3A are slightly lower than those of the high-pressure runs. Since the difference is very small ($\Delta \log k \sim 0.12$) they are presented on a separate figure (Figure 2). This small difference indicates that under our experimental conditions the reaction does not lie in the

first-order limit but very close to it. The overall reaction order is

$$n = 1 + \frac{\Delta \log k}{\Delta \log P} \sim 1.2$$

The slopes of the lines in Figures 1 and 2 are almost identical although one would expect the slope in Figure 2 to be slightly smaller than that in Figure 1. A least-squares analysis which includes all the points of the four groups of experiments together, to fit an equation of the type $k = 10^\alpha \exp(-E/RT)\rho^\beta$ yields $\alpha = 14.17 \pm 0.66$, $E = 61.2 \pm 2.5$, and $\beta = 0.20 \pm 0.09$ where ρ is the total density of the reaction mixture in units of mole/cc and 10^α is in units of sec^{-1}.
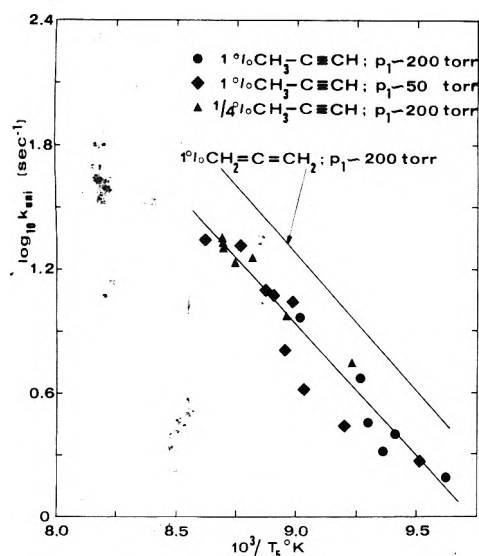
Figure 3. A plot of log k_{uni} vs. $1/T$ for groups of experiments 5P, 6P, and 7P (propyne). The line corresponding to the high-pressure allene points is also shown for comparison. The distance between the lines gives the value of K_{eq}.

Our low-pressure experiments which were run at the same pressure as the ones described by Levush et al.[2] lie above their corresponding points by $\Delta \log k \sim 0.28$ at $1100°K$. Also, our activation energy 60.4 ± 3.1 is slightly higher than theirs, which is 54.7 kcal/mol. However, in view of the fact that the experimental techniques are completely different and that their temperature range is almost $200°$ higher than ours, the agreement between the results can be considered very good. The slightly lower activation energy obtained in the flow experiments might be a result of some catalytic effect of the very narrow flow tube used.

B. The Equilibrium Constant. In order to evaluate the rate constant of the isomerization from the measured extent of reaction, the equilibrium constant must be known. The rate constant k_A is given by

$$k_A t = -\{K/K + 1)\} \ln \frac{1 - \{(K + 1)/K\}x_t/a}{1 - \{(K + 1)/K\}x_0/a} \quad (II)$$

where the subscript A denotes the allene → propyne direction, x_0 and x_t are the initial concentration of propyne and its concentration at time t, respectively, and a is the sum [allene] + [propyne]. K is the equilibrium constant of the reaction.

$RT \ln K$ is given by the difference in $\Delta F_f°$ of the two isomers. This is however a very small difference between two big numbers, and the error in the calculated K can be quite high. In fact, the ratio [propyne]/[allene] observed at the high temperature shocks was not equal to the one calculated from the difference in $\Delta F_f°$ of the two isomers although equilibrium has been attained in the shock tube. It was considerably smaller. The purpose in studying the propyne → allene direction was the evaluation of the equilibrium constant from the ratio of the rate constants of the forward and backward reactions.

In Figure 3 a plot of log $k_{(P)}$ vs. $1/T$ for groups of shocks 5P, 6P, and 7P is shown. It is hard to decide whether the low-pressure points are really below the high-pressure ones because of the relatively high scatter in the data. The best line which connects the high-pressure data points is clearly below the one which appears in Figure 1. From the vertical distance between the lines one can calculate the equilibrium constant of the allene ⇌ propyne conversion. The dis-

TABLE III: Cracking Pattern of Propyne[a] (a) and the Mass Spectrum of Propyne(b) Obtained from a Shocked Mixture of 1% CD_2=C=CD_2 and 1% CH_2=C=CH_2 in Argon (T_5 = 1190°K)

	Parent	–H	–2H	–3H	–4H
a. Ion Rel intensity	1	$f_1 = 0.92$	$f_2 = 0.36$	$f_3 = 0.28$	$f_4 = 0.09$
b. m/e	44	43	42	41	40	39
Intensity	0	78	27	45	100	110

[a] Reference 8.

tance corresponds to a value of 2.3 for K_{eq}. The heat of reaction is rather small (~ 2 kcal/mol) and it is impossible to isolate changes in K over the temperature range covered in this study because of the high activation energy (~ 60 kcal/mol). We therefore used the value of 2.3 for K_{eq} in our eq II over the entire range. This is acceptable as the rate constant k is not very sensitive to the value of the equilibrium constant K if the conversions are not too high.

The value of K calculated from the difference in $\Delta F_f°$ of the two isomers at $1100°K$ is 3.45, considerably higher than the value of 2.3 observed experimentally. In fact, 2.3 is roughly the ratio of the two isomers observed in the gas chromatograph from high-temperature shocks where equilibrium has been attained in the shock tube.

C. Studies with Perdeuterioallene. There are number of ways to investigate whether a reaction is unimolecular or whether it proceeds via another mechanism. The easiest one is the isotope labeling of the reactant and the examination of the isotopic distribution in the product. In the allene → propyne isomerization, the unimolecularity of the reaction can be examined by shocking a 50–50 mixture of CH_2=C=CH_2 and CD_2=C=CD_2. If the formed propynes are unscrambled, i.e., only the CH_3–C≡CH and CD_3–C≡CD are present, the reaction is clearly unimolecular. On the other hand, if C_3D_3H and C_3H_3D are observed then either isotope exchange reaction has occurred or the reaction is not unimolecular. The temperature dependence of the extent of scrambling, if scrambling is indeed found, can help to distinguish between these two possibilities.

The mass spectrum of the propyne formed in a mixture of 1% CD_2=C=CD_2 and 1% CH_2=C=CH_2 in argon at T_5 = 1190°K is shown in Table III. The cracking pattern of the propyne[8] molecule is also shown for the interpretation of the spectrum. To our great surprise, no peak at m/e 44 (CD_3–C≡CD) above the CO_2 background was observed, but a very intense peak at m/e 43 (C_3D_3H) showed up, as if the isomerization is not unimolecular or a lot of isotope exchange has occurred (in fact, more than the symmetry would allow). On the other hand, very intense peaks at m/e 40 and 39, which indicate the presence of large quantities of CH_3–C≡CH were observed as if the isomerization *is* unimolecular. The strange result was explained when 1% CD_2=C=CD_2 (in the absence of undeuterated allene) was shocked and then analyzed in the GC–MS. Instead of the perdeuterated propyne which should have been formed and shown up at m/e = 44, there was none at that mass but instead intense peaks appeared at m/e 43 and 41. This behavior was interpreted in view of the acidity of the acetylenic hydrogen in the propyne. CD_3–C≡CD behaves as a monobasic acid and exchanges one deuterium atom with the water absorbed on the gas injection system of the GC–MS or on the walls of the ion source of the mass spectrometer. The absence of a peak at m/e 44 and the appear-

ance of one at m/e 43 for propyne in the shocked mixture of 1% CH_2=C=CH_2 and 1% CD_2=C=CD_2 is no indication of scrambling during the reaction.

When this discrepancy has been cleared up, the mass spectrum was analyzed in order to isolate the peak heights of C_3H_4 and C_3H_3D from the contribution of the cracking pattern of the C_3D_3H and to examine the ratio of these two substances. In the analysis we have assumed that m/e 42 arises only from the parent ion C_3D_3H by removal of the hydrogen and that no double scrambling has occurred. (This assumption is not critical but simplifies the analysis.)

The ion which is produced by the removal of one hydrogen from the parent has an intensity of f_1 = 0.92 relative to the parent ion.[8] m/e 42 is the ion produced by the removal of H, and 41 by the removal of D. One can readily see in Table III that the sum of the peak heights of the m/e 42 and m/e 41, namely, 72 (in arbitrary units), is equal to $78f_1$. Clearly, within the limit of the experimental accuracy all the contribution to m/e 42 and 41 arise from the parent ion and there is no contribution from the original C_3H_3D or $C_3D_2H_2$ ions. It is interesting to note that the ratio (m/e 41):(m/e 42) is not 3, as has been expected, but considerably smaller. It seems that the removal of the acetylenic hydrogen (HC≡C—) is easier than the removal of a hydrogen from the methyl group in the pyropyne ion.

m/e 40 and 39 have very intense peaks; their major part is due to the existence of C_3H_4.

From the evidence gathered here, namely, the absence of C_3H_3D and the presence of a high intensity of C_3H_4, one can conclude that the propyne formed in the isomerization reaction is unscrambled.

D. The Mechanism of Isomerization. There are in principle three major reaction paths that can lead to isomerization: (1) a unimolecular reaction:

$$CH_2=C=CH_2 \longrightarrow [CH \overline{\equiv\equiv} C \overline{---} CH_2] \longrightarrow HC≡C—CH_3$$
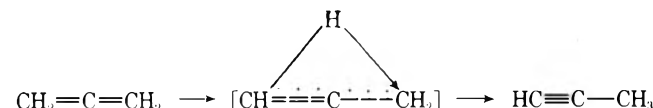
(2) a bimolecular four-center isomerization:

$$CH_2=C=CH_2 \atop CD_2=C=CD_2 \longrightarrow \begin{bmatrix} CH\overline{\equiv\equiv}C\overline{---}CH_2 \\ H \qquad\qquad D \\ CD_2\overline{---}C\overline{\equiv\equiv}CD \end{bmatrix} \longrightarrow \begin{matrix} HC≡C—CH_2D \\ \\ CD_2H—C≡CD \end{matrix}$$
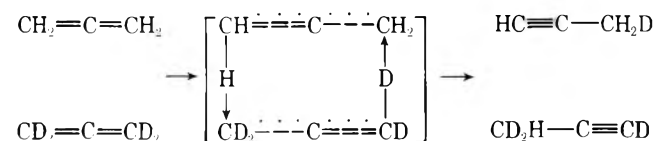
(3) isomerization via free-radical reactions:

$$CH_2=C=CH_2 \longrightarrow CH_2=C=\dot{C}H + H$$
$$CH_2=C=\dot{C}H \rightleftharpoons \dot{C}H_2—C≡CH$$
$$\dot{C}H_2—C≡CH + RD \longrightarrow CH_2D—C≡CH + \dot{R}$$
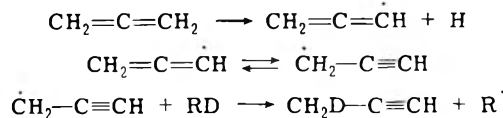
The experimental results described in the previous section indicate that mechanism 1 is operative to the largest extent and that there is very little contribution, if any, from the reaction paths 2 and 3. Unit reaction order with respect to the allene (Figure 1), clearly shows that the reaction is not bimolecular and that the isomerization does not proceed via the formation of a four-center dimer. In addition, mechanism 2 should have produced scrambled propynes in a shocked mixture of C_3D_4 and C_3H_4. As has been shown, only unscrambled products were observed. Mechanism 3 can also be ruled out on the basis of the extent of decomposition which accompanies the isomerization, in addition to the results of the isotope distribution studies. The production of free radicals in the system can lead to the production of other substances. The free radicals such as $CH_2=C=\dot{C}H$ and $\dot{C}H_2—C≡CH$ can undergo unimolecular decomposition as many C_3 free radicals do,[9] and thus produce a variety of decomposition products. It has been shown in the experimental section that even at the highest temperatures, where close to 30% of the allene has isomerized, the overall extent of decomposition did not exceed 0.17% of the initial allene concentration. In addition, mechanism 3 should have produced scrambled propynes which were not observed.

It is believed, therefore, that the allene → propyne isomerization is a unimolecular reaction.

References and Notes

(1) In partial fulfillment of the requirements for a Ph.D. Thesis, to be submitted to the Senate of the Hebrew University of Jerusalem by M.F.
(2) S. S. Levush, S. S. Abadzhev, and V. U. Shevchuk, *Neftechimia,* **9,** 215 (1969).
(3) Y. Sakakibara, *Bull. Chem. Soc. Jpn.,* **37,** 1262 (1964).
(4) Y. Sakakibara, *Bull. Chem. Soc. Jpn.,* **37,** 1268 (1964).
(5) A. Bar-Nun and A. Lifshitz, *J. Chem. Phys.,* **47,** 2878 (1967).
(6) A. Lifshitz and P. Schechner, *Isr. J. Chem.,* **12,** 729 (1974).
(7) F. D. Rossini, et al., "Selected Values of Physical and Thermodynamic Properties of Hydrocarbons and Related Compounds", Carnegie Press, Pittsburgh, Pa., 1953.
(8) A. Cornu and R. Massot, "Compilation of Mass Spectral Data", Heyden & Son, Ltd., 1966.
(9) S. W. Benson and H. E. O'Neal, *Nat. Stand. Ref. Data Ser., Natl. Bur. Stand.,* **No. 21** (1970).

CS–O₂ Flame Reaction Chemistry[1]

R. J. Richardson

McDonnell Douglas Research Laboratories, McDonnell Douglas Corporation, St. Louis, Missouri 63166

(Received May 28, 1974; Revised Manuscript Received February 28, 1975)

A low-pressure flame fueled with CS and O_2 is reported. The CS–O_2 mixture is hypergolic at room temperature and exhibits the characteristics of a branched chain reaction. Measurements of the velocity and temperature of the flame are reported, and a discussion of the probable chemistry based on the observations of the stable end products of the flame is included. In a separate experiment, the absolute rate of the bimolecular reaction between CS and O_2 was measured. The dominant reaction path produces OCS and O and has a rate constant of $2.7 \pm 1 \times 10^5$ cm³/mol sec at 293 K.

I. Introduction

Interest in the CO chemical laser[2] has prompted us to consider the chemistry of the CS_2–O_2 system. Although the basic reaction sequence responsible for vibrationally excited CO in the chemical laser is well understood, the detailed chemistry of this system is complicated by the multitude of possible reactions.[3,4] Many of the rates for the reactions in which short-lived species, such as CS and SO, participate are unknown because of the difficulty in handling these reactive molecules. The CS chemistry becomes critical if the CO chemical laser is fueled with CS, which has many advantages over CS_2-fueled systems.[5] For this reason and because of conflicting reports[6–8] about the rate of the reaction between CS and O_2, we have investigated the reactivity of CS with O_2.

The two possible paths for the reaction are

$$CS + O_2 \rightarrow OCS + O \quad (1)$$

$$CS + O_2 \rightarrow SO + CO \quad (2)$$
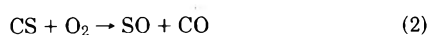
If reaction 2 was fast enough to compete with the laser pumping reaction[4]

$$CS + O \rightarrow CO^* + S \quad (3)$$

it would be necessary to include it in explanations of the chemical sequence responsible for the production of CO in the chemical laser. If reaction 1 was fast, it might be an important source of O for reaction 3 and permit experimental scaling of the CO laser. The rate for the direct reaction has been determined to be too slow to provide the needed O in an homogeneous mixture; however, a chain reaction process leading to the chain consumption of CS has been observed under the proper conditions. The laser pumping reaction is believed to be a major step in this chain which produces a flame characterized by a white chemiluminescence and CO, SO_2, OCS, and S_2O as end products.

The fast-flow reactor method of measuring a bimolecular rate constant was used to determine the rate of reaction 1 under dilute conditions. The method consists of monitoring changes in concentration of one of the molecules in a flow stream as the injection point of the second molecule is varied.

II. Experimental Section

Reaction Rate. The CS molecule is not short-lived because it is unstable, but because of a heterogeneous wall reaction that produces CS_2 and solid carbon at the wall.[9] Nevertheless, this reaction is slow enough that CS can be propagated downstream in a conventional fast-flow reactor.

The apparatus used to measure the rate of reaction 1 is illustrated in Figure 1. The CS was obtained from the dissociation of CS_2 which was injected into the positive column of an Ar dc discharge. Solid products and excess CS_2 were removed from the flow stream by an ethanol slurry trap. The wall reaction mentioned above produces CS_2 from CS so that at the detection point in these experiments the CS to CS_2 ratio was about six.

Instead of a movable injector, a two-point injector was used. Care was taken to ensure that the two flow paths and injectors were identical in every respect. Ar could be introduced into the flow stream to experimentally verify that no aerodynamic effects were present as a result of differences in the injectors. In addition, the O_2 mass spectrometer output signals were compared for the two injectors with Ar flowing in the main reactor to verify that the resultant concentration of O_2 was the same for the two injection points. Instabilities in the CS concentration associated with a movable injector were eliminated by this two-port injector.

The temperature-controlled reaction region consisted of a 55-mm diameter Pyrex tube wrapped with heating tape and insulation. Copper–constantan thermocouples were used to monitor the temperature. The detection apparatus consisted of a quadrupole mass spectrometer (Uthe Technology 100C) with a sampling tube having a 0.01-mm orifice.

A 300-cfm rotary vacuum pump (Stokes 412H) maintained the flow. This very slow reaction required the pump to be throttled, since flow velocities only of the order of 100 cm/sec were required.

Gas flows were controlled with needle valves and the flow rates determined from precalibrated rotameter flow meters (Matheson 600 series). The CS_2 was distilled and degassed before use. Research grade O_2 (99.996%, Matheson) and high-purity Ar (99.998%, Air Products) were used in the experiments. The pressure at various points in the system was monitored with a capacitance manometer (MKS Type 144).

CS–O_2 Flame. The apparatus used to observe the CS–O_2 flame is illustrated in Figure 2. With this apparatus the flame can be operated as either a premixed or diffusion flame depending on whether the O_2 is injected at point A or
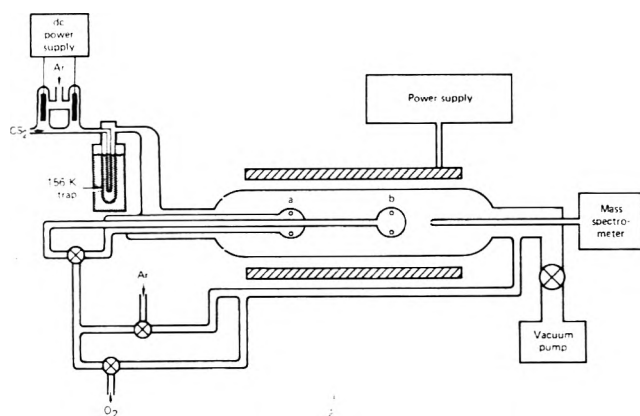
Figure 1. The fast flow reactor apparatus used to measure the rate of the reaction of CS with O_2.
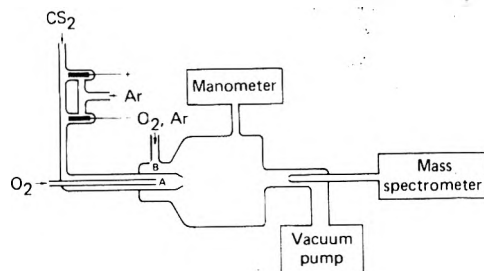
Figure 2. Apparatus used to observe the CS–O_2 flame.

B. Also, the ambient pressure and/or the diffusion atmosphere of the flame can be controlled by injecting gases such as Ar at point B. Both the nozzle burner position and the O_2 injection point A are adjustable by means of O-ring fittings.

The CS$_2$, Ar, and O_2 flows were controlled by needle valves and the flow rates determined from precalibrated flow meters (Matheson 600 series), which are not depicted. The CS/CS$_2$ ratio and thus the CS yield from the discharge were determined from the 44 and 76 mass peaks observed with the previously calibrated quadrupole mass spectrometer. Concentration ratios of the end products of the flame to the Ar diluent were also determined with the mass spectrometer. Calibration of the mass spectrometer was performed by comparing the signals obtained from mixtures of metered flows of Ar and each of the stable gases under flow conditions similar to those used for the flame. The calibration factor for the unstable species S$_2$O was interpolated from a plot of the calibration factors against mass number. The calibration factor for CS was measured directly by the procedure of ref 9. Pressure in the combustion chamber was monitored with the capacitance manometer.

The backing pressure for the CS$_2$ vapor was provided by reagent grade liquid CS$_2$ held at 20° by means of a water bath. Ultrapure O_2 (99.994%, Air Products) and high-purity Ar (99.998%, Air Products) were used in the study of the flame.

The temperature of the flame was determined by monitoring a chromel–alumel thermocouple which was encased in a quartz envelope to prevent catalytic heating due to atom recombination at the metal surface.

Survey optical spectra of the flame were taken through a quartz window (not shown) with a Jarrell-Ash 0.25-m Ebert monochromator.

Electron spin resonance (ESR) spectra were taken in the

2.5-cm section downstream from the combustion chamber with a modified Varian V-4502 spectrometer (not shown).

Results

Reaction Rate. The ratio of the reaction rates for (1) and (2) should be nearly proportional to the concentration of OCS and SO$_2$ observed, since any SO from reaction 2, provided it is not lost to the walls, will be converted to SO$_2$ through the reaction

$$SO + O_2 \rightarrow SO_2 + O \qquad (4)$$

at the flow rates employed. The fate of SO produced by reaction 2 is critical, however, since it can also react with CS to produce OCS

$$CS + SO \rightarrow OCS + S \qquad (5)$$

thereby tending to negate the above analysis. However, if reaction 5 was the source of OCS observed in the flow stream, the OCS to SO$_2$ ratio would depend on the ratio of the reactants, CS and O$_2$. The dominant reaction path was determined from an examination of the percentages of the product species found in the flow stream. Approximately equal molar percentages of CO and OCS were present whereas the percentage of SO$_2$ was an order of magnitude lower. These percentages were found to be independent of the initial concentration ratio of CS to O$_2$ and are therefore most easily explained by assuming that reaction 1 is the dominant path. It is concluded that reaction 1 dominates reaction 2 by at least an order of magnitude.

The observation of comparable concentrations of CO and OCS is consistent with this analysis, since O from reaction 1 will react with CS through the fast reaction 3 to form CO and S. Since O$_2$ makes up a small percentage of the total flow, most of the S from reaction 3 will be lost to the walls, although it cannot be determined whether the SO$_2$ observed in the flow stream results from the SO of reaction 2 or the SO from the relatively fast reaction

$$S + O_2 \rightarrow SO + O \qquad (6)$$

Westenberg and de Haas[10] have considered the case where one of the participating reactants is removed by a wall reaction other than the reaction of interest. Based on their results, the expression relating the kinetic rate constant k of reaction 1 to measurable parameters in a fast-flow reactor is

$$\ln \{[CS]_t/[CS]_{t,[O_2]=0}\} = k[O_2]t \qquad (7)$$

where $[CS]_t$ is the concentration of CS measured at the detector with O$_2$ flowing, $[CS]_{t,[O_2]=0}$ is the concentration measured at the detector with the O$_2$ flow off, $[O_2]$ is the concentration of O$_2$ in the flow stream, and t is the time required for the molecule to reach the detector from the injector. If the time of the interaction is varied by moving the injector, k can be determined from a plot of t vs. $\ln \{[CS]_t/[CS]_{t,[O_2]=0}\}$ for a particular $[O_2]$.

Some of the assumptions implicit in this analysis are: (1) the CS concentration does not vary appreciably in the reactor; (2) mixing at the injector is instantaneous; and (3) the pressure drops sufficiently at the sampling tube so that the reaction effectively stops.

With the two-port injector, expression 7 becomes

$$\ln \{[CS]_b/[CS]_a\} = k[O_2]\Delta t \qquad (8)$$

where $[CS]_a$ and $[CS]_b$ are the concentrations of CS detected at the probe with O$_2$ injected alternately from the two

TABLE I: Experimental Parameters Used in the Measurement of the Rate of the Reaction CS + O$_2$ → OCS + O at 293 and 500°K (Δx = 50.8 cm)

Temp, K	Pressure, Torr	Velocity, cm/sec	Concn × 10^8 mol/cm^3				k, cm^3/mol sec
			[Ar]	[O$_2$]	[CS]	Δ[OCS]	
293 ± 2	1.58	98	5.0	3.2	1.00	5.3 × 10^{-3}	3.1 × 10^5
293	1.30	80	4.8	1.5	1.24	4.1 × 10^{-3}	3.3 × 10^5
293	0.922	100	3.8	0.5	1.00	5.6 × 10^{-4}	4.1 × 10^5
293	0.982	94	3.8	0.5	1.5	5.8 × 10^{-4}	3.6 × 10^5
293	0.707	96	2.2	1.4	0.5	5.0 × 10^{-4}	1.4 × 10^5
293	0.976	70	2.9	2.0	0.77	1.3 × 10^{-3}	1.1 × 10^5
293	0.381	686	1.7	0.25	0.27	2.1 × 10^{-5}	4.0 × 10^5
293	0.440	250	0.89	1.35	0.33	2.3 × 10^{-5}	1.7 × 10^5
293	0.380	460	1.15	0.87	0.40	1.7 × 10^{-5}	2.1 × 10^5
293	0.467	514	1.85	0.78	0.41	1.9 × 10^{-5}	2.2 × 10^5
293 ± 2							2.7 ± 1.0 × 10^5
498 ± 5	1.25	189	3.0	3.0	0.72	2.0 × 10^{-2}	3.4 × 10^6
498	0.830	804	2.9	1.4	0.29	1.1 × 10^{-3}	4.4 × 10^6
493 ± 5	0.721	510	2.2	1.1	0.54	2.5 × 10^{-3}	2.1 × 10^6
493	0.783	458	2.6	1.4	0.32	2.2 × 10^{-3}	4.4 × 10^6
495 ± 5							3.6 ± 0.8 × 10^6
290–500	$k = A$ exp$(-E/RT)$; log A = 8.2 ± 0.5; E = 3.7 ± 0.9 kcal/mol						1.5 × 10^8 × exp$(-3700/RT)$

injectors a and b (see Figure 1), and Δt is the difference in transit time for the two injectors. In these experiments, data were taken for a series of O$_2$ concentrations and flow rates to verify that eq 8 is linear and to determine k.

The rate of reaction 1 is so slow that changes in CS concentration were found to be outside the detection limits of the mass spectrometer. For this reason it was necessary to infer the changes in CS concentration from changes in concentration of the product species OCS. The rate constant was measured at two temperatures, and the results for these temperatures are listed in Table I. The Arrhenius form of the rate constant based on only these two measurements is also included in Table I for completeness; however, the applicability of the Arrhenius form is limited in this case and should not be employed outside the range indicated. The error limits listed in Table I are an indication of the reproducibility of the data and do not take into account systematic errors such as other OCS production or destruction reactions. The two reactions most likely are reaction 5 and

$$OCS + O \rightarrow CO + SO \qquad (9)$$
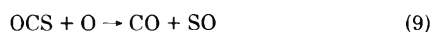
Reaction 5 would tend to increase k artificially but should be unimportant if reaction 1 is dominant. Reaction 9 is also expected to be negligible, since the fast reaction 3 will extract all O from the flow stream when the CS concentration appreciably exceeds that of OCS.

CS–O₂ Flame. The flame ignites spontaneously at room temperature as O$_2$ is added to the CS flow when the concentrations are of the order of [CS] = 0.015 μmol/cm^3 and [O$_2$] = 0.050 μmol/cm^3. A white glow region with a cone-shaped flame front is then observed extending from the nozzle burner (see Figure 3). The remainder of the reactor fills with the familiar SO$_2$ blue chemiluminescence as the O$_2$/CS ratio is increased beyond 1.5. Under these conditions the principal products of the flame are CO, SO$_2$, and S$_2$O, and the temperature of the flame is measured to be near 600° for a reactor pressure of 4 Torr and an O$_2$/CS ratio of 5. The temperature of a CS$_2$/O$_2$ flame in the same
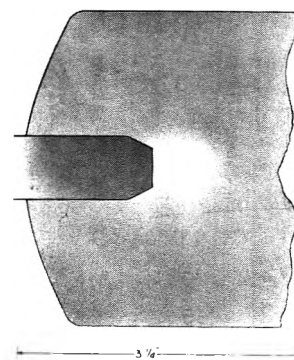
Figure 3. Schematic representation of the premixed flame front observed under oxygen-rich conditions.

apparatus under similar flow conditions was found to be 1100°.

With O$_2$/CS $\sim$ 1, in addition to the white luminescent flame front, a diffuse white glow fills the reactor and the blue SO$_2$ chemiluminescence is not observed, although SO$_2$ is observed among the end products. Comparable quantities of OCS and traces of S$_2$O are also found among the end products. These results are summarized in Table II. The final product ratios depend strongly on the CS/CS$_2$ ratio obtained from the discharge, which varies with time as the discharge tube fills with solid deposits. The concentration profile of the flame in Table II is meant to be representative, since the reproducibility of these data was no better than 20% from day to day. It is important to note, however, that the concentration of the CO product increases only moderately from O$_2$-lean to O$_2$-rich conditions.

The temperature recorded by the chromel–alumel thermocouple inserted at the CS–O$_2$ flame tip is shown in Figure 4 as a function of O$_2$ flow. The recorded temperature was relatively insensitive to changes (50–150 μmol/sec) in the Ar flow. At high pressure and high O$_2$ flow rates ($\sim$5 Torr, $\sim$500 μmol/sec), red streamers emerge from the flame front. Whether these are molecular-size luminescent particles or larger particles emitting black-body radiation is not

TABLE II: Flow Rates of the Initial and Final Species for the CS-O_2 Flame Expressed in μmol/sec[a]

Initial			Final						
CS	O_2	CS_2	CO	SO_2	OCS	S_2O	CS	CS_2	O_2
45	60	10	35	15	10	3	5	5	10
45	190	10	45	45		5			120

[a] The Ar flow is 60 μmol/sec in both cases.
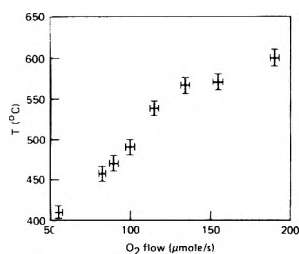
Figure 4. The temperature of the CS-O_2 flame as a function of O_2 flow. The CS flow rate was 45 μmol/sec.

clear, although 6328-Å radiation from a He–Ne laser is not visibly scattered in passing through this zone.

Despite the low mass flows a well-defined cone-shaped flame front was clearly visible for the CS-O_2 premixed flame (see Figure 3). The Gouy method[11] could therefore be employed to determine the approximate flame velocity as a function of O_2 flow rate for a series of O_2 and Ar diluent ratios. An indication of the effect of the Ar diluent on the measured flame velocity is illustrated in Figure 5. The CS_2-O_2 flame in our apparatus did not have a well-defined cone from which a flame velocity could be measured, but the velocity for this flame was estimated to be an order of magnitude smaller than that for the CS-O_2 flame by a comparison of the areas of the two flames.

The optical survey yielded four distinguishable spectra: intense CS ($A^1\Pi \rightarrow X^1\Sigma^+$) bands with their intensity peaking at O_2/CS ratios near 3, weak C_2 Swan bands ($A^3\Pi \rightarrow X^3\Pi$) observed under oxygen-rich conditions, a broad intense peak from 2750 to 4300 Å from the SO_2 blue chemiluminescence, and a weak flat continuum from 3600 to 5600 Å associated with the white chemiluminescence distinguishable under oxygen-lean conditions when the SO_2 blue chemiluminescence was not present.

The presence of O in the blue chemiluminescence was confirmed by observation of the ESR spectra of the $^3P_1$ and $^3P_2$ states of O downstream from the combustion chamber. Comparison with the O_2 spectrum indicated that the O concentration was 3–5% of the O_2 concentration.

Finally, the same white chemiluminescence observed in the flame is observed when Ar is passed through a microwave discharge and introduced at point A in the absence of O_2.

IV. Discussion

The possibility of some active species from the CS_2–Ar discharge, such as Ar ($^3P_1$), playing a role in the ignition of the flame, for example, by the dissociation[12] of O_2, was excluded by running the flame with purified CS obtained by inserting an ethanol slurry (156 K) cold trap in the CS stream.

The most likely initiating reaction is reaction 1. Although the rate of this reaction was found to be slow at
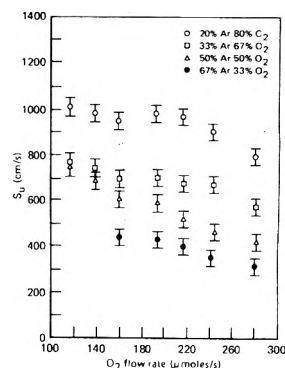
Figure 5. The flame velocity S_u for the premixed CS-O_2 flame as a function of O_2 flow rate and consequently CS-O_2 concentration ratios for a series of O_2–Ar mixtures. The CS flow rate was 45 μmol/sec in each case. The upturn in the flame velocity for low O_2 flow rates is artificial (see text).

room temperature, the production of O by reaction 1 should be sufficient to initiate a chain of the following sequence:

$$CS + O \rightarrow CO^* + S \qquad (3)$$

$$S + O_2 \rightarrow SO + O \qquad (6)$$

$$SO + CS \rightarrow OCS + S \qquad (5)$$

$$SO + O_2 \rightarrow SO_2 + O \qquad (4)$$
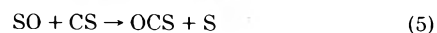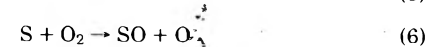
Each of these reactions returns one of the chain carriers S or O to the mixture. Reactions 3 and 6 are well-known features of the CO chemical laser reaction sequence and are relatively fast. As noted previously, most of the CS, even under O_2-lean conditions, is converted to CO apparently through reaction 3. Although (4) and (5) are expected to be slow, they are the most likely reactions to provide chain branching and the end products OCS and SO_2 which are observed under stoichiometric conditions. Without excess oxygen, some of the sulfur is eventually lost to the walls, since sulfur deposits accumulate downstream on the wall under O_2-lean conditions. Loss of chain carriers to the walls apparently prevents preignition in the 25-mm nozzle tube.

If O_2 is in excess, the O concentration builds up sufficiently to consume the remaining OCS and CS_2 through reactions 9 and

$$CS_2 + O \rightarrow CS + SO \qquad (10)$$

These reactions return the chain branching species SO to the mixture, and the reaction

$$SO + O + M \rightarrow SO_2^* + M \qquad (11)$$
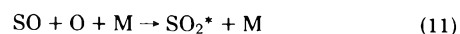
produces the familiar blue chemiluminescence observed in sulfur oxidation reactions. Under these conditions most of the sulfur is converted to SO_2 through one or the other of the reaction paths since no solid wall deposits are observed. In fact, the oxygen-rich flame will consume any deposits

previously accumulated on the walls from the oxygen-lean flame. These deposits apparently incorporate some oxides of sulfur, since a deficiency in the molar concentration of oxygen is always observed in the gas phase for the oxygen-lean flames.

The origin of the S$_2$O is somewhat more speculative but can be accounted for by three-body reactions such as

$$SO + S + M \rightarrow S_2O + M \qquad (12)$$
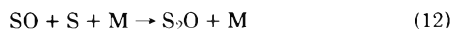
The S$_2$O is either converted to SO$_2$ or lost to the walls downstream, since it is not found as a product downstream under oxygen-rich conditions.

The enthalpy of the product gases in the CS–O$_2$ flame based on the thermocouple reading is a factor of 2 less than the calculated exothermicity of the reaction sequence postulated for the flame. All calculable heat sinks were considered in an attempt to remove this discrepancy. Such effects as heat conduction along the thermocouple leads and conduction to the walls were included in the analysis. Incomplete combustion and unknown heat losses such as conduction to the burner probably account for a major portion of the temperature discrepancy. It is well known, however, that approximately 50% of the energy of reaction 3 enters the long-lived vibrational states of CO rather than the translational energy states.[13,14] The low temperature recorded by the thermocouple could therefore be an indication that vibrationally excited CO is present and is not deactivated by the product gases of the flame.

The fact that a well-defined flame front can be maintained at such low concentrations and pressures indicates that the radical concentration is relatively high in the CS–O$_2$ flame compared with hydrocarbon flames. The high flame velocities measured for this flame also support this view. High radical concentrations would be expected from the branched chain reaction sequence previously discussed, since each of the reaction steps returns either a sulfur or an oxygen atom to the gas mixture.

The white chemiluminescence may arise from the ionization of CS, although attempts to determine whether ions are present in the flame were unsuccessful; the presence of excited CS and C$_2$ indicate that energies of 4 eV are available from reactions in the flame. Although no attempt to determine concentrations of these excited species was made, they are probably present in extremely low concentration and could be the result of three body recombination reactions such as

$$CS + O + O \rightarrow CS^* + O_2 \qquad (13)$$

$$CO^* + O + O \rightarrow CO + O_2 \qquad (14)$$

$$CS + O + O \rightarrow C + SO_2 \qquad (15)$$
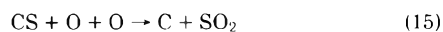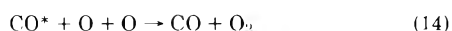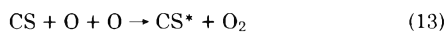
where the asterisk indicates an excited species. The CS (A$^1\Pi \rightarrow$ X$^1\Sigma^+$) bands have been previously observed[15] in O$_2$-lean CS$_2$–O$_2$ flames and (a$^3\Pi \rightarrow$ X$^1\Sigma^+$) bands from interactions between CS$_2$ and Ar (^{3}P$_1$) metastable atoms.[16]

A great many other gas-phase reactions in addition to those listed are possible in this complicated system, but (3) through (6) will dominate for O$_2$-rich mixtures. Under O$_2$-lean conditions, as the flame becomes more diffuse, heterogeneous reactions at the wall undoubtedly are important, however. Under these conditions, a major source of chain termination probably involves the loss of sulfur to the walls. In this connection, it should be mentioned that the upturn in flame velocity shown in Figure 5 for O$_2$-lean conditions is artificial and is a result of the breakdown in the

Guoy method as the flame front becomes diffuse rather than a real increase in velocity.

Although the basic chemistry of the CS–O$_2$ flame is similar in many respects to that postulated for the CS$_2$–O$_2$ flame,[17] it differs in several important aspects. First, the chemistry of the CS$_2$–O$_2$ flame is complicated by the conversion of the CS$_2$ to CS through reaction 10. This reaction is slower than reaction 3 and is expected to retard the overall reaction as well as add its exothermicity to the gases and thereby raise the flame temperature. The increases in temperature observed as the oxygen concentration is increased and the CS$_2$ is consumed in the CS–CS$_2$ mixed fuel flame are undoubtedly caused by this reaction and the highly exothermic reaction 11. Secondly, the low concentration of CS in the CS$_2$–O$_2$ flame is expected to inhibit reaction 5 and explains the relative ratios of OCS to SO$_2$ observed in the final products of the two different flames. Together, these important differences in the chemistry of the two flames reduce the radical concentration in the CS$_2$–O$_2$ flame which lowers the velocity of this flame. Finally, the self-ignition temperature of the CS–O$_2$ flame is lower than that of the CS$_2$–O$_2$ flame since reaction 1 is available to the CS–O$_2$ flame and not to the CS$_2$–O$_2$ flame.

Conclusions

The characteristics of a flame fueled with CS and O$_2$ have been presented. The chemistry postulated on the basis of the end products observed for the flame indicates that the CO laser pumping reaction is a major step in the chain reaction sequence for the flame. The low temperature measured for this flame may be a consequence of the fact that more than 50% of the energy from reaction 3 goes into producing vibrationally excited CO. If this is the case, the low-temperature product gases of the CS–O$_2$ flame should not promote CO vibrational deactivation, and the efficiency of a laser based on the CS–O$_2$ flame should be greater than that of the laser reported for the CS$_2$–O$_2$ flame.[18]

The measured rate for reaction 1 is so slow that it should be unimportant to the chemistry of the CS$_2$–O$_2$ system. Chain consumption of CS similar to that found in high concentration CS–O$_2$ mixtures was probably responsible for the reported fast reaction between CS and O$_2$. In fact, evidence of chain consumption as well as increased CS loss rate at high temperatures even in low concentration reactant streams precluded additional reliable measurements of k for temperatures higher than 500 K.

References and Notes

(1) This research was supported by the U.S. Army Missile Command under Contract No. DAAHO1-73-C-0372.

(2) For a recent listing of publications on the CO chemical laser see C. E. Wiswall, D. P. Ames, and T. J. Menne, *IEEE J. Quantum Electron.*, **QE-9**, 181 (1973).

(3) D. W. Howgate and T. A. Barr, Jr., *J. Chem. Phys.*, **59**, 2815 (1973).

(4) R. D. Suart, P. H. Dawson, and G. H. Kimbell, *J. Appl. Phys.*, **43**, 1022 (1972).

(5) W. Q. Jeffers, C. E. Wiswall, J. D. Kelley, and R. J. Richardson, *Appl. Phys. Lett.*, **22**, 587 (1973).

(6) M. de Sorgo, A. J. Yarwood, O. P. Strausz, and H. E. Gunning, *Can. J. Chem.*, **43**, 1886 (1965).

(7) W. P. Wood and J. Heicklen, *J. Phys. Chem.*, **75**, 861 (1971).

(8) For a recent discussion of the relative merits of previous reports of the reactivity of CS with O$_2$, see K. Schofield, *J. Phys. Chem. Ref. Data*, **2**, 25 (1973).

(9) R. J. Richardson, H. T. Powell, and J. D. Kelley, *J. Phys. Chem.*, **77**, 2601 (1973).
(10) A. A. Westenberg and N. de Haas, *J. Chem. Phys.*, **46**, 490 (1967).
(11) A. G. Gaydon and H. G. Wolfhard, "Flames", Chapman and Hall, London, 1970, p 55.
(12) W. H. Breckenridge and T. A. Miller, *Chem. Phys. Lett.*, **12**, 437 (1972).
(13) G. Hancock, C. Morley, and I. W. M. Smith, *Chem. Phys. Lett.*, **12**, 193

(1971).
(14) H. T. Powell and J. D. Kelley, *J. Chem. Phys.*, **60**, 2191 (1974).
(15) A. Tewarson and H. B. Palmer, *Symp. (Intl.) Combust.*, [Proc.], *13th*, 1970, 99 (1971).
(16) G. W. Taylor, *J. Phys. Chem.*, **77**, 124 (1973).
(17) See, for example, ref 3.
(18) H. S. Pillof, S. K. Searles, and N. Djeu, *Appl. Phys. Lett.*, **19**, 9 (1971).

An Equation Describing the Rate of the Photochemical Reaction of a Bulk Powdered Sample

E. L. Simmons*

Department of Chemistry, University of Natal, Durban, South Africa

and W. W. Wendlandt

Department of Chemistry, University of Houston, Houston, Texas 77004

(Received May 31, 1974; Revised Manuscript Received October 10, 1974)

An equation is derived which describes the rate of the photochemical reaction of an infinitely thick powdered sample. The equation is expressed in terms of the sample diffuse reflectance which is the most conveniently measured parameter for following the extent of the photochemical reaction of a powder. The equation is applied to experimental results for the photochemical reaction of powdered $K_3[Mn(C_2O_4)_3] \cdot 3H_2O$.

Introduction

A large number of solid-state photochemical reactions have been studied and the studies have been reviewed.[1] Most of the studies, however, have been concerned with the determination of reaction stoichiometries. Few quantum yield determinations have been made. The major reason for this is that the study of solid-state photochemical reactions is complicated by the fact that the diffusion of solid photoproducts is restricted and hence a concentration gradient is created in the sample by the photochemical reaction.

Equations have been derived which describe the rate of the photochemical reaction of a sample with slab geometry.[2-4] These equations appear to be applicable for the determination of quantum yield values of solid-state photochemical reactions. Equations have also been derived which describe the rate of the photochemical reaction of a thin powdered layer.[5-7] Most solid samples, however, are most conveniently handled in the form of bulk powdered samples. As yet, the most promising method of studying photochemical reactions of bulk powdered samples appears to be reflectance spectroscopy. The technique has been applied to study a number of photochemical reactions in a qualitative manner over the past few years.[8-12] The theory of reflectance spectroscopy, however, has not been sufficiently developed to allow calculations of quantum yield values from reflectance measurements of powdered samples undergoing photochemical reactions.

Recently, a model representing a powdered sample as a collection of uniformly sized rough-surfaced spherical particles has been used to relate the reflectance of a bulk pow-

dered sample to its fundamental optical parameters.[13-15] In this investigation, the same model is used to derive an equation describing the rate of the photochemical reaction of a bulk powdered sample in terms of the sample reflectance as a function of time. Although several approximations are made in the derivation, the equation appears to have promise as a means of estimating quantum yield values of solid-state photochemical reactions from reflectance measurements. The equation was applied to experimental results for the photochemical reaction of $K_3[Mn(C_2O_4)_3] \cdot 3H_2O$.

Phenomenological Description

Consider a powdered sample which can be considered as infinitely thick made up of substance, C, which reacts photochemically to give product, P. The sample is illuminated with monochromatic radiation of intensity, I_0, at the sample surface. The wavelength of the radiation is considered small compared with the diameters of the sample particles so that Rayleigh scattering can be ignored. Consider the ith particle located below the sample surface. The radiation intensity impinging on the ith particle from the upward direction is I_i while that impinging on it from the downward direction is J_{i+1}. Hence, the rate of change of the number of moles, N_i, of C in the ith particle due to photochemical reaction is given by

$$dN_i/dt = -A_{ci}\phi(I_i + J_{i+1})\pi d_i^2/4 \qquad (1)$$

where A_{ci} is the fraction of the impinging radiation absorbed by C in the ith particle, ϕ the quantum yield, and (I_i

$+ J_{i+1}) \pi d_i^2/4$ the total number of einsteins of radiation impinging on the ith particle in unit time.

Since the concentration, C_i, of C in the ith particle is given by

$$C_i = 6N_i/\pi d_i^3 \tag{2}$$

eq 1 can be written as

$$dC_i/dt = -A_{ci}\phi(I_i + J_{i+1})(3/2)d_i^{-1} \tag{3}$$

It has previously been shown[7,14] that A_{ci} is given by

$$A_{ci} = A_c C_i/C_0 = (2/3)n^2 k d_i C_i/C_0 \tag{4}$$

where n is the relative index of refraction (it is assumed here that n remains relatively constant throughout the reaction), k the absorption coefficient of C, and C_0 the concentration of C in pure solid C. Since C_0 is given by

$$C_0 = \rho/M \tag{5}$$

where ρ is the density of pure C and M the molecular mass of C it is convenient to express eq 4 in terms of the molar absorption coefficient, ϵ (in units of cm^2/mol), where

$$k = \epsilon\rho/M \tag{6}$$

Combining eq 4, 5, and 6 gives

$$A_{ci} = (2/3)n^2\epsilon d_i C_i \tag{7}$$

and therefore eq 3 becomes

$$dC_i/dt = -\phi\epsilon n^2 C_i(I_i + J_{i+1}) \tag{8}$$

If the radiation returning from the ith particle in the upward direction is J_i and that returning from the ith particle in the downward direction is I_{i+1}, then the following equation may be written:

$$(I_i + J_{i+1})(1 - A_i) = I_{i+1} + J_i \tag{9}$$

where A_i is the total fraction of impinging radiation absorbed by the ith particle. Equation 9 states simply that the radiation impinging on the particle is equal to that returning from it except for that which is absorbed. The parameter, A_i, is the sum of the fraction of radiation absorbed by C and that absorbed by the product, P:

$$A_i = A_c C_i/C_0 + A_p(1 - C_i/C_0)$$

$$A_i = (A_c - A_p)C_i/C_0 + A_p \tag{10}$$

Substituting eq 10 into eq 9 and solving for C_i gives

$$C_i = [C_0/(A_c - A_p)]\left[1 - A_p - \frac{I_{i+1} + J_i}{I_i + J_{i+1}}\right] \tag{11}$$

The reflectance, R_i, of the ith particle is given by

$$R_i = J_i/I_i \tag{12}$$

while the reflectance, R_{i+1}, of the particle(s) directly below the ith particle is given by

$$R_{i+1} = J_{i+1}/I_{i+1} \tag{13}$$

The particle is assumed to be an ideal diffuser of radiation and hence the radiation returning from the particle in the upward direction is equal to that returning from the particle in the downward direction:

$$I_{i+1} = J_i \tag{14}$$

In order to express C_i in terms of the reflectance, R_i, of the ith particle, it is necessary to make the assumption that the difference in reflectance of two adjacent layers of particles does not differ considerably, or that

$$R_i \cong R_{i+1} \tag{15}$$

This assumption is only valid for weakly absorbing samples. Combining eq 11-15 gives

$$C_i = [C_0/(A_c - A_p)](1 - A_p - 2R_i/(1 + R_i^2)) \tag{16}$$

By making use of eq 12-15, the rate equation (eq 8) may be written as

$$dC_i/dt = \phi\epsilon n^2 C_i I_i(1 + R_i^2) \tag{17}$$

Differentiating eq 16 gives

$$dC_i/dt = [C_0/(A_c - A_p)][-2/(1 + R_i^2) + 4R_i^2/(1 + R_i^2)^2]\frac{dR_i}{dt} \tag{18}$$

Combining eq 16-18, carrying out fundamental algebraic operations, and separating the resulting equation for integration gives

$$2\int_{R_c}^{R_i} \frac{(1 - R_i^2)\,dR_i}{(1 + R_i^2)^2[(1 - A_p)(1 + R_i^2) - 2R_i]} = \phi\epsilon n^2\int_0^t I_i\,dt \tag{19}$$

where R_c is the reflectance of pure C.

Finally, recognizing that only the reflectance value at the sample surface is experimentally measurable, eq 19 can be written as

$$2\int_{R_c}^{R} \frac{(1 - R^2)\,dR}{(1 + R^2)^2[(1 - A_p)(1 + R^2) - 2R]} = \phi\epsilon n^2 I_0 t \tag{20}$$

where R is the reflectance of the surface particles.

By the method of partial fractions, the integral in eq 20 can be expressed as the sum of the following six integrals

$$2\int \frac{(1 - R^2)\,dR}{(1 + R^2)^2((1 - A_p)(1 + R^2) - 2R)} =$$

$$(1 - A_p)\int\frac{dR}{(1 + R^2)^2} + 3\int\frac{R\,dR}{(1 + R^2)^2} +$$

$$(1 - A_p)\int\frac{R^2\,dR}{(1 + R^2)^2} + \int\frac{R^3\,dR}{(1 + R^2)^2} +$$

$$(1 + 2A_p - A_p^2)\int\frac{dR}{(1 - A_p)(1 + R^2) - 2R} -$$

$$(1 - A_p)\int\frac{R\,dR}{(1 - A_p)(1 + R^2) - 2R} \tag{21}$$

each of which can be evaluated to give

$$g(R) - g(R_c) = \phi\epsilon n^2 I_0 t \tag{22}$$

where

$$g(R) = -\frac{1}{1 + R^2} + (1 - A_p)\tan^{-1}R +$$

$$\frac{1}{2}\ln\left[\frac{1 + R^2}{(1 - A_p)(1 + R^2) - 2R}\right] + \frac{1}{2}(2A_p - A_p^2)^{1/2} \times$$

$$\ln\left[\frac{(1 - A_p)R - 1 - (2A_p - A_p^2)^{1/2}}{(1 - A_p)R - 1 + (2A_p - A_p^2)^{1/2}}\right] \tag{23}$$

Hence, a plot of $g(R)$ vs. t should be a straight line with a slope of $\phi\epsilon n^2 I_0$ so that if ϵ, n, and I_0 are known, the value of ϕ can be determined from such a plot.

The value of A_p can readily be calculated from the reflectance value, R_p, of the pure photoproducts using the equation[14]

$$(1 - A_p)(1 + R_p^2) = 2R_p \tag{24}$$
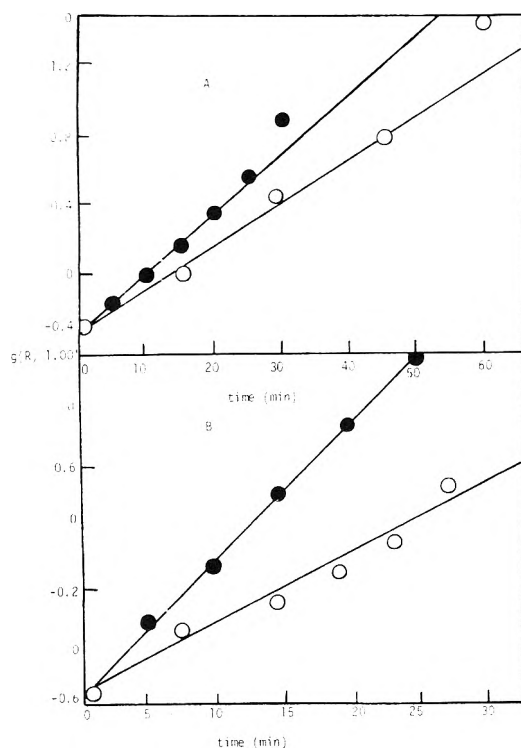
Figure 1. Plots of $g(R)$ vs. t for the photochemical reaction of $K_3[Mn(C_2O_4)_3] \cdot 3H_2O$: (A) 400 nm O, I_0 = 1.04 × 10^{-8}; ●, I_0 = 1.64 × 10^{-8}; (B) 350 nm O, I_0 = 1.11 × 10^{-8}; ●, I_0 = 1.67 × 10^{-8}.

Experimental Section

The equation obtained in this investigation was tested by studying the solid-state photochemical reaction of $K_3[Mn(C_2O_4)_3] \cdot 3H_2O$ which has been previously studied.[6,8] The deep red colored manganese complex undergoes the following reaction on exposure to ultraviolet radiation:[8]

$$2K_3[Mn(C_2O_4)_3] \cdot 3H_2O \longrightarrow$$

$$2K_2[Mn(C_2O_4)_2] + 2CO_2 + 6H_2O + K_2C_2O_4 \quad (25)$$
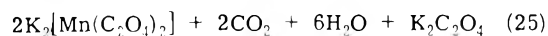
The material used was the same as that used in a previous investigation. Finely ground samples of the compound were pressed into a sample holder so that the sample thickness was several millimeters and could therefore be considered as infinitely thick. The sample was then illuminated with monochromatic light from a Bausch and Lomb monochromator equipped with a mercury lamp source. A Ys; Kettering Model 65 radiometer was used to measure the radiation intensity. The intensity was varied by simply changing the distance between the sample and the monochromator. During a photolysis experiment, the sample was removed periodically at measured time intervals and the diffuse reflectance of the sample obtained at the same wavelength as that of the illuminating light by the use of a Beckman DK-2A spectroreflectometer. Magnesium oxide was used as the reference material. Photochemical reactions were carried out at 350 and 400 nm since there is a sizeable change in the reflectance values during the reaction and the charge transfer band of the complex extends far enough into the visible region that the reaction occurs reasonably rapidly at these two wavelengths.

Results

Figure 1 illustrates plots of $g(R)$ vs. t for the solid-state photochemical reaction of $K_3[Mn(C_2O_4)_3] \cdot 3H_2O$ at 350

TABLE I: Data for the Photochemical Reaction of $K_3[Mn(C_2O_4)_3] \cdot 3H_2O$

I_0, einstein cm^2 sec	$\phi \epsilon n^2 I_0$, sec^{-1}	ϵn^2, cm^2/mol	ϕ, mol/einstein
λ 400 nm			
1.04 × 10^{-8}	0.70 × 10^{-3}	1.0 × 10^5	0.41
1.64 × 10^{-8}	1.12 × 10^{-3}	1.0 × 10^5	0.40
λ 350 nm			
1.11 × 10^{-8}	1.66 × 10^{-3}	4.9 × 10^5	0.13
1.67 × 10^{-8}	3.34 × 10^{-3}	4.9 × 10^5	0.12

and 400 nm and different radiation intensities. The curves Figure 1 are reasonably linear although there appears to be some deviations from linearity at higher reaction times. These derivations are undoubtedly due to the numerous assumptions and approximations made in the derivation of eq 22. From the slopes of the curves in Figure 1, the values of $\phi \epsilon n^2 I_0$ were obtained and are listed in Table I. Previous measurements[6,7] give a value for ϵn^2 for $K_3[Mn(C_2O_4)_3] \cdot 3H_2O$ at 400 nm of about 10^5 cm^2/mol and an aqueous solution value[16] for ϵ of 5.1 × 10^4 cm^2/mol. If it is assumed that ϵ is independent of the state of the system, then the value for n of 1 4 is obtained. A value of 2.5 × 10^5 cm^2/mol for ϵ at 350 nm has previously been obtained[16] for aqueous solutions of $K_3[Mn(C_2O_4)_3] \cdot 3H_2O$. Hence, at 350 nm, ϵn^2 = 4.9 × 10^5 cm^2/mol. Using these values for ϵn^2, the quantum yields for the solid-state photochemical reaction of $K_3[Mn(C_2O_4)_3] \cdot 3H_2O$ were calculated and are listed in Table I.

The quantum yield values listed in Table I can be considered as no more than rough approximations because of the assumptions and approximations made in the derivation of the photochemical rate equation for bulk powdered samples. However, the values are reasonable and, in fact, the values at 400 nm are reasonably close to those previously obtained[6] (0.47–0.63) from studies of the photochemical reaction of thin powdered layers of $K_3[Mn(C_2O_4)_3] \cdot 3H_2O$. Furthermore, the quantum yield values listed in Table I are not greatly different from those obtained[17] for the photochemical reaction of $K_3[Mn(C_2O_4)_3] \cdot 3H_2O$ in aqueous solutions (about 0.3 at 350 nm and about 0.5 at 400 nm).

Discussion

The quantum yield values of only a few solid-state photochemical reactions have been determined. Since the mechanisms of solid-state reactions are expected in general to be different from those of the corresponding reactions in aqueous solutions and since the quantum yield can tell much concerning the mechanism of a photochemical reaction, it is important to be able to determine reliable quantum yield values for solid-state photochemical reactions. Furthermore, since most solids are most conveniently handled in the form of bulk powdered samples and since reflectance spectroscopy is a convenient technique for following the extent of the reaction of a powdered sample, it is convenient to be able to determine quantum yield values from reflectance measurements.

Because of the complicated nature of the interaction of light with a powder, the equations derived in this investigation necessarily involve several assumptions and approximations. They are only valid for samples which can be considered infinitely thick, which ideally diffuse radiation, and which contain particles whose diameters are large compared to the wavelength of the radiation. The equation de-

rived is based on a one-dimensiona. model of the particle array and is only an approximation of the three-dimensional real powdered sample. Despite the undesirability of making so large a number of assumptions and approximations, the linearity of the plots in Figure 1 and the not unreasonable order of magnitude va.ues of the calculated quantum yields obtained indicates that the theory outlined here may be used to estimate quantum yield values from reflectance measurements. Considerable theoretical refinements and developments are, however, undoubtedly necessary for more accurate work.

References and Notes

(1) E. L. Simmons and W. W. Wendlandt, *Coord. Chem Rev.,* **7**, 11 (1971).
(2) P. G. Barker, M. P. Halstead, and J. H. Purnell, *Trans. Faraday Soc.,* **65**, 2404 (1969).

(3) E. L. Simmons, *J. Phys. Chem.,* **75**, 588 (1971).
(4) H. Mauser, *Z. Naturforsch.,* **226**, 569 (1967).
(5) H. E. Spencer and M. W. Schmidt, *J. Phys. Chem.,* **74**, 3472 (1970).
(6) E. L. Simmons and W. W. Wendlandt, *Anal. Chim. Acta,* **53**, 81 (1971).
(7) E. L. Simmons, *J. Phys. Chem.,* **78**, 1265 (1974).
(8) E. L. Simmons and W. W. Wendlandt, *J. Inorg. Nucl. Chem.,* **27**, 2325 (1965).
(9) W. W. Wendlandt and E. L. Simmons, *J. Inorg. Nucl. Chem.,* **27**, 2312 (1965).
(10) W. W. Wendlandt and E. L. Simmons, *J. Inorg. Nucl. Chem.,* **28**, 2420 (1966).
(11) W. W. Wendlandt and J. H. Woodlock, *J. Inorg. Nucl. Chem.,* **27**, 259 (1965).
(12) C. H. Stembridge and W. W. Wendlandt, *J. Inorg. Nucl. Chem.,* **27**, 129 (1965).
(13) N. T. Melamed, *J. Appl. Phys.,* **34**, 560 (1963).
(14) E. L. Simmons, *Opt. Acta,* **18**, 59 (1971).
(15) E. L. Simmons, *Opt. Acta,* **19**, 845 (1972).
(16) E. L. Simmons, Dissertation, Texas Tech University, 1968.
(17) G. B. Porter, J. G. W. Poering, and S. Karanka, *J. Amer. Chem. Soc.,* **84**, 4027 (1962).

Electron Affinities of Substituted Aromatic Compounds

W. E. Wentworth,* Lilly Wang Kao, and Ralph S. Becker

Chemistry Department, University of Houston, Houston, Texas 77004

(Received August 6, 1973; Revised Manuscript Received January 20, 1975)

The effect of the substituents F, Cl, CH_3, OCH_3, and $C\equiv N$ on the molecular electron affinities (EA) of benzaldehyde and acetophenone were measured experimentally. The substituents F, Cl, and CF_3 increase the EA in the order $CF_3 >$ Cl $>$ F whereas CH_3 lowers the EA. Hückel parameters for the substituents $C=O$, CH_3, F, and Cl were calculated using a general least-squares adjustment to the EA measurements. The inductive and resonance parameters for a substituent were highly correlated as revealed by the value of the correlation coefficients of 0.998 for F and 0.987 for Cl. It is suggested that this high correlation is the reason for many of the wide variations in Hückel parameters reported by different investigators, regardless of the experimenta. quantity being considered. This type of analysis can also be applied to other semiempirical calculations involving empirical parameters.

Introduction

A pulse sampling technique for the measurement of molecular electron affinities (EA) was developed several years ago.[1,2] The technique is restricted to compounds which undergo nondissociative electron attachment and have an EA in the range 0.2–0.8 eV. The upper limit of 0.8 or 0.9 eV can only be obtained with the ^{63}Ni detector which can be operated up to 350°.[3] For some compounds the negative molecular ion can dissociate into another negative ion and a radical, however, this occurs at a higher temperature and is distinguished by its temperature dependence.[4-6] A recent review discusses the various types of thermal electron attachment mechanisms and their possible temperature dependence.[7]

In this paper we wish to investigate the effect of substituents on the molecular EA of various aromatic compounds. The substituents F, Cl, CH_3, CF_3, OCH_3, and $C\equiv N$ on benzaldehyde, acetophenone, and 1-chloronaphthalene were considered in this study. Compounds with these substituents all appear to form a molecular negative ion for which the EA can be determined. The negative molecular ion of aromatics with the Cl substituent dissociate into Cl$^-$ plus an aromatic radical but this occurs only at higher temperatures ($>$180°).[4,6,7] More recent studies[8] indicate that acetophenone or similar compounds of the general structure $ArC(=O)R$ dissociate into $(ArC(=O))^-$ plus R-. However, this also occurs only at higher temperatures ($>$250°) which are accessible only with the ^{63}Ni detector. These dissociations at higher temperatures should not prohibit the determination of the EA of these compounds at lower temperatures.

Generally the effect of the substituents on the EA was in the direction which one would have expected from the chemical effects of these groups; e.g., F, Cl, and CF_3 increase the EA whereas CH_3 lowers the EA of the parent compound. In order to examine the substituent effect more quantitatively, Hückel calculations were carried out. Inductive and resonance parameters for each of the substituents were calculated using the EA results. However, it is

difficult to establish both parameters accurately since they are highly correlated when utilizing solely EA values.

Experimental Section

The electron affinity determinations were made using the pulse sampling technique for the measurement of electron attachment as a function of temperature.[2] Pulse periods of 1000 μsec with a pulse width of 0.5 μsec were used. An EC detector employing a tritium foil was operated up to 225° and to as low a temperature as permitted by the volatility of the compound. All compounds with the exception of the three Cl-substituted compounds were run relative to acetophenone. For every electron attachment measurement a corresponding measurement for acetophenone was obtained under similar conditions. The ratios of these electron capture coefficients were used in the data reduction. It was felt that this technique of relative capture coefficients would lead to more precise measurements since any variations in operating conditions should affect the reference acetophenone in a manner similar to the substituted derivative. Thus, the ratio should be almost unaffected by the variation in operating conditions.

The gas chromatographic columns used in this study were not critical. It was only necessary to separate the peak for particular compounds being studied from the reference peak and any impurities which were present. It was also necessary that the column bleed be minimized at the operational temperatures. All of the specific conditions are available from the authors but it is sufficient to state that the columns used were (1) a 10 ft, 0.25 in. stainless steel, 10% SE-30 on 60/80 Anakrom ABS; (2) a 2 ft, 0.25 in. copper, 5% Carbowax 20M, on 60/80 Gas Chrom; and (3) a 3 ft, 9 in., 0.25 in. copper, 7% Carbowax 20M, on 60/80 Anakrom ABS.

The sources of the chemicals were Aldrich Chemical Co. for the tolualdehydes, the fluorobenzaldehydes, and 3-methoxybenzaldehyde; Pierce Chemical Co. for the fluoroacetophenones and the trifluoromethylbenzaldehydes; Eastman Organic Chemicals for the benzaldehyde and benzonitrile; and Matheson Coleman and Bell for the propiophenone and the acetophenone. Phillip's 99 mol % heptane was purified by passing through a silica gel column and was used as the solvent. Solutions were prepared by weighing the sample and solvent. The concentrations were so chosen as to keep the peak height less than one-half of the total standing current.

The carrier gas was a 10% mixture of methane (Matheson CP) and argon (Big Three Industries) and was passed through a 5A molecular sieve. The flow rate was 150 ml/min measured by a bubble flow meter and a stop watch. The temperature was measured with a thermometer in the detector block. Both the fixed temperature method[2] and the temperature programmed mode[5] were used in this study. In addition, the response was converted and integrated using both a digital computer[2] and an analog computer.[5]

Electron Affinities

The relationship between the electron capture coefficient, K, and the EA has been shown to be[1,2]

$$\ln KT^{3/2} = \ln A + \ln \frac{k_L}{k_D} + \frac{EA}{RT} \quad (1)$$

where A is composed of fundamental constants and the mass of the electron, and k_L and k_D are rate constants for

neutralization cf the negative ion and the electron, respectively. The ratio of the electron capture coefficient for a compound relative to acetophenone would be given by

$$\ln K/K_A = \ln k_L - \ln (k_L)_A + \frac{\Delta EA}{RT} \quad (2)$$

where the subscript A refers to acetophenone and $\Delta EA = EA - (EA)_A$. Since most compounds in this study are substituted aldehydes and ketones, the k_L should be nearly identical with the k_L for acetophenone. On this premise the k_L terms in eq 2 can be cancelled and the ΔEA can be calculated assuming a zero intercept in a $\ln K/K_A$ vs. $1/T$ graph. The calculated ΔEA assuming a zero intercept is much more precise than that calculated with the intercept variable. However, it should be kept in mind that the actual precision of the calculated ΔEA assuming a zero intercept is limited by the assumption of $k_L = (k_L)_A$. In this work the ΔEA's were calculated according to the principle of least squares, with both an assumed zero intercept and a variable intercept. These are shown in Table I in columns two and three, respectively. A linear least-squares program was used with equal weights for $\ln K/K_A$ since the relative standard deviation in K is assumed constant.

Conventionally the electron attachment results have been presented graphically in $\ln KT^{3/2}$ vs. $1/T$ plots.[2,4-7] In order to be consistent with this graphical presentation, the experimental $\ln K/K_A$ were added to the least-squares $\ln KT^{3/2}$ vs. $1/T$ curve established for acetophenone. Such data are shown in Figure 1. Obviously the straight lines with a common intercept are the least-squares estimates assuming a zero intercept in a $\ln K/K_A$ vs. $1/T$ plot as discussed previously. Generally, one can see that the data in Figure 1 show a positive slope at higher temperatures breaking over to a near zero slope at lower temperatures if the capture is sufficiently high. This is in agreement with previous results in which the assumption that a stable molecular negative ion seemed justified.[1,9] At an upper temperature of 200–225°, there is no appearance of a negative slope characteristic of a dissociative mechanism.[7] At higher temperatures, attainable with a [63]Ni detector, the acetophenone curves begin to break upward at lower $1/T$ values giving a negative slope.[8] As explained earlier this is apparently due to dissociation into Ar(=O)$^-$ + R·. The PhC(=O)–H bond in benzaldehyde is sufficiently strong to prevent the dissociation into PhC(=O)$^-$ + H· and consequently no change in slope is observed at higher temperatures.[8]

Some general observations of the effect of substitution on the EA of benzaldehyde and acetophenone can be made. In column 4 of Table I are given the changes in electron affinity upon substitution relative to the parent compound. It should first be noted that substitution of F, Cl, CF$_3$, and OCH$_3$ increases the EA whereas substitution of CH$_3$ on the ring lowers the EA. Generally this would be expected due to the inductive electron-withdrawing effect generally associated with the F, Cl, CF$_3$, and OCH$_3$ groups whereas CH$_3$ is considered electron releasing. The effect of F, Cl, and CF$_3$ on substitution can be compared directly since they have been substituted on the same parent compounds acetophenone and benzaldehyde. The order of effectiveness in increasing the EA is CF$_3$ > Cl > F > OCH$_3$.

A second aspect of the change in EA upon substitution can be noted in Table I. The substitution of F in both acetophenone and benzaldehyde in the 2, 3. or 4 positions follows the same trend and the same order of magnitude. Substitution in the 2 and 3 positions results in the largest in-

TABLE I:

Compound	EA ± σEA[b] (zero intercept)	EA ± σEA (variable intercept)	(EA − EA parent)[a] ± σ	Parent compound
Benzaldehyde[c]	0.430 ± 0.005	0.408 ± 0.010		
2-Fluorobenzaldehyde	0.564 ± 0.006	0.637 ± 0.042	0.134 ± 0.008	Benzaldehyde
3-Fluorobenzaldehyde	0.537 ± 0.006	0.667 ± 0.054	0.157 ± 0.008	Benzaldehyde
4-Fluorobenzaldehyde	0.476 ± 0.005	0.484 ± 0.017	0.046 ± 0.008	Benzaldehyde
Acetophenone[c]	0.334 ± 0.006	0.334 ± 0.006		
2-Fluoroacetophenone	0.458 ± 0.006	0.443 ± 0.01	0.124 ± 0.009	Acetophenone
3-Fluoroacetophenone	0.546 ± 0.006	0.576 ± 0.026	0.212 ± 0.009	Acetophenone
4-Fluoroacetophenone	0.391 ± 0.006	0.396 ± 0.014	0.057 ± 0.009	Acetophenone
3-Chloroacetophenone[d]	0.581 ± 0.030		0.247 ± 0.030	Acetophenone
4-Chloroacetophenone[d]	0.566 ± 0.030		0.232 ± 0.030	Acetophenone
2-Trifluoromethylacetophenone	0.640 ± 0.007		0.306 ± 0.010	Acetophenone
3-Trifluoromethylacetophenone	0.662 ± 0.007		0.330 ± 0.010	Acetophenone
4-Trifluoromethylacetophenone	0.641 ± 0.007		0.307 ± 0.010	Acetophenone
3-Methylbenzaldehyde	0.416 ± 0.005	0.407 ± 0.014	−0.014 ± 0.008	Benzaldehyde
4-Methylbenzaldehyde	0.385 ± 0.005	0.374 ± 0.017	−0.045 ± 0.008	Benzaldehyde
3-Methoxybenzaldehyde	0.484 ± 0.006	0.431 ± 0.043	0.054 ± 0.010	Benzaldehyde
Propiophenone	0.352 ± 0.005	0.361 ± 0.013	−0.078 ± 0.008	Benzaldehyde
Benzonitrile	0.239 ± 0.005	0.258 ± 0.018		

[a] The EA's used in calculating this change from the parent compound are those calculated assuming a zero intercept. [b] σ in this table and subsequent tables refer to standard deviations, sometimes referred to as marginal standard deviations. [c] Reference 9. [d] Reference 6.
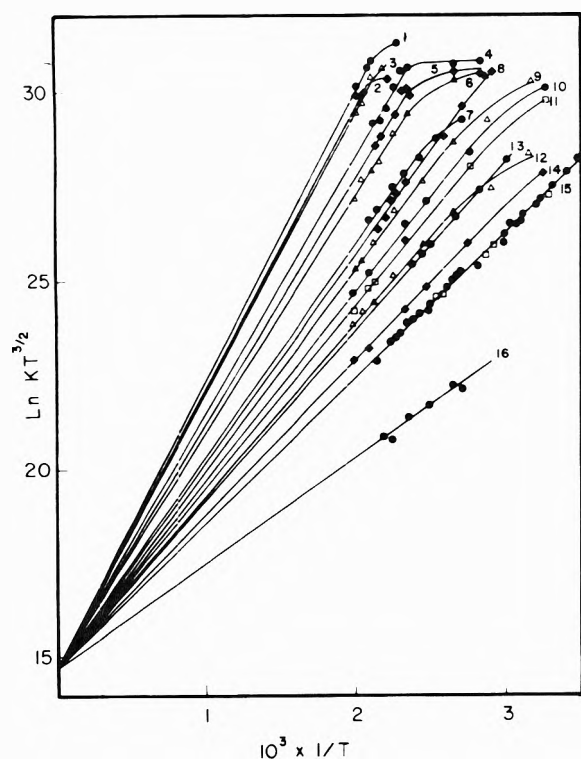
Figure 1. Ln $KT^{3/2}$ vs. $1/T$ for all the compounds from the common intercept least-squares adjustment: (1) m-trifluoromethylacetophenone; (2) p-trifluoromethylacetophenone; (3) o-trifluoromethylacetophenone; (4) m-fluorobenzaldehyde; (5) o-fluorobenzaldehyde; (6) m-fluoroacetophenone; (7) 3-methoxybenzaldehyde; (8) p-fluorobenzaldehyde; (9) o-fluoroacetophenone; (10) benzaldehyde; (11) m-tolualdehyde; (12) p-fluoroacetophenone; (13) p-tolualdehyde; (14) propiophenone; (15) acetophenone; (16) benzonitrile.

crease in EA which is about 2 to 3 times the effect of substitution in the 4 position. This result was somewhat unexpected since resonance of the F with the phenyl ring would predict an increase in EA for substitution in the 2 and 4 positions. As will be seen in the subsequent section, a combi-

nation of resonance and inductive parameters are necessary in order to account for these substitution effects within the framework of the Hückel theory.

Hückel Calculations of EA

In order to investigate the effect of substitution on EA more quantitatively, Hückel calculations were undertaken.[10] Furthermore, considering the large effect which substitution has upon the EA, it was felt that the comparison of Hückel calculations with EA's would establish precisely the inductive (h) and resonance (k) parameters for these substituents. Note that F substitution on acetophenone increases the EA by about 30–40%. However, as will be seen shortly, both parameters are not established precisely by comparison of the Hückel calculations with the experimental EA. Contrarily, the two parameters for a given substituent are highly correlated, i.e., the choice of h highly influences the choice of k.

Initially a rather straightforward approach was taken to adjust the h and k parameters to give a satisfactory agreement with the experimental EA. The α and β parameters for carbon[10] were established by comparison of the Hückel calculation of EA[11] (energy of the lowest unfilled orbital) with the experimental EA[2,11] for the two-, three-, and four-ring polycyclic aromatic hydrocarbons (AHC). The EA is related to α and β by

$$EA = -\alpha - m_{n+1}\beta \tag{3}$$

where m_{n+1} is the root from the Hückel calculation for the lowest unfilled MO ($2n$ electrons occupy the first n orbitals). A graph of the experimental EA vs. $-m_{n+1}$ yields estimates of the α and β parameters from the intercept and slope. Such a graph is shown in Figure 2 where the AHC are designated by squares about the data points. The fit to the straight line is not very good as revealed by a $\sigma_{ext} = \pm 0.09$ for these compounds. σ_{ext} is calculated from the residuals (res)

$$res = EA_i + \alpha + m_{n+1}\beta \tag{4}$$

$$\sigma_{ext} = \sqrt{(res)^2/(n-2)} \tag{5}$$
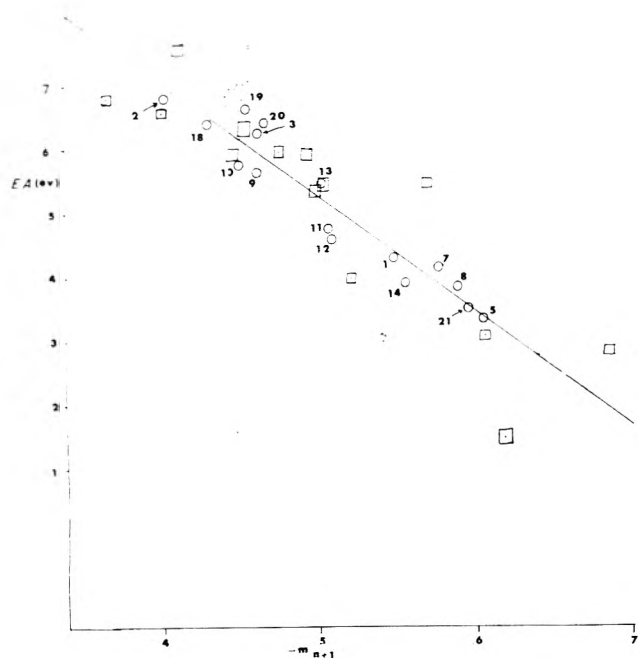
Figure 2. Electron affinity vs. root for lowest unoccupied molecular orbital from Hückel calculations: (□) aromatic hydrocarbons; (⊙) substituted aromatic compound identified by number in Table II.

where EA_i refers to the EA for the ith AHC.

The parameters for the carbonyl group $h\dot{o}$ and k_{C-O} were then established by proper adjustment to give a satisfactory agreement between the Hückel estimates and the experimental EA. The EA for the compounds benzaldehyde, 1-naphthaldehyde, 2-naphthaldehyde, and 9-phenanthraldehyde, which were reported in another study,[9] were used. An $h\dot{o} = 1.16$ and $k_{C-O} = 1.68$ gave reasonable agreement between the Hückel estimate and experimental EA_i. The data are also plotted in Figure 2. The residuals for the compounds are shown in Table II. The residuals for these four compounds are considerably lower than those for the AHC, however, it should be recalled that there are two additional adjustable parameters. The σ_{ext} for the four compounds, which takes into account the number of adjustable parameters, is ±0.04. This is considerably better than σ_{ext} for the AHC. The value for cinnamaldehyde is also shown in Figure 2 and gives reasonable agreement. The experimental EA for cinnamaldehyde has considerable error,[9] however, and for that reason was not used in establishing the carbonyl parameters.

An auxiliary inductive parameter[10] $(1/\delta)$ of 0.4 was used in these calculations and seemed to give a better fit of the data. The exact value of the auxiliary parameter is not critical to the adjustment; however, the h and k values determined are a function of the auxiliary parameter selected. That is to say, the h and k are highly correlated with $1/\delta$. This will be shown more explicitly later when the least-squares adjustment of the parameters is discussed.

The simple inductive model for CH_3 was used and an inductive of parameter of $h_{CH_3} = -0.18$ was established in a manner similar to that used for the carbonyl parameters. The four compounds shown in Table II were used. The residuals are reasonably small; however, the effect of CH_3 on the EA is also small. The data are also plotted in Figure 2. The negative inductive parameter is expected since CH_3 is electron releasing.

Having established parameters for the C=O and CH_3, the inductive and resonance parameters for F were obtained in a like manner. The 2-, 3-, and 4-fluoro-substituted acetophenones and benzaldehydes were used as shown in Table I. The residuals are reasonably small, indicating that the Hückel theory can account reasonably well for the unique effect of substitution on the EA, i.e., substitution in the 2 and 3 positions makes the EA increase more than the 4 position. Again the results are plotted in Figure 2.

General Least-Squares Adjustment of Inductive and Resonance Parameters

As one can see from the results in Figure 2, there is good agreement between the Hückel estimate of EA and the experimental EA_i. This is gratifying; however, the procedure for establishing the parameters leaves much to be desired if any significance is to be placed upon the relative values of the parameters. The problem arises from the sequential adjustment of the parameters for different substituents and the inherent inadequacies of the Hückel calculations. As a case in point, let us consider the adjustment of the carbonyl parameters so as to give good agreement with the EA_i for benzaldehyde according to our previous procedure. The values for α and β were obtained from the AHC. The Hückel estimate of the EA for benzene $(m_{n+1} = -1.0)$ would be

$$EA = -\alpha + \beta = 1.237 - 1.48$$
$$EA = -0.25 \text{ eV}$$

This estimate of EA for benzene differs greatly from the best experimental estimate.

Since the EA for benzene is most certainly negative it is difficult to determine a precise value for it experimentally. However, a reasonable estimate can be obtained from the electron attachment cross section as a function of electron energy. This has been obtained in a unique experiment employing a mixture of SF_6 with the compound being measured, e.g., benzene.[12] Extrapolation of the SF_6^- current curve to the abscissa (electron energy) gives an upper estimate of the adiabatic EA. For benzene this is -0.7 ± 0.2 eV. This error estimate should include any inherent discrepancy between the true extrapolated value and the true adiabatic EA. There is considerable error in this extrapolation; however, the discrepancy between this value and the Hückel estimate of -0.25 is well outside the possible error. If this point were included in Figure 2, it would fall 0.45 eV below the straight line at $-m_{n+1} = 1.0$. Now upon adjustment of $h\dot{o}$ and k_{C-O}, in order to give agreement with the experimental EA_i, the parameters will take on values so as to take up this discrepancy of 0.45 eV. This is a sizeable amount compared to the difference in the experimental EA of benzaldehyde and benzene which is on the order of 1.1 eV. In other words, the $h\dot{o}$ and k_{C-O} will not reflect the true substituent effect of the carbonyl group since they will also be accounting for the inherent inadequacy of the Hückel theory to predict the EA for benzene. The same argument can be given for any of the hydrocarbons since the Hückel theory does not exactly predict the EA of any hydrocarbon and the severity of the effect will be governed by the deviation from the straight line in Figure 2. Similarly, the same argument can be given for the subsequent adjustment of any other parameters where the unsubstituted compound deviates from the straight line in Figure 2.

As stated previously, this problem would not exist if Hückel calculations gave the exact EA of the parent compound. However, the problem will exist for any type of mo-

TABLE II:

Subst	No.	Compound	EA ± σEA	Res	σext	Parameters	$|l|_{n+1}$	EA + α_j	Res	Parameters
			(ref 2) σEA = ±0.01						General least-squares adjustment	
		13 2,3,4-ring polycyclic aromatic hydrocarbons								
C=O	1	Benzaldehyde	0.430 ± 0.005	−0.013	±0.09	$\alpha = -1.42$	−0.476	−0.972	−0.001	$l_{\dot{0}} = 0.962 \pm 0.05$
	2	1-Naphthaldehyde	0.680 ± 0.025	−0.022		$\beta = -1.79$	−0.365	−0.720	+0.025	$k_{CO} = 1.369 \pm 0.05$
	3	2-Naphthaldehyde	0.625 ± 0.015	+0.025		$l_{\dot{0}} = 1.0$	−0.420	−0.775	+0.080	
	4	9-Phenanthraldehyde	0.724 ± 0.010			$k_{CO} = 1.6$	−0.359	−0.776	−0.045	
	5	Acetophenone	0.334 ± 0.006	−0.007			−0.525	−1.068	+0.002	$l_{CH_3} = -0.121 \pm 0.005$
	6	1-Acetonaphthone	0.598 ± 0.03				−0.397	−0.804	+0.007	
CH₃	7	III-Acetonaphthone	0.416 ± 0.006	+0.035		$l_{CH_3} = -0.18$	−0.492	−0.986	+0.015	
	8	p-Tolualdehyde	0.385 ± 0.006	+0.015			−0.498	−1.017	−0.002	
F	9	2-Fluorobenzaldehyde	0.564 ± 0.006	−0.033	±0.04	$l_F = 1.4$	−0.410	−0.838	−0.002	$l_F = 2.309 \pm 0.12$
	10	3-Fluorobenzaldehyde	0.587 ± 0.006	−0.029		$k_{CF} = 1.0$	−0.396	−0.815	−0.009	$k_{CF} = 1.470 \pm 0.07$
	11	4-Fluorobenzaldehyde	0.476 ± 0.005	−0.039			−0.455	−0.926	0.000	
	12	2-Fluoroacetophenone	0.458 ± 0.006	−0.054			−0.454	−0.944	−0.020	
	13	3-Fluoroacetophenone	0.546 ± 0.006	+0.023			−0.440	−0.856	+0.040	
	14	4-Fluoroacetophenone	0.391 ± 0.006	−0.037			−0.511	−1.011	+0.029	
Cl	15	1-Chloronaphthalene	0.266 ± 0.020				−0.536	−1.134	−0.043	$h_{Cl} = 2.904 \pm 0.39$
	16	3-Chloroacetophenone	0.581 ± 0.030				−0.415	−0.821	+0.025	$k_{CCl} = 1.666 \pm 0.26$
	17	4-Chloroacetophenone	0.566 ± 0.030				−0.467	−0.836	+0.116	
CF₃	18	2-Trifluoromethyl-acetophenone	0.640 ± 0.006	−0.004		$l_{CF_3} = 2.0$				
	19	3-Trifluoromethyl-acetophenone	0.664 ± 0.006	+0.053		$k_{CF_3} = 1.0$				
	20	4-Trifluoromethyl-acetophenone	0.641 ± 0.053	+0.052						
C₂H₅	21	Propiophenone	0.352 ± 0.006	−0.005		$h_{C_2H_5} = -0.15$				

lecular orbital calculation which employs adjustable parameters since none at present is capable of giving the exact EA. The problem will be less severe for more exact theoretical techniques and in general the following comments should be applicable to any mode of calculation which necessitates empirical parameters for a substituent.

In order to circumvent this problem as well as possible, a general adjustment to all parameters simultaneously according to the principle of least squares was carried out. Furthermore, the inadequacy of the Hückel theory to exactly calculate the EA was eliminated essentially by adjusting the parameters to the change in EA from the parent compound. This was not done explicitly, for reasons which will be pointed out shortly, however, it had that same effect on the adjustment. It is not essential that the adjustment be made according to the principle of least squares, however, it has the following advantages. (1) Estimates of errors in the adjusted parameters arise automatically from the general least-squares adjustment.[13] (2) Correlations which exist between the parameters are readily obtained from the variance–covariance matrix for the adjusted parameters. (3) The parameters themselves are obtained objectively without any personal bias or judgement. (4) The least-squares adjustment can be carried out for all parameters simultaneously.

The deviation of the Hückel calculation of the parent hydrocarbon from the experimental value was taken into account by assigning individual α_j to each parent hydrocarbon. The parameters α_j are essentially determined from the experimental EA for the parent hydrocarbon and in effect the adjustment of the substituent parameters accounts for the change in EA of the substituted compound from the parent AHC. The least-squares adjustment is then made to the condition equations

$$EA = -\alpha_j - m_{n+1}\beta \qquad (6)$$

where α_j will be different for benzene, naphthalene, and phenanthrene and m_{n+1} is a function of the substituent parameters. The least-squares adjustment to eq 6 is preferred to adjustment to the change in EA from the parent. The latter would automatically have a bias error in the change in EA since the error in the EA of the parent compound would exist in all ΔEA values. The adjustment to eq 6 is complicated only by the fact that the α_j must be carried as parameters. This does not affect the convergence of the least-squares adjustment since the α_j are so well established from the EA's for those AHC.

The inital attempt at the least-squares adjustment utilized only the EA for the three parent AHC and the substituted aromatic compounds. The α_j, β, and the h and k for each substituent were carried as adjustable parameters. β was very poorly defined since it was highly correlated with the k parameters for the substituents and in particular k_{C-O}. In order to eliminate this correlation, the β parameter was better defined by adding two additional condition equations using the first two ionization potentials for benzene.[14] The condition equations are

$$IP_1 = -\alpha_4 - \beta$$
$$IP_2 = -\alpha_4 - 2\beta \qquad (7)$$

α_4 must be introduced since the α's for correlating EA are quite different for IP.[11] Introducing eq 7 into the general least-squares adjustment eliminated the correlation with β, however, $h\dot{o}$ and k_{C-O} remained highly correlated making the determination of both $h\dot{o}$ and k_{C-O} very inaccurate. The $h\dot{o}$ was established quite precisely by adding another

condition equation involving the IP for benzaldehyde. It was assumed that the first IP for benzaldehyde involved the removal of a nonbonding electron. Hence

$$IP = -\alpha_4 - h_{\dot{o}}$$

In total 13 quantities were carried as adjustable parameters. Of these, α_1, α_2, α_3, α_4, and β were essentially determined by the observations: EA benzene, EA naphthalene, EA phenanthrene, IP$_1$ and IP$_2$ for benzene. The auxiliary inductive parameter $(1/\delta)$ was carried as an adjustable parameter along with an h and k for each substituent except for CH$_3$ for which only the inductive parameter (h_{CH_3}) was included. The latter eight parameters are the only ones which are really of concern and are the only ones which are varying. In the least-squares adjustment the condition equations are first expanded in a Taylor's series involving only the first derivative terms. These derivatives of EA with respect to the previously mentioned eight parameters are shown in Table III.

The magnitude of a derivative in Table III is a measure of the sensitivity of the EA of the compound to that specific parameter. For example, $\partial EA/\partial h\dot{o}$ in benzaldehyde is -0.617 whereas in 1-naphthaldehyde it is -0.419. Since the magnitude of the derivative is larger for benzaldehyde one would expect the EA for benzaldehyde to be more sensitive to a change in $h\dot{o}$. The magnitude of the derivatives are thus helpful in evaluating whether a given compound is of value in determining a given substituent.

The matrix of derivatives in Table III are also of value in determining whether two or more parameters can be determined accurately from a given set of data. If any two columns have corresponding elements whose ratios are all approximately the same value, the parameters corresponding to these derivatives will be highly correlated and both parameters cannot be determined accurately. This arises from the fact that the equations relating the change in EA with change in parameters are not linearly independent. Again to cite an example, let us consider the parameters $h\dot{o}$ and k_{C-O}. The derivatives with respect to these parameters are found in columns 1 and 2 of Table III. Note that the ratio of $\partial EA/\partial k_{C-O}$ to $\partial EA/\partial h\dot{o}$ is approximately -1.9 for all four unsubstituted aldehyde compounds. Consequently EA measurements alone will not determine $h\dot{o}$ and k_{C-O} simultaneously. The ratio could be established quite accurately but the absolute values would be poorly defined. The $\partial IP/\partial h\dot{o}$ for benzaldehyde is -2.11 and $\partial IP/\partial k_{C-O}$ is zero since the IP is assumed to arise from a nonbonding electron on oxygen. This establishes or defines $h\dot{o}$ quite precisely and thus k_{C-O} can be determined from the EA measurements.

Similarly the derivatives with respect to other parameters can be compared. For example, the ratio of $\partial EA/\partial k_{C-F}$ to $\partial EA/\partial h_F$ is approximately -2 for the 2 and 4 F substituents on benzaldehyde and acetophenone. The 3 F derivatives do not have this ratio, however, the $\partial EA/\partial h_F$ and $\partial EA/\partial k_{C-F}$ is so small for these compounds that they do not contribute much to the determination of these parameters. Hence h_F and k_{C-F} will be poorly defined by EA data alone since h_F and k_{C-F} will be highly correlated, i.e., as h_F increases k_{C-F} must increase correspondly in order for the ratio to be constant.

The correlation of other parameters can be investigated in a similar manner. However, this is a very awkward way to detect correlation. In the least-squares analysis this information is obtained almost automatically. Associated with any general least-squares adjustment is the variance–

TABLE III: Partial Derivatives of EA_i with Respect to Parameters

Compound	$\partial EA/\partial h_O$	$\partial EA/\partial k_{CO}$	$\partial EA/\partial h_{CH_3}$	$\partial EA/\partial h_F$	$\partial EA/\partial k_{CF}$	$\partial EA/\partial h_{Cl}$	$\partial EA/\partial k_{CCl}$	$\partial EA/\partial \delta$
Benzaldehyde	−0.617	1.111	0	0	0	0	0	0.0252
1-Naphthaldehyde	−0.419	0.712	0	0	0	0	0	0.0164
2-Naphthaldehyde	−0.457	0.799	0	0	0	0	0	0.0186
9-Phenanthraldehyde	−0.412	0.696	0	0	0	0	0	0.0165
3-Tolualdehyde	−0.622	1.112	−0.135	0	0	0	0	0.0224
4-Tolualdehyde	−0.627	1.114	−0.330	0	0	0	0	0.0249
Acetophenone	−0.574	1.040	−0.731	0	0	0	0	0.0211
1-Acetonaphthone	−0.375	0.635	−0.440	0	0	0	0	0.0125
2-Fluorobenzaldehyde	−0.563	0.987	0	−0.0969	0.192	0	0	0.1425
3-Fluorobenzaldehyde	−0.583	1.007	0	−0.0266	0.009	0	0	0.0986
4-Fluorobenzaldehyde	−0.583	1.037	0	−0.1294	0.289	0	0	0.1409
2-Fluoroacetophenone	−0.519	0.912	−0.631	−0.0979	0.191	0	0	0.1422
3-Fluoroacetophenone	−0.540	0.934	−0.648	−0.0288	0.011	0	0	0.0992
4-Fluoroacetophenone	−0.540	0.965	−0.640	−0.1384	0.309	0	0	0.1462
1-Chloronaphthalene	0	0	0	0	0	−0.163	0.352	0.1902
3-Chloroacetophenone	−0.531	0.911	−0.631	0	0	−0.029	0.011	0.1139
4-Chloroacetophenone	−0.518	0.913	−0.635	0	0	−0.145	0.321	0.1788

TABLE IV: Correlation Coefficient Matrix

	h_O	k_{CO}	h_{CH_3}	h_F	k_{CF}	h_{Cl}	k_{CCl}	δ
h_O	1	0.801	0.060	−0.193	−0.059	−0.034	−0.048	0.022
k_{CO}		1	0.251	−0.424	−0.453	−0.384	−0.380	−0.312
h_{CH_3}			1	−0.365	−0.372	−0.347	−0.332	−0.335
h_F				1	0.998	0.913	0.837	0.985
k_{CF}					1	0.907	0.836	0.975
h_{Cl}						1	0.987	0.902
k_{CCl}							1	0.824
δ								1

covariance matrix.[12] In this matrix we will represent the variances by $\sigma_{ii}{}^2$ and $\sigma_{jj}{}^2$ corresponding to the ith and jth parameters. σ_{ij} is the covariance term between the ith and jth parameters. The correlation coefficient between the ith and jth parameters is given by

$$\rho_{ij} = \frac{\sigma_{ij}}{(\sigma_{ii}{}^2 \sigma_{jj}{}^2)^{1/2}} \qquad i \neq j$$

Thus we can compute a correlation coefficient matrix from the variance–covariance matrix. The matrix will be symmetrical since the variance–covariance matrix is symmetrical. The diagonal elements are unity ($i = j$) since a parameter must be perfectly correlated with itself.

The correlation coefficient for the least-squares adjustment previously described is given in Table IV. This matrix is calculated after the least-squares solution has converged on a final set of parameters. The convergence of the procedure will be discussed shortly.

The magnitude of the correlation coefficient can range from −1 to +1. Values near −1 or +1 indicate nearly perfect correlation of the errors in the parameters, −1 referring to negative correlation and +1 to positive correlation. The parameters whose errors are highly correlated are obvious from Table IV. In particular, note the high correlation between δ and h_F, k_{C-F}, and h_{Cl} (column 8). As will be seen shortly from the variation of these parameters upon iteration, as δ increases, the parameters h_F, k_{C-F}, h_{Cl}, k_{C-Cl} increase. Also note the high correlation between h_F and k_{C-F} (row 4, column 5) and between h_{Cl} and k_{C-Cl} (row 6, column 7). In conclusion this particular set of EA data define these parameters very poorly.

The values of the parameters upon iteration are given in Table V. Iteration numbered zero is the initial approximation to the parameters. Only 1/4 the correction was applied for the first three iterations in order to ensure convergence. The fraction of the correction was increased until near the end the full correction was applied. The last column gives the sum of the weighted squared residuals. The variation in δ along with the h and k for F and Cl should be noted. An increase in δ from approximately 3 to 5 corresponds to a four- to fivefold increase in h_F and h_{Cl}. This simply illustrates the high positive correlation between δ and the h_F and h_{Cl}. Similarly, as the h_F and h_{Cl} increase the k_{C-F} and k_{C-Cl}, correspondingly increase, again illustrating the high correlation between these parameters.

Despite the fact that the parameters δ, h_F, k_{C-F}, h_{Cl}, and k_{C-Cl} are changing drastically, the $\Sigma W_i(\mathrm{res}_i)^2$ is lowered by only a factor of 3. This is really quite small especially when it is realized that the external estimate of the standard deviation, σ_{ext}, is related to the square root of $\Sigma W_i(\mathrm{res}_i)^2$. Thus σ_{ext} will vary by only a factor of ≈ 1.7. This simply means that the parameters are very poorly defined. This is shown quantitatively by the standard deviations in the parameters shown in the final row of Table V immediately under the final values of the parameters. These errors in the parameters are low estimates, since the errors ascribed to the EA_i assuming a common intercept are probably low. Evidence for this lies in the calculated $\sigma_{ext} = 3.5$ compared to $\sigma_0 = 1.0$. Part of this discrepancy lies in the limitations of the Hückel theory to adequately calculate electron affinities.

Obviously a precise value of δ cannot be established with

TABLE V: Variation in the Parameters upon Iteration

Iteration	h_r	k_{CO}	k_{CH_3}	h_F	k_{CF}	h_{Cl}	k_{C-Cl}	δ	S
0	0.922	1.357	-0.105	1.799	1.048	1.986	1.095	2.951	375
1	0.936	1.322	-0.109	2.652	1.450	2.967	1.551	3.885	274
2	0.946	1.304	-0.113	3.600	1.859	4.074	2.017	3.957	214
3	0.955	1.297	-0.115	4.534	2.236	5.180	2.452	4.338	178
4	0.968	1.291	-0.118	6.368	2.884	7.187	3.207	4.921	152
5	0.975	1.294	-0.119	7.283	3.273	8.504	3.669	5.197	134
6	0.979	1.297	-0.120	7.800	3.456	9.150	3.888	5.301	125
7	0.985	1.303	-0.121	8.246	3.613	9.707	4.075	5.373	121
8	0.986	1.305	-0.121	8.165	3.587	9.614	4.042	5.352	121
9	0.986	1.305	-0.121	8.180	3.591	9.633	4.048	5.357	121
10	0.987	1.305	-0.121	8.180	3.591	9.630	4.047	5.356	121
Std dev	±0.052	±0.044	±0.006	±2.44	±0.79	±3.05	±1.06	±0.74	

TABLE VI: Literature Values for h_{Cl} and k_{C-Cl}

h_{Cl}	k_{C-Cl}	Method	Ref
0.8	0.56	Valence state and molecular IP	15
1.0–1.6	0.5–0.9	IP chlorobenzene	16
1.63	0.89	IP, e^- density	17
2.5	1.0	Spectral data	18
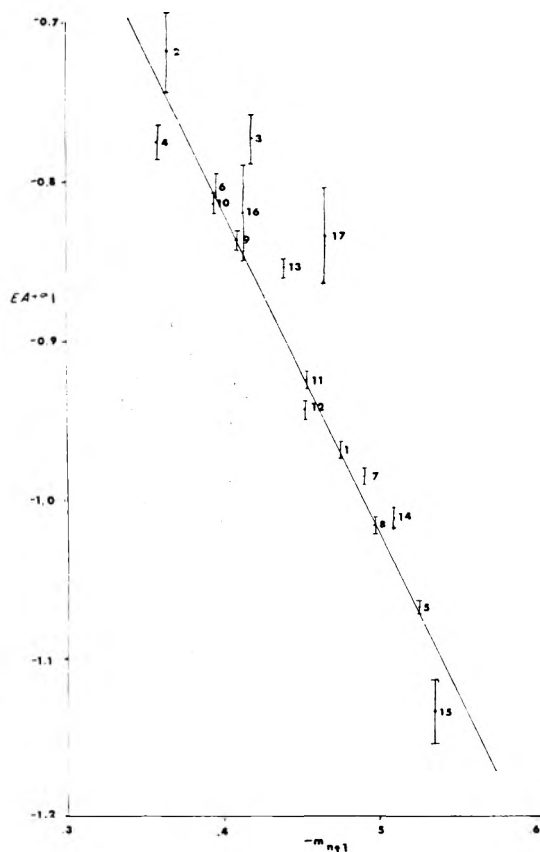
Figure 3. Graph of Hückel results from the general least-squares adjustment with $1/\delta = 1/3$

this set of EA_i. Since h_F and h_{Cl} on the order of 2 seems most reasonable, a value of $1/\delta$ of $1/3$ was chosen. This value has been used by other authors.[10] The least-squares adjustment was therefore rerun with $1/\delta = 1/3$ as a fixed quantity. The other parameters in Table V were carried as

adjustible parameters. The final parameters are shown in the last column of Table II. A graph of $(EA + \alpha_j)$ vs. $-m_{n+1}$ is shown in Figure 3.

Very little can be said regarding the absolute magnitude of the h and k parameters because of the high correlation between them. However, we might note that the ratio of k/h is much higher for O than for F or Cl which is generally what has been found from other studies.[10] Furthermore, the h_F and h_{Cl} are significantly higher than h_O which also has been observed in other studies.[10]

The correlation in Figure 3 appears to be satisfactory as revealed by the reasonably small residuals, column 10 in Table II, which are generally in the range 0.0–0.04 eV. The external estimate of the variance for this data is 0.035 eV which is larger than a typical $\sigma_{EA} \approx 0.02$ eV, but the discrepancy is not excessive.

As we have seen, the correlation which we observe between the various parameters δ and h, h and k, β and k prohibits the establishment of an accurate set of parameters. Most likely, use of experimental measurements such as ionization potentials will result in the same correlation. Possibly this is one explanation why the use of seemingly accurate experimental results can result in widely different Hückel parameters.

To support this hypothesis values of h_{Cl} and k_{C-Cl} reported in the literature are shown in Table VI. The values of h_{Cl} vary from 0.8 to 2.5 and k_{C-Cl} from 0.56 to 1.0. However, note that the magnitude of k_{C-Cl} appears to depend upon the magnitude of h_{Cl} and when h_{Cl} is large, the corresponding k_{C-Cl} is large. In other words h_{Cl} and k_{C-Cl} appear to be positively correlated, just as was noted previously in this study using EA measurements.

Conclusions

From this study of the EA of various substituted aromatic compounds the following conclusions can be summarized. (1) The change in EA upon substitution is generally in the direction which one would expect from the chemical aspects of these substituents; i.e., CH_3 generally lowers the EA whereas F, Cl, CF_3, $C\equiv N$, OCH_3, increase the EA. (2) Use of inductive and resonance parameters in the framework of Hückel theory satisfactorily accounts for the EA for different substituents and positions of the substituents in the compounds. (3) Comparisons of calculated with experimental EA do not adequately define the auxiliary inductive parameter. Other experimental quantities similarly may not define the parameter with any greater accuracy and this could explain the wide variation of values in the

literature. A value of $1/\delta = 1/3$ seems to give more reasonable values for h and k. (4) Comparisons of calculated and experimental EA do not adequately define both h and k parameters. The parameters are highly correlated. Again, this may well explain the wide variation in h and k values given in the literature. (5) The relative magnitudes of h and k for O, F, and Cl are in reasonable agreement with similar parameters derived from other experimental measurements.

References and Notes

(1) W. E. Wentworth and R. S. Becker, *J. Am. Chem. Soc.*, **84**, 4263 (1962).
(2) W. E. Wentworth, E. Chen, and J. E. Lovelock, *J. Phys. Chem.*, **70**, 445 (1966).
(3) P. G. Simmonds, D. C. Fenimore, B. C. Pettitt, J. E. Lovelock, and A. Zlatkis, *Anal. Chem.*, **39**, 1428 (1967).
(4) W. E. Wentworth, R. S. Becker, and R. Tung, *J. Phys. Chem.*, **71**, 1652 (1967).
(5) W. E. Wentworth, E. Chen, and J. C. Steelhammer, *J. Phys. Chem.*, **72**, 2671 (1968).
(6) J. C. Steelhammer and W. E. Wentworth, *J. Chem. Phys.*, **51**, 1802 (1969).
(7) W. E. Wentworth and J. C. Steelhammer in "Advances in Chemistry Series", "Radiation Chemistry II", E. S. Hart, Ed., American Chemical Society Publications, Washington, D.C., 1968, Chapter 4.
(8) W. E. Wentworth and J. Wiley, unpublished results.
(9) W. E. Wentworth and E. Chen, *J. Phys. Chem.*, **71**, 1929 (1967).
(10) A. Streitwieser, "Molecular Orbital Theory", Wiley, New York, N.Y., 1961, p 117.
(11) R. S. Becker and E. Chen, *J. Chem. Phys.*, **45**, 2403 (1966).
(12) R. N. Compton, L. G. Christophorou, and R. H. Huebner, *Phys. Lett.*, **23**, 656 (1966).
(13) W. E. Wentworth, *J. Chem. Educ.*, **42**, 96, 162 (1965).
(14) M. J. Al-Joboury and D. W. Turner, *J. Chem. Soc.*, 4439 (1969).
(15) J. A. Howe and J. H. Goldstein, *J. Chem. Phys.*, **26**, 7 (1957).
(16) Y. I'Haya, *J. Am. Chem. Soc.*, **81**, 6120 (1959).
(17) H. H. Jaffe, *J. Chem. Phys.*, **20**, 279, 1554 (1952).
(18) W. W. Robertson and F. A. Matsen, *J. Am. Chem. Soc.*, **72**, 5252 (1950).

Cooperativity of Linked Polymerization and Ligand Binding Equilibria[1]

Jan Hermans, Jr.,*[2] and Samuel Premilat

Department of Biochemistry, University of North Carolina, Chapel Hill, North Carolina 27514   (Received December 16, 1974)

Publication cost assisted by the National Science Foundation

Several different physical cases are proposed in which reversible linear polymerization of macromolecules (also polymerization to give helical structures) and ligand binding are linked. The partition function for these models is obtained in closed form; for one case this is done using a new formalism by which the "matrix method" for solving the linear Ising lattice can be extended to describe linear polymerization as well as conformation changes and ligand binding. The behavior of examples of these models is calculated. Cooperativity, that is linkage between two similar steps (i.e., two or more binding steps, two or more polymerization steps) is found to occur in some of the models. It is analyzed how one might proceed to use experimental data (binding and polymerization as a function of concentration of both macromolecule and ligand) in order to determine an appropriate model and its parameters. It is shown that the variation (a) of fraction bound with fraction polymerized, obtained by varying the polymer concentration at constant ligand activity, and (b) of the ratio between weight average and number average molecular weight with the extent of the polymerization are useful in this respect.

I. Introduction

In the assembly of large biological structures from macromolecular components, the specific fit between similar (or dissimilar) parts is responsible for the uniqueness of the result. This fit or recognition ensures a very great relative stability for one or only a very few possible arrangements of the parts and the assembled product is often much more stable than the dissociated complex.[3,4] One can reasonably expect that the final stability would be greatest for those structures whose function does not require a redissociation. In those cases, the state of the final product is most probably the result of the kinetics of the association processes. On the other hand, structures which are frequently dissociated and re-formed will more often correspond to equilibrium distributions of the components. In either case, the assembly process may be controlled by the binding of smaller molecules to the components, to intermediates, or to the final assembly. We shall here discuss the special case of reversible polymerization of linear (or helical) assemblies, linked to reversible ligand binding.

II. Specific Models

A formal definition of linkage of two equilibria, a and b, is simply this: to the various states of equilibrium a correspond values of the equilibrium constant for equilibrium b which are not at all alike.[5] While this abstraction is most suitable for the development of the theory, we wish first to describe several probable linkage mechanisms in terms of the structure of the components and of the polymerized assembly.

As our first case (case a, cf. Figure 1a) the binding of the ligand favors the polymerization because the polymer possesses powerful binding sites at the interfaces between the monomers: each monomer has two different weak binding sites.[6] This linkage may be called direct. In the not unusual case where the monomer is built up of two identical halves, there might be twice as many of each kind of site per monomer unit (case b, cf. Figure 1b). This case becomes somewhat more complex if the binding sites for ligand are adjacent, and the binding reactions thereby linked. Particularly interesting is the case where binding of the second ligand molecule at any interface between two units is easier than the binding of the first. The two ligand binding steps are then linked, and this introduces what is generally called cooperativity.[5]

Linkage between the polymerization steps is also a possibility. If the structure of the assembly is helical, and each unit interacts both with nearest neighbors and with units further distant along the helix, then the equilibrium constant for adding a monomer to a long polymer may be much greater than that for the formation of dimer from two monomers.[3,7] (The intermediates are, therefore, relatively unlikely species and this will cause the rate of polymerization to be correspondingly low.)

A most interesting additional possibility is that linkage is indirect, namely, via linkage to a conformation change of the building block. The binding of one ligand molecule may improve one of the polymerization sites (case c), or this may require two ligand molecules in a cooperative step; the binding of the two ligand molecules to a free monomer (case d) may be cooperative or not (Figure 1c and 1d). The binding of a single ligand molecule may alter the conformation of an asymmetrical unit so that *two* new binding sites arise which are mutually complementary (case e). In this case, two units *each* bearing a ligand molecule join more readily than any other two units. This is also a cooperative situation; here the binding of the two ligand molecules is linked via the polymerization reaction and the occurence of the conformation change is almost incidental. In the last case which we discuss (case f, cf. Figure 1f) we have symmetrical units in which the binding of a ligand causes a conformation change of one half of the molecule, and the half in the new conformation associates more readily with halves of like conformation.

III. Mathematical Description

The one-dimensional or linear Ising lattice is a suitable simple model for treating conformational equilibria of macromolecules when these macromolecules can exist in distinguishable states (e.g., coiled and helical), and one wishes to express mathematically the fact that the transition of the molecules from one state to the other is cooperative. The cooperativity finds its cause in the fact that two macromolecular conformations in which the structure is distributed over the two states in equal proportion (e.g., one to one) are not necessarily equally probable, the relative probabilities being determined by how many stretches of units in one state, interrupted by stretches of units in the other state, there are in these conformations. The Ising model simulates this behavior by being divided into sites, each of which can be in one of two (or more) well-defined states. The likelihood of finding a given site in one of the states is a number which depends on external parameters, e.g., the temperature, and has different values, depending on the state of the neighboring sites. This immediate envi-
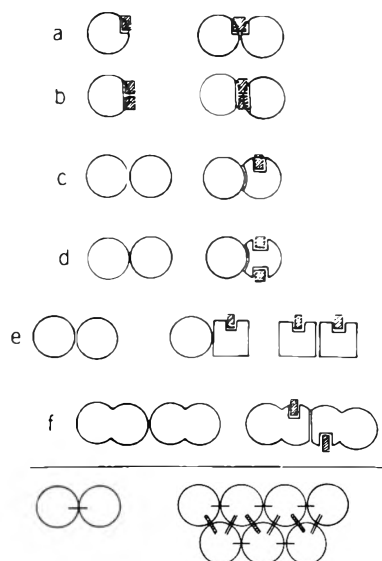
Figure 1. Schematic representations of the linked equilibria for six different models, a through f, discussed in the text. Hashed rectangles indicate ligand molecules bound to the units, which are indicated with different shapes: square, circle, circles with a piece removed indicate different conformations. A better "fit" in the figure indicates a more stable dimer. In case f, the figure eight shapes indicate symmetrical units. The two diagrams at the bottom illustrate how in polymerization to a helical structure the formation of the dimer results in fewer favorable contacts per step than does elongation of oligomers.

ronment may be composed of the two nearest neighbors, or it may extend farther. However, the influential environment must be finite in size.

This model can be used effectively to describe helix–coil equilibria of macromolecules (synthetic polypeptides),[8-11] the binding of ligands to macromolecules,[12,13] and the linkage of helix–coil equilibria and ligand binding equilibria.[14] The solution of the algebraic problems which occur in the mathematical analysis may be performed by several methods, of which the matrix method is used below.[8]

We present here a new method by which polymerizing systems can be treated with the same model. Examples of such were described in the preceding section. Of the cases described, only case e requires the use of this new method. The other systems do not require the application of the Ising model even when there are cooperative effects.

Conformational Transitions and Ligand Binding. A description according to the one-dimensional Ising lattice implies that the behavior of each site is linked to the state of only a finite number of sites on either side. We restrict this to a single site on either side. For such systems, methods exist to evaluate the partition function

$$z = \Sigma c_i \qquad (1)$$

which is the sum of the concentrations (in moles per unit of volume) of all the species which can occur, and of the derivatives of z, which are related to the measurable parameters of the system.

For the helix–coil transition z may be written as the summation over groups of molecules having the same number, i, of helical units grouped in j stretches of helix

$$z_t = \sum_i \sum_j w_{ij} s^i \sigma^j \qquad (2)$$

where w_{ij} is the number of ways in which this combination can be obtained in this particular molecule, s the equilibrium constant for lengthening a helical region by one unit,

and σ the equilibrium constant for separating a helical region into two helical regions with the same number of helical units. For cooperative ligand binding to a polymer, one has

$$z_t = \sum_i \sum_j w_{ij}(ly)^i \tau^j \tag{3}$$

where now the ligands are bound on j stretches of adjacent sites; l is the equilibrium constant for ligand binding to a site with one neighbor carrying a ligand, the product $l\tau$ the equilibrium constant for binding a ligand to a site with unliganded neighbors, and y the activity of unbound ligand. This summation is the same as that in eq 2.

We here follow the well-known matrix method for carrying out this summation and others like it. In this method,[8] one constructs a matrix containing as elements the various values of the equilibrium constants for going in one site from one state to another, which differ depending on the state of one neighboring site. Repeated multiplication of this matrix by itself generates a matrix with elements which are sums of relative concentrations (products of powers of equilibrium constants) of the type $s^i \sigma^j$, one for each distinct realizable overall state of the molecule. Thus, in order to perform the summation in eq 2 one writes the matrix

$$\mathbf{M_t} = \begin{bmatrix} 1 & 1 \\ \sigma s & s \end{bmatrix} \tag{4}$$

and finds that elements (1,1) and (2,1) of the matrix $\mathbf{M_t}^n$ contain all the terms of the sum in eq 2, i.e.

$$z_t = \begin{bmatrix} 1 & 1 \end{bmatrix} \mathbf{M_t}^n \begin{bmatrix} 1 \\ 0 \end{bmatrix} \tag{5}$$

The power of the method lies in the possibility of simplifying $\mathbf{M}^n$ by diagonalizing $\mathbf{M}$

$$\mathbf{M} = \mathbf{U} \begin{bmatrix} \lambda_1 & 0 \\ 0 & \lambda_2 \end{bmatrix} \mathbf{U}^{-1} = \mathbf{U}\Lambda\mathbf{U}^{-1} \tag{6}$$

and using

$$\mathbf{M}^n = \mathbf{U}\Lambda^n\mathbf{U}^{-1} = \mathbf{U} \begin{bmatrix} \lambda_1{}^n & 0 \\ 0 & \lambda_2{}^n \end{bmatrix} \mathbf{U}^{-1} \tag{7}$$

This method can easily be extended to a situation where a cooperative helix–coil equilibrium and cooperative ligand binding are linked.[14] Table I lists the possible states of each site and the statistical weight for each state when the preceding site is in the four different states. (This array of expressions is the matrix $\mathbf{M}$ for this problem.) As written, Table I describes a situation where ligand binding to the coil (equilibrium constant l_1) is not cooperative, but that to the helix is (equilibrium constant l_2 or $l_2\tau$ depending on the state of the preceding site. With $\tau = 1$, the matrix describes linkage of noncooperative ligand binding and a cooperative helix–coil equilibrium.)

Polymerizing Systems. For a simple polymerizing system

$$z_p = x \sum_{i=0}^{\infty} (kx)^i = x/(1 - kx) \tag{8}$$

where x, the activity of the monomer, is assumed equal to the concentration of the free monomer, and k is the equilibrium constant for adding a unit to the monomer to form a dimer, or to any polymer to form the next higher polymer.

For cooperative linear polymerization, lengthening of the first oligomers is more difficult than lengthening of the longer polymers.[5,8] In the most simple case, formation of

TABLE I: The Matrix M for Linked Cooperative Ligand Binding and a Cooperative Helix–Coil Transition[a]

		1	2	3	4
1.	ligand free coil	1	1	1	1
2.	ligand free helix	σs	s	σs	s
3.	ligand carrying coil	$l_1 y$	$l_1 y$	$l_1 y$	$l_1 y$
4.	ligand carrying helix	$l_2 y \sigma s \tau$	$l_2 y \tau s$	$l_2 y \sigma s \tau$	$l_2 y s$

[a] With $\tau = 1$, the ligand binding is not cooperative.

the dimer alone is unfavorable, the equilibrium constant for dimerization being σk, $\sigma < 1$. The partition function may be written as the sum of one term for the monomer and the terms of a geometric series

$$z_{pc} = x + \sigma x \sum_{i=1}^{\infty} (kx)^i = x - \sigma x + \sigma z_p =$$
$$\{x - kx^2(1 - \sigma)\}/(1 - kx) \tag{9}$$

How can one now use the power of the matrix method in treating linked equilibria involving polymerizing systems? This can be accomplished by considering the polymer as a linear arrangement of sites, which are either filled or not filled with a monomer molecule. There are then two states and the matrix for this system should have the form

$$\begin{matrix} \text{empty site} \\ \text{monomer in site} \end{matrix} \begin{bmatrix} 1 & 1 \\ 0 & kx \end{bmatrix} = \mathbf{M_p} \tag{10}$$

where *the zero element indicates that the chain is not restarted once it has been terminated.* One can easily verify that the sum occurring in the partition function (eq 8) is given by the (1,2) element of the matrix obtained by taking $\mathbf{M_p}$ to the limit of a very high power, i.e.

$$z_p = x \sum_{i=0}^{\infty} (kx)^i = x[1\ 0] \lim_{n \to \infty} \begin{bmatrix} 1 & 1 \\ 0 & kx \end{bmatrix}^n \begin{bmatrix} 0 \\ 1 \end{bmatrix} \tag{11}$$

The value of using this formalism lies in the possibility of describing linked ligand binding and polymerization using a somewhat larger matrix.

Linkage of Polymerization, Binding, and Conformation Change. We distinguish between the specific models described above (cf. Figure 1). In cases a and c, the equilibrium constant for ligand binding to polymerized subunits, l_2, is different from the binding to the first in any polymer (including the polymer of length one = the monomer), l_1. This description is expected to hold, for example, when the ligand participates in the contact between two adjacent monomers, but does not affect the conformation of the monomers (Figure 1, case a). The matrix for this case is given in Table II, y being the activity of the ligand. The partition function is then

$$z_{p11} = x[1\ 0\ 0] \lim_{n \to \infty} \mathbf{M}^n \begin{bmatrix} 0 \\ 1 \\ l_1 y \end{bmatrix} \tag{12}$$

This case is not cooperative. In subsequent calculations we shall ignore ligand binding to the first unit, and let $l_1 = 0$, using l for l_2.

In cases b and d, cooperativity is introduced by having several, e.g., m, ligand molecules bind cooperatively to each monomer unit, thereby enhancing its affinity for binding to

TABLE II: The Matrix for Linked Ligand Binding and Polymerization

	1	2	3
1. no monomer unit	1	1	1
2. ligand free unit	0	kx	kx
3. liganded unit	0	kxl_2y	kxl_2y

TABLE III: The Matrix for Cooperatively Linked Ligand Binding and Polymerization

	1	2	3
1. no monomer unit	1	1	1
2. ligand free unit	0	kx	kx
3. liganded unit	0	$kxly$	$kxlyq$

other units. The cooperativity of the binding to each unit implies that any mcnomer unit carries either no ligand molecules or m ligand molecules. This case is described by replacing l_2y in the matrix of Table II with $(l_2y)^m$, and writing

$$z_{pl2} = x[1\ 0\ 0] \lim_{n \to \infty} \mathbf{M}^n \begin{bmatrix} 0 \\ 1 \\ (l_1y)^m \end{bmatrix} \qquad (13)$$

In case e, cooperativity obtains when the binding of a ligand to a unit adjacent to another unit already carrying a ligand is stronger (or weaker, for negative cooperativity) than to a unit not so placed. With the simplifying assumption that the binding has no effect on the polymerization except when adjacent units in a polymer carry ligand, the matrix for this case is given in Table III; l is the equilibrium constant for ligand binding to the monomer or to isolated units in the polymer, the product lq is the equilibrium constant for binding ligand to a unit following a ligand carrying unit. The partition function is

$$z_{pl3} = x[1\ 0\ 0] \lim_{n \to \infty} \mathbf{M}^n \begin{bmatrix} 0 \\ 1 \\ ly \end{bmatrix} \qquad (14)$$

Summation of the Partition Function. In the first two cases the formalism given here is superfluous. The partition functions are obtainable by simply extending eq 9.[6] For linked noncooperative ligand binding (m sites per unit) and polymerization (case a) one obtains

$$z_{pl1} = x/\{1 - kx(1 + ly)^m\} \qquad (15)$$

which is simply the partition function of eq 9 with k replaced by $k(1 + ly)^m$; for cooperative ligand binding (case b with strong cooperativity)

$$z_{pl2} = x/[1 - kx(1 + l^m y^m)] \qquad (16)$$

For linkage of cooperative polymerization and ligand binding one can similarly obtain the partition function by replacing k with $k(1 + ly)^m$ or $k(1 + l^m y^m)$ in eq 9.

The partition function for case c is the same as for case a and the analogous cooperative case d behaves as case b. For the case of cooperative linkage of ligand binding and polymerization (case e) one does need eq 14 in order to evaluate z, and we obtain

$$z_{pl3} = \frac{1 + kxly(1 - q) + lv}{1 - kx(1 + lyq) - (kx)^2 ly(1 - q)} x \qquad (17)$$

(This result is derived in the final section of this article.) Finally, the partition function for case f is the same as for case b.

We remain with three different partition functions. It is an easy matter to modify any of these in order to describe a cooperative polymerization equilibrium linked to a binding equilibrium. In these situations the first or the first few polymerization steps have lower equilibrium constants than the succeeding ones. One expresses the concentrations of the first oligomers in terms of l, y, k, and x and (one or

more) σ, where σ has the same meaning as in eq 9. With $\sigma = 1$, the sum of the concentrations is one of the partition functions given in eq 15–17. All the terms except those with a lower power of x will differ only by a factor σ (or the product of the σ's for the several difficult steps). The partition function is, therefore

$$z_\sigma = \sigma z_{\sigma=1} + \sum_{i=1}^m (c_{i,\sigma} - \sigma c_{i,1}) \qquad (18)$$

where m is small (often = 1) and $c_{i,\sigma}$ and $c_{i,1}$ the concentrations of i-mer in case the polymerization, respectively, is and is not cooperative.[3,7]

Use of the Partition Function. The measurable parameters of the system, such as, average number of helical sites per molecule, average ligand binding, average degree of polymerization, can all be obtained by differentiation of z[5,15,16] For a polymerizing system, also capable of ligand binding, the partition function may be written as a double sum of concentrations over i, the number of monomer units associated to form a polymer, and j, the number of ligand molecules bound to this polymer:

$$z = \sum_i \sum_j c_{ij} = \sum_i \sum_j w_{ij} x^i (ly)^j \qquad (19)$$

cf. also eq 2 and 3. The total concentration in terms of monomer units is

$$c_0 = \sum_i i c_i = \sum_i \sum_j i w_{ij} x^i (ly)^j = \partial z / \partial \ln x \qquad (20)$$

Often, the activity ($\simeq$ concentration) of free ligand is known from measurement (potentiometric; equilibrium dialysis), in other cases it may essentially be equal to the total ligand concentration, y_0. In these instances, the free monomer concentration is found as the value of x satisfying ec 20.[17] In all other cases, one also needs

$$y_0 = \sum_j j c_j + y = \partial z / \partial \ln (ly) + y \qquad (21)$$

Since z is a function of both x and y, these unknowns are obtained by solving eq 20 and 21 for x and y. These relationships depend only on the occurence of the i-th power of x in the expression for the concentration of any i-mer and of the j-th power of y in the expression for the concentration of any species carrying j ligand molecules.

One will easily see that the reacted fraction of the polymerization sites is given by

$$f_p = 1 - \Sigma c_i / \Sigma i c_i = 1 - 1/\langle i \rangle_n = \\ 1 - \partial \ln x / \partial \ln z \qquad (22)$$

where $\langle i \rangle_n$ is the number average degree of polymerization. The weight average degree of polymerization is given by

$$\langle i \rangle_w = \Sigma i^2 c_i / \Sigma i c_i = \{\partial^2 z / (\partial \ln x)^2 / (\partial z / \partial \ln x)\} \qquad (23)$$

For a most probable distribution of polymer size, which obtains in noncooperative polymerization, i.e., when z is given

by eq 8, 15, or 16, the ratio between the two averages is[18]

$$\langle i \rangle_w / \langle i \rangle_n = 2 - 1/\langle i \rangle_r = 1 + f_p \qquad (24)$$

Finally, the fraction of all binding sites which are occupied by a ligand molecule is given by

$$f_b = (1/\nu) \sum_j jc_j / \sum_i ic_i = (\partial z/\partial \ln ly)/(\nu \, \partial z/\partial \ln x) \qquad (25)$$

where ν is the number of binding sites per monomer unit.

Neglecting binding to the monomer, one may relate the binding in the case of a single binding site per monomer unit to that in the case of multiple sites. For the models with a single site one can write the partition function, z, as a function of $k(1 + ly)$. For multiple sites, z is the same function of $k(1 + ly)^m$ in case the binding to a single unit is not cooperative, and of $k(1 + l^m y^m)$ if the binding is cooperative. One then has

$$z_1 = F\{k(1 + (ly)_1)\}$$
$$z_m = F\{k(1 + (ly)_m)^m\} \qquad (26)$$

and

$$z_{m,c} = F\{k(1 + (l^m y^m)_{m,c})\}$$

The derivatives of z with respect to k will be the same for the same value of the argument of the function F. Hence, given the same value of k, the distribution over polymers of different size in the three cases will be the same when, respectively, $(1 + ly)$, $(1 + ly)^m$, and $(1 + l^m y^m)$ have the same value. The fraction of sites carrying ligand is proportional to $ly \, \partial z/\partial ly$. Given the same values of the argument (i.e., not at equal values of ly), the fractions bound in the three cases are related as follows

$$f_b(1) = f_b(m, c) = \frac{\{1 + (ly)_m\}^{m-1}}{(ly)_m\{1 + (ly)_{ml}\}^{m-1}} f_b(m) \qquad (27)$$

In particular

$$f_b(2) = \frac{1 + (l_1)_2}{2 + (l_1)_2} f_b(1) \qquad (28)$$

IV. Calculated Examples

We now present several calculated examples, in order to show in what way the behavior according to the three models differs, and how one might treat experimental data in order to choose the best model, and then obtain estimates for the various parameters. This must be done in such a way that use is made of those experimental data which are most readily obtained. We must also avoid using properties of the models which are trivial. Since our interest lies in the promotion of polymerization by ligand binding we have neglected ligand binding to the monomer in some of the calculations. This is only a convenience; more probably than not, a unit which can bind a ligand when polymerized can also bind the ligand when a monomer. As a consequence, the polymerization will no longer be dependent on the ligand concentration when the latter is very large. In case each of the polymer's ligand binding sites were shared by two adjacent monomeric units, each free monomer might have twice the number of ligand binding sites of the polymerized unit, and, as a result, very high ligand concentration would reverse the polymerization. However, we do not wish to rely on these and other properties of the models which can only be determined at very high or at very low
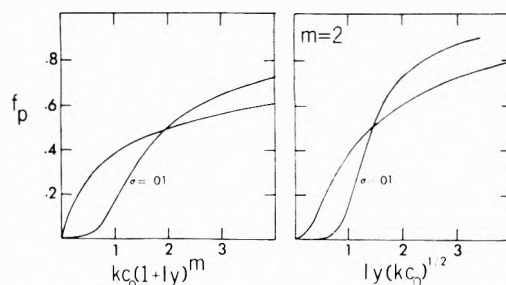
Figure 2. Polymerization curves for cases a through d, with noncooperative polymerization and for the case of cooperative polymerization with dimerization less easy than subsequent steps by a factor σ = 0.01. On the left the curves are plotted for any number, m, of ligand binding sites per unit. On the right the same values are plotted vs. free ligand concentration, y, for units with two ligand binding sites (for small values of kc_0).
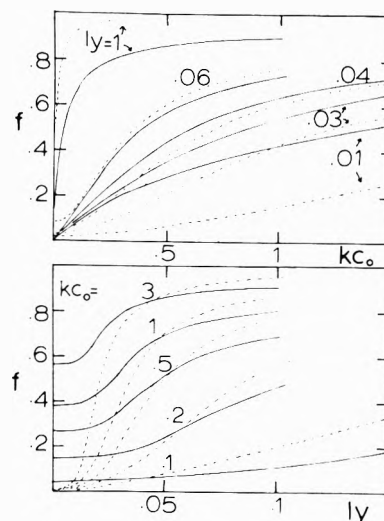
Figure 3. Polymerization and ligand binding curves for case e, with q = 100: solid curves, polymerization; dashed curves, binding.

concentrations, since the necessary experiments often are not feasible or give ambiguous results for other reasons.

In a polymerizing system which one is studying in order to make a careful theoretical analysis one usually knows the size of the monomer unit and the number of ligand binding sites per unit. (Notice, however, possible complications when the number of binding sites per unit is different in the monomer than in the polymer.) Linkage between binding and polymerization is usually established by detecting changes in polymerization (e.g., in average molecular weight) with the concentration of added ligand. A complete study of linked binding and polymerization subsequently should yield data on the extent of both ligand binding and polymerization as a function of both ligand concentration and macromolecular concentration. We must, therefore, examine how the different models behave in this respect, keeping in mind that the range of accessible experimental conditions is finite.

Binding Curves and Polymerization Curves. Figure 2 shows how the fraction polymerized (cf. eq 22) depends on the total protein concentration, c_0, and the concentration of free ligand, y, for noncooperative linear polymerization and for the cooperative case in which the equilibrium constant for dimerization is smaller than that for any other association by a factor σ = 0.01.[3,6,7] The sigmoid behavior shown in the latter case is typical of cooperative equilibria
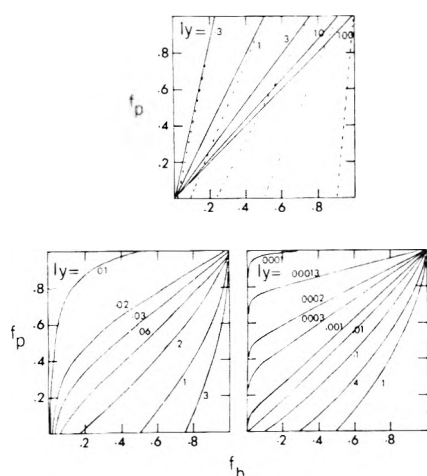
Figure 4. Plots of fraction polymerized vs. fraction bound for each curve, the polymer concentration varies and the ligand activity is constant. Top: for cases a through d. Solid lines are for the case where ligand binding to free monomer may be neglected; the dashed lines are for the case where the ligand binding constant for free monomer is one-tenth that for polymerized monomer (case a). Bottom: For case e, with $q = 10^2$ and 10^4, respectively.

Figure 5. Two size distributions for case e with two different sets of parameters, plotted on a semilogarithmic scale.

in general. When there is one binding site per unit, the curves are also linear plots of degree of polymerization vs. free ligand concentration. In the noncooperative case the curve will not be sigmoid. With multiple sites, the degree of polymerization vs. the ligand concentration easily becomes sigmoid even when the binding to a single unit is not cooperative. This happens when $kc_0 \ll 1$, i.e., there is essentially no polymerization in the absence of ligand, a not unusual situation. In order to get polymerization ly must in that case be large and then $(1 + ly)^m \approx l^m y^m \approx 1 + l^m y^m$. It is impossible to distinguish if the binding is cooperative per se, or not. The resulting polymerization curves are given in Figure 2b for $m = 2$. The curves of Figure 2b do not serve to make a qualitative distinction between the case where the polymerization is cooperative or not. However if m is known, a plot of f_p vs. y^m will serve for this purpose.

When kc_0 is small, the binding curves are the same as the polymerization curves since the ligand will be bound to all units except free monomer and one terminal unit of each polymer. There is, therefore, a linear relation between fraction polymerized and fraction bound. This relation holds rigorously if each pair of values of f_b and f_p was determined at the same free ligand concentration, but different polymer concentration. This is still true for multiple binding sites and if there is (weaker) binding to the free monomer. In the absence of the latter f_b and f_p are simply equal for all measurements whenever kc_0 is very small.

Calculated results for case e, obtained using eq 16, are given in Figure 3. The value of q, a parameter somewhat comparable to the *reciprocal* of σ in the cooperative case a, is 10^2. All polymerization and binding curves are sigmoid, except in extreme situations where there is not much linkage, as when $ly = 1$ and the free monomer is already half saturated with ligand. A qualitative distinction between this case and per se cooperative polymerization linked to binding to multiple sites can be made on the basis of the variation of f_p with f_b at constant free ligand concentration. These plots are notably curved, and cover the available area in a completely different way than do the straight lines obtained for the simpler cases a through d (Figure 4).

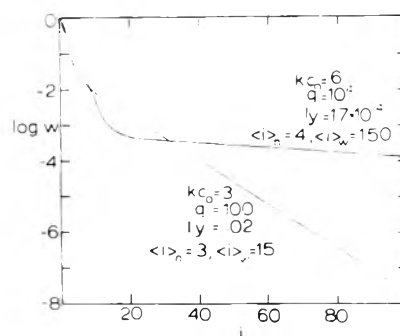*Size Distributions and Averages.* In the absence of coop-

erativity or when the cooperativity is positive, i.e., when σ < 1 or q > 1, the molar concentrations of the species containing different number, i, of monomers decreases monotonically as i increases. The corresponding concentrations by weight may, however, have a maximum for some length greater than one. The maximum occurs for a higher length, the larger the degree of polymerization. For cases a through d the maximum concentration occurs at a length near

$$i^* = -1/\ln (k'x) \qquad (29)$$

and is

$$i^* c_{i^*} = i^* x/e \qquad e = 2.718\ldots \qquad (30)$$

where k' may represent k, $k(1 + ly)$, etc. The weight concentration is greater than one-half the maximum for a size between about one-fourth and twice the length i^*.

For cases a through d with cooperative polymerization, one may consider the distribution to be altered only by there being an inappropriately high concentration of monomer (and perhaps a few other oligomers); the length at which the concentration has its maximum, if any, is still given by eq 29. For both cooperative and noncooperative cases a through d, as the polymer gets longer, the amount of ligand bound per unit increases gradually.

For the special cooperative case e, the distribution is not so transparent. The relative concentration of any i-mer will be equal to the concentration of the ligand-free i-mer multiplied by the partition function for binding ligand to a linear molecule with i sites, $z_{l,i}$, as given by eq 3

$$c_i = x(kx)^{i-1} z_{l,i} \qquad (31)$$

where $z_{l,i}$ may be evaluated with the matrix method. The distribution of the number concentration decreases monotonically, but the distribution of the weight concentration may now show two maxima. In Figure 5 we show a semilogarithmic plot of two such distributions; the curves consist of two linear portions, whereas for noncooperative polymerization such plots are straight lines, and for cooperative polymerization in cases a through d all the points except that for $i = 1$ would lie on a straight line. For the cases represented in Figure 5, the two parts correspond essentially to oligomers without ligand and polymers with all units carrying ligand, respectively. A necessary condition in getting significant amounts of both classes of molecules is, of course, that measurable polymerization occur in the absence of ligand but otherwise under the same conditions, and that the product qly be just large enough that a portion of the material turn into high polymers binding ligand.

Experimental information about molecular size distributions is obtainable only when the polymerization equilibri-
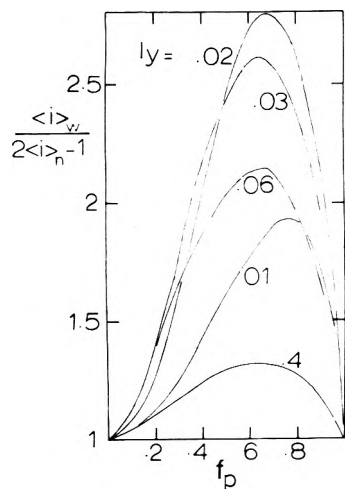
Figure 6. Deviation of the molecular weight distribution from a most probable distribution, as measured by the ratio $\langle i \rangle_w/(2\langle i \rangle_n - 1)$, for case e with $q = 100$.

um is established very slowly, or has been "frozen" by some artificial condition. More often, the only available information about the distribution comes from a comparison of different averages: the number average $\langle i \rangle_n$ and the weight average $\langle i \rangle_w$ being most easily obtained. It is a problem that techniques for obtaining $\langle i \rangle_w$ are more readily used than those for obtaining $\langle i \rangle_n$. Yet it proved convenient to express our results in terms of the fraction polymerized, f_p, which is directly related to $\langle i \rangle_n$ by eq 22. Only for a most probable distribution, which obtains with models a through d when the polymerization is not cooperative per se, can one use the simple relation 24 to obtain f_F from $\langle i \rangle_w$. We have calculated in what proportion $\langle i \rangle_w/\langle i \rangle_n$ deviates from that for a most probable distribution with the same $\langle i \rangle_n$. For cooperative polymerization, the ratio goes to 4.4 for $\sigma = 10^{-2}$ and 38.3 for $\sigma = 10^{-4}$. For case e, the maximum ratio is ca. 1.5 for $q = 10$, 1.9 for $q = 100$, and 20 for $q = 10^4$. A difference is that for the cooperative case a, the same maximum ratio dependent only on σ is always reached for the same extent of the reaction (at $f_p = 0.67$ for $\sigma = 10^{-2}$), while in case e the maximum ratio obtainable by varying the total polymer concentration depends on the concentration of free ligand (Figure 6).

V. Evaluation of the Partition Function for a Polymerization

It is asked to solve eq 11 using the matrix of Table III. The solution of this problem turns out to be very different from when one uses eq 11 to describe helix–coil equilibria,[8] e.g., using the matrix of Table I.

The diagonalization of the matrix gives

$$\mathbf{M} = \mathbf{U\Lambda U^{-1}} = \begin{bmatrix} a & b & c \\ d & e & f \\ g & h & i \end{bmatrix} \begin{bmatrix} \lambda_1 & 0 & 0 \\ 0 & \lambda_2 & 0 \\ 0 & 0 & \lambda_3 \end{bmatrix} \begin{bmatrix} a' & b' & c' \\ d' & e' & f' \\ g' & h' & i' \end{bmatrix} \quad (32)$$

where λ_1, λ_2, and λ_3 are the three eigenvalues of the matrix, obtained as roots of the equation

$$(1 - \lambda)\{(kx - \lambda)(kxl y q - \lambda) - (kx)^2 l y\} = 0 \quad (33)$$

(The symbols a through i represent the elements of a matrix $\mathbf{U}$ and a' through i' the elements of the matrix $\mathbf{U}^{-1}$.) Thus one of the eigenvalues is equal to one, and one can show that the other two are always positive and less than one for a physically meaningful set of values of kx, ly, and q. When Λ is raised to a very high power (cf. eq 7 and 13) the (1,1) element will be equal to one, all the other elements will be zero or tend to zero. If one carries out the operations of eq 13, one is left with

$$z_{pl_3} = x(ab' + ac'ly) \quad (34)$$

Using the equalities

$$\mathbf{U^{-1}M} = \mathbf{\Lambda U^{-1}} \text{ and } \mathbf{MU} = \mathbf{U\Lambda} \quad (35)$$

one finds that $d = g = d' = g' = 0$, $a = 1/a'$, and the values of b' and c' follow from the equations

$$\begin{aligned} b' &= kxb' + kxlyc' + 1/a \\ c' &= kxb' + kxlyqc' + 1/a \end{aligned} \quad (36)$$

Solving for b' and c' in terms of kx, ly, q, and a and substituting the result in eq 34 one obtains the partition function, eq 17.

Acknowledgment. The authors record with pleasure a long discussion with Professor Gary Ackers, whose insight into the problem of these linked equilibria provided the stimulus for doing this work.

References and Notes

(1) Supported by a Research Grant from the National Science Foundation (GB-16420) and a Research Career Development Award (GM-22015) from the Institute of General Medical Sciences, National Institutes of Health, U.S. Public Health Service.
(2) To whom requests for reprints should be addressed.
(3) F. Oosawa and M. Kasai, *J. Mol. Biol.*, **4**, 10 (1962).
(4) E. Kellenberger in "Polymerization in Biological Systems", Associated Scientific Publishers, New York, N.Y., 1972, pp 189 and 295.
(5) J. Wyman, *Adv. Protein Chem.*, **19**, 223 (1964).
(6) D. A. Deranleau, *J. Chem. Phys.*, **40**, 2134 (1964).
(7) J. Engel and D. Winklmair in "Protein-Protein Interactions", R. Jaenicke and E. Helmreich, Ed., Springer, New York, N.Y., 1972, p 159.
(8) B. H. Zimm and J. K. Bragg, *J. Chem. Phys.*, **31**, 526 (1959).
(9) J. H. Gibbs and E. A. DiMarzio, *J. Chem. Phys.*, **30**, 271 (1959).
(10) L. Peller, *J. Phys. Chem.*, **63**, 1194 (1959).
(11) T. L. Hill, *J. Chem. Phys.*, **30**, 383 (1959).
(12) B. H. Robinson, A. Loffler, and G. Schwarz, *Trans. Faraday Soc.*, **69**, 56 (1973).
(13) G. Schwarz and H. Klose, *Eur. J. Biochem.*, **29**, 249 (1972).
(14) B. H. Zimm and S. A. Rice, *Mol. Phys.*, **3**, 391 (1960).
(15) F. E. Harris and S. A. Rice, *J. Phys. Chem.*, **58**, 725 (1954).
(16) R. F. Steiner, *J. Theor. Biol.*, **45**, 93 (1974).
(17) If eq 20 has multiple roots, then the correct choice appears to be the smallest positive root. Rewriting (20) as $f(x) = 0$, one may find the correct root by using as a first approximation $x = 0$ and iteratively calculating approximations $x_{i+1} = x_i - f(x_i)/f'(x_i)$.
(18) P. J. Flory, "Principles of Polymer Chemistry", Cornell University Press, Ithaca, N.Y., 1953, Chapter 8.

Acid–Base Equilibria in Methanol, Acetonitrile, and Dimethyl Sulfoxide in Acids and Salts of Oxalic Acid and Homologs, Fumaric and o-Phthalic Acids. Transfer Activity Coefficients of Acids and Ions

M. K. Chantooni, Jr., and I. M. Kolthoff*

School of Chemistry, University of Minnesota, Minneapolis, Minnesota 55455 (*Received December 11, 1974*)

The first and second dissociation and the homoconjugation constants of the homologous series of oxalic to azelaic acid, fumaric, and o-phthalic acids and $K(HE)$ of some of their monoesters have been determined in dimethyl sulfoxide (DMSO) and methanol (M). From the data values of $K' = [\overline{HA^-}]/[HA^-]$, $\overline{HA^-}$ denoting the intramolecularly hydrogen bonded monoanion, have been found. The monoanions of malonic and o-phthalic acids in M are strongly intramolecularly hydrogen bonded (but not in water, W). In agreement with the above potentiometric data, ir spectra of biglutarate solutions yielded conclusive evidence that the biglutarate ion contains an intramolecular hydrogen bond in acetonitrile (AN) and $(CD_3)_2SO$. The ratio $K'(AN)/K'(DMSO) = 10^{1.7\pm0.2}$ closely corresponds to the difference in hydrogen bond accepting capacity previously reported between these two solvents. From this it is inferred that the carboxylic acid group in $\overline{HA^-}$ is not hydrogen bonded to the solvent DMSO, in contrast to that in HA^-. This has been confirmed by ir spectrometry. Ir spectra of mixtures of glutaric acid with biglutarate in AN indicate the presence of an intermolecular hydrogen bond between the carboxylate group of $\overline{HA^-}$ and the acid in the homoconjugate $\overline{HA^-}\cdots H_2A$. No indication of intramolecular hydrogen bonding in the bioxalate ion was found in W, M, and DMSO. From solubilities of the dicarboxylic acids and silver salts of some of the monoesters in AN and the other solvents transfer activity coefficients of the various acids and their ions between AN and W, M, and DMSO have been obtained.

Introduction

In a previous paper[1] we reported in acetonitrile (AN) first and second dissociation constants, K_1 and K_2, homoconjugation constants, K_{homo}, of the homologous series of oxalic to and including azelaic acid, also of fumaric and o-phthalic acid, and the dissociation constants $K(HE)$ and homoconjugation constants $K(HE_2^-)$ of the corresponding monomethyl or -ethyl esters (HE). Using eq 1, first proposed by Westheimer and Benfy,[2] we calculated the equilibrium constants K' between intramolecular and nonintramolecular hydrogen bonded monoanions, $\overline{HA^-}$ and HA^-, respectively. The corresponding values of K' of the above

$$K' = [\overline{HA^-}]/[HA^-] = K_1/2K(HE) - 1 \qquad (1)$$

acids in water are equal to or close to zero.[2] In the present paper these studies are extended to the solvents methanol (M) and dimethyl sulfoxide (DMSO). Compared as solvents (not as solutes), methanol is a slightly stronger hydrogen bond acceptor than water[3] and about an equally strong hydrogen bond donor. Dimethyl sulfoxide, a typical dipolar protophilic solvent, is a much stronger hydrogen bond acceptor than acetonitrile, but about an equally poor hydrogen bond donor. In contrast to water and methanol, solvation of a carboxylate ion by hydrogen bonding in AN, DMF, and DMSO is negligible.[3,4] With the nonintramolecularly hydrogen bonded monoanion HA^-, DMSO forms an intermolecular hydrogen bond with the carboxylic acid group. Evidence is presented in this paper that this does not occur with $\overline{HA^-}$. Consequently, the values of K' in DMSO should be smaller than in AN. An additional reason for the inclusion of M and DMSO in the present study is to obtain values of the transfer activity coefficients, γ, of H_2A, ΣHA^- (= $\overline{HA^-}$ + HA^-) and A^{2-} between the amphiprotic solvents M and water (W) on one hand and AN and DMSO

on the other. Also, the Born effect on transfer activity coefficients of ions between the close to isodielectric solvents M, AN, and DMSO is almost negligible and small even for $p\gamma(A^{2-})$. Our values of γ_{ion} are based on the tetraphenylborate assumption which yields almost the same values for the organic solvents as the ferrocene assumption.[5,6]

Values of $^{AN}\gamma^S(H_2A)$ and $^{AN}\gamma^S(HE)$ were determined from solubility data of the diacids and monoesters, respectively, while those of $^{AN}\gamma^S(\Sigma HA^-)$ and $^{AN}\gamma^S(A^{2-})$ were obtained from the relations

$$(pK_1)_S - (pK_1)_{AN} = {}^S\Delta^{AN}pK_1 =$$
$$p^{AN}\gamma^S(H^+) + p^{AN}\gamma^S(\Sigma HA^-) - p^{AN}\gamma^S(H_2A) \qquad (2)$$

$$(pK_2)_S - (pK_2)_{AN} = {}^S\Delta^{AN}pK_2 =$$
$$p^{AN}\gamma^S(H^+) + p^{AN}\gamma^S(A^{2-}) - p^{AN}\gamma^S(\Sigma HA^-) \qquad (3)$$

Calculation of values of $p^{AN}\gamma^S(H_2A)$ and $p^{AN}\gamma^S(HE)$ do not involve any extrathermodynamic assumption. From the experimental results the effect of $-CH_2-$ groups on $^{AN}\gamma^S(H_2A)$ and $^{AN}\gamma^S(HE)$ was found.

An ir study has been made of biglutarate and of the homoconjugate of biglutarate with glutaric acid in AN in order to obtain conclusive evidence that in the homoconjugate H_2A is *inter*molecularly hydrogen bonded to the carboxylate group in the monoanion $\overline{HA^-}$. In order to show that DMSO is not hydrogen bonded to the carboxylic acid group in $\overline{HSuc^-}$, ir spectra were obtained in solutions of bisuccinate in DMSO.

Experimental Section

Solvents. Acetonitrile,[1] *N,N*-dimethylformamide,[7] dimethyl sulfoxide,[1] and methanol[1] have been purified and dispensed as described previously. Acetonitrile-d_3 and dimethyl-d_6 sulfoxide were Aldrich and Baker Co. products, respectively, used without further purification.

TABLE I: Molecular Solubility of Diprotic Acids and Their Monoesters in Various Solvents

Acid	$(CH_2)_n$ n	W $[H_2A]_{sat.}$	$[HE]_{sat.}{}^c$	M $[H_2A]_{sat.}{}^c$	$[HE]_{sat.}{}^c$	AN $[H_2A]_{sat.}{}^c$	$[HE]_{sat.}{}^c$	DMF $[H_2A]_{sat.}{}^c$	DMSO $[H_2A]_{sat.}{}^c$	$[HE]_{sat.}{}^c$
Succinic	2	0.70^c 0.65^a	7.45^d	1.28	6.26^d	0.0404	5.06^d	3.53	Solvate	
Glutaric	3			4.58		0.715				
Adipic	4	$0.13_6{}^c$ 0.16^b	0.19^c	1.12	5.3^e	0.039	5.2^e	2.86	3.69	5.12^e
Pimelic	5	0.324^c		2.76		0.19_7		3.52		
Suberic	6	$0.015_2{}^c$ 0.34^a		0.85		0.028		2.29	2.78	
Azelaic	7	0.013^c 0.015^a		1.48		0.063		2.73	3.15	
Sebacic	8	0.0015^d	3.4×10^{-3e}	0.51	3.54^e	0.016	3.80^e	1.86	2.59	3.73^e
Fumaric		0.051^c 0.053^a	0.185^d	0.51	1.87^d	0.0055	0.418^d	Solvate	3.74	5.45^d
o-Phthalic		0.0368^c	0.206^d	1.15	4.91^d	0.0245	2.93^d		3.77	

^{a} A. Seidell, "Solubilities of Organic Compounds", 3rd ed, Vol. 2, Van Nostrand, New York, N.Y., 1941. ^{b} N. P. Komar, V. Mel'nik, K. Zimina, and A. Kozachenko, *Vestn. Khark. Univ.*, 73, 67 (1971); *Chem. Abstr.*, 78, 8478t (1973). ^{c} This work. ^{d} Methyl ester. ^{e} Ethyl ester.

TABLE II: Values of pK_1 and pK_2 of Diprotic Acids in Various Solvents and Homoconjugation Constants, K_{homo}, in AN and DMSO

		pK_1 and pK_2 W^a	M^f	AN^f	DMF	DMSO	K_{homc} AN^f	DMSO^f
H_2Ox	pK_1	1.2_3	6.1	14.5_0		6.2^e	4.0×10^3	
	pK_2	4.2_9	10.7	27.7		14.9^e		
H_2Mal	pK_1	2.8_7	7.5	15.3	7.8^b 8.2^c	7.2^j	0.9×10^3	
	pK_2	5.6_7	12.4	30.5	20.8^b $>16^c$	$18.5_5{}^f$		
H_2Suc	pK_1	4.2_0	9.1	17.60	10.4^b 10.05^d	$9.5_0{}^f$	0.2×10^3	<2
	pK_2	5.5_5	11.5	29.0	19.9^b 17.2^d	16.7^j		
H_2Glu	pK_1	4.3_4	9.4	19.2_0		10.9^j	$0.6_2 \times 10^3$	1.0×10^1
	pK_2	$5.4_2{}^j$	11.5	27.9_5		15.3^j		
H_2Ad	pK_1	4.4_{2}	9.4_5	20.3_5		11.9^j	1.4×10^3	8×10^1
	pK_2	5.4_2	11.1	26.9		14.1^j		
H_2Az	pK_1	4.5_5		20.8		$11.9_5{}^f$	2.7×10^3	
	pK_2	5.4_1		24.8		$13.5_5{}^f$		
H_2Fum	pK_1	3.0_2	8.0_3	18.6		9.2^f		
	pK_2	4.3_9	10.4_4	22.9		$11.2_3{}^f$		
o-H_2Pth	pK_1	3.0_0		14.2		6.2^e	0.9×10^2	
	pK_2	5.40		29.8		16.0^j		
Butyric			9.9_7	22.7_3		$12.8_6{}^f$		7×10^1
Acetic			$9.5^g9.7_2{}^h$ 9.8^f	22.3^i	13.5^d	12.6^i	4.7×10^{3i}	3×10^{1i}
Monochloroacetic			7.7^j	18.8	9.0^j	8.9^j		
Dichloroacetic			6.4^j	15.8_1	7.2^j			

^{a} Average values taken from various sources, i.e., R. Gane and C. K. Ingold, *J. Chem. Soc.*, 2153 (1931); "Treatise on Analytical Chemistry", I. M. Kolthoff, P. J. Elving, and E. B. Sandell, Ed., Part I, Vol. 1, Wiley-Interscience, New York, N.Y., 1959, p 432; E. Gelles and G. Nancollas, *Trans. Faraday Soc.*, 52, 680 (1956); H. Harned and L. Fallow, *J. Am. Chem. Soc.*, 61, 3111 (1939); N. Topp and C. Davies, *J. Chem. Soc.*, 87 (1940); G. Pinching and R. G. Bates, *J. Res. Natl. Bur. Stand.*, 45, 322, 444 (1950); A. Cavallo and P. Viéles, *Bull. Soc. Chim. Fr.*, 806 (1963); G. Kortüm, W. Vogel, and K. Andrussow, "Dissociation Constants of Organic Acids in Aqueous Solution", Butterworths, London, 1961. ^{b} E. Roletto and J. Juillard, *J. Solution Chem.*, 3, 127 (1974). ^{c} E. Boulanger, Thesis, Paris, 1971. ^{d} Reference 7. ^{e} J. Courtot-Coupez and M. Le Démézet, *Bull. Soc. Chim. Fr.*, 1033 (1969) (μ = 0.1). ^{f} This work; ref 1. ^{g} J. Juillard, *ibid.*, 1727 (1966). ^{h} E. Grunwald and E. Price, *J. Am. Chem. Soc.*, 86, 4517 (1964). ^{i} I. M. Kolthoff, M. K. Chantooni, Jr., and S. Bhowmik, *ibid.*, 90, 23 (1968). ^{j} B. Clare, D. Cook, E. Ko, Y. Mac, and A. J. Parker, *ibid.*, 88, 1911 (1966).

Acids and Salts. The same diprotic acids, their monoesters, their mono- and ditetraethylammonium salts, mono- and dichloroacetic acids, and tetramethylammonium hydroxide titrant in M were used as in previous studies.[1,3] Assay of potassium monoethyloxalate (Pfaltz and Bauer,

Inc.) gravimetrically as tetraphenylborate yielded 101.0%. Only a trace of free oxalic acid was found. Pimelic, suberic, and sebacic acids and the monoethyl ester of the latter were Eastman Kodak White Label products recrystallized from water or methanol. Assay by alkalimetric titration

TABLE III: Dissociation Constants of Monoesters, pK(HE), and Values of log K'
of Monoanions, HA⁻, of Dicarboxylic Acids in Various Solvents

HE (or HA⁻)	pK(HE)				log K'		
	W	M^c	AN^f	DMSO^c	M^e	AN^f	DMSO^e eq 1
EtHOx	1.50^e	6.3_0		6.5_2	g		g
MeHMal	3.35^a	3.46^b					
EtHMal	3.34^d	8.8_0	20.0	10.2_6	1.0	4.4	2.7_6
MeHSuc	4.49^d	9.6	21.6	11.9_1	(−0.2)	3.7	2.1
EtHSuc	4.52^d						
McHGlu		9.7_1	22.2_6	12.4_5	g	2.7_6	1.2
MeHAd		9.8_7	22.2_4	12.6_4	g	1.6	(0.2)
EtHAd	(4.6_0)^d						
MeHAz					g	1.2	(0.1)
McHFum	3.40^c	8.2_4	19.2	9.4_5	g	g	g
EtHFum	3.43^d						
MeHPth	3.18^c	8.5_7	20.0	9.9_3	1.3	5.5	3.4
EtHPth	3.26^c						

a W. D. Treadwell and E. Wettstein, *Helv. Chim. Acta*, 18, 200 (1935). *b* P. Glasoe and J. Hutchinson, *J. Phys. Chem.*, 68, 1562 (1964). *c* G. Dahlgren and F. A. Long, *J. Am. Chem. Soc.*, 82, 1303 (1960). *d* J. Walker, *J. Chem. Soc.*, 61, 696 (1892). *e* This work. *f* Reference 1. *g* K' ~ 0.

yielded 99.7 ± 0.5% purity. n-Butyric acid was Eastman Kodak White Label product distilled at atmospheric pressure. Silver salts of the monoesters were prepared as described for silver benzoate.[8] To avoid hydrolysis of the monoester (or its anion), the preparation was carried out in aqueous solution in an ice bath. The salts were not recrystallized. Assay gravimetrically as silver bromide yielded 97.8 and 98.9% purity for the monosuccinate and adipate, respectively.

Techniques. Solubilities of the diprotic acids and their monoesters have been determined by alkalimetric titration in ethanol–water mixtures. Also, paH and paAg measurements with the glass and silver wire electrode, respectively, were carried out in the same way as in previous publications. All measurements were made at 25 ± 0.1°. The method used for preparation and assay of solid solvates of diprotic acids and monoesters with DMF or DMSO has been described previously.[3] A Beckman IR-20 spectrophotometer with double beam was used to record ir spectra. An Irtran cell of 50-μ path length was used. The reference beam passed through air.

Results

Solubility of Diacids, Monoesters, and Silver Salts. Solubility data in W, M, AN, DMF, and DMSO of the diacids in the homologous series of oxalic acid, fumaric and o-phthalic acids, and the corresponding monomethyl or -ethyl esters are presented in Table I. The second column lists the number of CH_2 groups in the acid. Correction has been made for incomplete dissociation of the diacids and monoesters in water, using the dissociation constants in Tables II and III. In the other solvents dissociation of the diacids and monoesters in their saturated solutions is negligible. A number of short-chained diacids and monoesters with high solubilities have been checked for crystal solvate formation in AN, DMF, and DMSO. Only succinic acid formed the solid solvate, $H_2Suc \cdot 1.0_0 DMSO$, while the following did not form solvates: adipic acid and monomethyl-fumarate with DMSO and succinic and pimelic acids with DMF or AN.

As the solubilities of monomethylsuccinate in W, M, and AN and monoethyladipate in M and AN in Table I are par-

ticularly large (>5 M), values of their $p^{AN}\gamma^S(HE)$ were also obtained from $^S\Delta^{AN}pK(HE)$ and $^S\Delta^{AN}pK^{sp}(AgE)$ using

$$^S\Delta^{AN}pK(HE) - {}^S\Delta^{AN}pK^{sp}(AgE) =$$
$$p^{AN}\gamma^S(H^+) - p^{AN}\gamma^S(Ag^+) - p^{AN}\gamma^S(HE) \quad (4)$$

in which γ denotes transfer activity coefficients. Values of K^{sp} of the silver salts of the monoesters were estimated from paH and paAg in their saturated solutions containing a known amount of ester.[9] Silver wire and glass electrodes were used to measure paAg and paH, respectively. The data are presented in Table a.[10] The following values of pK^{sp} were obtained: AgMeSuc, 8.3_2 in AN, 7.4 in M, and 3.5_6 in W; AgMeAd, 8.9 in AN, 7.6 in M, and 4.0_4 in W. Under our experimental conditions both silver salts are uncomplexed and practically completely dissociated in water. However, in M and AN, complexation and incomplete dissociation are appreciable, $K(AgE_2^-)$ being of the order of 10^7 and $K^d(AgE) = 7 \times 10^{-5}$ in M for both salts. Owing to the low solubility of the silver salts in AN, reliable values of these constants in this solvent could not be evaluated. Values of $\beta(HE_2^-) = [H_2E_3^-]/[HE_2^-][HE]$ were calculated in AN from paH and paAg in mixtures of HE and AgE, as described previously for silver benzoate,[9] and were found equal to 1.8×10^1 and 2.7×10^1 for the monomethylsuccinate and adipate ester anions, respectively.

Values of pK_1, pK_2, $pK(HE)$, and Homoconjugation Constants from Potentiometric Data. In DMSO and M, pK_1 and pK_2 values of malonic, succinic, glutaric, and adipic acids were estimated from the paH, measured with the glass electrode, in mixtures of the diacid and mono-tetraethylammonium salt or mono- and ditetraethylammonium salts. Figure 1 presents plots in DMSO of paH vs. log $C(H_2A)/(HA^-)f_-$. In addition, in DMSO or M, paH was measured in equimolar mixtures of H_2A–HA^- and of HA^-–A^{2-} prepared by partial neutralization of azelaic or fumaric acid with 1.1 M tetramethylammonium hydroxide (in M).[1] Since monoesters of oxalic acid are unstable, values of $K(HE)$ of monoethyloxalate in W, M, and DMSO were obtained from the paH of mixtures of 0.001 to 0.02 M potassium monoethyloxalate with standard hydrogen chloride. Data are presented in Table b.[10] In these three solvents hydrogen chloride and the potassium salt of the monoester at
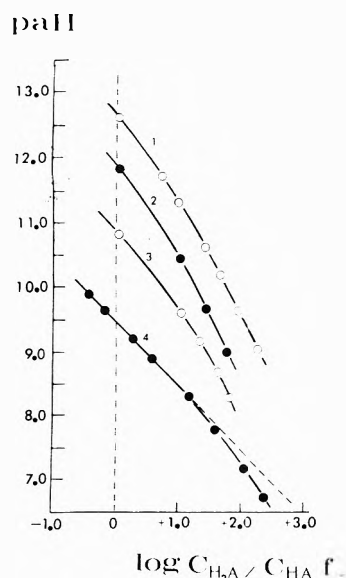
Figure 1. Plots of paH vs. log $C(H_2A)/fC(HA^-)$ in DMSO: (1) butyric acid (with Me_4NOH in M) $C(A^-) = 0.00258$; (2) adipic acid, $C(HA^-) = 0.00354$; (3) glutaric acid, $C(HA^-) = 0.0050$; (4) succinic acid, $C(HA^-) = 0.0042$. Dashed line has a slope of -1.00.
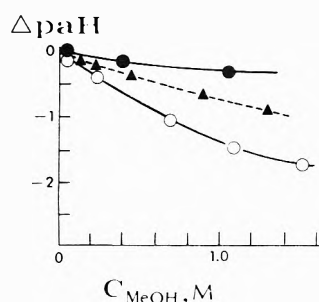

Figure 2. Effect of methanol on paH of mixtures of monomethylsuccinate and its tetramethylammonium salt in AN and in DMSO: (●) $C_a = 0.0203$, $C_s = 0.00279$ M in AN, $paH_0 = 18.54$; (O) $C_a = 0.00400$, $C_s = 0.00334$ M in AN, $paH_0 = 21.06$; (Δ) $C_a = C_s = 0.00215$ M in DMSO, $paH_0 = 11.81$.

the concentrations used can be regarded as strong electrolytes. In dilute solutions in these solvents the monoester appears to be remarkably stable. The potassium salt of the ester has too small a solubility in AN to permit making in this solvent similar measurements as above. Values of $K(HE)$ of the other monoesters in DMSO and M and of $K(HA)$ of butyric and mono- and dichloroacetic acids in AN were obtained from paH in equimolar mixtures of the acids and tetramethylammonium hydroxide.[11]

In all instances the effect of M introduced with the titrant on paH of mixtures of H_2A. HA, or HE was taken into account. It was assumed that the methanolation constants of the monovalent anions were the same as that of the monomethylsuccinate ester anion. From the effect of M on paH of nearly equimolar mixtures of monomethylsuccinate and its anion in AN and in DMSO, plotted in Figure 2, the following values were found: $K(MeOH \cdot E^-) \sim 1.0$, $K(2MeOH \cdot E^-) = 4.6 \times 10^1$ in AN and 3.0 and 3.5, respectively, in DMSO. For the fumarate and azelate dianions in DMSO $K(MeOH \cdot Fum^{2-}) = 4$ (unpublished data) was used. Activity coefficients were calculated from the partially extended Debye–Hückel limiting law, $-\log f = Az^2\sqrt{\mu}/(1 + Ba\sqrt{\mu})$ where $A = 1.64$ in AN, 1.10 in DMSO, 1.90 in M
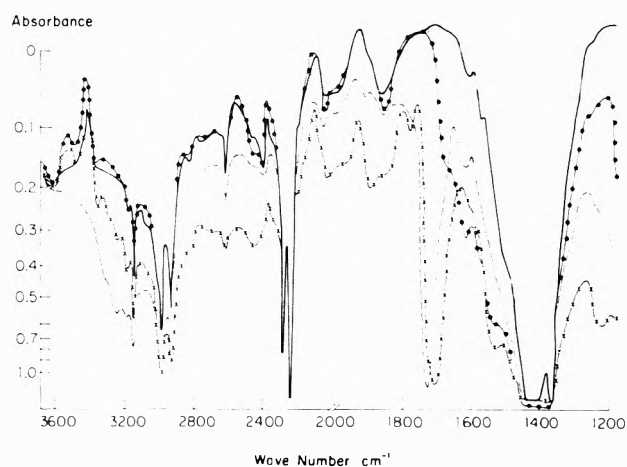

Figure 3. Ir spectra of glutaric acid, tetraethylammonium biglutarate, and a 1:1 mixture of the two in acetonitrile: (——) solvent, (- - - -) 0.261 M H_2Glu, (-·-·-·-) 0.263 M Et_4NHGlu, (-X-X-X-X-) 0.252 M H_2Glu, 0.259 M Et_4NHGlu.
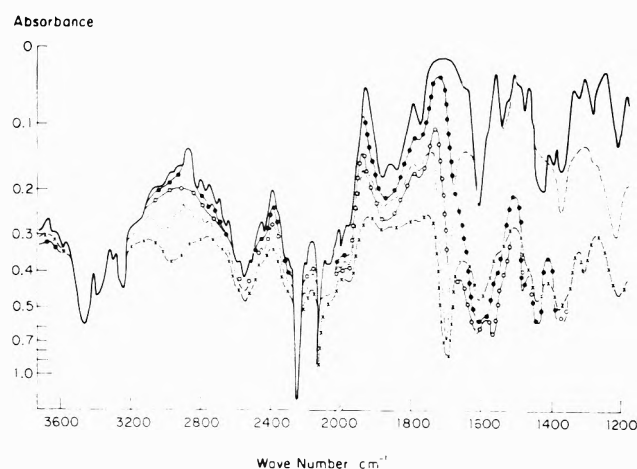
Figure 4. Ir spectra in $(CD_3)_2SO$ of succinic acid, tetraethylammonium bisuccinate, the mixture of the two. and of tetraethylammonium biglutarate: (——) solvent, (- - - - -) 0.172 M succinic acid, (-·-·-·) 0.282 M tetraethylammonium bisuccinate, (-O-O-) 0.374 M tetraethylammonium biglutarate, (-X-X-X) 0.151 M succinic acid, 0.132 M tetraethylammonium bisuccinate.

and $B = 0.49$ in AN, 0.42 in DMSO, and 0.51 in M. In Table II are presented pK_1 and pK_2 values of diacids in W, M, AN, DMF, and DMSO and overall homoconjugation constants, K_{homo}, of H_2A with HA^- and $\overline{HA}^-$ in AN and DMSO. Values of pK_1 and pK_2 in M reported by Liteanu and Blazsek-Bodó[12] were obtained from glass electrode measurements using sodium methoxide as titrant. The presence of Na^+ ions may give rise to relatively large alkaline glass electrode errors. With malonic and oxalic acids our pK_2 values are some 2 units greater than those reported by Liteanu et al. For these reasons their values are not included in Table II. In Table III are listed values of log K' of the monoanions and $pK(HE)$ of the monoesters in W, M, AN, and DMSO.

Infrared Spectra. Ir spectra in AN of glutaric acid, tetraethylammonium biglutarate, and a 1:1 mixture of the two are presented in Figure 3, while Figure 4 presents ir spectra in $(CD_3)_2SO$ of succinic acid, tetraethylammonium bisuccinate, and a mixture of succinic acid and bisuccinate. A spectrum of biglutarate in $(CD_3)_2SO$ is included in Figure 4 for comparison with that in AN.

Discussion

Transfer Activity Coefficients. The solubility in W and AN of most of the diacids is such that their saturated solutions can be considered as ideal. From the values of $[H_2A]_{sat.}$ expressed in molarity (Table I) values of $p^{AN}\gamma^W(H_2A)$ were calculated and are listed in Table IV. It is of interest to note that $p^{AN}\gamma^W(H_2A)$ increases by 0.37 unit per $-CH_2-$ group in the chain. For example, $p^{AN}\gamma^W(H_2A) = -1.2$ for succinic and $+1.0$ for sebacic acids, the difference yielding $2.2/6 = 0.37$ per $-CH_2-$ group. The solubility of most of the diacids, H_2A, in DMSO and DMF, and of the diacids with an odd number of $-CH_2-$ groups in M, is too large to consider molarity equal to activity in the saturated solutions. For these acids values of $p^{AN}\gamma^{DMF,DMSO}(H_2A)$ from solubility data involve an uncertainty of ±0.3 unit and they are reported in parentheses in Table IV. It is striking that for the acids with an even number of $-CH_2-$ groups $p^{AN}\gamma^{M,DMSO}(H_2A)$ is constant and equal to -1.5 for AN $\rightarrow$ M and -2.0 for AN $\rightarrow$ DMSO. Hence for these acids $p^{M,DMSO}\gamma^W(H_2A)$ also increases by $+0.37$ unit per $-CH_2-$ group. In this connection it is of interest to note that from solubility data[13] it appears that $p^M\gamma^W$ of normal aliphatic hydrocarbons becomes 0.48 unit more positive per $-CH_2-$ group. This suggests that changes in $p^M\gamma^W(H_2A)$ (H_2A with an even number of $-CH_2-$ groups) with the number of $-CH_2-$ groups can be identified with the hydrocarbon part of H_2A. Making the reasonable assumption that the solvation of the carboxyl groups by hydrogen bonding to the solvents is independent of A in H_2A, we write

$$p^{AN}\gamma^S(H_2A) = 2p^{AN}\gamma^S(H_a) + p^{AN}\gamma^S(n) = p^{AN}\gamma^S(H_a) + p^{AN}\gamma^S(HE) \quad (5)$$

In eq 5 $p^{AN}\gamma^S(H_a)$ denotes the difference in hydrogen bond accepting capacity between AN and S and $p^{AN}\gamma^S(n)$ the contribution of the nonhydrogen bonded nonelectric component of the transfer activity coefficient. Using values of $p^{AN}\gamma^M(H_a) = -1.5^3$ and $p^{AN}\gamma^{DMSO}(H_a) = -1.9^3$ we obtain from eq 5 $p^{AN}\gamma^M(n) = +1.5^3$ and $p^{AN}\gamma^{DMSO}(n) = +1.8$ for H_2A with an even number of $-CH_2-$ groups. These values of $p^{AN}\gamma^{M,DMSO}(n)$ represent the effect of the two carboxyl groups, this effect being the same in H_2A as in the corresponding HE.

We now consider values of $p^{AN}\gamma^S(HE)$ (reported in brackets in Table IV) calculated from eq 5 using $p^{AN}\gamma^S(H_2A)$ values in Table IV and the above values of $p^{AN}\gamma^S(H_a)$. When S = W, a correction of $+0.6$ unit per $-CH_2-$ group in the alcohol part of the ester has been added, as was done for the benzoate esters.[14] Using the value of $p^{AN}\gamma^W(H_a) = -0.8$ previously reported[3] and the values of $p^{AN}\gamma^W(H_2A)$ in Table IV, we calculate from eq 5 $p^{AN}\gamma^W(MeHSuc) = +0.2$ and $p^{AN}\gamma^W(MeHAd) = +0.9$. Similarly, the corresponding values for AN $\rightarrow$ M are 0.0 for both acids. These values are to be compared with those obtained from eq 4. Using values of $^{W,M}\Delta^{AN}pK(HE)$ (Table III), $^{W,M}\Delta^{AN}pK^{sp}(AgE)$ (Results), $p^{AN}\gamma^W(Ag^+) = +3.8$,[6] $p^{AN}\gamma^M(Ag^+) = +5.1$,[6] $p^{AN}\gamma^W(H^+) = -10.2$,[6] and $p^{AN}\gamma^M(H^+) = -6.2$,[6] good agreement is found between the values of $p^{AN}\gamma^{W,M}(MeHSuc)$ and $p^{AN}\gamma^{W,M}(MeHAd)$ in Table IV obtained from eq 4 and 5. It is reasonable to expect that $p^{AN}\gamma^{M,DMSO}(HE) \sim 0$, as the solubilities in AN, DMSO, and M of a given monoester of the homologous series of oxalic acid (with an even number of $-CH_2-$ groups) are practically the same.

Intramolecular Hydrogen Bonding in Monoanions. An expression describing the effect of solvent on K' is simply derived from eq 6–8. Regarding that $\overline{HA^-}$ is not intermole-

$$\log(K')_{AN} - \log(K')_S = {}^{AN}\Delta^S \log K' = p^{AN}\gamma^S(\overline{HA^-}) - p^{AN}\gamma^S(HA^-) \quad (6)$$

(cf. eq 1)

$$p^{AN}\gamma^S(HA^-) = p^{AN}\gamma^S(n) + p^{AN}\gamma^S(HA^-)_{el} + p^{AN}\gamma^S(H_a) \quad (7)$$

$$p^{AN}\gamma^S(\overline{HA^-}) = p^{AN}\gamma^S(n) + p^{AN}\gamma^S(\overline{HA^-})_{el} \quad (8)$$

cularly hydrogen bonded to the solvents (eq 8) and considering that $p^{AN}\gamma^S(n)$ is the same in $\overline{HA^-}$ as in HA^-, eq 9 results

$${}^{AN}\Delta^S \log K' = -p^{AN}\gamma^S(H_a) + p^{AN}\gamma^S(\overline{HA^-})_{el} - p^{AN}\gamma^S(HA^-)_{el} \quad (9)$$

When S is an aprotic solvent, $p^{AN}\gamma^S(\overline{HA^-})_{el} \sim p^{AN}\gamma^S(HA^-)_{el} \sim 0$, and

$${}^{AN}\Delta^S \log K' = -p^{AN}\gamma^S(H_a) \quad (9')$$

The values of K' of the various diacids in DMSO and of succinic acid in DMF in Table III are all considerably smaller than those in AN, as expected. Between the solvents AN and DMSO the average value of $^{DMSO}\Delta^{AN} \log K' = -1.7 \pm 0.1$, which agrees well with $p^{AN}\gamma^{DMSO}(H_a) = -1.9$,[3] omitting azelaic acid, the K' value of which is too small in DMSO to be considered reliable. For succinic acid in DMF $^{DMF}\Delta^{AN} \log K' = -1.3$,[15] in agreement with $p^{AN}\gamma^{DMF}(H_a) = -1.4$.[3] This agreement lends strong support to the assumptions made in deriving eq 9'. The premise that intermolecular hydrogen bonding of $\overline{HA^-}$ with the aprotic solvents is negligible is supported by the ir results (vide infra) and the fact that no appreciable effect of DMSO up to 0.7 M on the paH of mixtures of tetraethylammonium bisuccinate and succinate is observed in AN.[1] For biphthalate ion in DMSO Forsen[16] observed a large downfield PMR chemical shift (-15 ppm from H_2O as external standard) and attributed this to a strong symmetrical intramolecular hydrogen bond and to the effect of placing a negative charge in proximity of the hydrogen bonded proton.[17] The fact that intramolecular hydrogen bonding is absent in bioxalate in the solvents W, M, and DMSO ($K' \sim 0$) must be attributed to steric hindrance.

Considering that methanol is a slightly stronger hydrogen bond acceptor and about an equally strong donor as water, it is expected that values of K' in M of monoanions, whose conformation would not greatly favor intramolecular hydrogen bonding in water, would be practically equal to zero. This has been found for succinic and longer straight-chained acid monoanions in Table III and for bicyclo[2.2.2]octane-1,4-dicarboxylic acid monoanion,[18] while Christol et al.[19] found $K' \sim 0$ for the trans-4-cyclohexene-1,2-dicarboxylic acids in methyl cellosolve (ϵ 17) in contrast to values of log K' equal to 1–2 for the cis isomer. It is unexpected that bimalonate and biphthalate ions are rather strongly intramolecularly hydrogen bonded in M, the values of K' being about 10 and 12, respectively, while K' of these monoanions in water is zero.[2,20] From $^{AN}\Delta^M \log K' = 3.4$ and 4.2 for bimalonate and biphthalate, respectively, and eq 9 taking $p^{AN}\gamma^M(H_a) = -1.5^3$ and assuming $p^{AN}\gamma^M(HA^-)_{el} \sim p^{AN}\gamma^M(OAc^-)_{el} = -8$,[3] we obtain $p^{AN}\gamma^M(HA^-)_{el}$ of the order of -5 to -6, attesting to a large electrostatic free energy of solvation to the carboxylate group of HA^- by M. It deserves further study to establish

TABLE IV: Transfer Activity Coefficients of Dibasic Acid Species and Monoesters of Diprotic Acids

		Acetic	Succinic	Glutaric	Adipic	Pimelic	Suberic	Azelaic	Sebacic	Fumaric	o-Phthalic
$p\gamma(H_2A)$	AN → W	-0.4	-1.2_1	$(-0.9)^c$	-0.5_4	-0.2_2	$+0.2_6$	$+0.6_8$	$+1.0_2$	-1.0	-0.2
AN	AN → M	-0.4	-1.5_0	(-0.8_0)	-1.4_5	(-1.14)	-1.4_8	-1.3_7	-1.5_0	-1.9_6	-1.7
	AN → DMF	-0.2	(-1.9)		(-1.9)	(-1.2_5)	-1.9_1	(-1.6)	-2.0_6	^{b}	
	AN → DMSO	-1.2	$(-1.9)^{a,b}$	$(-1.9)^a$	(-1.9)		(-2.0)	(-1.7)	-2.2	(-2.8)	(-2.2)
$p\gamma(\Sigma HA^-)$	AN → W	-9.8	-6.5	(-7.7)	-8.3			-7.4		-8.5	-3.4
	AN → M	-7.0	-3.8	(-4.4_5)	-6.1_5					-6.4	-2.5
	AN → DMF	+1.6	$(+1.2)$								
	AN → DMSO	+0.5	$(+1.4)$	$(+1.2)$	$(+1.0)$			$(+0.9)$		(-0.8)	$(+1.2)$
$p\gamma(A^{2-})^h$	AN → W		-21.9	(-22.1)	-21.7			-18.7		-18.3	-19.7
	AN → M		-15.1	(-14.7)	-15.8					-12.7	(-16.3)
	AN → DMSO		$(+0.5)$	(-0.1)	(-0.4)			$(+1.1)$		(-1.1)	(-1.2)
$p\gamma(MeHA)$	AN → W		$\{+0.4^d, [+0.2]^g, (-0.2)^e\}$		$\{+0.8^d, [+0.9]^g, (+1.4_4)^{e,f}\}$				$\{[+2.4]^g, (+3.0_5)^{e,f}\}$	$\{[+0.4]^g, +0.4^e\}$	$\{[+1.2]^g, (+1.1_5)^e\}$
	AN → M		$\{-0.2^d, [0.0]^g, (-0.1)^e\}$		$\{-0.3^d, [+0.0_5]^g, (0.0)^{e,f}\}$				$\{[0.0]^g, [0.0]^{e,f}\}$	$\{[-0.5]^g, [-0.7]^c\}$	$\{[-0.2]^g, -0.2^e\}$
$p\gamma(MeHA)$	AN → DMSO				$\{[0.0]^g, (0.0)^{e,f}\}$				$\{[-0.3]^g, (0.0)^{e,f}\}$	$\{[-0.9]^g, (-1.1)^e\}$	

^{a} Value of -1.9 taken for $p^{AN}\gamma^{DMSO}(H_2A)$, since $p^{AN}\gamma^{DMSO}(H_2A)$ is independent of chain length. ^{b} Solid solvate formed. ^{c} Interpolated from plot of $p^{AN}\gamma^W(H_2A)$ vs. n in $(CH_2)_n(COOH)_2$. ^{d} From solubility of silver salt of monomethyl ester and eq 4. ^{e} From solubility of monoester. ^{f} $P\gamma(EtHA)$, corresponding values of $p^{AN}\gamma^W(MeHAd) = +0.8$ and $p^{AN}\gamma^W(MeHSeb) = +2.4$; $p^{AN}\gamma^{M,DMSO}(EtHA) = AN\gamma^{M,DMSO}(MeHA)$. ^{g} Calculated from $p\gamma(H_2A)$ using eq 5, see text. ^{h} $p^{AN}\gamma^{DMF}(Suc^{2-}) = 0.0$.

whether the stronger intramolecular hydrogen bonding in M than in W is to be attributed to the lower dielectric constant of the latter.

Infrared Spectra. In 0.26–0.37 M tetraethylammonium biglutarate and biadipate solutions in CH_3CN, CD_3CN, and bisuccinate in $(CD_3)_2SO$ strong absorption starting at 1730 cm^{-1} to at least 900 cm^{-1} is observed, while little or no absorption is found at higher frequencies (Figures 3 and 4). The carbonyl band is practically absent in these spectra. This pattern indicates strong symmetrical intramolecular hydrogen bonding[21] in $\overline{HA}^-$ in AN and DMSO, possibly with extensive proton tunneling and absence of significant intermolecular hydrogen bonding with these solvents. As expected, glutaric and acetic acid (the spectrum of the latter not given) in CH_3CN (Figure 3) and CD_3CN (not in a Figure) exhibit the "free" OH stretching band[22] from 3500 to 2900 cm^{-1}, the absorption of glutaric acid being about twice that of an equimolar solution of acetic acid. On the other hand, this band is absent in 0.17 M succinic acid in $(CD_3)_2SO$ and is replaced by a broad absorption from 3200 to <1000 cm^{-1} (Figure 4). A similar result is found in solutions of trifluoroacetic acid in sulfolane to which dimethyl sulfoxide has been added[23] which has been ascribed to intermolecular hydrogen bonding of the carboxyl group with DMSO. This is supported by the fact that the carbonyl stretching band at 1734 and 1746 cm^{-1} for glutaric (Figure 3) and acetic acids, respectively, in CH_3CN is shifted to 1700 cm^{-1} in succinic acid solution in $(CD_3)_2SO$ (Figure 4).

Of particular interest is the spectrum of the homoconjugate of the glutaric acid–biglutarate mixture in CH_3CN and CD_3CN. The "free" OH stretching band in the homoconjugate is reduced to about half that in an equimolar solution of the free acid (Figure 3), only one carboxylic acid group in $\overline{HA}^-\cdot H_2A$ containing a "free" hydroxyl group. Strong absorption is found from 2900 cm^{-1} to the Irtran cell cutoff at 760 cm^{-1}, which is much greater than that of glutaric acid

alone. Considering that the biglutarate does not absorb between 2900 and 1900 cm^{-1}, the strong absorption in this region is attributed to intermolecular hydrogen bonding between the carboxylate ion and the acid, H_2A, in the homoconjugate, while the strong absorption at lower frequencies is attributed to both inter- and intramolecular hydrogen bonding. Furthermore, the broad carbonyl band(s) in $H_2A\cdot \overline{HA}^-$ occur(s) at $\sim$1700 cm^{-1} in AN. Thus the spectrum of the glutaric acid–biglutarate mixture in AN (Figure 3) lends strong support to the conclusion drawn from equilibrium data in much more dilute solutions that in the homoconjugate the carboxylate group is intramolecularly hydrogen bonded to the carboxylic acid group in $\overline{HA}^-$ and intermolecularly to H_2A. The spectrum does not exclude homoconjugation between HA^- and H_2A, the contribution of which must be very small. As expected, the spectrum of the mixture of succinic acid and bisuccinate in DMSO is roughly the sum of the components (Figure 4) as homoconjugation is negligible.

Inductive Effects on pK(HE) and pK₁. The values of $pK(HE)$ of the monoesters in M, AN, and DMSO in Table III increase markedly at first with increasing chain length, level off at monomethylglutarate, and become practically equal to $pK(HOAc)$ for monomethyladipate. This is attributed to the inductive effect of the carbalkoxyl group as in water.[2] As expected, the inductive effect is particularly large in monomethyloxalate and monomethylfumarate, while in the o-phthalate half ester the steric inhibition of resonance effect operates in addition to the polar effect of the ortho carbalkoxyl group. In a given monoester the inductive effect on $pK(HE)$ of the carbalkoxy group is greater in the dipolar aprotic solvents than in water or methanol, which gives rise to resolution of acid strength. Thus, a plot of $pK(HE)$ of monomethyladipate, -glutarate, -succinate, -fumarate, including $pK(HA)$ of acetic, butyric, and monochloro- and dichloroacetic acids in AN vs. that in M is

linear with some scattering and has a slope of 1.8, which is practically equal to that observed of non-ortho-substituted benzoic acids[3] of 1.7_1. A similar plot in DMSO vs. M (including monoethyloxalate) has a slope of 1.8. Like for the substituted benzoic acids (HA), no resolution of acid strength of the monoesters is found between AN and DMSO. $^{AN}\Delta^{DMSO}pK(HE) = {}^{AN}\Delta^{DMSO}pK(HA) = 9.7 \pm 0.1_5$. For fumaric acid, whose monoanion is not intramolecularly hydrogen bonded in any of the solvents used, $^{AN}\Delta^{DMSO}pK(HE) = {}^{AN}\Delta^{DMSO}pK(HA) = 9.7 \pm 0.1_5$. For fumaric acid, whose monoanion is not intramolecularly hydrogen bonded in any of the solvents used, $^{AN}\Delta^{DMSO}pK_1 = 9.4$. Also. pK_1 of fumaric acid lies on the plot of $pK(HE)_{M-AN}$. The values of $^{AN}\Delta^{M}pK_1(H_2Fum)$ and $^{AN}\Delta^{M}pK(MeHFum)$ are equal to 10.6 and 10.9_6, respectively.

From the analytical viewpoint it is of interest to mention that $(pK_2 - pK_1)$ in AN as an average is 4.2 units greater than for the same diprotic acid in DMSO. Hence the break in pH at the first equivalence point with water- and alcohol-free titrant is considerably greater in AN than in DMSO.

Supplementary Material Available. Tables a and b will appear following these pages in the microfilm edition of this volume of the journal. Photocopies of the supplementary material from this paper only or microfiche (105 × 148 mm, 24× reduction, negatives) containing all of the supplementary material for the papers in this issue may be obtained from the Journals Department, American Chemical Society, 1155 16th St., N.W., Washington, D.C. 20036. Remit check or money order for $4.00 for photocopy or $2.50 for microfiche, referring to code number JPC-75-1176.

References and Notes

(1) I. M. Kolthoff and M. K. Chantooni, Jr., *J. Am. Chem. Soc.*, **97**, 1376 (1975).
(2) F. Westheimer and O. Benfy, *J. Am. Chem. Soc.*, **78**, 5309 (1956).
(3) M. K. Chantooni, Jr., and I. M. Kolthoff, *J. Phys. Chem.*, **77**, 527 (1973).
(4) C. D. Ritchie in "Solute-Solvent Interactions", J. F. Coetzee and C. D. Ritchie, Ed., Marcel Dekker, New York, N.Y., 1969, pp 224-225.
(5) B. Cox and A. J. Parker, *J. Am. Chem. Soc.*, **95**, 402 (1973).
(6) I. M. Kolthoff and M. K. Chantooni, Jr., *J. Phys. Chem.*, **76**, 2024 (1972).
(7) I. M. Kolthoff, M. K. Chantooni, Jr., and H. Smagowski, *Anal. Chem.*, **42**, 1622 (1970).
(8) I. M. Kolthoff, J. J. Lingane, and W. Larson, *J. Am. Chem. Soc.*, **60**, 2512 (1938).
(9) M. K. Chantooni, Jr., and I. M. Kolthoff, *J. Phys. Chem.*, **77**, 1 (1973).
(10) See paragraph at end of paper regarding supplementary material.
(11) Raw data will be supplied by the authors upon request.
(12) C. Liteanu and A. Blazsek-Bodó, *Rev. Roum. Chim.*, **17**, 1465 (1972).
(13) M. Abraham and J. Johnston, *J. Chem. Soc. A*, 1610 (1971).
(14) M. K. Chantooni, Jr., and I. M. Kolthoff, *J. Phys. Chem.*, **78**, 839 (1974).
(15) This value of $^{DMF}\Delta^{AN}$ log K' was derived from the value of $pK(H_2Suc)$ = 10.0_5 in Table II[7] and assuming that $^{AN}\Delta^{DMF}pK(MeHSuc) = {}^{AN}\Delta^{DMF}pK(HOAc) = 8.8$ (Table II). Hence $pK(MeHSuc) = 21.6 - 8.8 = 12.8$ in DMF from which log $K' = 2.4$ for succinic acid in DMF, yielding $^{DMF}\Delta^{AN}$ log $K' = 2.4 - 3.7 = -1.3$.
(16) S. Forsen, *J. Chem. Phys.*, **30**, 852 (1959).
(17) J. Pople, W. Schneider, and H. Bernstein. "High Resolution Nuclear Magnetic Resonance", McGraw-Hill, New York, N.Y., 1959, p 408.
(18) C. D. Ritchie and G. H. Megerle, *J. Am. Chem. Soc.*, **89**, 1452 (1967).
(19) H. Christol, D. Moers, and Y. Pietrasanta, *J. Chim. Phys.*, **67**, 2024 (1970).
(20) D. Chapman, D. Lloyd, and H. Prince, *J. Chem. Soc.*, 550 (1964).
(21) L. Eberson, *Acta Chem. Scand.*, **13**, 224 (1959).
(22) L. J. Bellamy, "The Infrared Spectra of Complex Molecules", Wiley, New York, N.Y., 1959, pp 162-165.
(23) J. Husar and M. M. Kreevoy, *J. Am. Chem. Soc.*, **94**, 2902 (1972).

Unusual Behavior of Vaporized Magnesium under Low Pressure Conditions

L. B. Knight, Jr.,* R. D. Brittain, M. Duncan, and C. H. Joyner

Department of Chemistry, Furman University, Greenville, South Carolina 29613 (Received November 22, 1974)

Publication costs assisted by Furman University

The simultaneous impingement of an atomic beam of magnesium and certain volatile species containing halogen atoms under high vacuum ($\approx 10^{-6}$ Torr) can condition metal and glass surfaces so that magnesium does not condense or stick to such surfaces even at temperatures less than 300°K. The reduced sticking coefficient under such carefully adjusted conditions causes atomic magnesium to behave as if it were a semipermanent gas. The equilibrium vapor pressure of magnesium metal is negligibly small, $\approx 10^{-21}$, at 300°K, however, room temperature reservoirs containing apparent magnesium partial pressures of approximately 10^{-6} Torr have been produced. A large number of volatile substances have been tried to determine which types can cause the effect. Alkyl bromides and iodides produce the effect but alkyl chlorides do not. Experimental evidence supporting the assignment of the volatile magnesium species as atomic magnesium has been obtained from several independent areas including mass spectrometric studies, matrix isolation spectroscopy, and effusion rate measurements. Numerous other metals have been studied under similar conditions but none have demonstrated the magnesium behavior except for a weak effect observed for zinc. Based on general experimental observation, a possible surface layer responsible for the magnesium effect is proposed.

Introduction

Magnesium was one of the first high temperature species investigated utilizing the rare gas matrix isolation technique.[1] Recently, new findings have been reported for atomic magnesium trapped in argon, nitrogen, and krypton matrices at 12°K that indicate a strong interaction between excited magnesium atoms and the rare gas atom which produces an unusual ultraviolet emission band.[2] The reactions of vaporized magnesium with hydrogen atoms to form the paramagnetic species, MgH, and with oxygen to form Mg_3O_3 have also been reported.[3,4] The condensation of atomic magnesium at 77°K with alkyl halides and other volatile organic compounds have produced interesting chemical reaction systems.[5]

Experiments originally designed to study the vibrational characteristics of frozen deposits of sublimed magnesium atoms and alkyl halides at 77°K utilizing infrared and Raman spectroscopy have resulted in the study and characterization of an unexpected property of magnesium atoms. Admittance of trace amounts of certain volatile chemical species simultaneous to the Knudsen cell vaporization of magnesium metal in a high vacuum (10^{-7} Torr) apparatus appears to significantly reduce the effective sticking coefficient of magnesium atoms on the various metal and glass surfaces present. Under such conditions magnesium atoms are transferred through various sections of the apparatus and tubing at ambient temperatures in a manner usually associated with permanent gases. Ordinarily nonvolatile materials vaporized from high temperature Knudsen cells under high vacuum conditions are expected to condense or stick with 100% efficiency on ambient temperature surfaces and hence their presence can be detected only in direct line-of sight regions relative to the effusion source. The normal expectation is observed when magnesium is vaporized in the absence of trace quantities of certain volatile components.

Extensive mass spectrometric and optical spectroscopic studies have been conducted to ascertain that the volatile species is actually magnesium atoms and not a volatile magnesium containing compound. The approximate equilibrium vapor pressure of magnesium at 300°K, obtained by extrapolation of existing data at higher temperatures, is 10^{-21} Torr.[6] The effective partial pressure of magnesium atoms at 300°K under the experimental conditions described in this report is approximately 10^{-6} Torr. The type of experimental observations reported here for magnesium atoms have apparently not been previously described for vaporized metals.

Experimental Section

Equipment. A schematic of the basic apparatus is shown in Figure 1. An ionization pressure gauge, not shown, is mounted directly in the wall of the vaporization chamber on level with the gas inlet tube. The chamber was constructed from 4-in. i.d. stainless steel tubing with the various flanges and parts heliarced in place to form leak-tight joints. The flange containing the water cooled copper electrodes is bolted in place over a viton O ring and can be removed for sample loading purposes. The vaporization cell is resistively heated and constructed from tantalum tubing, end plugs, and mounting straps. Typically, the effusion hole diameter was 0.066 in. The gas inlet tube usually employed was a 0.125-in. diameter stainless steel tube which was connected through a needle valve to the gas manifold and reservoir system. Ordinarily, a quartz window was used as a target so that visual inspection of the metallic deposit was possible. A copper cup mounted horizontally on a steel flange as indicated by the dashed lines in Figure 1 was substituted for the quartz window on several experiments. The cup served the purpose of confining the region of encounter between the metallic deposit and gas impingement. The cup was supported inside a coil of copper tubing whose ends extended through the support flange. Hence, subambient temperature control of the target cup was possible by passing cold nitrogen gas through the support coil. The temperature was measured by a chromel–alumel thermo-
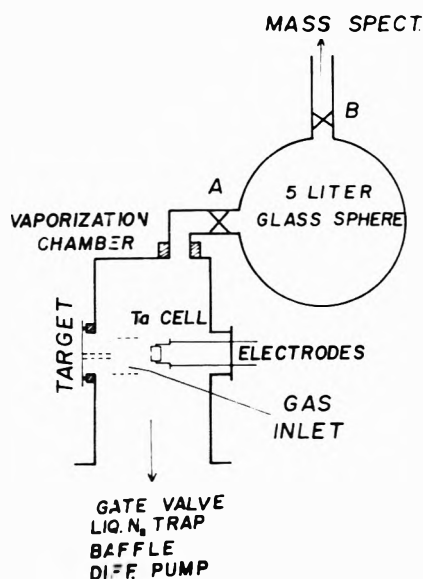
Figure 1. The basic vaporization apparatus is shown in relation to its vacuum system and the connection to the time-of-flight mass spectrometer. Valves A and B are 15-mm teflon and glass stopcocks. The electrodes are 0.5-in. water-cooled copper tubes.

Figure 2. A shows the mass range from 20 to 30 at an electron energy of ≈ 10 eV. The three magnesium isotopes, 24, 25, and 26, are clearly distinguishable from the more complex pattern shown in B at 70 eV. At 8 eV the magnesium peaks are the only ones detectable from mass 1 to 300.

couple attached to the cup. A Bendix 4-in. pumping system consisting of a gate valve, liquid nitrogen trap, water baffle, and diffusion pump is mounted directly below the vaporization chamber. Background pressure for a thoroughly clean and baked system utilizing liquid nitrogen was approximately 5×10^{-3} Torr. Helium mass spectrometric leak testing was performed on the gas handling and vaporization chamber on a routine basis. The tantalum cells were outgassed by heating to 2000° under high vacuum before usage.

The exit port (O-ring quick connect couple, 0.75-in. i.d.) located at the top of the vaporization chamber (Figure 1) allows for convenient interchange of various apparatus used to study volatile components effusing from the chamber. A 5-l. glass bulb is shown at this position in Figure 1 for the effusion rate studies. Condensation cold traps and metal and quartz pyrolysis tubes were also used between the vaporization chamber and the mass spectrometer as discussed in later sections. The exit of the 0.75-in. o.d. glass tube leading into the mass spectrometer was positioned directly into the ion source region. The mass spectrometer employed was a Bendix time-of-flight Model 12-101 outfitted with the MA-RK-IV solid state electronic unit. Initial phases of the study were conducted on a Picker AEI Model 10 magnetic mass spectrometer. Concern over possible thermal degradation of sample in the ion source region as well as the need for higher mass coverage prompted the change to the time-of-flight model. However, the preliminary findings on the magnetic spectrometer did not conflict with those obtained on the time-of-flight instrument.

General Procedure and Basic Observations. A typical procedure for the various experiments is described below. Every part of the apparatus was thoroughly cleaned with hydrochloric acid followed by boiling water and rinsing with a nonpolar solvent such as pentane. The apparatus was then assembled, loaded with an empty tantalum vaporization cell, evacuated and leak tested. The cell was outgassed and heating wire was used to bakeout all surfaces at $\approx 100°$ under vacuum overnight. A mass spectrogram of the system showed no increase in any background masses over
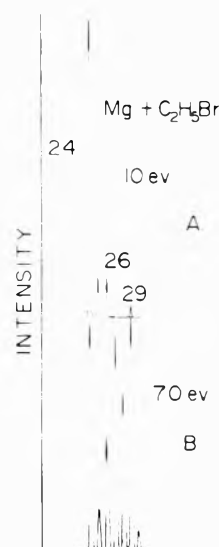
those commonly seen in the mass spectrometer alone. Next the liquid or gas sample was loaded into the gas manifold and leaked into the vaporization chamber via the gas inlet tube. Liquid samples were purified prior to use on a concentric tube distillation column until their refractive indices matched those reported in the literature. A careful mass spectrometric analysis was performed on the admitted gas sample to ascertain that the hot tantalum cell did not produce any measurable thermal degradation by-products. The only masses observed were those that could be assigned to the expected cracking pattern of the particular sample used. The cell was then removed and loaded with chunks of magnesium metal. Several different sources of magnesium metal, ranging from 99 to 99.99% purity, were used with no perceptible difference in the results. In addition, Alfa Inorganic magnesium chips, 99.99% purity, were sublimed in this laboratory before use. For an actual magnesium experiment the vaporization cell was heated to approximately 440° where the vapor pressure of magnesium is about 10^{-2} Torr. Since the cell was heated resistively and supported at its ends, there was obviously a substantial thermal gradient along its length. Consequently these temperatures measured at the cell center and corresponding vapor pressures represent approximate ranges only. The melting point of magnesium is 650°. With the gas flow off and the vaporization cell at $\approx 440°$ no unusual masses were detected in the mass spectrometer. Background pressure under these conditions as measured on the ionization gauge was approximately 5×10^{-8} Torr. After several minutes a metallic film was readily detectable on the line-of-sight quartz target. With the magnesium vaporization cell on, admission of certain gases at rates sufficient to cause the background pressure in the vaporization chamber to increase from 5×10^{-8} to $\sim 1 \times 10^{-6}$ Torr would cause the appearance of signals in the mass spectrometer at masses 24, 25, 26 in the intensity ratio consistent with the isotopes of magnesium atoms, 79, 10, 11, respectively (see Figure 2). Hereafter, gases that cause such an effect will be referred to as "active". The magnesium signals would disappear immediately upon cooling the vaporization cell and would

gradually vanish over a period of several minutes after closing the gas inlet valve. In all cases the signals were only observed during the simultaneous vaporization and gas impingement process. Passage of gas over freshly deposited magnesium (with cell off) would not produce the signals.

Results

Specific experiments were conducted to determine the identity of the magnesium species effusing from the vaporization chamber under the conditions described above. Apparently, all the known compounds of magnesium have negligible vapor pressure at room temperature. Extensive searches were made to detect higher mass fragments or parent masses containing magnesium. Utilizing ionization energies from 6 to 70 eV we expected to find a type of magnesium complex or compound which was sufficiently volatile to explain the appearance of magnesium ion signals in the mass spectrometer. However, no higher masses were detected that could be associated with the Mg^+ signals. Lack of detection of such a parent peak could result from instability of the parent ion formed from electron bombardment in the ion source region. However, parent ions from such weakly bonded species as Ar_2 and $ArHCl$ can be readily detected.[7] The failure to detect a parent mass is certainly not sufficient evidence alone to conclude that the volatile magnesium species is atomic magnesium, but coupled with the following observations such a conclusion seems to be a valid one.

Mg+ Appearance Potential. The appearance potential of Mg^+ was determined by the standard linear extrapolation method for all three isotopes and checked for internal accuracy with several reference gases including argon, mercury, and ethyl bromide. The measurement was performed in both the time-of-flight and magnetic mass spectrometers yielding a consistent value of 7.6 ± 0.2 eV compared with the known ionization potential of atomic magnesium of 7.64 eV.[8] The uncertainty in the appearance potential measurement and the lack of knowledge concerning possible ionization fragment species does not permit a definite assignment of the observed magnesium ion peaks. The measured appearance potential was independent of the particular active gas employed.

Active and Nonactive Gases. Numerous experiments were conducted to determine what types of gases were active and if there existed varying degrees of activity. Nonactive gases include Ar, Xe, O_2, N_2, H_2O, Cl_2, CO, CO_2, SO_2, NO, N_2O, CS_2, NH_3, CF_4, CH_3Cl, CH_3OH, CH_3CN, n-C_6H_{14}, $(C_2H_5)_2O$, and 1-hexyne. Careful experiments were done with several of these to eliminate the possibility of magnesium vapor transport by entrainment in the gas beam. Such a process would certainly not be expected at the extremely low system pressures used. In fact, we tried to produce such an effect with unusually high argon and methyl chloride flow rates but with no success.

Active gases found were straight and branched alkyl bromides and iodides, HCl, HBr, CH_2Cl_2, $CHCl_3$, CCl_4, and CH_3COCl. The relationship between background pressures in the active series, CH_2Cl_2, $CHCl_3$, and CCl_4 and intensity of the Mg^+ signal is illustrated in Figure 3. The pressures are those taken directly from the ionization gauge and have not been corrected for inherent differences in ionization efficiency of the various gases. The constancy of the vaporization rate of magnesium metal was confirmed by repeating the series of measurements in reverse order. The increased activity as determined by the Mg^+ signal intensity
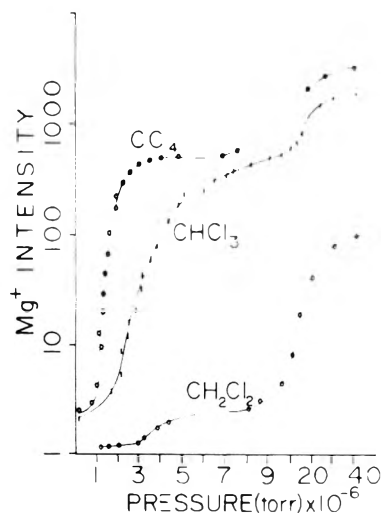
Figure 3. The relative intensity of the Mg^+ signal is plotted vs. the background pressures of the indicated active gases. For these measurements the Mg deposit rate was kept constant. Note the large difference in Mg^+ intensity produced by CH_2Cl_2 compared to CCl_4. CH_3Cl is totally inactive (see text).

for a given pressure of active gas as the number of chlorine atoms increases can be readily seen from the plot. A similar curve for ethyl bromide and iodide occurs approximately between CCl_4 and $CHCl_3$. Note that each gas has a final plateau region at the highest pressures shown. Further increases in pressure resulted in decreased intensity of the Mg^+ signal. Both HCl and HBr appeared to have high activities although accurate comparative measurements for these were not made.

Matrix Isolation Spectroscopy. The matrix isolation technique for spectroscopic application is well established and will not be discussed in detail.[9,10] The method was applied to aid in the identification of the volatile magnesium species. Apparatus details for the system used have been reported elsewhere.[2]

Valve A (Figure 1) was connected via a bent section of flexible metal tubing to the matrix isolation apparatus. An Air Products Model CS-202 closed cycle helium refrigerator system was used to cool a lithium floride window to $12°K$ where Matheson research grade argon and the effusion species from the vaporization chamber were condensed. The argon inlet tube was located 3 cm directly in front of the 1-in. diameter lithium fluoride window. The matrix dewar apparatus had an independent high vacuum system and utilized outer quartz windows mounted on level with the inner lithium fluoride deposition surface. Ultraviolet light from a deuterium continuum source operating at approximately 40 W was passed through the room temperature outer quartz window and the inner lithium fluoride window. The transmitted light was then focused onto the slits of a Jarrell-Ash 0.5-m Ebert scanning spectrometer employing a 1140 lines/mm grating blazed at 3000 Å and photomultiplier detection. The ratio of argon to trapped species (commonly referred to as the M/A ratio) was varied over a range from approximately 1000/1 to 100,000/1 on various experiments.

The ultraviolet spectrum obtained was in agreement with previous studies reported for magnesium atoms in rare gas matrices utilizing a direct atomic beam magnesium source.[1,2] The atomic absorption attributed to isolated magnesium atoms in an argon matrix occurs at 2815 ± 5 Å
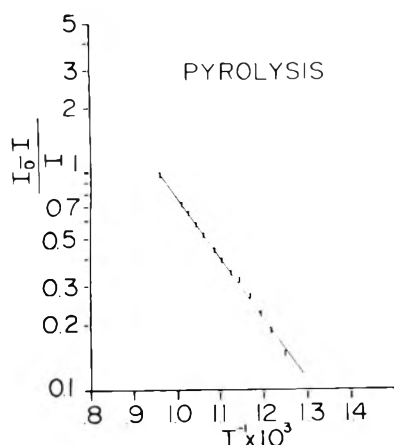
Figure 4. A function showing the decrease in Mg^+ intensity is plotted against $1/T$. I_0 is the Mg^+ intensity at $300°K$ and I is the intensity at higher temperatures. The quantity $[(I_0 - I)/I]$ is assumed to be proportional to the first-order rate constant of the process responsible for removing Mg from the vapor phase (see text).

and is assigned to the $(3s3p)^1P \leftarrow (3s^2)^1S$ transition. Atomic bands in rare gas matrices are usually quite broad (250–1000 cm^{-1}) and exhibit structure not seen in the gas-phase spectrum. All the active gases tested, the bromides, iodides, HCl, HBr, and CCl_4, produced identical matrix spectra. No bands were detected from 2000 to 7000 Å which have not been previously associated with isolated magnesium atoms. The necessary experimental conditions for producing the ultraviolet bands in the matrix isolation experiment were identical with those required for Mg^+ detection in the mass spectrometer. As mentioned previously, the gas flow and vaporization cell had to be operated simultaneously.

The results of the matrix isolation study support the atomic magnesium assignment but are not conclusive since the bands are broad and interactions with the matrix atoms themselves might dominate. In other words, magnesium atoms bound and transported in a van der Waals type complex might appear atomic in nature, at least in the matrix experiment.

Pyrolysis. Volatile species effusing from the vaporization chamber were pyrolyzed by passage through either quartz or stainless steel tubes 0.62 in. i.d. and approximately 18 in. long connected between valve A (Figure 1) and the mass spectrometer. The tube was wrapped with several layers of heating tape and insulated to improve temperature uniformity. Three thermocouples were stationed against the tube wall at different positions for temperature measurement. All thermocouples agreed within 3° over the range investigated. Dissociation data for bicyclopentadiene was measured on our apparatus as a function of temperature so that it could be compared to earlier VLPP ("very low pressure pyrolysis") work reported by Benson and Stokes.[11] The 20% dissociation value they obtained at $720°K$ was satisfactorily duplicated.

Prior to a specific pyrolysis experiment the active gas alone was passed through the tube at the highest temperature to be used and its mass spectrogram recorded to ascertain that it would not dissociate. The pyrolysis measurements consisted of recording the Mg^+ intensity as a function of temperature with the active gas flow rate and vaporization cell temperature constant. The temperature dependence of the apparent first-order rate constant is plotted in Figure 4. The percent dissociation was reversible with tem-

perature in the sense that heating and cooling measurements produced the same results. The form of the rate constant expression is taken from Benson and Stoke's analysis, namely, $k = k_{ea} [(I_0 - I)/I]$ where I_0 is the intensity of the Mg^+ peak at room temperature, I is the intensity at high temperatures, and k_{ea} is a constant except for a $T^{1/2}$ temperature dependence. Standard analysis of the slope (neglecting preexponential temperature dependence) yields an activation energy for the "process". The Mg^+ intensity begins to noticably decrease for pyrolysis tube temperatures greater than $710°K$ for HBr and C_2H_5Br and has decreased by one third at approximately $910°K$. Extensive efforts were made to obtain a consistent set of activation energies for HBr, HCl, CH_3Br, C_2H_5Br, C_2H_5I, and CCl_4 for comparative purposes. However, successive experiments with a given active gas revealed that some type of "aging effect" on the pyrolysis tube surface was operative. The longer the effusion species from the vaporization chamber were allowed to pass through the pyrolysis tube the larger the measured activation energy. Initial values of approximately 7 kcal mol^{-1} would gradually increase and appear to reach steady values at approximately 14 kcal mol^{-1} over several days of near continuous operation. No differences were noted between the quartz or stainless steel pyrolysis tubes. These complications plus experimental uncertainties make meaningful comparisons for the various active gases quantitatively unreliable.

Inspection of the pyrolysis tube after several hours of operation at temperatures sufficiently high to reduce the Mg^+ signal by about 30% revealed a shinny metallic looking mirror or film at the entrance region and brown deposits further into the tube. Passage of the effusion species through an unheated tube did not produce deposits detectable by visual inspection.

Tesla Coil Discharge and Ultraviolet Effect. In the experimental configuration used in the pyrolysis study, it was observed that a tesla coil discharge directed at the outer glass surface of the tube leading to the mass spectrometer would cause the Mg^+ signal to rapidly decrease by 80–95%. The pressure in the tube, $\approx 10^{-6}$ Torr, was too low for visible detection of the discharge in the tube. The Mg^+ peak would return rapidly to about 85% of its value before discharging but would require several minutes to fully reach its original intensity. No unusual mass peaks were observed in the mass spectrometer as a result of the discharge. The active gas parent mass intensity was found to momentarily increase about 10–20% at the beginning of each discharge exposure then stabilize near the original level. As the discharge was moved to other areas of the tube, another momentary increase was observed then stabilization near the original, nondischarge intensity level.

Ultraviolet irradiation of the tube through a LiF window mounted in its side with a deuterium discharge source operating at 40 W produced a 30% attenuation in the Mg^+ signal. The ultraviolet light struck part of the interior surface of the tube. As observed in the discharge experiment, the signal intensity would not immediately return to its original level after terminating the irradiation but would gradually approach that level over a period of several minutes.

Condensation. A Pyrex U-tube, 0.62 in. i.d., was connected between valve A, Figure 1, and the mass spectrometer. The U-tube was cooled by submersion in various low temperature cold slushes and the effects on the Mg^+ and active gas parent mass signal intensity noted. The Mg^+ signal decreased by 30, 65, and 100% at cold trap tempera-
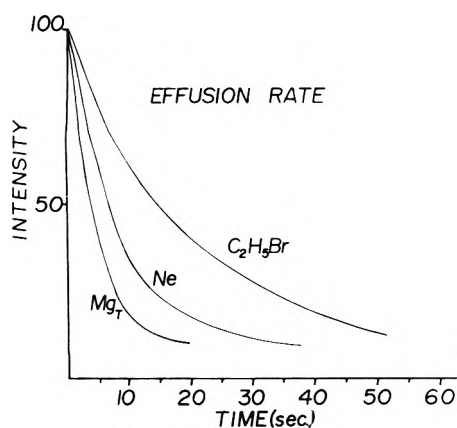
Figure 5. The time decrease in the signal intensity of the indicated species is plotted. Time = 0 corresponds to the closing of valve A.

tures of -96, -112, and $-126°$, respectively. After several minutes of trapping, visual evidence of solid deposit in the trap was noted. The active gas signal, CH_3Br, did not begin to decrease until temperatures below $-112°$ were obtained. Condensation of the volatile magnesium species in the trap between valves A and B at $-112°$, followed by gradually warming the trap to room temperature with valve A closed and valve B leading to the mass spectrometer open, did not produce the Mg^+ signal nor any other unusual mass peak.

Condensation experiments conducted using the cooled copper cup target described in the experimental section yielded results similar to that obtained in the U-trap arrangement.

Effusion Rate Measurement. An experiment was designed so that the molecular weights of volatile species effusing from the vaporization chamber into the mass spectrometer could be measured by their effusion rates. To positively identify the volatile magnesium species as atomic magnesium an extremely delicate method of mass determination was sought since the failure to detect a possible parent mass ion constitutes only strong negative evidence. Experiments were performed on the apparatus shown in Figure 1 to determine if the masses of known gases could be measured by using the mass spectrometer to monitor effusion rates by recording intensity changes as a function of time under the following conditions. Various known volatile species were introduced into the vaporization chamber at background pressures of 1×10^{-6} Torr and allowed to effuse through valve A into the 5-l. glass bulb then through valve B into the mass spectrometer. Once a steady-state rate of effusion into the mass spectrometer was established as determined by a constant peak height, valve A was abruptly closed. The peak height for the particular identifying mass being monitored would then begin to decrease as the low pressure sample in the 5-l. bulb gradually became depleted by leakage into the mass spectrometer. A strip chart recorder monitored the time decrease with the spectrometer set on a particular mass. The pressures are sufficiently low so that the mean free paths of the molecules are large compared with the exit dimensions at valve B. By assuming that the signal intensity, I, measured in the mass spectrometer at time t is proportional to, N, the particle number in the 5-l. bulb and applying the molecular leak rate equation,[12] one obtains

$$-dN/dt = N\bar{c}A/4V$$

or

$$-dI/dt = I\bar{c}A/4V$$

where $\bar{c}$ is the mean velocity of the gas molecules at room temperature, A is the area of the exit, and V is the volume. The integrated form of the above rate expression yields

$$\ln (I_0/I) = (\bar{c}A/4V)t$$

where I_0 is the steady-state intensity at $t = 0$ or before valve A is closed. The slope, S, obtained by plotting ln (I_0/I) against t can be related to the mass, M, of the effusing species through $\bar{c}$ at constant A, V, and temperature. Hence, the measured slope for a known gas, A, can be used to determine the mass of an unknown gas, B, from such effusion rate measurements using the final result $S_A/S_B = (M_B)^{1/2}/(M_A)^{1/2}$.

The reliability of the procedure described was first confirmed by measuring the slopes for several known gases that covered the mass range from 4 to 154. Calculated masses for a given gas based on its measured slope ratio for another gas agreed within 2 to 3 mass units over the entire range cited. Actual effusion rate measurement curves as taken from the strip chart recorder are shown in Figure 5. The parent mass for each of the gases was monitored to obtain the data. The effusion rate for helium and CCl_4 not shown in Figure 5 was also measured.

The experimental conditions for the measurements on the known gases were chosen to be as similar as possible for the mass determination of the volatile species responsible for producing the Mg^+ signal in the mass spectrometer. The active gas flow rate and magnesium vaporization cell temperature were adjusted to produce a constant signal level for the Mg^+ peak. Valve A was abruptly closed and the decreasing signal intensity for both the active gas parent mass and the Mg^+ peak was recorded as a function of time. The decay curve and analysis for the active gas signal, i.e., C_2H_5Br, was identical with previous measurements on the active gas alone.

The measured decay rate for the Mg^+ signal was found to vary depending upon the length of time the active gas and magnesium species were allowed to pass through the system and the 5-l. glass bulb. The longer the system was used for a given experiment the smaller the decay rate became. However, after approximately 20–30 hr of operation the decay reached a steady value that showed little or no subsequent change. If the system was opened to atmospheric pressure and the glass bulb cleaned in a dilute hydrofluoric acid solution, the same "aging process" was again observed. The calculated effective mass of the volatile species producing the Mg^+ signal using the above experimental procedure was correspondingly found to vary from 1 to 17. A larger effective mass was obtained the longer the system was "aged". The highest mass, 17, corresponds to the smallest decay rates obtained after 20–30 hr of continuous operation since the slope of the decay plot is inversely related to the square root of the mass.

The above results indicate that the Mg^+ signal decay rate is too fast even in an aged system to result solely from a simple effusion process. A fraction of the volatile magnesium species in the 5-l. bulb might "stick" or condense on the internal surface before they could effuse into the mass spectrometer. To determine whether the total decay rate could be analyzed as the sum of two independent processes the following experiments were conducted to measure the "internal decay" rate. After obtaining a steady Mg^+ signal, both valves A and B (Figure 1) were rapidly closed simulta-
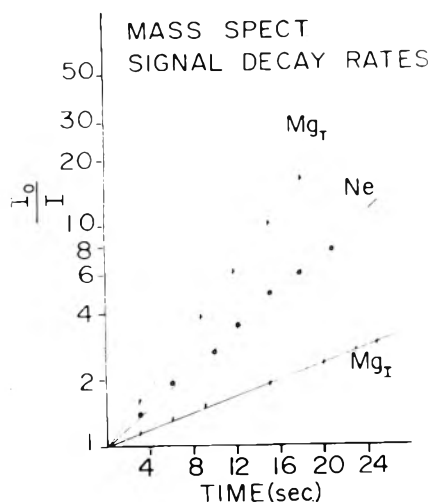
Figure 6. Data for Mg_T and Ne were obtained by closing valve A and monitoring the signal decrease with time. Mg_I Data were obtained by measuring the signal decrease for various times that both valve A and B were closed. The slopes of these curves are used to calculate the mass of the volatile magnesium species producing the Mg^+ signal.

neously for a measured time period after which valve B was quickly opened. The instantaneous signal level reached after opening valve B for Mg^+ was measured as a function of time that the 5-l. bulb was isolated, i.e., the time both valves A and B were kept closed. Assuming a first-order law for the internal decay rate $\ln I_0/I$ vs. t was plotted to determine the internal decay rate constant where I_0 is the intensity level reached after immediately opening valve B and I is the intensity reached after having the bulb isolated for time, t.

An extremely interesting result emerged from this analysis. Subtraction of the "internal decay rate constant" from the total signal decay rate should yield just the effusive rate constant which can be used to determine the mass as before. The calculated mass of 17 for an aged system based on the total decay increased to 22 after correcting for the internal decay mechanism. This final result of 22 is clearly within experimental uncertainty of mass 24 which would be the expected mass if the volatile magnesium species were actually atomic magnesium. Since the condensation rate in a well-aged system is small relative to the total decay rate, subtraction of the condensation rate from the total rate to obtain the effusive rate does not introduce significant uncertainty in the calculated molecular weight. These measurements were confirmed on at least 20 separate experiments. For a "fresh" system, one not completely aged, the total decay rate would be quite fast, the reason being that the internal decay rate was dominate over the simple effusive rate. Even under these conditions the total rate minus the internal rate would still result in a constant effusive rate and predict the same mass result. The longest half-life measured for the internal decay in an aged system was approximately 16 ± 1 sec. Figure 6 shows a logarithmic plot of the various mass spectrometric signal decays with time. The Mg curve labeled Mg_T is the total decay curve obtained from just closing valve A and Mg_I is the data for the internal, isolated bulb experiment. The average number of surface collisions that a volatile species makes in the 5-l. bulb before effusing through valve B is given by the ratio of internal surface area to exit area since the mean free path

of the species for the pressures employed is very large relative to the exit dimension. For the system used, the average collision number is 800. Data from the closed bulb experiment can be used to estimate a sticking probability of $4 \pm 1\%$.

Discussion

The experimental results indicate that atomic magnesium is the volatile magnesium species and that the effective sticking coefficient of atomic magnesium in the presence of certain active gases is significantly less than the normally expected value of one. Evidence that a reaction occurs between the active gas and the magnesium metal on the direct line-of-sight deposition surface can be obtained by monitoring the active gas parent peak intensity as the magnesium vaporization cell is gradually heated. The reduction in parent peak intensity is proportional to the rate of magnesium deposit. For a constant gas flow rate, the Mg^+ signal is detectable before the active gas parent signal is reduced by more than a few percent. The Mg^+ intensity passes through a distinct maximum value as the vaporization cell temperature is raised for a constant gas flow. Further increases in the cell temperature produces a sharp decrease in the Mg^+ intensity, unless the gas rate is also increased. However, for background gas pressures above approximately 1×10^{-5} Torr no additional increases in the maximum Mg^+ level is observed. Careful searches were made in the mass spectrometer for ordinarily volatile reaction products. The only species detected were H_2 and trace amounts of R_2 for RBr and RI active gases. The reaction with methyl halides produced small amounts of CH_4 relative to the parent halide peak.

The decrease in the parent alkyl halide peak as the magnesium is deposited is not surprising since magnesium halides, which are nonvolatile, are likely to be produced. Whether any primary reaction products formed in the direct line-of-sight deposition region are involved in the transport mechanism of magnesium atoms is not known. The aging process observed in the pyrolysis, discharge, and internal decay rate experiments suggests a necessary surface conditioning period before the sticking coefficient of atomic magnesium is significantly reduced. A surface effect is also indicated by the slow recovery time of the Mg^+ intensity following ultraviolet irradiation and the tesla discharge. The momentary increases in the parent mass active gas peaks during discharge exposure accompanied by the simultaneous and large decreases in the Mg^+ signal suggest that the active gas is at least partially involved in the surface conditioning process that causes the reduced sticking efficiency of atomic magnesium. Applying this simple argument to the pyrolysis measurements would imply that the increasing temperatures gradually alter the surface causing Mg atoms to condense in the cooler entrance region producing the shinny metallic film described previously. A necessary surface conditioning period is consistent with the observation that for a freshly cleaned system, both active gas flow and magnesium deposition must be maintained for about 30 min before Mg^+ is detectable in the mass spectrometer. The Mg^+ signal intensity continues to increase until a constant level is reached after about 20–30 hr of nearly continuous operation. The effective partial pressure of Mg in the glass bulb was estimated by producing incremental background pressure changes in the vaporization chamber by introducing an argon flow in addition to the active gas flow. Mass spectrometric intensity comparisons

between the Ar^+ and Mg^+ signals were then made assuming that the bulb pressure and vaporization chamber pressure were similar. These measurements indicate an approximate range of 10^{-6} to 10^{-7} Torr for the effective partial pressure of magnesium in the 5-l. glass bulb (see Figure 1). The equilibrium vapor pressure of magnesium metal at 300°K is approximately 10^{-21} Torr as estimated by extrapolation of existing data at higher temperatures. Typical ranges for the rates of magnesium deposit and active gas flow are approximately 0.05–0.2 mmol/hr. Apparently the surface is conditioned by the adsorption or chemisorption of some substances. A definite assignment of the substance responsible for a given active gas will be a difficult problem. The substance could be simply the active gas species or a reaction product. If a reaction product is responsible, it is possible that it contains magnesium atoms. This possibility suggests that a species containing magnesium should also be observed in the mass spectrometer since it would likely be volatile in order to cover the surfaces. Obviously no such species has been observed as discussed in the Results section. Another mechanism could involve the initial adsorption of the active gas molecules followed by a magnesium atom which reacts to form a nonvolatile magnesium complex on the surface. Subsequent magnesium atoms impinging on the surface could experience an initial repulsion that could prevent their condensation or they could undergo exchange with the atoms bound in the surface complex. Additional experiments are planned to determine whether the volatile magnesium atoms do in fact undergo exchange with surface bound atoms. Such information would be extremely valuable in formulating a reasonable mechanism that would account for the observed phenomenon. The system will be thoroughly "aged" or conditioned using natural magnesium containing the abundances of 79, 10, and 11% for the isotopes of mass 24, 25, and 26, respectively. Vaporization from the cell containing natural magnesium will then be stopped and another cell already mounted in the vaporization chamber containing magnesium metal enriched in isotope of mass 26 will be utilized. The cell substitution can be accomplished in less than 1 min without breaking the vacuum by employing a four-electrode flange that can accommodate two independently heated vaporization cells. If there is no surface exchange of magnesium atoms, the intensity ratio for the various Mg^+ signals should reflect the known mass 26 percentage of the enriched metal. However, exchange with natural magnesium on the surface would decrease the relative amount of mass 26 reaching the mass spectrometer thus producing a signal intensity ratio of mass 26 to mass 24 below that expected for the enriched magnesium metal sample.

Another area that is difficult to explain is the distinction between active and nonactive gases. Alkyl chlorides and chlorine, for example, are not active, although the parent mass signals for these species are reduced in a similar manner for active gases when magnesium vaporization is initiated. Neither the structure nor the length of the alkyl group makes any apparent difference in the active, nonactive classification. However, RCl_2, RCl_3, RCl_4, and HCl are active gases as well as volatile RBr and RI compounds. There exists an interesting parallel among the series RCl, RBr, and RI regarding their relative activity in reducing the sticking coefficient of magnesium atoms in an aged system and their relative reaction rates with magnesium metal measured in solution reactions. A competition kinetic technique has recently been reported to obtain reliable relative

reaction rates of alkyl halides with magnesium metal in ether solutions.[13] The results demonstrate that RBr and RI have similar reaction rates and that the RCl rate is approximately 2 orders of magnitude smaller. The organic moiety has no significant effect on the relative rates. For our experiment, the relative activity refers to the strength of the Mg^+ signal obtainable in an aged system for a given background pressure of active gas. As discussed previously, this type of data is plotted in Figure 3 for the RCl_x series. Results for RI and RBr are quite similar to one another. The proposed rate-determining step in the solution reaction involves the electron transfer from the metal to the alkyl halide. At the background pressures employed in our experiments the entire surface would rapidly become covered with perhaps several monolayers of adsorbed active gas molecules. An impinging magnesium atom could transfer an electron to the alkyl halide forming a charge transfer surface bound complex represented by $R-Br^-$--Mg^{2+}--Br^--R. The qualitative observation that both the active gas flow and metal deposit must be conducted simultaneously during the aging or conditioning phase as well as for the actual generation of volatile magnesium atoms is at least consistent with the above proposition. The reason why a significant number of other magnesium atoms do not permanently bond to such a surface layer would have to be explained on the basis of short-range repulsive forces. The observation that RCl is not an active gas might result from the smaller size of Cl relative to Br and I. If this were the case, one could argue that the increased number of Cl atoms in the RCl_x series would compensate for the smaller size of Cl and account for the increased activity as x increases.

Obviously the above explanation raises many questions that cannot be answered satisfactorily without detailed and sophisticated calculations for the various potential energy coordinates involved and experimental work designed to study the surface directly. Qualitatively it cannot explain why similar metals such as calcium, lithium, sodium, and aluminum do not behave in a similar manner. Preliminary experiments with zinc do yield similar results, although the Zn^+ signals obtained thus far are extremely weak. Two exciting possibilities are suggested by these results. Perhaps other metals could be made volatile in the sense that magnesium was if the proper conditions and active gases were found. Since extremely high temperatures are required for the production of most atomic metal vapors, the ability to conduct experiments on metallic vapors at or even below room temperature could offer significant advantages in many applied areas as well as suggest new types of fundamental studies.

References and Notes

(1) O. Schnepp, *J. Phys. Chem. Solids*, **17**, 188 (1961).
(2) L. B. Knight, Jr., R. D. Brittain, M. A. Starr, and C. H. Joyner, *J. Chem. Phys.*, in press.
(3) L. B. Knight and W. Weltner, Jr., *J. Chem. Phys.*, **54**, 3875 (1971).

(4) M. Spoliti, G. Marini, S. Nanzionte Cesaro, and G. DeMaria, J. Mol. Struct., **19**, 563 (1973).
(5) P. S. Skell and J. E. Girard, J. Am. Chem. Soc., **94**, 5518 (1972).
(6) "Handbook of Chemistry and Physics", 46th ed, Chemical Rubber Publishing Company, Cleveland, Ohio, 1965 p D96.
(7) S. E. Novick, P. Davies, S. J. Harris, and W. Klemperer, J. Chem. Phys., **59**, 2273 (1973).
(8) C. E. Moore, Natl. Bur. Stand. U.S. Circ., **No. 467** (1949).

(9) B. Meyer, "Low Temperature Spectroscopy", American Elsevier, New York, N.Y., 1971.
(10) W. Weltner, Jr., Adv. High Temp. Chem., **2**, 85 (1970).
(11) S. W. Benson and G. N. Stokes, J. Am. Chem. Soc., **89**, 2525 (1967).
(12) R. D. Present, "Kinetic Theory of Gases", McGraw-Hill, New York, N.Y., 1958.
(13) R. J. Rogers, H. L. Mitchell, Y. Fujirvara, and G. M. Whitesides, J. Org. Chem., **39**, 857 (1974).

Molecular Orientation of Chemisorbed Formates and Nitric Monoxides on Evaporated Metal Surfaces by Infrared Reflectance Spectroscopy

Masatoki Ito* and Wataru Suetaka

Laboratory of Interface Science of Metals, Faculty of Engineering, Tohoku University, Aramaki, Sendai, 980, Japan (Received September 18, 1974; Revised Manuscript Received December 9, 1974)

The adsorption of formic acid on evaporated copper and aluminum surfaces was studied using an infrared reflection method. The molecular orientation of the chemisorbed species on metal surfaces was successfully observed by this technique. When formic acid vapor was introduced over copper or aluminum surfaces, formate ions were observed. The reflection spectra of formate ions on copper showed the 1360-cm^{-1} band of the symmetric OCO stretching vibration but not the 1600-cm^{-1} antisymmetric OCO band; whereas the reverse was true of the transmission spectra of smooth copper films deposited on the polished KBr plates. These results lead to the conclusion that the chemisorbed formate molecules are oriented almost vertically on the smooth copper surface. Nitric monoxide and isoamyl nitrite adsorbed on evaporated copper, nickel, and iron surfaces were also investigated and discussed.

Introduction

Infrared spectroscopic measurements of chemisorbed molecules on metal surfaces have been widely studied by infrared transmission through thin evaporated films.[1] However, recent investigations on chemisorption on the metal surface using multiple reflection technique have indicated the feasibility of using the reflection method.[2,3] The advantage of this method can be seen in its application to bulk metal surfaces, and furthermore the great advantage of this method is its ability to determine orientations of adsorbed species in relation to the plane of the metal surface. Since Francis and Ellison first applied this method to the investigation of monolayers on a metal mirror[4] and Greenler developed its theoretical and practical bases,[5] this valuable technique has been considered as one of the powerful tools for chemisorption study.

In all reflection spectra so far reported, however, the observed chemisorbed species on bulk metal surfaces were confined to carbon monoxide. Although chemisorbed formates have been investigated by many workers with transmission method,[6,7] no direct evidence indicating the molecular orientation of this species on bulk metal surfaces has been obtained.

The result to be reported here about formates on copper, a part of which was briefly communicated,[8] is the first infrared reflection observation of oriented chemisorbed molecules on metal surfaces. This paper is mainly concerned with the spectra of formates adsorbed on copper and aluminum surface, but nitric monoxide, isoamyl nitrite (CH$_3$CH(CH$_3$)CH$_2$CH$_2$ONO) adsorbed on copper, iron, and nickel surfaces will be mentioned briefly in order to elucidate the chemisorption to the metal surfaces.

Experimental Section

The whole apparatus is shown schematically in Figure 1. The infrared radiation was focused onto the sample mirror (S.M.) at an incidence angle of 85°. The reflected radiation was collected by a spherical mirror (M$_4$), and entered into the spectrometer entrance slit of Jasco IR-G grating spectrometer. The stainless-steel high vacuum cell equipped with the infrared transmitting KBr windows (64 × 12 mm) is also shown in this figure. The cell was pumped using an oil diffusion vacuum system. The ultimate pressure of 2.0 × 10^{-6} Torr was measured with an ionization gauge. As substrates we used smooth quartz glass plates on which gold films were previously deposited in another vacuum evaporator. Their dimensions were 30 × 50 mm. After evaporating the metal to form the substrate, background spectra were taken and stored in a spectrum computer JEC-5 (Japan Electronic Co.). The formic acid vapors were effused in the cell by breaking the ampoule using a breaker. The pressure of the vapor was about 1 Torr. Ten minutes later, the gas was evacuated to 10^{-5} Torr, and the reflection spectra were measured. The spectrum was scanned at a rate of 0.8 cm^{-1} sec^{-1}. The differences between the background and the sample spectra were calculated at 0.5-cm^{-1}
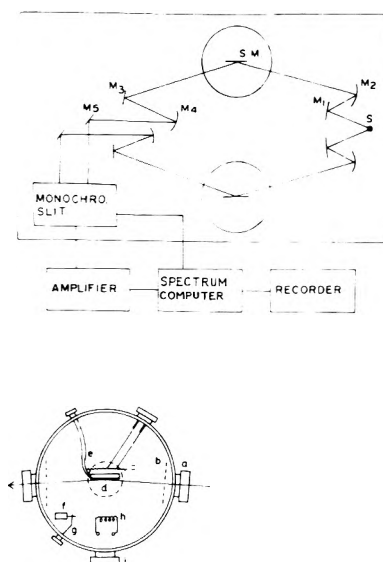
Figure 1. Schematic view of the whole instrument and a drawing of the high vacuum cell: (a) KBr window; (b) shutter; (c) heater; (d) sample mirror (S.M.); (e) thermocouple; (f) ampoule of gas source; (g) breaker; (h) tungsten filament; (i) viewing port; (S) infrared source; (M_1, M_3, M_5) mirrors; (M_2, M_4) spherical mirrors.

Figure 2. Transmission spectra of adsorbed $HCOO^-$ on a copper deposited surface (a,b) and reflection spectra of adsorbed $HCOO^-$ and $DCOO^-$ on copper or aluminum surfaces (c–f): (a) on well-ground KBr plate; (b) on cleaved KBr plate; (c) $DCOO^-$ on aluminum; (d) $HCOO^-$ on aluminum; (e) $DCOO^-$ on copper; (f) $HCOO^-$ on copper.

frequency intervals over 1650–1250-cm^{-1} region. Tenfold scale expansion was employed and multiscannings (eight times in ordinary cases) were adopted. The point-by-point digital difference data were plotted on a chart recorder.

The signal (1–3% in transmittance) was sufficiently measurable in comparison with the noise level of 0.5%. The signal enhancement procedure and repetitive scanning of the spectrum and computer averaging made it possible to obtain sufficiently measurable signals from a monomolecular layer.

The transmission metal films, used in the transmission measurement, were evaporated on 30×30 mm KBr plates in such a way that both sides of the plates were coated with a film ca. 100 Å thick. One plate was used in each measurement.

The formic acid used in this work was obtained from Wako Chemical Co. and the isoamyl nitrite was from Nakarai Chemical Co. which was distilled three times. Pure metals of copper (99.999%), aluminum (99.99%), and nickel (99.998%) were used.

Result

The transmission spectrum of the Cu(II) formate tetrahydrate shows two strong absorption bands in the 1650–1250-cm^{-1} region due to OCO stretching vibrations.[9] The spectra of chemisorbed formate on copper show that the strongest absorption band at 1600 cm^{-1} disappeared completely and the band at 1360 cm^{-1} occurred as shown in Figure 2e. On the other hand, in the spectra on aluminum both absorption bands appeared just like the transmission spectrum. The similar spectra were obtained for deuterated formate (dotted lines). These bands were relatively broad, having a half-width of about 80 cm^{-1}. On deuteration, the band maxima shifted to lower frequencies (1590, 1355 cm^{-1}). These bands remained undiminished upon evacuation below 10^{-4} Torr at room temperature. The reflectivity decrease at these bands is 1–3%.

Figure 2 also shows the transmission spectra of the adsorbed formates on thin deposited copper film (100 Å) on

Figure 3. Replica electron micrographs of vacuum deposited metal surfaces: (a) on copper $\times 10,000$; (b) on aluminum $\times 10,000$.

KBr plates. The solid line (Figure 2a) shows the spectrum of the well-ground specular surface and dotted line (Figure 2b) shows the spectrum from the cleaved surface which is assumed to be very rough. On the smooth surface only the 1600-cm^{-1} band appeared and the band near 1350 cm^{-1} disappeared, but the latter band appeared when the cleaved KBr plate was used as the substrate.

As these differences in the spectrum may arise from surface roughness, some of the evaporated metal films used in this work were examined by electron microscopy. Figure 3a is the replica electron micrograph from the copper surface
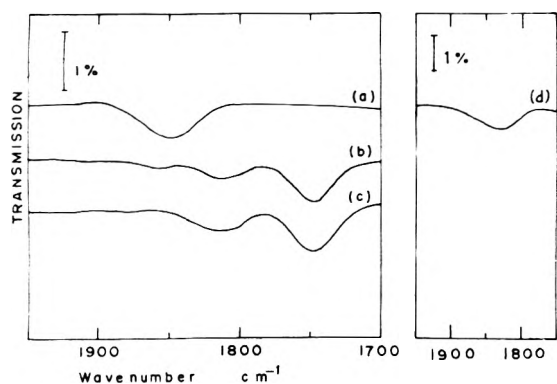
Figure 4. Reflection spectra of adsorbed isoamyl nitrite (a) on copper, (b) on nickel, and (c) on iron. Reflection spectrum of adsorbed nitric monoxide (d) on iron.

evaporated at room temperature, whereas Figure 3b is from the aluminum surface.

The 2–3% increase in reflectance was also observed just after the evaporation of copper, corresponding to sintering. These observed absorption bands were decreased in intensity by raising the substrate temperature to near 150°.

Figure 4 shows the reflectance spectra of chemisorbed nitric monoxide on evaporated iron surface and chemisorbed isoamyl nitrite on evaporated copper, nickel, and iron surfaces. The spectrum of nitric monoxide on iron shows a weak band near 1825 cm^{-1} (Figure 4d). The reflectance spectra of chemisorbed isoamyl nitrite show absorption bands at 1850 (on copper, Figure 4a) and 1750 and 1820 cm^{-1} (on nickel and iron, Figure 4b,c). These spectra are in fair agreement with those from transmission studies on small particles of iron and iron oxide dispersed on silica, which has been already reported by Poling and Eischens.[10]

Discussion

Chemisorption of Formic Acid. The interaction between the oscillating molecular dipole in the adsorbed molecules and the electric vector of the incident radiation is highly related to the incident angle and the states of polarization of the beam as shown in Figure 5. The amplitude (A) of the standing wave at the metal surface increases with incident angle θ and reaches its maximum at a large incident angle, which changes depending upon the optical constants of metal. The parallel component (p) of the incident radiation can produce at large incidence angles the strong resultant standing wave field as a result of interference between the incident and the reflected wave as shown in Figure 5b. The perpendicular component (s) cannot make the sizeable standing electric field because the phase change of the incident and reflected wave is about 180° and nearly complete cancellation occurs (Figure 5a). Accordingly the electric field at the metal surface is predominantly perpendicular to the mirror surface, therefore, it can interact with the vibrational mode for which the effective component of the dipole moment change is perpendicular to the surface. The formate ion has strong infrared absorption bands at 1360 and 1590 cm^{-1}, and these bands are assigned to the symmetric OCO stretching vibration, in which the dipole moment change is parallel to the C_2 axis of the ion, and the antisymmetric vibration, in which the change is perpendicular, respectively (Figure 6a,b). Therefore it can be said that the dipole moment change parallel to the C_2 axis of the ion, namely, the symmetric OCO stretching vibration, does interact with the standing wave field and results in a
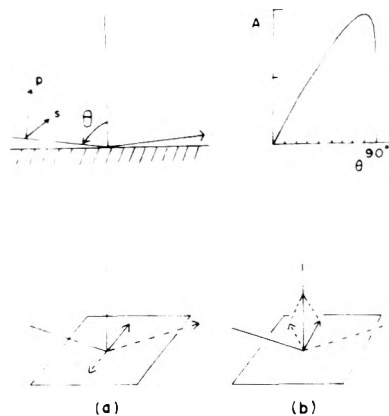

Figure 5. The explanation for high-sensitivity reflection spectroscopy: (p) parallel component of radiation; (s) perpendicular component of radiation; (A) amplitude of standing wave field; (θ) incident angle.
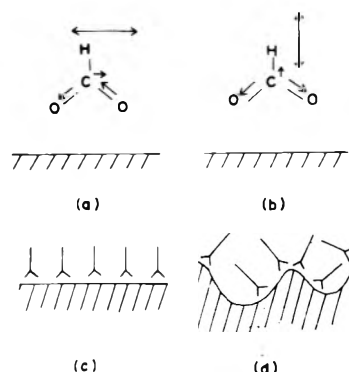
Figure 6. Adsorptive form of formates on metal: (a) antisymmetric stretching vibrational mode; (b) symmetric stretching vibrational mode. Schematic view of adsorptive form: (c) on smooth copper surface; (d) on porous aluminum surface.

strong band in the reflection spectra, provided the C_2 axes of the adsorbed species are normal to the surface. The antisymmetrical mode of vibration, on the contrary, cannot interact with the infrared radiation and the corresponding band does not appear in the reflection spectra.

It has been said that the evaporated copper surface is completely sintered at room temperature and its whole surface area corresponds to its geographical area.[11] On the other hand, the evaporated aluminum is porous with a very rough surface. The electron micrographs (Figure 3) of these metals clearly show the change in surface roughness. It can easily be seen from the photographs that the copper surface is very smooth whereas the aluminum surface is very rough.

It has been already suggested in a transmission study[12] that the formate molecules adsorb on the metal surface by oxygen atoms and the C_2 axis of the molecule becomes perpendicular to the surfaces. The missing 1590-cm^{-1} OCO antisymmetric stretching vibration band in the reflection spectra can be explained by the fact that the dipole moment change of the antisymmetric vibration becomes parallel to the mirror surface and it cannot interact with the electric field perpendicular to the surface.

Similarly, the absence of the 1360-cm^{-1} OCO symmetric stretching band in the transmission spectra (Figure 2a) indicates that the dipole moment change in the vibration becomes perpendicular to the surface and it cannot interact with the electric field parallel to the surface.

Figure 6c,d shows the orientation of the adsorbed molecules to the microscopic metal surface. On the copper surface, all of the formate ions oriented vertically to the smooth copper surface and on the aluminum surface the adsorbed formate ions appear in a relatively random orientation to the macroscopic metal surface due to the surface roughness. The above-mentioned transmission data on smooth and rough KBr plates confirm these features of orientation on the metal surfaces.

Chemisorption of Nitric Monoxide and Isoamyl Nitrite. The infrared study of butyl nitrite and nitric monoxide on iron and iron oxide has been investigated by Poling and Eischens using a transmission method.[10] Both nitric monoxide and butyl nitrite retard the corrosion of iron and steel probably by the same mechanism, because butyl nitrite dissociates during chemisorption and the fragment appears to be nitric monoxide. They reported that the nitric monoxide on a preoxidized iron surface produces a band at 1820 cm^{-1} which is assigned to Fe^{2+}:N=O$^+$, and oxidative chemisorption on initially reduced iron produces a band at 1750 cm^{-1} which is assigned to Fe-O-N=O. The reflectance spectrum of nitric monoxide on the iron surface shows a band at 1825 cm^{-1}, which is in good accord with the transmission spectra of chemisorbed nitric monoxide on the nickel surface.[13] Recently, Calahorra and Folman studied the adsorption of nitric monoxide on germanium.[14] They ascribed two peaks at 1853 and 1750 cm^{-1} to the NO dimer formed on the surface and assumed the higher frequency is that of the symmetric mode, whereas the lower one is due to the asymmetric mode of the NO bond. In the present investigation, the reflectance spectra of isoamyl nitrite on evaporated nickel and iron showed two absorption bands at 1820 and 1750 cm^{-1}, and showed a band at 1850 cm^{-1} on copper. These results suggest that the nitric monoxide, formed as fragments of the isoamyl nitrite, adsorbs perpendicularly on the metal surfaces because the species adsorbed parallel to the smooth metal surface give rise to extremely weak absorptions as mentioned above.

Our samples were probably contaminated by the residual gas or the diffusion pump oil under our vacuum system near 2×10^{-6} Torr. The ultrahigh vacuum system is essential to investigate the accurate molecular orientation on atomically clean metal surfaces, which is now in progress in our laboratory.

The reflection spectra of a monolayer or less of carbon monoxide adsorbed on clean metal surfaces have already been obtained from the single reflection technique.[3,5] The chemisorbed formates and nitric monoxides show strong absorption bands as well as carbon monoxide, and the measurable signals were also detected from these species with a single reflection apparatus. This infrared reflection absorption technique, if applied to the surface phenomena of the catalytic reaction, will become a very powerful technique to obtain information on chemisorbed species.

References and Notes

(1) For example, L. H. Little, "Infrared Spectra of Adsorbed Species", Academic Press, London, 1966.
(2) R. G. Greenler, *J. Chem. Phys.*, **44**, 310 (1966).
(3) M. A. Chesters, J. Pritchard, and M. L. Sims, *Chem. Commun.*, 1454 (1970).
(4) S. A. Francis and A. H. Ellison, *J. Opt. Soc. Am.*, **49**, 131 (1959).
(5) H. G. Tompkins and R. G. Greenler, *Surface Sci.*, **28** 194 (1971).
(6) K. Kishi, T. Ogawa, and K. Hirota, *J. Catal.*, **5**, 464 (1966).
(7) A. Ueno, T. Onishi, and K. Tamaru, *Trans. Faraday Soc.*, **65**, 756 (1969).
(8) M. Ito and W. Suetaka, *Chem. Lett.*, 757 (1973).
(9) Y. Kuroda and M. Kubo, *Spectrochim. Acta, Sect. A*, **23**, 2779 (1967).
(10) G. W. Poling and R. P. Eischens, *J. Electrochem. Soc.*, **113**, No. 3, 218 (1966).
(11) A. R. L. Moss and B. H. Blott, *Surface Sci.*, **17**, 240 (1969).
(12) K. Hirota and Y. Nakai, *Nihon Kagaku Zashi*, **80**, No. 7, 700 (1959).
(13) G. Blyholder and M. C. Allen *J. Phys. Chem.*, **69**, 3998 (1965).
(14) Z. Calahorra and M. Folman, The Second International Conference on Solid Surface, Kyoto, March 1974, No. 29a C2 4.

Structural Characterization of Hydrothermally Treated Lanthanum Y Zeolites. I. Framework Vibrational Spectra and Crystal Structure

Julius Scherzer,* Jonathan L. Bass, Fred D. Hunter

W. R. Grace & Co., Washington Research Center, Columbia, Maryland 21044 (Received November 25, 1974)

Publication costs assisted by W. R. Grace & Co.

The effects of several thermal and hydrothermal treatments of low soda Y zeolites of different lanthanum content have been investigated by infrared and X-ray powder methods. The absorption maxima of the framework vibrational bands shifted toward higher frequencies after steaming at 540 and 820°. The cationic and framework atom coordinates, interatomic distances, and angles of low and high lanthanum Y zeolites steamed at 540° were determined. The changes in location of infrared absorption maxima are attributed to partial framework dealumination. Observed unit cell shrinkage supports this assumption. The detection of a nonframework position at $X = Y = Z = 0.028$ in the structure of steamed, low-lanthanum Y has been attributed to nonframework aluminum. We conclude that steaming results in partial framework dealumination and possible structural rearrangement in the framework. These effects are more pronounced for low-lanthanum zeolites.

I. Introduction

The rare earth forms of Y zeolites are of great interest due to their high catalytic activity for many reactions.[1-5] The structure of these zeolites has been investigated by a number of authors. Infrared spectroscopic studies of rare earth exchanged Y zeolites have been reported by Rabo,[4] Ward,[6] Bolton,[7] and others. Using X-ray crystallography, several authors have established the cationic distribution in rare earth exchanged, natural faujasite as well as in LaX and CeX zeolites.[8-10] Diffuse reflectance spectra in the visible region have also been used in an attempt to localize cations in calcined, steamed, and vacuum dehydrated rare earth X and Y zeolites.[25]

In their use as catalytic promoters, rare earth Y zeolites are frequently exposed to high-temperature calcination and steaming, especially during the catalyst regeneration process. However, there is little information in the literature concerning the structural characteristics of hydrothermally treated lanthanum Y zeolites. We have therefore investigated the effect of hydrothermal treatment upon the structure and catalytic characteristics of these zeolites. For comparison, a similar study was carried out on low-soda, lanthanum Y zeolites thermally treated in the absence of steam.

In this paper we present and discuss the framework vibrational spectra and crystal structure of lanthanum Y zeolites with different lanthanum content which have undergone different thermal and hydrothermal treatments.

II. Experimental Section

A. Materials. Lanthanum Y zeolites were prepared by exchanging a thoroughly washed NaY zeolite with lanthanum chloride solutions. A NaY sieve with a relatively low SiO_2/Al_2O_3 ratio (4.2) was selected as starting material in order to enhance the changes that occur during the thermal and hydrothermal treatment of the corresponding lanthanum Y sieves. The exchange was carried out by mixing the NaY zeolite into the lanthanum chloride solution, adjusting the pH of the slurry to 3.5 with diluted hydrochloric acid, and heating the mixture under stirring for 1 hr at 90°.

After filtering and washing the cake chloride free, the material was oven-dried at 110° for 1 hr.

Part of the oven-dried material was calcined under vacuum at 540° for 3 hr and then repeatedly ammonium exchanged until the sodium level dropped below 1 wt % Na_2O. A 10 wt % ammonium sulfate solution was used in the exchange process.

Portions of the ammonium salt treated lanthanum Y zeolite were calcined (a) under vacuum at 540° for 3 hr; (b) under 100% steam at 540° for 3 hr; and (c) under 100% steam at 820° for 3 hr, respectively.

Using different amounts of lanthanum chloride, 24 and 53% lanthanum exchanged sieves were prepared by the procedure described.

In another preparation, a lanthanum Y zeolite was prepared by the following procedure: a sample of NaY was exchanged with an excess of lanthanum chloride, the resulting material was calcined at 540° for 3 hr under vacuum, and then again lanthanum exchanged until the sodium content dropped below 1 wt % Na_2O. Portions of the resulting lanthanum Y zeolite were thermally treated as described. A 98% lanthanum exchanged sieve was prepared by this procedure.

The unit cell composition prior to the thermal treatment, the percent of lanthanum exchange in the different samples prepared, and the unit cell sizes after thermal treatment are given in Table I.

The following notation is used for the samples prepared: the number preceding the LaY formula indicates the percent of lanthanum exchange in that zeolite; the temperature and conditions of the treatment (under vacuum or steam) are indicated in parentheses after the formula.

B. Infrared Instrumentation and Measurements. The details of the infrared experiments have been previously reported.[11] The spectra were recorded on a Beckman IR-12 spectrophotometer and were obtained with a Wilks Model 38 attenuated total reflection (ATR) unit.

A 10 wt % slurry of zeolite powder in ethanol was evaporated onto one side of a 2-mm thick KRA-5 ATR plate and placed in the Wilks ATR unit. Because of energy losses from the optical arrangement of this unit an attenuator was

TABLE I: Composition and Unit Cell Size of Lanthanum Y Zeolites

Sample no.	Unit cell composition (prior to thermal treatment)	% La exch	Unit cell size, Å (after)[a]		
			540° v	540° stm	820° stm
1	$(NH_4, H)_{45.5}Na_{1.5}La_{4.9}(AlO_2)_{62}(SiO_2)_{130} \cdot nH_2O$	24	24.64	24.49	24.31
2	$(NH_4, H)_{27.7}Na_{1.5}La_{11}(AlO_2)_{62}(SiO_2)_{130} \cdot nH_2O$	53	24.73	24.64	24.47
3	$Na_{2.1}La_{20.1}(AlO_2)_{62}(SiO_2)_{130} \cdot nH_2O$	98	24.75	24.75	24.70

[a] v = vacuum; stm = steam.

Figure 1. Framework bands of thermally treated 24-LaY zeolites: (A) 540°, vacuum; (B) 540°, steam; (C) 820°, steam.
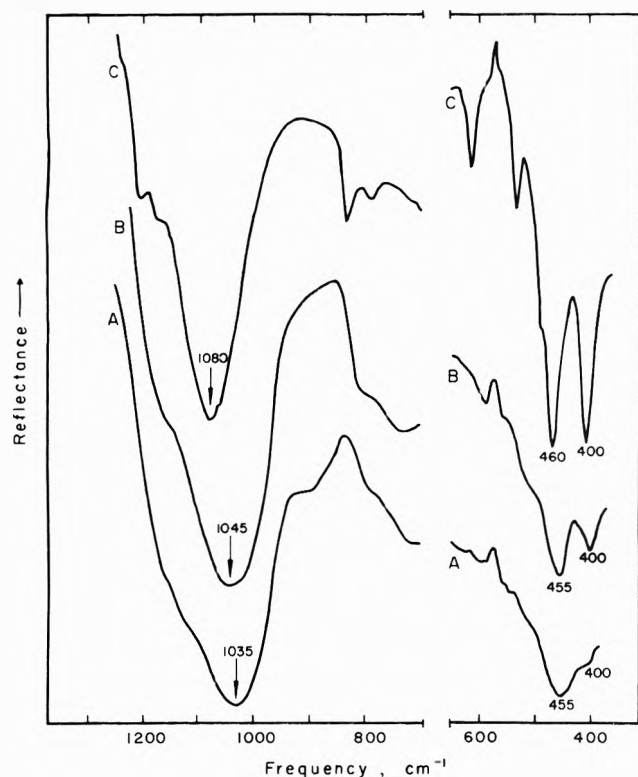

Figure 2. Framework bands of thermally treated 53-LaY zeolites: (A) 540°, vacuum; (B) 540°, steam; (C) 820°, steam.

placed in the reference beam to obtain full scale deflection.

C. X-Ray Instrumentation and Data Collection Method. The X-ray data were collected on a Norelco powder diffractometer. A Hamner solid state detection system, equipped with a scintillation counter and a pulse height analyzer, was employed. The scans were taken using Cu Kα radiation, a 0.003-in. receiving slit, and a scanning speed of ⅛ deg/min. The data were measured while the sample was under partial vacuum of about 88 mmHg. The instrumentation, data collection methods, and data analyses have been described in more detail elsewhere.[10]

III. Results

A. Infrared Data. Characteristic bands in the framework vibrational spectra of lanthanum Y zeolites are illustrated in Figures 1–3. Figure 1 shows the effect of different thermal treatments of 24-LaY on the low-frequency region of the spectrum. 24-LaY (540, v) shows a strong band at 1035 cm^{-1}, whereas 24-LaY (540, stm) has this band shifted to about 1045 cm^{-1}. 24-LaY (820, stm) has the corresponding band at 1080 cm^{-1}.

The spectra of steamed materials show also additional bands or more intense bands as compared to the spectra of vacuum-calcined materials. Thus, for example, the spec-

trum of 24-LaY (540, stm) shows a band at about 400 cm^{-1}, which is considerably weaker in the spectrum of the vacuum-calcined sample. An increase in the steaming temperature from 540 to 820° results in a dramatic increase in intensity and sharpness of many of the existing bands in the framework region. New bands (e.g., at about 530 cm^{-1}) can also be detected. As a whole, the spectrum appears drastically changed.

Figures 2 and 3 provide a similar comparison for 53-LaY and 98-LaY submitted to different thermal treatments. As in the previous case, steaming results in a shift of characteristic bands toward higher frequencies. Additional bands can be identified in the spectra of the steamed materials, as compared to the corresponding spectra of the vacuum-calcined samples. An increase of the steaming temperature from 540 to 820° also results in significant changes in the spectra.

Table II shows the assignment of several characteristic bands in the spectra of different zeolitic frameworks. Table III contains characteristic bands in the framework region of the LaY zeolites investigated.

TABLE II: Zeolite Framework Infrared Assignments[a]

Internal tetrahedra		External lincages (structure sensitive)	
Asym stretch	1250–950 cm^{-1}	Double ring	650–500 cm^{-1}
Sym stretch	720–650 cm^{-1}	Pore opening	420–300 cm^{-1}
T–O bend	500–420 cm^{-1}	Sym stretch	820–750 cm^{-1}
		Asym stretch	1150–1050 (sh) cm^{-1}

[a] Reference 12. [b] T represents Si or Al.

Figure 4. Faujasite framework with indication of oxygen type (●) and nonframework sites (○).

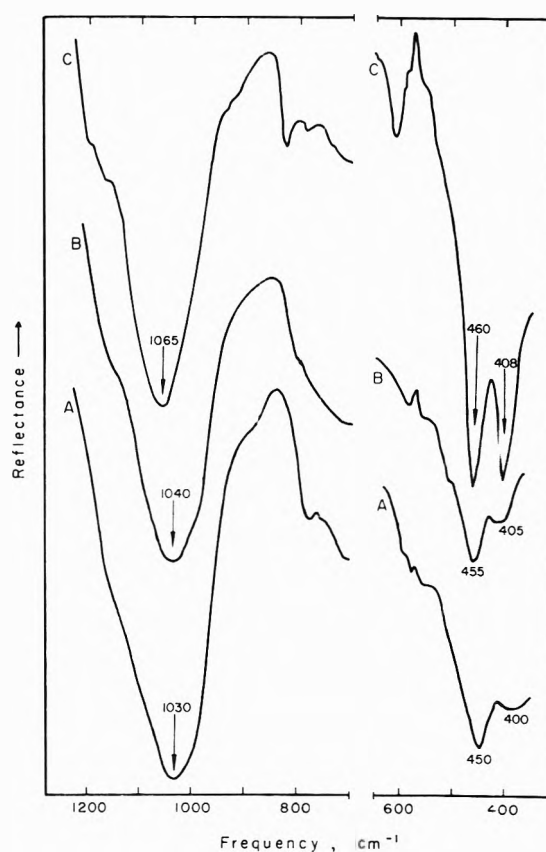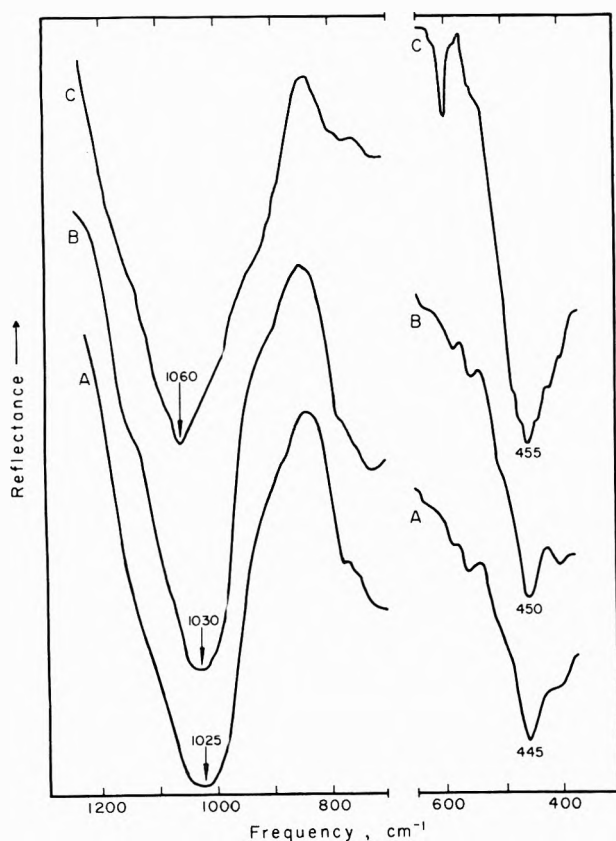**Figure 3.** Framework bands of thermally treated 98-LaY zeolites: (A) 540°, vacuum; (B) 540°, steam; (C) 820°, steam.

B. X-Ray Data. Framework and nonframework positions have been determined for 24-LaY (540, stm) and 98-LaY (540, stm) by X-ray diffraction. Atomic coordinates for these materials are given in Table IV. Interatomic distances and angles are shown in Table V.

The detection of a nonframework position at $X = Y = Z = 0.028$ in the structure of 24-LaY (540, stm) was attributed to nonframework aluminum. 4.5 atoms of this type were found per unit cell. Their location is in the vicinity of sites I', but more displaced toward the hexagonal prism.[26] We will tentatively call such sites I*. Sites I' adjacent to occupied sites I* are vacant. Other nonframework sites found occupied in 24-LaY (540, stm) are sites I' (by lanthanum) and sites U (by oxygen).

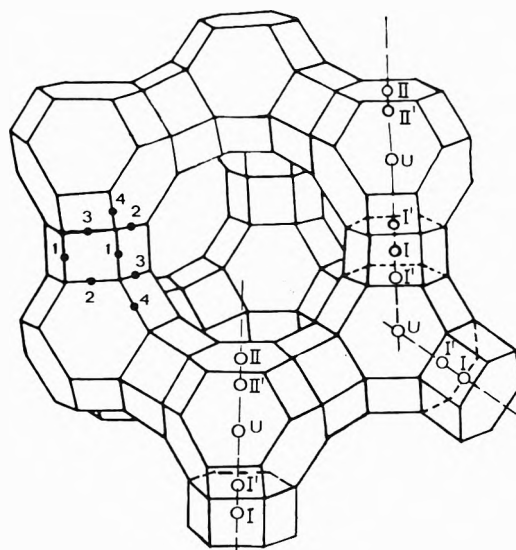In 98-LaY (540, stm), the nonframework positions are occupied as follows: all lanthanum ions in sites I', 32 oxy-

gen in sites II', and 2.2 oxygen in sites U. Nonframework aluminum species could not be detected in this material.

IV. Discussion

The bands in the vibrational spectra of the faujasite framework have been assigned by Flanigen et al.[12] Some of these assignments are summarized in Table II. It is known that the silica/alumina ratio of the faujasite type framework affects the position of absorption bands in the framework region of the spectra. An increase in the silica/alumina ratio results in a shift of absorption bands toward higher frequencies.[13–15] Such a band shift occurs when the silica/alumina ratio in the framework is increased either by direct synthesis or by partial aluminum removal from the framework.[16,17] The most visible shift occurs for the T–O asymmetric stretching band.

In the case of NH$_4$Y zeolites, it has been shown that steam interacts with the zeolite, resulting in a partially dealuminated framework and cationic aluminum species. In the framework vibrational spectrum, this is reflected in a shift of framework bands to higher frequencies.[11]

It is reasonable to assume that in the presence of steam different lanthanum Y zeolites can also undergo a dealumination process.

Jacobs and Uytterhoeven have reached a similar conclusion based on the analysis of the hydroxyl stretching region of ir spectra of steamed LaY zeolites.[21]

Besides temperature and amount of steam, the degree of framework dealumination will also depend upon the concentration of lanthanum cations in the zeolites. We assume that an increase in lanthanum ion concentration in La, NH$_4$Y, and LaY zeolites will tend to inhibit the generation of new cationic species, due to electrostatic repulsion. Therefore, under otherwise equal conditions, the most advanced dealumination can be expected in 24-LaY (540, stm) and the least dealumination in 98-LaY (540, stm).

An increase in temperature from 540 to 820° will further enhance the dealumination process. This is reflected by the spectra shown in Figures 1–3. In the spectra of 24-LaY, the T–O asymmetric stretching band is shifted from 1034 cm^{-1} (540°, v) to 1045 cm^{-1} (540, stm), and to 1075 cm^{-1} (820°, stm), respectively. Structural X-ray data for 24-LaY (540°,

TABLE III: Framework Vibrational Frequencies (in cm^{-1})[a]

Zeolite type	Thermal treatm	T–O asym stretch	T–O sym stretch	Double 6 ring	T–O bend	12-Ring pore opening
24-LaY	540°, vacuum	1035 vs, 890 sh	780, w sh	565 w, 550 sh	455 m	400 sh
24-LaY	540°, steam	1045 vs	815 sh,	588 w, 555 sh	455 m	410 m
24-LaY	820°, steam	1080 vs	835 m 790 w	612 s 580 sh 530 m[b]	460 vs	400 vs
53-LaY	540°, vacuum	1030 vs	775 w	580 w 555 sh	450 m	400 sh
53-LaY	540°, steam	1040 vs	800 w, sh	585 w 555 sh	455 m	405 w
53-LaY	820°, steam	1065 vs	825 m 785 w	615 s 585 sh	460 vs	408 vs
98-LaY	540°, vacuum	1025 vs	775 sh	575 w 560 sh	445 s	400 sh
98-LaY	540°, steam	1030 vs	780 sh 725 w	580 w 555 w	450 s	405 w
98-LaY	820°, steam	1060 vs	800 sh	600 s 585 sh 550 sh[b]	455 vs 420 sh	400 sh

[a] w = weak; m = medium; s = strong; vs = very strong; sh = shoulder. [b] Assignment uncertain.

TABLE IV: Atomic Coordinates for 24-LaY (540, stm) and 98 LaY (540, stm)[a]

Atom type	X	Y	Z	Occup	Temp factor
	24-LaY (540, stm)			$R(I) = 0.143$	
T[b]	−0.0525(8)	0.1284(8)	0.0358(9)	1.00(4)	2.58(46)
O1	−0.1073(10)	0.1073(10)	0.0	1.00(5)	1.00(191)
O2	−0.0018(13)	−0.0018(13)	0.1367(19)	0.93(6)	6.71(230)
O3	0.1713(13)	0.1713(13)	−0.0338(21)	1.01(5)	7.22(194)
O4	0.1788(15)	0.1788(15)	0.3224(18)	1.00(6)	5.60(226)
Al1	0.0280(58)	0.0280(58)	0.0280(58)	0.14(4)	0.85(820)
La1	0.0729(11)	0.0729(11)	0.0729(11)	0.215(9)[c]	5.64(101)
Ow2	0.1250	0.1250	0.1250	0.85(13)	7.71(522)
	98-LaY (540, stm)			$R(I) = 0.156$	
T	−0.0572(10)	0.1290(14)	0.0353(10)	1.00	2.74(68)
O1	−0.1099(18)	0.1099(18)	0.0	1.00	2.62(182)
O2	−0.0040(16)	−0.0040(16)	0.1272(24)	1.00	3.09(184)
O3	0.1754(17)	0.1754(17)	−0.0321(23)	1.00	6.16(201)
O4	0.1770(18)	0.1770(18)	0.3276(27)	1.00	2.85(209)
La1	0.0667(4)	0.0667(4)	0.0667(4)	0.66(2)[c]	2.99(44)
Ow2	0.1250	0.1250	0.1250	0.28(22)	3.00
Ow3	0.1668(17)	0.1668(17)	0.1668(17)	1.00	1.00

[a] Tables of calculated and observed intensities and structure factors are available from the authors upon request. [b] T represents tetrahedral silicon or aluminum atoms. The numbers in parentheses are the estimated standard deviations. [c] There are differences between the lanthanum content obtained by chemical analysis and from X-ray diffraction data: 4.9 vs. 6.8 La/unit cell in 24-LaY and 20.1 vs. 21.1 La/unit cell in 53-LaY. Similar discrepancies have also been observed by others.[8] They are probably due to basic differences between the two methods used to determine the lanthanum content of zeolites, although partial substitution of water for lanthanum cannot be ruled out.

stm) have shown the presence of nonframework aluminum in the zeolitic cavities in sites I* (Table IV). Cationic aluminum could not be identified in 24-LaY (540, v). As a result of the dealumination process, the unit cell size decreases from 24.64 Å for 24-LaY (540, v) to 24.49 Å for 24-LaY (540, stm).

The assignment of the nonframework position at $X = Y = Z = 0.028$ to nonframework aluminum is not unequivocal, since the X-ray diffraction data give only a count of electronic density and not the element present. However, all the lanthanum has been accounted for and the sodium content is less than two ions per unit cell. Therefore, the only rational assignment for this position would be an alu-

minum or oxygen species. Since the decrease in unit cell size and the shorter mean T–O distance, as well as the shift of infrared bands, support the contention that aluminum has been removed from the framework of 24-LaY (540, stm), the above indicated nonframework position was assigned to aluminum.

It is possible that the nonframework aluminum interacts with O3 framework atoms, since the measured Al–O3 distance of 2.32 Å involves a significant estimated standard deviation.

Since framework dealumination leaves voids in the framework, we would expect the occupancy parameter for Si and Al atoms in the framework of 24-LaY (540, stm) to

TABLE V: Bond Distances and Angles

	24-LaY (540, stm)	98-LaY (540, stm)
T–O1	1.68(3) Å	1.64(5) Å
T–O2	1.56(4)^a	1.64(5)
T–O3	1.67(4)	1.77(5)
T–O4	1.59(4)	1.59(6)
Mean value	1.62	1.66
T–O1–T	139.5(1.6)°	138.0(2.8)°
T–O2–T	157.5(2.9)	128.4(2.7)
T–O3–T	147.2(2.8)	135.3(3.1)
T–O4–T	139.1(2.9)	140.8(3.9)
Mean value	145.8	135.6
O1–O2	2.68(4) Å	2.66(6) Å
O1–O3	2.72(4)	2.81(6)
O1–O4	2.62(4)	2.58(6)
O2–O3	2.55(5)	2.44(6)
O2–O4	2.69(5)	2.91(7)
O3–O4	2.63(5)	2.77(7)
Mean value	2.65	2.70
O1–T–O2	111.4(1.9)°	108.4(2.6)°
O1–T–O3	108.8(1.9)	110.6(2.5)
O1–T–O4	106.1(2.0)	106.0(2.8)
O2–T–O3	104.5(2.2)	91.4(2.6)
O2–T–O4	117.8(2.4)	128.6(3.1)
O3–T–O4	107.9(2.3)	110.7(2.9)
La1–La1	3.61(4) Å	4.08(1) Å
La1–Ow2	2.21(3)	2.49(9)
La1–O3	2.62(6)	2.46(6)
La1–Ow3		2.54(4)
La1–O2		2.89(5)
Ow3–Ow3		2.93
Al1–O3	2.32(15) Å	
Al1–O2	2.86(15)	
Al1–La1	1.90(15)	
Al1–Al1	2.38(20)	

^{a} Values in parentheses are the estimated standard deviations.

be less than one. However, the X-ray data in Table IV show a parameter of 1.00 (100% occupancy). This may be due to the inability of X-ray powder data to discern whether 4.5 out of 192 atoms have been removed from tetrahedral sites in the framework. Furthermore, it is probable that the voids created by dealumination have been filled by migrating silica. The silica can originate either from silicious impurities or from degraded portions of the steamed zeolite. Such a process would result in a shortening of the mean T–O bond. The mean T–O distance of 1.62 Å in the framework of 24-LaY (540, stm) compared to the mean T–O distance of 1.66 Å in 98-LaY (540, stm) (Table V) tends to support this assumption.

The infrared spectra of 53-LaY and 98-LaY steamed at 540 and 820° show a less pronounced shift of the T–O band than the corresponding 24-LaY zeolites, due to the lower degree of framework dealumination expected for high lanthanum Y zeolites. This is in line with structural X-ray data obtained for 98-LaY (540, stm), which indicate the absence of nonframework aluminum (Table IV). The decrease in unit cell size is also smaller: from 24.73 Å for 53-LaY (540, v) to 24.64 Å for 53-LaY (540, stm). In the case of 98-LaY, the unit cell size of the vacuum-calcined and steamed material is practically the same (Table I).

Besides the band shifts to higher frequencies, the frame-

work vibrational spectra of the steamed materials show increased band intensities and additional absorption bands, which are not observed in the spectra of vacuum-calcined zeolites. These changes in the spectra become especially significant when the steaming temperature is increased from 540 to 820°. For example, the band in the 400-cm^{-1} region, assigned by Flanigan et al. to a "pore opening" (12-R) vibration, appears as a shoulder in the spectrum of 24-LaY (540, v), as a band of medium intensity in 24-LaY (540, stm), and as a very sharp and strong band in 24-LaY (820, stm). Similarly, the band assigned to the double six-member ring (D-6) vibration, which is located in the spectra of 24-LaY (540, v) and 24-LaY (540, stm) in the 560–580-cm^{-1} region, increases sharply in intensity and shifts to about 610 cm^{-1} in the spectrum of 24-LaY (820, stm). Several new bands can also be seen in the spectrum of the zeolite steamed at 820°.

A similar effect of calcination conditions upon the spectra is observed for different 53-LaY zeolites, although the complexity of the spectrum of 53-LaY (820, stm) is less pronounced than that of 24-LaY (820, stm).

The least pronounced modifications in the spectra as a result of changing calcination conditions are found for 98-LaY.

It is reasonable to assume that the changes observed in the spectra with changing calcination conditions are not only the result of framework dealumination. Cation movement and associated framework distortions resulting from the hydrothermal treatment of the zeolite will clearly affect the infrared pattern of the zeolites. Bennett and Smith[22] have shown that dehydration and dehydroxylation of calcium exchanged Y zeolites causes migration of the calcium ions, which in turn results in framework distortion and changes in the infrared spectrum. There is also evidence for the migration of lanthanum ions in LaY at high temperature.[23]

Data obtained in our structural X-ray work have shown that cationic migration occurs readily under proper thermal treatment. Freshly exchanged La,NaY zeolites, which have been outgassed at room temperature, contain most of the lanthanum ions in supercage positions. However, by increasing the lanthanum input into the sieve (e.g., to about 50 equiv % or higher), some lanthanum ions penetrate into the sodalite cages even during the exchange process. Thermal treatment at 540° under vacuum or steam results in a shift of all lanthanum ions into sodalite cages, primarily into sites I'. Nonsteamed 98-LaY, which has already been submitted to a thermal treatment during its preparation process, contains about 75% of its lanthanum in sites I' and the remaining lanthanum in sites II. Steaming of this material at 540° results in a shift of practically all lanthanum ions into sites I'. As more lanthanum ions occupy positions within the sodalite cages, the average distance between these ions increases due to electrostatic repulsion. This repulsion causes the lanthanum ions to occupy average positions closer to the center of the hexagonal prisms and thus reduces the average La–O3 distance from 2.62 Å in 24-LaY (540, stm) to 2.46 Å in 98-LaY (540, stm) (Table V). This reduced distance and the resulting increased lanthanum to oxygen attraction increases the T–O3 bond distance from 1.67 to 1.77 Å.

The high concentration of lanthanum ions in the sodalite cages can also account for the higher number of nonframework oxygen atoms in 98-LaY (540, stm), since they act as electrostatic shields between the cations.

There is a similar lanthanum ion distribution in LaY zeolites steamed at 540° and those dehydrated under vacuum at 350°. Smith et al.[23] have shown that in the later case the lanthanum ions occupy sites I'. However, in LaY calcined at 725° and cooled to room temperature, the lanthanum ions occupy sites I' and II'.

Cationic migrations and the associated framework modifications will be evidently most pronounced for LaY samples steamed at 820°. For example, a partial migration of lanthanum ions from inside the sodalite cages to a position near the center of the hexagonal prism (site I) could affect the position and shape of the D-6 ring band. Other structure sensitive bands can also be affected by cationic migration.

The structural changes which take place in the zeolite framework during steaming at 820° are irreversible. This is reflected by the permanent modification of the framework region of their spectra.

The drastic changes observed in the spectra of LaY zeolites steamed at 820° suggest the possibility of structural rearrangement in the zeolitic framework. Such a rearrangement is more likely in low-lanthanum Y sieves in which a considerable number of sites is occupied by ammonium ions prior to the thermal treatment and the dealumination process is more advanced during the thermal treatment. This is supported by the similarity between the framework vibrational spectrum of 24-LaY (820, stm) and the corresponding spectrum of a high-temperature steamed NH_4Y sieve. For this latter material, X-ray and infrared data strongly support the hypothesis of a structural rearrangement.[11,19,24]

References and Notes

(1) J. A. Rabo, P. E. Pickert, D. N. Stamires, and J. E. Boyle, *Actes Congr. Int. Catal. 2nd, 1960,* **2,** 2055 (1961).
(2) P. B. Venuto, L. A. Hamilton, P. S. Landis, and J. J. Wise, *J. Catal.,* **5,** 484 (1966).
(3) E. L. Boreskova, V. I. Lygin, and K. V. Topchieva, *Kinet. Catal. (USSR),* **5,** 991 (1964).
(4) J. A. Rabo, C. L. Angel, and V. Schomaker, *Proc. Int. Congr. Catal., 4th, 1967* (1968).
(5) D. A. Hickson and S. M. Csicsery, *J. Catal.,* **10,** 27 (1965).
(6) J. W. Ward, *J. Phys. Chem.,* **72,** 4211 (1968).
(7) A. P. Bolton, *J. Catal.,* **22,** 9 (1971).
(8) D. H. Olson, G. T. Kokotailo, and J. F. Charnel, *J. Colloid. Interface Sci.,* **28,** 305 (1968).
(9) J. M. Bennett and J. V. Smith, *Mater. Res. Bull.,* **3,** 865 (1968); **4,** 7, 77, 343 (1969).
(10) F. D. Hunter and J. Scherzer, *J. Catal.,* **20,** 246 (1971).
(11) J. Scherzer and J. L. Bass, *J. Catal.,* **28,** 101 (1973).
(12) E. M. Flanigen, H. Kathami, and H. A. Szymansky, *Adv. Chem. Ser.,* **No. 101,** 201 (1971).
(13) S. P. Zhdanov, A. V. Kiselev, V. I. Lygin, and T. I. Titova, *Russ. J. Phys. Chem.,* **38,** 1299 (1964).
(14) A. V. Kiselev and L. I. Lygin, "Infrared Spectra of Adsorbed Species", L. H. Little, Ed., Academic Press, London, 1967, p 361–367.
(15) A. C. Wright, J. P. Rupert, and W. T. Granquist, *Am. Mineral.,* **53,** 1293 (1968).
(16) P. Pichat, R. Beaumont, and C. Barthomeuf, *C. R. Acad. Sci.,* **272,** 612 (1971).
(17) O. Lahodny-Šarc and J. L. White, *J. Phys. Chem.,* **75,** 2408 (1971).
(18) G. T. Kerr, *J. Phys. Chem.,* **71,** 4155 (1967).
(19) P. K. Maher, F. D. Hunter, and J. Scherzer, *Adv. Chem. Ser.,* **No. 101,** 266 (1971).
(20) P. Jacobs and J. B. Uytterhoeven, *J. Catal.,* **22,** 193 (1971).
(21) P. A. Jacobs and J. B. Uytterhoeven, *J. Chem. Soc., Faraday Trans 1,* **69,** 373 (1973).
(22) J. M. Bennett and J. V. Smith, *Mater. Res. Bull.,* **3,** 933 (1969).
(23) J. V. Smith, J. M. Bennet, and E. M. Flanigen, *Nature (London),* **215,** 241 (1967).
(24) J. B. Peri, *Catal., Proc. Int. Congr. 5th, 1972,* **18,** 329 (1973).
(25) I. R. Feins and P. A. Mullen, *Prepr., Div. Pet. Chem., Am. Chem. Soc.,* **15,** No. 1, A89 (1970).
(26) The location of nonframework sites is shown in Figure 4. Site I, a 16-fold site, is in the center of the hexagonal prism, between two six-member rings. Site I', a 32-fold site, is within the sodalite cage, close to the six-member ring shared by the sodalite cage and the hexagonal prism. Site II', a 32-fold site, is within the sodalite cage, close to the six-member ring shared by the sodalite cage and the supercage. Site U, an 8-fold site, is near the center of the sodalite cage. Site II, a 32-fold site, is within the supercage, close to the six-member ring shared by the supercage and the sodalite cage.

Structural Characterization of Hydrothermally Treated Lanthanum Y Zeolites.
II. Infrared Spectra in the Hydroxyl Stretching Region and Acid Sites

Julius Scherzer* and Jonathan L. Bass

W. R. Grace & Co., Washington Research Center, Columbia, Maryland 21044   (Received January 13, 1975)

Publication costs assisted by W. R. Grace & Co.

The hydroxyl stretching region in the infrared spectra of thermally and hydrothermally treated low-soda lanthanum Y zeolites has been investigated. The spectra show that both the lanthanum content of the zeolite and the type of treatment affect significantly the hydroxyl stretching region. Steaming of the zeolites between 540 and 820° can result in partial dealumination of the framework, as reflected by the presence of absorption bands in the 3600- and 3700-cm^{-1} regions and by shrinking of the unit cell. Lower lanthanum content and higher steaming temperatures enhance the dealumination process. Brønsted and Lewis type acidity are maintained by the zeolites even after steaming at 820°. The cationic distribution in steamed lanthanum Y zeolites is being discussed. Interaction of the zeolite samples with ammonia, pyridine, and sodium hydroxide has been used to characterize the acidity of the OH groups. The bands at 3650 and 3600 cm^{-1} are acidic, whereas the band at 3700 cm^{-1} is nonacidic. The band at 3540 cm^{-1} is acidic in low-lanthanum Y zeolites, but is practically nonacidic in high-lanthanum zeolites. The bands at 3700, 3650, and 3540 cm^{-1} are generated primarily by O4, O1, and O3 framework atoms, respectively. The 3540-cm^{-1} band is also generated by OH groups attached to lanthanum ions. The type of oxygen atoms involved in OH groups responsible for the band in the 3600-cm^{-1} region is less certain, but it is assumed to belong to the framework.

I. Introduction

The hydroxyl stretching region in the infrared spectra of rare earth exchanged Y zeolites has been extensively described in the literature. Based on infrared data, Rabo et al. suggested that rare earth ions located in the sodalite cages of the zeolite framework ionize adjacent water molecules. The resulting OH groups are retained as shields between neighboring cations. Upon subsequent dehydroxylation, a structure results in which an oxygen ion is shared by two rare earth ions. Ward[2] suggests similar structures resulting from the hydrolysis of rare earth cations. Bolton[3] has shown that in rare earth exchanged Y zeolites each rare earth cation is associated with one molecule of water. In a more recent paper, Moné and Moskou[4] discuss the infrared spectra of steamed rare earth Y zeolites and suggest that partial dealumination has occurred in these materials. Jacobs and Uytterhoeven reach similar conclusions for "deep bed" calcined lanthanum Y.[15] Ballivet et al.[5] used infrared spectroscopy to study the acidic properties of thermally treated lanthanum Y zeolites.

In this paper we present and discuss the hydroxyl region in the infrared spectra of lanthanum Y zeolites with variable lanthanum content, after submitting these materials to different thermal and hydrothermal treatments. The framework vibrational spectra of these zeolites have been described in ref 6.

II. Experimental Section

A. Materials. Different lanthanum Y zeolites were prepared as described in ref 6. Two of the samples were prepared by exchanging a NaY zeolite with different amounts of lanthanum chloride, calcining the lanthanum exchanged zeolite at 540° for 3 hr under vacuum, and subsequently removing the remaining sodium ions by ammonium exchange. In another preparation, the ammonium exchange step was replaced by lanthanum exchange until the re-

maining sodium content dropped below 1% Na$_2$O. The resulting materials contained 24, 53, and 98 equiv % lanthanum, respectively. Portions of these materials were calcined under vacuum at 540°, under steam at 540°, and under steam at 820°, for 3 hr each, respectively. Several samples were calcined at 400° for 3 hr under vacuum. The composition prior to thermal treatment and the unit cell size after thermal treatment are the same as in ref 6.

In our notation, the number preceding the LaY formula indicates the equivalent percent of lanthanum exchanged into the zeolite. The temperature and conditions of the treatment (vacuum or steam) are indicated in parentheses at the end of the formula.

To establish the effect of sodium hydroxide upon the different OH groups in these materials, 2 g of sample 53-LaY (540, stm) was allowed to react for 2 hr with 200 ml of 0.1 *N* solution of NaOH, at room temperature. Part of the resulting material was treated with a 0.1 *N* (NH$_4$)$_2$SO$_4$ solution.

B. Instrumental and Infrared Measurements. The details of the infrared experiments have been previously described.[7] The spectra were recorded on a Beckman IR-12 spectrophotometer, using self supporting pellets ranging in "thickness" from 8 to 12 mg/cm^2. The pellets were heated under vacuum at 500° for 1 hr to remove physically adsorbed water, except for those calcined under vacuum at 540°. The latter were calcined for 3 hr at this temperature in the cell after being formed from filter dried materials. An attenuator was placed in the reference beam to obtain full scale deflection.

Dry Baker analyzed reagent grade pyridine was adsorbed at room temperature vapor pressure for 2 hr after a freeze-pump–thaw cycle. Physically adsorbed pyridine was removed by heating at 200° under vacuum overnight.

Matheson anhydrous ammonia was adsorbed at several pressures at room temperature for 1 hr and pumped to remove excess ammonia before running the spectrum.
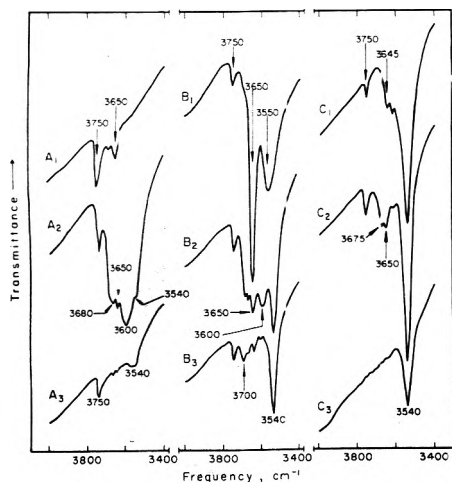
Deionized water was adsorbed following a freeze–pump–

Figure 1. Hydroxyl stretching region of thermally treated LaY zeolites: (A₁) 24-LaY (540, v); (B₁) 53-LaY (540, v); (C₁) 98-LaY (540, v); (A₂) 24 LaY (540, stm); (B₂) 53-LaY (540, stm); (C₂) 98-LaY (540, stm); (A₃) 24-LaY (820, stm); (B₃) 53-LaY (820, stm); (C₃) 98-LaY (820, stm).

thaw cycle at either 150 or 370°. After 2 hr the temperature was raised to 400° to remove physically adsorbed water and then cooled so that the spectrum was run at room temperature.

III. Results

The spectra in the OH stretching region of lanthanum Y zeolites with different lanthanum content recorded after calcination at 540° under vacuum or steam and at 820° under steam are shown in Figure 1. All spectra have an absorption band at 3750 cm⁻¹. In addition to this, the spectra of samples calcined under vacuum show distinct bands at about 3650 and 3540 cm⁻¹ of variable intensities. The spectra of samples calcined under steam show additional bands in the 3600- and 3670–3690-cm⁻¹ regions. The spectra of samples steamed at 820° show considerably more advanced dehydroxylation than those samples steamed at 540°.

The adsorption characteristics in the hydroxyl region of thermally treated LaY zeolites are summarized in Table I. The effect of temperature upon the relative band intensities in the OH stretching region is compared in Figure 2.

Figure 3 shows the effect of rehydration upon the hydroxyl region of 24-LaY (820, atm), 53-LaY (820, stm), and 98-LaY (820, stm).

Figure 4 compares the OH stretching region for 53-LaY (540, stm) before and after treatment with 0.1 N NaOH solution and subsequent treatment with ammonium sulfate. The sodium hydroxyl treatment affects drastically the bands in the 3600- and 3650-cm⁻¹ region, and to a lesser degree the bands in the 3540- and 3700-cm⁻¹ region. Reexchange with ammonium ions regenerates the initial bands. The same results were obtained whether the sodium hydroxide treatment and subsequent ammonium exchange was done at room temperature or at 90°.

The OH stretching region for 24-LaY (400, v) and 98-LaY (400, v) before and after interaction with NH₃ gas is shown in Figure 5. Figure 6 compares the OH stretching region for 53-LaY (540, stm) before and after interaction with NH₃ gas.

Figure 7 shows the OH stretching region of spectra obtained before and after pyridine adsorption on LaY zeolites steamed at 820°.
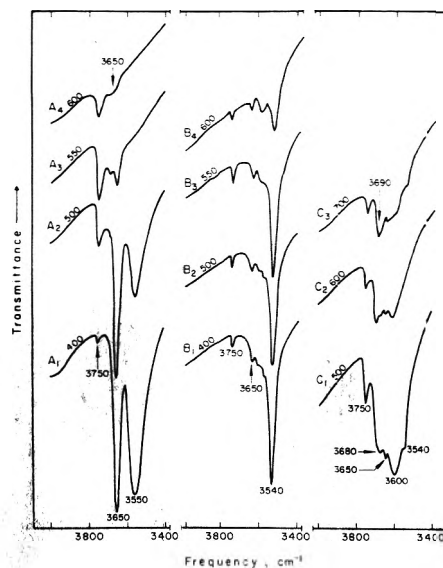

Figure 2. Effect of outgasing temperature upon the hydroxyl stretching region of different LaY zeolites. Outgasing conditions, 1 hr under vacuum; (A) for 24-LaY·nH₂O; (B) for 98-LaY·nH₂O; (C) for 24-LaY (540, stm): (A₁) 400°; (A₂) 500°; (A₃) 550°; (A₄) 600°; (B₁) 400°; (B₂) 500°; (B₃) 550°; (B₄) 600°; (C₁) 500°; (C₂) 600°; (C₃) 700°.
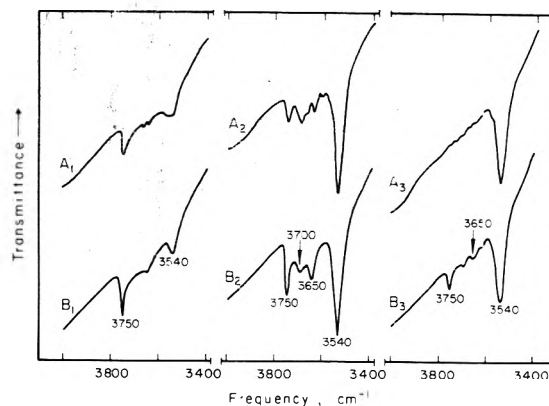
Figure 3. Effect of rehydration upon the hydroxyl stretching region of different LaY zeolites steamed at 820°. Rehydration conditions: 4 mm of H₂O pressure at 150°, then outgasing at 400° for 1 hr. Before rehydration: (A₁) 24-LaY (820, stm); (A₂) 53-LaY (820, stm); (A₃) 98-LaY (820, stm). After rehydration: (B₁) 24-LaY (820, stm); (B₂) 53-LaY (820, stm); (B₃) 98-LaY (820, stm).
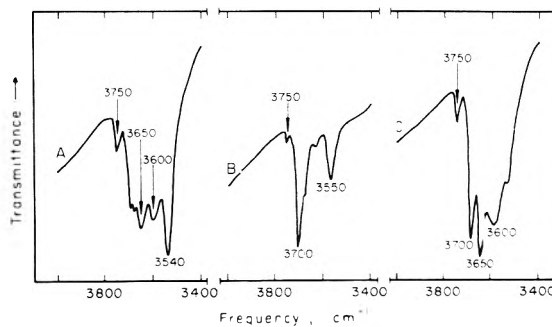
Figure 4. Effect on the hydroxyl stretching region of NaOH and subsequent (NH₄)₂SO₄ treatment of 53-LaY (540, stm): (A) before treatment; (B) after treatment with 0.1 N NaOH; (C) after treatment as B and subsequent treatment with 0.1 N (NH₄)₂SO₄.

Figures 8 and 9 show the spectra in the 1400–1600-cm⁻¹ region for pyridine adsorbed on different LaY samples steamed at 540 and 820°, respectively.

TABLE I: Hydroxyl Stretching Frequencies for LaY Zeolites

| Zeolite Type	Thermal treatm		Absorption bands[a]			
24-LaY	540°, vacuum	3680(w)	3650(m)			
24-LaY	540°, steam	3680(s)	3650(s)	3600(vs)	3550(sh)	
24-LaY	820°, steam		3650(vw)		3550(w)	
53-LaY	540°, vacuum		3650(vs)		3550(s)	
53-LaY	540°, steam	3690(m) 3675(w)	3650(s)	3600(s)	3540(vs)	
53-LaY	820°, steam	3695(m) 3670(sh)	3640(m)	3610(w)	3540(s)	
98-LaY	540°, vacuum		3645(w)	3610(w)	3540(vs)	
98-LaY	540°, steam	3675(m)	3650(m)	3615(w)	3540(vs)	
98-LaY	820°, steam		3640(vw)		3540(s)	

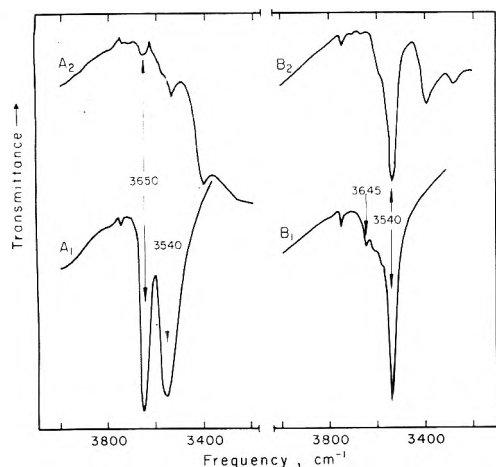[a] w = weak; m = medium; s = strong; sh = shoulder; v = very.

Figure 5. Hydroxyl stretching region of 24-LaY (400, v) and 98-LaY (400, v) before and after treatment with NH_3 gas (4 mm pressure): (A₁) 24-LaY (400, v) before treatment; (A₂) 24-LaY (400, v) after treatment; (B₁) 98-LaY (400, v) before treatment; (B₂) 98-LaY (400, v) after treatment.
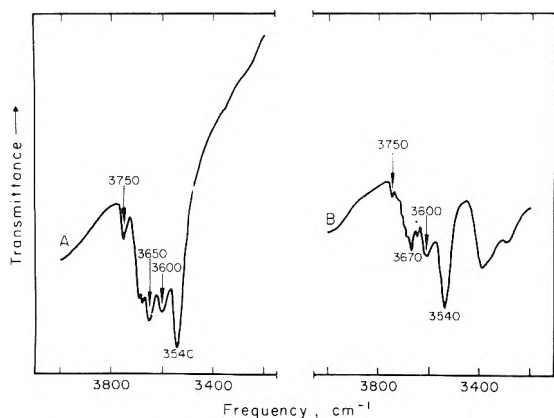

Figure 7. Effect of pyridine adsorption on the hydroxyl stretching region of LaY (540, stm) zeolites: (A₁) 24-LaY (540, stm) before Py adsorption; (B₁) 24-LaY (540, stm) after Py adsorption; (A₂) 53-LaY (540, stm) before Py adsorption; (B₂) 53-LaY (540, stm) after Py adsorption; (A₃) 98-LaY (540, stm) before Py adsorption; (B₃) 98-LaY (540, stm) after Py adsorption.

Figure 6. Hydroxyl stretching region of 53-LaY (540, stm) before and after treatment with NH_3 gas (4 mm pressure): (A) before treatment; (B) after treatment.

Figure 8. Spectra of pyridine adsorbed on LaY (540, stm) zeolites: B, Brϕnsted acidity band; L, Lewis acidity band: (A₁) Py adsorbed on 24-LaY (540, stm); (A₂) Py adsorbed on 53-LaY (540, stm); (A₃) Py adsorbed on 98-LaY (540, stm).

IV. Discussion

Figure 1 clearly illustrates that both the degree of lanthanum exchange and the thermal treatment affect drastically the OH stretching region in the spectra of lanthanum Y zeolites.

A. OH Stretching Region of Vacuum-Calcined Zeolites. The band at 3750 cm⁻¹ has been attributed to surface OH
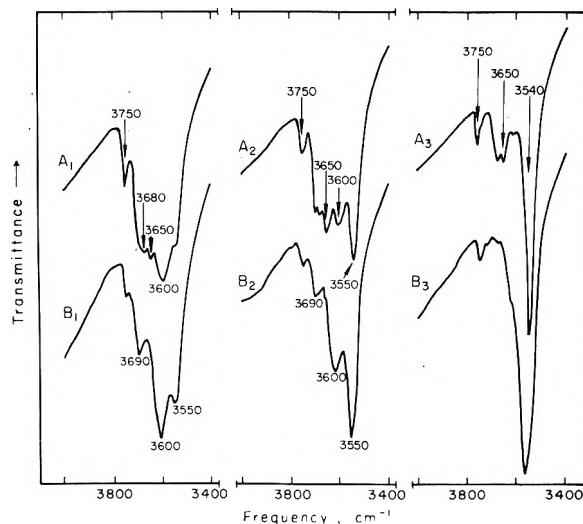
groups or to amorphous silica impurities. The bands at 3650 and 3540 cm⁻¹, which are characteristic for Y-type ze-
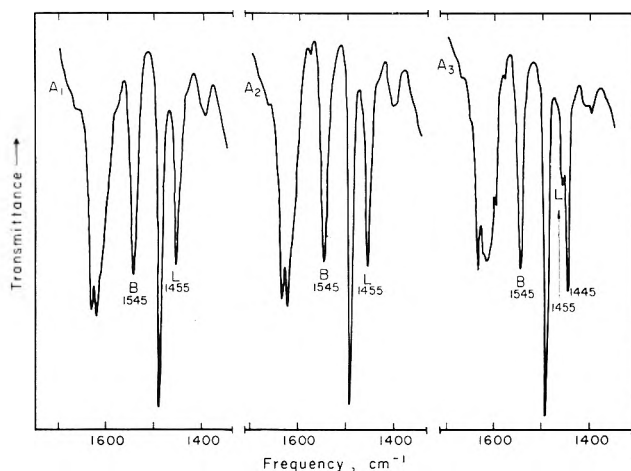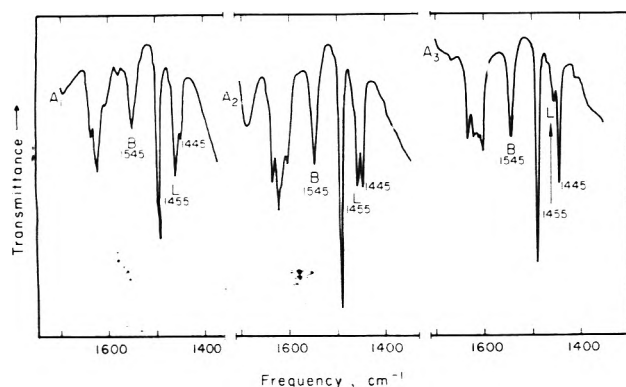
Figure 9. Spectra of pyridine adsorbed on LaY (820, stm) zeolites: B, Brφnsted acidity band: L, Lewis acidity band: (A_1) Py adsorbed on 24-LaY (820, stm); (A_2) Py adsorbed on 53-LaY (820, stm); (A_3) Py adsorbed on 98-LaY (820, stm).

olites, become more intense when the percent of lanthanum exchange is increased from 24 to 53 (see Figure 1, spectra A and B). Such an increase in band intensities is explained by the assumption that OH groups responsible for these bands result from the hydrolysis of the lanthanum cations, as suggested by several authors.[1,2,8] The probable mechanism for such a process is $La(OH_2)^{3+} \rightleftharpoons La(OH)^{2+} + H^+$. The resulting protons attach themselves to negatively charged O1 atoms in the framework and generate acidic OH groups, which are responsible for the absorption band at 3650 cm^{-1}. The OH groups associated with the lanthanum ions generate the band at 3540 cm^{-1}.[1,3] Since the relative band intensities are not the same in the spectra of lanthanum Y zeolites with different lanthanum content, it is assumed that both hydrolysis and hydrogen ion exchange contribute to the intensity of the band at 3650 cm^{-1}; the hydrogen ions originate in the acidic exchange solution.[3,9]

In the case of low lanthanum sample 24-LaY, the band in the 3540-cm^{-1} region is probably generated not only by OH groups attached to lanthanum ions, but also by OH groups of the type encountered in HY zeolites, which absorb in the same spectral region; the latter are attached preferentially to O3 atoms in the framework. The relative broadness of this band in the spectrum of 24-LaY supports this assumption and suggests band overlapping. Thus, for 24-LaY (400, v) the band width at half the maximum intensity value is 56 cm^{-1}, whereas for 98-LaY (400, v) it is 32 cm^{-1}. The band in the 3540-cm^{-1} region for both vacuum calcined 24-LaY and HY has a relatively low thermal stability (Figure 2). By increasing the percent of lanthanum exchange in the zeolite the number of the thermally more stable OH groups attached to lanthanum increases; this results in a relatively strong and sharp band at 3540 cm^{-1} in the spectra of 53-LaY and 98-LaY which remains intense even at high temperatures (Figure 2). The change in the type of OH groups absorbing in the 3540-cm^{-1} region will also contribute to the already mentioned change in relative band intensities.

An advanced degree of lanthanum exchange, as in 98-LaY (540, v), results in the replacement by the highly selective lanthanum ions not only of the remaining sodium ions, but also of part of the hydrogen ions in the acidic OH groups responsible for the band at 3650 cm^{-1}.[3] This is reflected in Figure 1, spectrum C_1, in which the band at 3650 cm^{-1} is considerably weaker than in spectrum B_1.

B. OH Stretching Region of Zeolites Steamed At 540°. The additional bands at about 3600 and 3670–3690 cm^{-1},

which appear in the spectra of lanthanum Y zeolites steamed at 540°, are the result of chemical interaction between steam and the zeolite. These bands are not generated by physically adsorbed water, since no band could be detected in the 1640-cm^{-1} region of the spectra.

Absorption bands in the 3600- and 3700-cm^{-1} region occur in the spectra of steamed ammonium Y zeolites and have been related to framework dealumination.[7,10–12] The dealumination of LaY zeolites in the presence of steam has already been discussed.[6] It was shown that, under otherwise equal conditions, the most advanced dealumination can be expected in 24-LaY (540, stm) and the least dealumination in 98-LaY (540, stm).

If we assume that the band intensities at 3600 and 3670–3690 cm^{-1} reflect the degree of dealumination of the zeolitic framework, then the spectra shown in Figure 1 tend to support the concept outlined above. The two bands are the strongest in the spectrum of 24-LaY (540, stm), which has the lowest lanthanum content. Their intensities decrease with increasing lanthanum content, with the 3600-cm^{-1} band decreasing much faster. In the spectrum of 98-LaY (540, stm), only a relatively weak band can be seen at 3680 cm^{-1} and the band in the 3600-cm^{-1} region has almost disappeared. At constant lanthanum content, the thermal stability of the band in the 3600-cm^{-1} region is less than that at 3700 cm^{-1} (Figure 2).

As in the case of vacuum-calcined samples, the spectra of steamed samples show that the intensity of the 3540-cm^{-1} band increases with increasing lanthanum content in the zeolite. In 24-LaY (540, stm) this band is strong enough to appear as a shoulder, while it is almost undetectable in 24-LaY (540, v). The 3650-cm^{-1} band is also more intense in the spectrum of the steamed sample compared to the vacuum-calcined zeolite. These stronger absorptions are probably due to a suppression of dehydroxylation in the presence of steam and an increase of thermal stability of OH groups attached to the partially dealuminated framework. A similar phenomenon has been observed in the case of NH_4Y zeolites.[7]

The effect of increased lanthanum content on hydroxyl groups in steamed LaY zeolites has also been investigated by X-ray diffraction. A summary of nonframework species found in 24-LaY (540, stm) and 98-LaY (540, stm) from X-ray data is given in Table II (ref 6). Our structural investigation[6] has shown that in 24 LaY (540, stm) there is practically an equal number of lanthanum ions (in sites I') and oxygen species (in sites U) within the sodalite cages, at an interatomic distance of 2.21 Å between sites. The short La–O bond strongly suggests the existence of $La(OH)^{2+}$ species in the sodalite cage. The X-ray data indicate that the nonframework aluminum ions (about 4.5 Al^{3+} per unit cell) are not bonded to any nonframework species.

The occupancy of nonframework sites in 98-LaY (540, stm) is somewhat different. As more lanthanum ions occupy positions within the sodalite cages, the average La to La distance increases due to electrostatic repulsion. The repulsion causes the lanthanum ions to occupy average positions closer to the center of the hexagonal prism and thus reduces the average La–O3 bond distance from 2.62 to 2.46 Å (see Table V in ref 6).

The high concentration of lanthanum ions in the sodalite cages of 98-LaY (540, stm) could also explain the very high concentration of nonframework oxygen species. For each lanthanum ion we found about 1.5 nonframework oxygen atoms, located primarily in sites II'.

TABLE II: Occupancy of Nonframework Sites in 24-LaY (540, stm) and 98-LaY (540, stm)[a]

		24-LaY (540, stm)		98-LaY (540, stm)	
Sites	No. of sites per unit cell	No. of species per unit cell	Occupancy parameter	No. of species per unit cell	Occupancy parameter
SI	16				
SI'	32	6.8 La	0.21	21.1 La	0.66
SI*	32	4.5 Al	0.14		
SU	8	6.8 O_w	0.85	2.2 O_w	0.28
SII'	32			32.0 O_w'	1.00

[a] Reference

TABLE III: T–O Distances in Lanthanum Y Zeolites[a,b]

Distance, Å	24-LaY (540, v)	24-LaY (540, stm)	53-LaY (540, stm)	98-LaY (540, stm)
T-O1	1.73(4)	1.63(3)	1.64(2)	1.64(5)
T-O2	1.56(5)	1.56(4)	1.62(3)	1.64(5)
T-O3	1.85(5)	1.67(4)	1.70(3)	1.77(5)
T-O4	1.49(6)	1.59(4)	1.61(3)	1.59(6)

[a] Reference 6. [b] T represents Si or Al atoms. The numbers in parentheses represent the estimated standard deviation.

Infrared data strongly suggest that these oxygen species are hydroxyl groups, acting as electrostatic shields between lanthanum ions. The large number of these hydroxyl groups per sodalite cage suggests the existence of multiple (double and triple) OH bridges between La atoms in 98-LaY (540, stm). This is in agreement with the high intensity of the 3540-cm^{-1} band in the infrared spectrum of this material. The stabilizing role of lanthanum-bound OH groups probably accounts for the relatively high thermal stability of the corresponding infrared band in the spectra of steamed 98-LaY.

C. OH Region of Zeolites Steamed at 820°. The OH stretching region in the spectra of lanthanum Y zeolites steamed at 820° shows a very advanced degree of dehydroxylation, as expected at such high temperatures. Under these conditions, the absorption band at 3540 cm^{-1} appears the most stable of all the bands encountered in the OH stretching region of high-lanthanum LaY, reflecting the high stability of lanthanum-bound OH groups.

Low-lanthanum Y zeolites exhibit low thermal stability for the 3540-cm^{-1} band. This is due to the presence of framework-bound hydroxyls, as well as to the lesser stabilizing role of lanthanum-bound hydroxyls.

Rehydration of the zeolites steamed at 820° results only in a minor regeneration of hydroxyl groups (Figure 3). This suggests that the dehydroxylation of the zeolite during high-temperature steaming is largely an irreversible process, due to the structural changes in the zeolitic framework. Such framework modifications under steam can result from dealumination and possibly from a structural rearrangement as discussed in ref 6. It has been shown that rehydration of lanthanum Y samples calcined at 900° in the absence of steam gives rise to the expected hydroxyl bands.[5]

D. Location of OH Groups from X-Ray Data. The lengthening of Si(Al)–O distances has been used to assign the location of different OH groups in zeolites,[13,14] although bond distances obtained from X-ray powder data can involve relatively large errors. Table III shows the Si(Al)–O distances for several lanthanum Y zeolites.[6] The data for 24-LaY (540, v) suggest that the OH groups responsible for the bands at 3650 and 3540 cm^{-1} are generated primarily by O1 and O3 atoms, respectively. A comparison of distances obtained for 24-LaY (540, v) and 24-LaY (540, stm) indicates that additional OH groups formed during the steaming process contain O4 atoms. Such OH groups are located in the zeolitic supercages. Based on their interaction with pyridine (vide infra), we conclude that they generate the band in the 3670–3690-cm^{-1} region.

The location of OH groups responsible for the band at 3600 cm^{-1} is less certain. We have seen that the intensity of this band decreases faster than that of the 3690-cm^{-1} band when the lanthanum content of the zeolite increases. This could suggest that the OH groups corresponding to the 3600-cm^{-1} band are located in the sodalite cages of the zeolite and are attached to the framework. The available data do not allow a more accurate assignment.

The relatively large Si(Al)–O3 distance in 98-LaY (540, stm) is due to the close proximity of lanthanum ions, and not to a large concentration of hydrogen atoms attached to O3 atoms.

E. Acidity of OH Groups in LaY. The acidity of different OH groups in LaY zeolites can be evaluated from their interaction with NaOH, NH_3, and pyridine (Figures 4–7). The nearly complete disappearance of the 3540-cm^{-1} band after NH_3 adsorption in the spectrum of 24-LaY (400, v) indicates that it is generated mainly by acidic OH groups attached to the framework, similar to those encountered in NH_4Y zeolites. The OH groups attached to lanthanum are not acidic and account for the band remaining after NH_3 adsorption. An increase in the number of lanthanum ions in the zeolite increases the number of these nonacidic hydroxyls. Hence the intense 3540-cm^{-1} band in 98-LaY (400, v) remains practically unaffected by NH_3. In an intermediate lanthanum level zeolite, 53-LaY (540, stm), this band shows its partially acidic nature since its intensity decreases when treated with 0.1 N NaOH. A shift of this band toward higher frequency after NaOH addition could reflect changes in the local electrostatic field resulting from the reaction between sodium hydroxide and other OH groups. The band in the 3540-cm^{-1} region in all LaY zeolites is unaffected by pyridine adsorption, since the OH groups responsible for this band are located in the sodalite cages where they are inaccessible to this organic base.

The band at 3600 cm^{-1} in the spectrum of 53-LaY (540, stm) disappears when treated with 0.1 N NaOH, revealing its acidic character. This effect was also observed in the spectra of steamed NH$_4$Y zeolites.[7,10] The band was regenerated by ammonium salt treatment suggesting that the OH group was not eliminated by reaction with NaOH but underwent an ion exchange process in which the protons were replaced by sodium ions. However, the 3600-cm^{-1} band is unaffected by NH$_3$ indicating the weakly acidic nature of this OH group. The band is also unaffected by pyridine adsorption, due to both weak acidity and inaccessibility of these OH groups.

The strong interaction of the 3650-cm^{-1} band with 0.1 N NaOH, NH$_3$, and pyridine reflects the strong acidity of this band, which disappears upon the addition of any of these bases. The effect of pyridine on this band in both vacuum and steamed samples indicates that this hydroxyl group is obviously located in the zeolite supercage. The 3650-cm^{-1} band in the alkali-treated 53-LaY (540, stm) sample is regenerated by ammonium salt treatment.

The band in the 3670–3700-cm^{-1} region in 24-LaY (540, stm) and 53-LaY (540, stm) appears to be composite in nature. After sodium hydroxide and pyridine treatment, a nonacidic component near 3700 cm^{-1} becomes more distinct. The acidic component predominates in 98-LaY (540, stm) and disappears after pyridine adsorption. These results tend to support our conclusion that the OH groups responsible for the band in this region are located in the supercages.

Finally, the decreased intensity observed for the silanol band at 3750 cm^{-1} after pyridine adsorption is probably due to a weak hydrogen bond type interaction. The band appears also to be affected in this way by NH$_3$ adsorption.

F. Effect of Zeolite on Adsorbed Pyridine Spectra. The presence of a band at 1545 cm^{-1} in the spectra of adsorbed pyridine indicates the presence of Brϕnsted acidity in all the zeolite samples, even in those steamed at 820° (Figures 8 and 9). These spectra also show the presence of two species of Lewis-bound pyridine: one characterized by the band at 1455 cm^{-1}, which is indicative of the presence of tricoordinated framework aluminum; the other evidenced by a band at 1445 cm^{-1}, which is due to a pyridine–cation bond. An increase in lanthanum content and higher steaming temperature increases the density of species characterized by the 1445-cm^{-1} band, with a corresponding decrease in the density of species characterized by the 1455-cm^{-1} band.

The absence of a band at 1445 cm^{-1} in the spectra of vacuum-calcined materials at 540° indicates the absence of lanthanum cations in the supercages of these zeolites. Among the lanthanum Y zeolites steamed at 540°, only 98-LaY (540, stm) shows a band at about 1445 cm^{-1}, suggesting the presence of some lanthanum ions in the supercage. However, lanthanum ions could not be detected in the supercages of 98-LaY (540, stm) by X-ray diffraction, and we therefore assume that their presence in supercages is marginal. Since the spectra of pyridine adsorbed on 24-LaY (540, stm) and 53-LaY (540, stm) do not show a band in the 1445-cm^{-1} region, we conclude that neither lanthanum nor cationic aluminum species are located in the supercages of these samples. Structural X-ray data support this assumption.[6]

All the spectra of pyridine adsorbed on samples steamed at 820° show the presence of a band at 1445 cm^{-1}, indicating the presence of cationic species in the supercages of these materials. The intensity of this band increases with increasing lanthanum content, reflecting the higher concentration of lanthanum ions in the zeolite supercages. Since the framework dealumination process under steam is fairly advanced at 820°, it is conceivable that some of the nonframework aluminum species will also end up in the supercage.

References and Notes

(1) J. A. Rabo, C. L. Angel, and V. Schomaker, *Proc. Int. Congr. Catal., 4th, 1968* (1971).
(2) J. W. Ward, *J. Phys. Chem.,* 72, 4211 (1968).
(3) A. P. Bolton, *J. Catal.,* 22, 9 (1971).
(4) R. Mone and L. Moskou, 3rd International Conference on Molecular Sieves, Zurich, Switzerland, 1973. Preprint no. 154.
(5) D. Ballivet, P. Pichat, and D. Barthomeuf, *Adv. Chem. Ser.,* No. 121, 469 (1973).
(6) J. Scherzer and J. L. Bass, *J. Phys. Chem.,* preceding paper in this issue.
(7) J. Scherzer and J. L. Bass, *J. Catal.,* 28, 101 (1973).
(8) P. B. Venuto, L. A. Hamilton, P. S. Landis, and J. J. Wise, *J. Catal.,* 5, 484 (1966).
(9) L. G. Christner, B. V. Liengme, and W. K. Hall, *Trans. Faraday Soc.,* 1679 (1968).
(10) P. Jacobs and J. B. Uytterhoeven, *J. Catal.,* 22, 193 (1971).
(11) J. B. Peri, *Catal., Proc. Int. Congr., 5th, 1972,* 18, 329 (1972).
(12) R. Beaumont, P. Pichat, D. Barthomeuf, and Y. Tramtouze, *Catal., Proc. Int. Congr., 5th, 1972,* 19, 343 (1972).
(13) D. H. Olson and E. Dempsey, *J. Catal.,* 13, 221 (1969).
(14) P. Gallezot and B. Imelik, *C. R. Acad. Sci., Ser. B,* 271, 912 (1970).
(15) P. Jacobs and J. B. Uytterhoeven, *J. Chem. Soc., Faraday Trans. 1,* 69, 373 (1973).

Calculation of Pseudocontact Shifts for Co(CH₃OH)₅X²⁺ Complexes

Jerry Goodisman

Department of Chemistry, Syracuse University, Syracuse, New York 13210 (Received October 16, 1974)

In this article, we calculate pseudocontact shifts for tetragonal high-spin Co(II) complexes using a crystal field model. Calculated results for the dipolar field strength and its variation with temperature are compared with values derived from experimental measurements on complexes of the form Co(CH₃OH)₅X²⁺. The calculation involves evaluation of the anisotropy of the magnetic susceptibility, and proceeds by the following steps: (a) from the crystal field parameters Dq, Ds, Dt, and B the three orbital wave functions of lowest energy are found. (b) The effect of spin–orbit coupling over the 12 states (three orbital wave functions coupled with four spin states) is evaluated. (c) The parallel and perpendicular components of the magnetic susceptibility are calculated, considering only these 12 states but taking into account thermal populations. It is shown that good numerical agreement can be obtained with experimental results for the dipole field strength and its temperature dependence. However, the calculations show that the linearity found when pseudocontact shifts are plotted against reciprocal temperature is only apparent, making simple interpretations, or extrapolation of the plots so obtained, meaningless.

I. Introduction

The pseudocontact or dipolar shift, caused by the proximity to the nucleus studied of a paramagnetic center in an anisotropic environment, has recently been an extremely active field of research, both theoretical and experimental.[1] Much of this work involves the use of the pseudocontact shift and "shift reagents" in studies of molecular structure and bonding. However, it has been emphasized by many authors in this field that pseudocontact shift studies are often fraught with ambiguity, so that theoretical studies which can be of help in adding to our understanding of the effect are still welcome.

Recent studies by Vriesenga and coworkers[2] measured contact NMR shifts for the cis and trans methanol methyl resonances of a series of Co(CH₃OH)₅X²⁺ complexes. In these systems, many of the ambiguities connected with interpretation of the spectra and of the shifts, which enter other studies, are absent. We have discussed a method[3] of separating the observed shifts into Fermi contact and pseudocontact contributions. The pseudocontact shift for nucleus i is given as

$$\nu_i^{\,\text{D}} = -D \left\langle \frac{3\cos^2 \chi_i - 1}{r_i^3} \right\rangle \nu_0 \qquad (1)$$

where the triangular bracket is the average over internal vibrations and rotations of a factor depending on the location of nucleus i relative to the paramagnetic center. (Here, ν_0 is the resonance frequency, 100 MHz.) By calculating this, we derived values of D for the Co(CH₃OH)₅X²⁺ complexes.

Subsequently, experimental information was obtained on D as a function of temperature.[4] Some of this data are given in section V (see eq 22 and Table II). The apparent straight lines obtained when D was plotted against $1/T$ suggested a simple qualitative explanation of the pseudocontact shifts in terms of a crystal field model for the paramagnetic ion. The value of D depends on the anisotropy of the magnetic susceptibility of this ion. Normally, magnetic susceptibilities consist of a term proportional to $1/T$ (the "g factor" term) and a term independent of T (the "high-frequency" term). Both are calculable within the crystal field model. Furthermore, plots of shifts $\nu_i^{\,\text{D}}$ for cis and trans protons vs. $1/T$, extrapolated to low values of $1/T$, crossed for positive values of $1/T$.

We now believe that the thermal population of excited levels is important, and that the straight lines on the $\nu_i^{\,\text{D}}$ vs. $1/T$ plots are only apparent, so that extrapolation to a crossing point is not meaningful. However, calculations with the crystal field model using reasonable values for the parameters led to values in accord with experiment for D and its variation with temperature for the region for which experimental measurements were made.

This means that, at least in the present case, pseudocontact shifts can be explained in a crystal field framework. It should be emphasized that the number and quality of measured shifts, plus the simple and well-known geometries of the methanol complexes, make the available information on D more reliable and extensive than for most other systems studied. Obtaining exact agreement with experiment is not our principal goal, since the exact values of the parameters used in the calculation cannot be determined independently. Thus, only a few complete calculations are given.

We are more interested in explaining the signs, magnitudes, and temperature dependencies of the shifts in different Co(CH₃OH)₅X²⁺ complexes. As late as 1971, Forster[5] could note that, while the importance of the pseudocontact contributions to NMR shifts of Co complexes had been clearly demonstrated, the explanation of the signs and magnitudes of the shifts was as yet lacking.

Of course, other calculations of D for various systems have been performed. Gerloch and Mackey[6] performed calculations of energy levels and magnetic moments for ytterbium (f¹³) and cerium (f¹) ions as a function of spectroscopic and other parameters, using a crystal field model. Values of the parameters were determined to fit experimentally measured susceptibilities. Subsequently, these authors systematically extended[7] this work to other lanthanide ions: terbium (f⁸), neodymium (f³), erbium (f¹¹), thulium, (f¹²), europium (f⁶), praseodymium (f²), and dysprosium (f⁹). Similar calculations on lanthanides were recently present-

ed by Golding and Pyykkö.[8] Using a generalization of a theory developed by Bleaney,[9] pseudocontact shifts and their temperature dependence were calculated and compared to experiment. Bleaney[9] used a spin hamiltonian to take into account zero field splitting due to the crystal field. His theory considers only the thermally accessible states, but corrections for neglect of higher states in the high-frequency susceptibility are estimated. The sign of D and relative magnitudes for different lanthanides are predicted and experimental evidence confirms the predictions.

Extensive ligand field calculations on tetragonal low-spin cobalt(II) phthalocyanine derivatives were performed by Engelhardt and Green.[10] (Our compounds are tetragonal high-spin.) Kurland and McGarvey[11] carried out calculations of pseudocontact shifts for some theoretically simple cases to illustrate their theoretical discussion. McGarvey[12] used the Kurland–McGarvey formulas (see below) to calculate contact and pseudocontact shifts in trigonal Co(II) complexes. As we do below, McGarvey found the high-frequency terms comparable in size to the g factor terms. Using values of spin–orbit coupling parameters and energy level splittings employed by Jesson[13] for related compounds, McGarvey[12] calculated D at 30° in good agreement with a measured value. Contributions of excited electronic energy levels (except those from the lowest crystal field terms) were neglected, as we do below. Jesson[13] had, in an ad hoc way, corrected g values to take this into account and also corrected the spin–orbit coupling for covalency, but McGarvey found the corrections largely cancelled. LaMar et al.[14] measured temperature dependence of shifts and found excellent agreement with McGarvey's results.

Their studies, of the temperature dependence of pseudocontact shifts in trigonal Co(II) complexes, considered particularly the deviations from a Curie law (L proportional to T^{-1}). They emphasized that one must have results at a series of temperatures in order to demonstrate agreement of theory with experiment, as they did using McGarvey's theory.[12] The temperature dependence of pseudocontact shifts due to Yb(DPM)$_3$ was studied by Beauté et al.,[15] who found that straight lines were obtained by plotting shifts vs. $T^{-1/2}$, and that there always existed a value of T for which the shifts were nearly zero. They explained the $T^{-1/2}$ behavior in terms of formation of a collision-type complex. Perry and Drago,[16] discussing the temperature dependence of contact shifts, considered a number of possible causes for nonzero intercepts in plots of shifts against T^{-1}.

For some trigonal Co(II) systems, Jesson[17] calculated D using values for g factors obtained from solid state EPR data. He noted the importance of thermal population of low-lying states but did not consider high-frequency terms in the susceptibility. Other workers have continued to use this technique, although possible sources of error in using solid-state data for species in solution are recognized. Pseudocontact shifts for tetrahedral Ni(II) and Co(II) complexes, low-spin trigonal Co(II) complexes, as well as other species, have thus been predicted.[18] Data on magnetic properties from EPR and on level spacings from spectroscopy may also be used for such predictions, and good agreement with experiment is found.[14]

In the next section, we review the theory needed for the calculation of pseudocontact shifts due to Co(II) in a tetragonal environment, in the framework of a crystal field model. Subsequent sections give analysis of the secular equations with an aim of showing how the calculated values of D arise from crystal field and other parameters. In sec-

tion V, we consider the dependence of D on temperature and give some results of a complete calculation.

II. Theory

The basic theory of the pseudocontact shifts for tumbling molecules was formulated by McConnell and Robertson.[19] Additions to the theory, to take into account different relative time scales for electronic relaxation, molecular tumbling, and the Zeeman anisotropy energy; high-frequency terms in the susceptibilities; and thermal population of excited states, were given by LaMar,[20] by Jesson,[21] and by Kurland and McGarvey.[11] Different formulas for the pseudocontact shift, differing in the expression for the dipolar field strength, are obtained for different relative time scales. Because of the fast electronic relaxation, the Co^{2+} complexes discussed in the present work fall under the "solid-state" case, wherein $1/\tau \ll |g_\parallel - g_\perp|\mu_B/H\hbar^{-1}$ and $T_{1e} \ll \tau$. Here, τ is the tumbling correlation time, T_{1e} the electronic relaxation time, $g_\parallel - g_\perp$ the anisotropy in g factors, and μ_B the Bohr magneton.

Kurland and McGarvey,[11] following an earlier suggestion by Horrocks et al.,[22] gave the dipolar field strength in terms of the principal components of the magnetic susceptibility, and emphasized the importance of the paramagnetic, or high-frequency terms. They carried out calculations for orbital singlets. Their theory, which was extended and used successfully by McGarvey[12] (see preceding section), included thermal population of several states, zero-field splitting, and a ligand contribution to the pseudocontact shift. Horrocks et al.[22] investigated components of the susceptibility for some Co compounds, including measurements of the solid state, wherein the parallel and perpendicular components can be measured separately. Forster[5] obtained pseudocontact shift data for trans Co(py)$_4$X$_2$ and Co(γ-pic)$_4$X$_2$ complexes, and deduced $g_\parallel > g_\perp$ for X = Cl or NCS, $g_\parallel < g_\perp$ for X = I or Br. Buckingham and Stiles[23] generalized the pseudocontact shift formulas to include higher magnetic moments than dipole moments.

We shall consider only magnetic dipoles, but include thermal population of excited levels and the temperature-independent terms in the susceptibility. The agreement of the experimental results of LaMar et al.[14] on trigonal Co(II) complexes with the calculations[12] based on the Kurland–McGarvey theory[11] shows that both effects make extremely important contributions. Presumably, our system really possesses axial symmetry, so that complications due to deviations from such symmetry[21,24] are ignored.

With the values of time constants that obtain for our systems, the origin of the pseudocontact shifts may be thought of as follows. For each orientation of the molecule in the magnetic field, a magnetic dipole moment, proportional to the field and to the magnetic susceptibilities, is induced at the paramagnetic center (metal ion), which in turn leads to an additional magnetic field at a proton. Because of the asymmetric environment of the paramagnetic center, the induced moment is generally not in the direction of the field, and averaging over all orientations of the molecule does not lead to a zero result. Instead, one obtains a net shift proportional to the asymmetry of the magnetic susceptibility of the paramagnetic center.

In general, the pseudocontact shift for a proton in a molecule becomes a product of a geometric factor, which depends on the proton's position, and a dipolar field factor, which is the same for all protons in the molecule. The latter factor is the subject of our calculations; for our systems,

this requires the anisotropy of the magnetic susceptibility, $\chi_\parallel - \chi_\perp$, where $\parallel$ and $\perp$ refer to the fourfold symmetry axis of the monosubstituted tetragonal complex.

The susceptibilities have temperature-independent (high-frequency) and temperature-dependent (g factor) parts for a given electronic state. The formula (eq 2) for the

$$\chi_\parallel - \chi_\perp = \frac{J(J + 1)(g_\parallel{}^2 - g_\perp{}^2)\mu_B{}^2}{3kT} +$$

$$\sum_j{}' 2\frac{|\langle j|L_z + 2S_z|i\rangle|^2 - |\langle j|L_x + 2S_x|i\rangle|^2 \mu_B{}^2}{E_j - E_i} \quad (2)$$

anisotropy of the susceptibility for a single state must in general be multiplied by a Boltzmann weighting factor and summed over occupied states. In eq 2, J is the effective spin for a level and will generally be ½ (Kramers' doublet), μ_B is the Bohr magneton, and the sum is over states j not including i, with energy E_j. Also, $g_\parallel$ and $g_\perp$ are the g values for the state in the parallel and perpendicular directions, while L_z and S_z (L_x and S_x) are the orbital and spin angular momentum operators in the parallel (perpendicular) directions. The diamagnetic contributions to the susceptibilities

$$H = (7/2)Ds$$

$$I = (35/8)Dt$$

If one agrees to use the free-ion value for B and the value obtained for the octahedral hexamethanol complex for Dq, two free parameters, describing the degree of tetragonality, remain. It is common to obtain Dt from the Dq values of the axial (z) and equatorial (x) ligands in a monosubstituted octahedral complex according to the formula[27]

$$Dt = \frac{2}{7}(Dq_x - Dq_z) \quad (3)$$

Unfortunately, in the present case Dq values for the ligands considered are insufficiently known with Co^{2+}. The parameter Ds can be shown to be proportional to Dt for a simple point charge model,[28] the constant of proportionality depending on the metal; we have estimated $Ds \sim 1.42Dt$. Such a proportionality holds in the vast majority of cases that have been studied, but exceptions to the rule exist as well.[29]

In terms of the parameters Dq, Ds, Dt, and B, the two secular equations of AP are given in eq 4a and 4b. The or-

$$\phi_z \quad \begin{bmatrix} -6Dq + 6Dt - \dfrac{4}{5}Ds & 4Dq - 4Dt + \dfrac{12}{5}Ds \\[2mm] 4Dq - 4Dt + \dfrac{12}{5}Ds & 15B + \dfrac{14}{5}Ds \end{bmatrix} \quad (4a)$$

$$\pi_z$$

$$\phi_x \quad \begin{bmatrix} -6Dq + \dfrac{9Dt}{4} + \dfrac{2}{5}Ds & 4Dq - \dfrac{3}{2}Dt - \dfrac{6}{5}Ds & -\sqrt{\dfrac{3}{5}}\left(Ds + \dfrac{5}{4}Dt\right) \\[3mm] 4Dq - \dfrac{3}{2}Dt - \dfrac{6}{5}Ds & 15B - \dfrac{7}{5}Ds & -\sqrt{\dfrac{3}{5}}\left(2Ds + \dfrac{5}{2}Dt\right) \\[3mm] -\sqrt{\dfrac{3}{5}}\left(Ds + \dfrac{5}{4}Dt\right) & -\sqrt{\dfrac{3}{5}}\left(2Ds + \dfrac{5}{2}Dt\right) & 2Dq + \dfrac{7}{4}Dt \end{bmatrix} \quad (4b)$$

$$\pi_x$$

$$\psi_x$$

have been ignored; they are easily shown to be very small compared to the others.

The formalism needed for computation of $\chi_\parallel - \chi_\perp$ in the case of high-spin tetragonal Co^{2+} complexes (as well as complexes with trigonal symmetry) has almost all been given by Abragam and Pryce.[25] The Co^{2+} ion, with seven d electrons, has a ^4F ground term, and a relatively low-lying ^4P term ($\sim$14,000 cm^{-1} above the ground term) arising from the same configuration. In the presence of an octahedral field, there is significant mixing of the three states of the ^4P term (of orbital symmetry T_{1g}) with the states of the ^4F term. When a tetragonal field is added, one obtains two low-lying energy levels, one singly degenerate and one doubly degenerate, from the lowest T_{1g} state. The effect of spin–orbit coupling on the 12 states arising from the coupling of the two low-lying levels with the spin quartet is to give six Kramers' doublets, spread over an energy range of the order of 10^3 cm^{-1}. We will use these states for the calculation of $\chi_\parallel$ and $\chi_\perp$.

Let us consider the above with attention to the parameters that enter. The difference in energy between the free ion ^4P and ^4F terms is designated by Abragam and Pryce[25] (henceforth referred to as AP) as E_p; a more common nomenclature is $15B$. The parameters for the crystal field used by AP are G (for the octahedral field), H, and I (for the tetragonal part). In terms of the more usual quantities[26] for describing a tetragonal field

$$G = 21Dq - (49/4)Dt$$

bital functions π arise from the excited P term and the others from the F term, with ϕ being the T_{1g} species and ψ the T_{2g} species. The ϕ_y, π_y, and ψ_y functions of course have a secular equation identical with the x; the remaining two functions (χ and ψ in AP's notation) are of symmetries A_{2g} and B_{1g} and hence not mixed in the tetragonal field. The solution of the secular equations gives, as wave functions for the lowest level of each secular equation

$$\phi_x{}' = \epsilon\phi_x - \tau\pi_x - \rho\psi_x, \quad \text{energy } E_x \quad (5a)$$

$$\phi_z{}' = \epsilon'\phi_z - \tau'\pi_z, \quad \text{energy } E_z \quad (5b)$$

The energy difference $E_z - E_x$ is denoted by Δ.

The perturbation hamiltonian for spin–orbit coupling, $\lambda \mathbf{L}\cdot\mathbf{S}$, is now introduced. The value of the spin–orbit coupling constant λ is so far not known. One has to diagonalize $\lambda \mathbf{L}\cdot\mathbf{S}$ over the 12 states formed from coupling $\phi_x{}'$, $\phi_y{}'$, and $\phi_z{}'$ with the spin states for $m_s = \pm 1/2$ and $\pm 3/2$. By forming from $\phi_x{}'$ and $\phi_y{}'$ the symmetric and antisymmetric combinations, AP achieve a simplification in the secular equation. If the symmetric and antisymmetric combinations are assigned fictitious magnetic quantum numbers m_l of 1 and -1, and $\phi_z{}'$ the quantum number m_l of 0, the spin–orbit operator, operating on these 12 states, may be shown to be equivalent to

$$-\alpha\lambda L_z S_z - \alpha'\lambda(L_x S_x + L_y S_y)$$

with

$$\alpha = \frac{3}{2}\epsilon^2 - \sqrt{15}\epsilon\rho + \frac{1}{2}\rho^2 - \tau^2 \quad (6a)$$

$$\alpha' = \frac{3}{2}\epsilon\epsilon' + \frac{1}{2}\sqrt{15}\epsilon'\rho - \tau\tau' \qquad (6b)$$

The effective hamiltonian is written as

$$W = \Delta(1 - L_z^2) - \alpha\lambda L_z S_z - \alpha'\lambda(L_x S_x + L_y S_y) \quad (7)$$

The 12 × 12 matrix of W actually breaks down into six blocks, corresponding to values of m, the eigenvalue of $L_z + S_z$, equal to 5/2, 3/2, 1/2, -1/2, -3/2, -5/2. The dimensions of the blocks are, respectively, 1, 2, 3, 3, 2, 1; and the first three are identical with the last three.

At this level, there are thus three parameters: Δ, $\alpha\lambda$, and $\alpha'\lambda$. The free-ion value of λ is about -180 cm^{-1}, while α and α' turn out to be about 1.4. Of course Δ, α, and α' are calculable from a knowledge of B, Dq, Ds, and Dt. It is well known that in using the ligand field model it is generally necessary to reduce λ from the free ion value.[26,30] A reduction of about 20% for Co^{2+} seems appropriate.[30]

It is convenient to express energies in units of $\alpha\lambda$ (a negative quantity). Letting $d = \Delta/\alpha\lambda$ and $c = (\alpha'/\alpha) - 1$, the secular equations have the following forms (the states are labeled with m_l and m_s):

$$m = \pm\frac{5}{2}: \left[\begin{array}{c} -\frac{3}{2} \end{array}\right] \pm 1 \ \pm\frac{3}{2} \qquad (8a)$$

$$m = \pm\frac{3}{2}: \left[\begin{array}{cc} d & -\sqrt{\frac{3}{2}}(c+1) \\ -\sqrt{\frac{3}{2}}(c+1) & -\frac{1}{2} \end{array}\right] \begin{array}{c} 0 \ \pm\frac{3}{2} \\ \pm 1 \ \pm\frac{1}{2} \end{array} \qquad (8b)$$

$$m = \pm\frac{1}{2}: \left[\begin{array}{ccc} \frac{3}{2} & -\sqrt{\frac{3}{2}}(c+1) & 0 \\ -\sqrt{\frac{3}{2}}(c+1) & d & -\sqrt{2}(c+1) \\ 0 & -\sqrt{2}(c+1) & \frac{1}{2} \end{array}\right] \begin{array}{c} \pm 1 \ \pm\frac{3}{2} \\ 0 \ \pm\frac{1}{2} \\ \pm 1 \ \pm\frac{3}{2} \end{array} \qquad (8c)$$

The anisotropy is expressed by the values of c and d; in octahedral symmetry $c = d = 0$. The state of lowest energy corresponds to the highest eigenvalue of these matrices. Clearly, the higher eigenvalue for $m = \pm 3/2$ is higher than that for $m = \pm 5/2$, while that for $m = \pm 1/2$ is the highest, as can be seen by comparing its upper left 2 × 2 block with the $m = \pm 3/2$ submatrix. Therefore, the lowest energy, which is obtained from the eigenvalue by multiplication by the negative quantity $\alpha\lambda$, arises from the $m = \pm 1/2$ block.

Having determined the six eigenvalues and eigenvectors for the Kramers' doublets, we can use them to calculate $\chi_{\parallel}$ and $\chi_{\perp}$ for any of them by eq 2. The g values are simply

$$g_{\parallel} = 2\langle i_+ | L_z + 2S_z | i_+\rangle \qquad (9a)$$

$$g_{\perp} = 2\langle i_+ | L_x + 2S_x | i_-\rangle \qquad (9b)$$

where i_+ and i_- are the two members of the Kramers' doublet. A correction must be made to take into account mixing in, by the spin-orbit coupling, of orbital states with energies above the ϕ' states (eq 5). This is discussed by AP, who find corrections of a few percent, which represents the size of the ratio of $|\alpha\lambda|$ to the energy difference, i.e. ~250/9000. We shall neglect these corrections to $g_{\parallel}$ and $g_{\perp}$ (see ref 25, 12, and 13). Correspondingly, we neglect contributions of higher orbital states to the high-frequency terms of the susceptibility, so that both i and j in eq 2 will always be members of the set of six Kramers' doublets. This and the use of a crystal field formalism are the basic approximations in our calculations.

To go from the parameters Ds and Dt to susceptibilities requires, in the present models, solution of two secular equations. The first is eq 4, and produces calculated values of α, α', and Δ, from which $c = (\alpha'/\alpha) - 1$ and $d = \Delta/(\alpha\lambda)$ are calculated; this will be discussed in section III. The second secular equation, eq 8, leads to wave functions from which magnetic properties are calculated, and will be considered in section IV.

III. The Parameters c and d

We consider the secular eq 4 for ϕ_x' and ϕ_z', assuming that values are known for B, Dq, Ds, and Dt. Calculating Dt from estimated values of the substituent and of methanol (eq 3), we find relatively small values for all the cases of interest to us. For example, estimated values[32] of Dq for CH$_3$OH and γ-picoline are 900 and 1100 cm^{-1}, respectively, so that $Dt = -57$ cm^{-1}. The value of Ds is estimated as $1.42Dt = -81$ cm^{-1} according to an interpolation formula[28] for the Ds/Dt ratio. Similarly, Dt is estimated as 1 cm^{-1} for DMSO and -2 cm^{-1} for H$_2$O. We can therefore say that we are always dealing with cases of low tetragonality. This allows a perturbative treatment of the effect of Ds and Dt. We first neglect Ds and Dt in (4) and solve the resulting 2 × 2 secular equations, yielding energies E_1 and E_2 ($E_1 < E_2$) and corresponding eigenvectors (coefficients) (a, b) and $(b, -a)$. Here, $a^2 + b^2 = 1$, and the values of a and b depend on the values of B and Dq. For the reasonable values, $B = 825$ cm^{-1} and $Dq = 900$ cm^{-1}, $a \sim 0.98$ and $b \sim -0.20$. We now transform the secular equations for x and z to the basis of these eigenvectors.[33] The lowest eigenvalues of each matrix may now be evaluated by perturbation theory to second order. It is in each case the upper left diagonal matrix element plus a sum of squares of first-row off-diagonal elements divided by differences of diagonal elements. In calculating Δ, E_1 cancels out as expected. Performing the necessary algebra we obtain

$$\Delta = a^2\left(\frac{15}{4}Dt - \frac{6}{5}Ds\right) + 2ab\left(-\frac{5}{2}Dt + \frac{18}{5}Ds\right) + b^2\left(\frac{21}{5}Ds\right) \qquad (10)$$

after dropping second-order terms in Ds and Dt.

We expect ab to be negative; a^2 and b^2 are of course positive. Let us write K for the ratio Ds/Dt; we expect K to be about 1.4. With $a = 0.98$ and $b = -0.20$, the first-order terms become $(4.5 - 2.4\,K)Dt$. Thus Δ has the sign of Dt unless K is unexpectedly large and positive. With $K = 1.42$, Δ has about the numerical value of Dt. That the first-order terms suffice is shown by the case of γ-picoline, for which the exact calculation for $K = 1.42$, using the secular equations, gave $\Delta = -66$ cm^{-1}, while the above formula yields -68 cm^{-1}. It may be repeated that Δ and Dt will not have the same signs if K is greater than 1.9, as is the case[31] for Cu^{2+}.

We now consider the α' to α ratio and the value of c by a similar method. The coefficients ϵ, τ, ρ, ϵ', and τ' are computed by first-order perturbation theory. The eigenfunctions, written as column vectors, are, from (4a) for ϕ_z'

$$\binom{a}{b} + \frac{ab\left(6Dt - \frac{18}{5}Ds\right) + (b^2 - a^2)\left(-4Dt + \frac{12}{5}Ds\right)}{E_1 - E_2}\binom{b}{-a} \qquad (11a)$$

and, from (4b) for ϕ_x

$$\begin{pmatrix} a \\ b \\ 0 \end{pmatrix} +$$

$$\frac{ab\left(\dfrac{9Dt}{4} + \dfrac{9Ds}{5}\right) - (b^2 - a^2)\left(\dfrac{-3Dt}{2} - \dfrac{6Ds}{5}\right)}{E_1 - E_2}\begin{pmatrix} b \\ -a \\ 0 \end{pmatrix} +$$

$$\frac{-\sqrt{\dfrac{3}{5}}(a + 2b)\left(Ds + \dfrac{5}{4}Dt\right)}{E_1 - 2Dq}\begin{pmatrix} 0 \\ 0 \\ 1 \end{pmatrix} \quad (11b)$$

From these, the parameters of eq 5 can be read off directly, for evaluation of α and α' using eq 6. We keep terms to first order, and, after considerable algebra, obtain

$$c =$$

$$\frac{a^2b^2\left(\dfrac{75}{8}Dt - \dfrac{27}{2}Ds\right) + (ab^3 - a^3b)\left(9Ds - \dfrac{25}{4}Dt\right)}{\left(\dfrac{3}{2}a^2 - b^2\right)(E_1 - E_2)} -$$

$$\frac{a(a + 2b)\left(\dfrac{9}{2}Ds + \dfrac{45}{8}Dt\right)}{\left(\dfrac{3}{2}a^2 - b^2\right)(E_1 - 2Dq)} \quad (12)$$

For γ-picoline, with the parameter values quoted above, this formula gives $c = -0.033$, to be compared to the exact value (from secular equations) of -0.035.

In considering the sign of c, we find that the expression is dominated by the second term. The denominator is clearly negative, while $a(a + 2b)$ is positive. Therefore c should have the sign of Ds and Dt; if Ds and Dt have different signs, their relative magnitudes determine which sign dominates. With $a = 0.98$, $b = -0.2$, and $Dq = 900$ cm^{-1}, the second term gives

$$c = 23 \times 10^{-5}\left(K + \frac{5}{4}\right)Dt \text{ (cm}^{-1}) \quad (13)$$

which, for our γ-picoline data, yields $c = -0.035$.

Therefore, we expect c and Δ to have the sign of Ds and Dt. This means c and $d = \Delta/\alpha\lambda$ should have opposite signs. Both c and d may be considered, under these circumstances, as reflecting the relative crystal field strengths of the substituent and methanol.

IV. Susceptibilities for Low Asymmetry

We now turn to the secular eq 8, where both c and d are small compared to unity, signifying that the tetragonality is low. The states used as basis for these secular equations are products of spin functions for spin 3/2 and spatial functions over which the orbital angular momentum matrices are known. The secular eq 8 break down into blocks[25] by $m = m_l + m_s$, and the matrices of $L_z + 2S_z$ and $L_x + 2S_x$ are easily calculable in this basis. The former is diagonal in m, and the latter has nonvanishing elements between functions differing by unity in m.

To obtain the eigenfunctions, we again resort to perturbation theory. If $c = d = 0$ (pure octahedral symmetry) the secular equations may be solved exactly to give the eigenfunctions and energies (m values in parentheses) of Table I. The basis functions are labeled by the eigenvalues m_l and m_s; overbars represent minus. Since $\alpha\lambda$ is negative, the lowest energy is $(5/2)\alpha\lambda$. As long as c and d are small, the pres-

TABLE I: Eigenfunctions and Eigenvalues of the Secular Eq 8 for Octahedral Symmetry ($c = d = 0$)

Eigenfunction	Eigen-value	Value of m
$\|1\tfrac{3}{2}\rangle$	$\dfrac{-3}{2}\alpha\lambda$	$\left(\dfrac{5}{2}\right)$
$\sqrt{\dfrac{3}{5}}\,\|1\tfrac{1}{2}\rangle + \sqrt{\dfrac{2}{5}}\,\|0\tfrac{3}{2}\rangle$	$\dfrac{-3}{2}\alpha\lambda$	$\left(\dfrac{3}{2}\right)$
$\sqrt{\dfrac{2}{5}}\,\|1\tfrac{1}{2}\rangle - \sqrt{\dfrac{3}{5}}\,\|0\tfrac{3}{2}\rangle$	$1\alpha\lambda$	$\left(\dfrac{3}{2}\right)$
$\sqrt{\dfrac{1}{10}}\,\|\bar{1}\tfrac{3}{2}\rangle + \sqrt{\dfrac{6}{10}}\,\|0\tfrac{1}{2}\rangle + \sqrt{\dfrac{3}{10}}\,\|1\tfrac{\bar{1}}{2}\rangle$	$\dfrac{-3}{2}\alpha\lambda$	$\left(\dfrac{1}{2}\right)$
$\sqrt{\dfrac{6}{15}}\,\|\bar{1}\tfrac{3}{2}\rangle + \sqrt{\dfrac{1}{15}}\,\|0\tfrac{1}{2}\rangle - \sqrt{\dfrac{8}{15}}\,\|1\tfrac{\bar{1}}{2}\rangle$	$1\alpha\lambda$	$\left(\dfrac{1}{2}\right)$
$-\sqrt{\dfrac{1}{2}}\,\|1\tfrac{3}{2}\rangle + \sqrt{\dfrac{1}{3}}\,\|0\tfrac{1}{2}\rangle - \sqrt{\dfrac{1}{6}}\,\|1\tfrac{1}{2}\rangle$	$\dfrac{5}{2}\alpha\lambda$	$\left(\dfrac{1}{2}\right)$
$-\sqrt{\dfrac{1}{2}}\,\|1\tfrac{3}{2}\rangle + \sqrt{\dfrac{1}{3}}\,\|0\tfrac{\bar{1}}{2}\rangle - \sqrt{\dfrac{1}{6}}\,\|\bar{1}\tfrac{1}{2}\rangle$	$\dfrac{5}{2}\alpha\lambda$	$\left(\dfrac{-1}{2}\right)$
$\sqrt{\dfrac{6}{15}}\,\|1\tfrac{3}{2}\rangle + \sqrt{\dfrac{1}{15}}\,\|0\tfrac{\bar{1}}{2}\rangle - \sqrt{\dfrac{1}{6}}\,\|\bar{1}\tfrac{1}{2}\rangle$	$1\alpha\lambda$	$\left(\dfrac{-1}{2}\right)$

ence of tetragonality will not change this. It is now straightforward to transform the matrices of $L_z + 2S_z$, $L_x + 2S_x$, and the effective hamiltonian to the basis of Table I.[33]

Then one can write the eigenfunctions of the secular equations using first-order perturbation theory. Of course, these are expressed in terms of the eigenfunctions for pure octahedral symmetry. For instance, the ground state wave function is

$$\|1\rangle = \left|E = \frac{5}{2},\ m = \frac{1}{2}\right\rangle + \frac{7c + 2d}{9\sqrt{5}}\left|E = 1,\right.$$

$$\left.m = \frac{1}{2}\right\rangle + \frac{c + d}{4\sqrt{5}}\left|E = \frac{-3}{2},\ m = \frac{1}{2}\right\rangle \quad (14)$$

where we have labeled the octahedral eigenfunctions by their energies (in units of $\alpha\lambda$) and their m values. They are given in terms of the original basis by the coefficients in Table I. The g values are easily calculated to this order using the matrices of $L_z + 2S_z$ and $L_x + 2S_x$

$$g_\| = 2\langle 1| L_z + 2S_z |1\rangle = \frac{2}{27}[9(\alpha + 5) -$$

$$(14c + 4d)(\alpha + 2)] \quad (15a)$$

$$g_\perp = 2\langle 1| L_x + 2S_x |\bar{1}\rangle = \frac{2}{27}[9(\alpha' + 5) +$$

$$(7c + 2d)(\alpha' + 2)] \quad (15b)$$

The state $|\bar{1}\rangle$ is the degenerate partner of $|1\rangle$, with $m = 1/2$. For γ-picoline, eq 15 give $g_\| = 4.56$ and $g_\perp = 4.323$, which differ by only 0.1% from the values calculated from the full secular equation. When $c = d = 0$ and $\alpha = \alpha'$ (octahedral symmetry), $g_\|^2 = g_\perp^2$ as expected. A direct calculation of the anisotropy to first order gives

$$g_\|^2 - g_\perp^2 = -(8/27)[(7c + 2d)(\alpha + 5)(\alpha + 2) +$$

$$3c\alpha(\alpha + 5)] \quad (16)$$

For γ-picoline, this formula gives -1.428 while the correct value is -1.467. It may be noted that we are here calculating the small difference between two almost equal numbers.

Since c and d are expected to have opposite signs, the sign of eq 16 is not evident. With $\alpha \sim 1.4$, the right side of eq 16 becomes roughly $-53c - 13d$, into which we insert

our approximate expressions for c and d: $d = 1.19Dt/(\alpha\lambda)$ $= -0.0047Dt$, $c = 0.00061Dt$ ($\lambda = -180$ cm^{-1} used here). This gives

$$g_{\parallel}^2 - g_{\perp}^2 \sim 0.029Dt \ (\text{cm}^{-1})$$

which is -1.6 for λ-picoline (exact value, -1.5). If $\lambda = -150$ cm^{-1} is used instead of -180 cm^{-1}, -2.4 is obtained, indicating a high sensitivity of results to the value of this parameter.

We turn to calculation of the second term in eq 2, the "high-frequency terms". The matrix elements required for $\chi_{\parallel}$ are between $|1\rangle$ and the other $m = 1/2$ states

$$|2\rangle = \frac{7c + 2d}{-9\sqrt{5}}\left|E = \frac{5}{2}, \ m = \frac{1}{2}\right\rangle + \left|E = 1, \right.$$
$$\left. m = \frac{1}{2}\right\rangle + \frac{2d - c}{25}\left|E = \frac{-3}{2}, \ m = \frac{1}{2}\right\rangle \quad (17a)$$

and

$$|3\rangle = \frac{c + d}{-4\sqrt{5}}\left|E = \frac{5}{2}, \ m = \frac{1}{2}\right\rangle + \frac{2d - c}{25}\left|E = 1, \right.$$
$$\left. m = \frac{1}{2}\right\rangle + \left|E = \frac{-3}{2}, \ m = \frac{1}{2}\right\rangle \quad (17b)$$

A direct calculation gives

$$\frac{1}{2}\chi_{\parallel}^{hf} = (\alpha + 2)^2\left(\frac{10}{27} - \frac{23c + 7d}{81}\right)$$

This formula gives 4.195 for γ-picoline; the directly calculated value (via the secular equation) is 4.213. For the high-frequency part of $\chi_{\perp}$, we need matrix elements between $|1\rangle$ and the functions $|\bar{2}\rangle$ and $|\bar{3}\rangle$ (for $m = -1/2$) as well as the functions for $m = 3/2$. After lengthy algebra, we find

$$\frac{1}{2}\chi_{\perp}^{hf} = (\alpha' + 2)^2\left(\frac{10}{27} + \frac{7d - 37c}{162}\right)$$

which gives 4.436 for λ-picoline, to be compared with 4.480 from complete solution of the secular equation. Putting $\alpha' = \alpha(1 + c)$, we find

$$\chi_{\parallel}^{hf} - \chi_{\perp}^{hf} = \frac{(\alpha + 2)^2}{81}\left(-9c - 21d - 120\frac{c\alpha}{\alpha + 2}\right) \quad (18)$$

which gives -0.564 for this data, to be compared with the directly calculated value of -0.534. All the high-frequency terms are in units of $\mu_B^2/|\alpha\lambda|$. Like $g_{\parallel}^2 - g_{\perp}^2$, (18) represents a small difference between large numbers.

The dipole strength is given by

$$D = \frac{1}{3}(\chi_{\parallel} - \chi_{\perp})$$
$$= \frac{(g_{\parallel}^2 - g_{\perp}^2)\mu_B^2}{12kT} + \frac{\chi_{\parallel}^{hf} - \chi_{\perp}^{hf}}{|\alpha\lambda|}\frac{\mu_B^2}{3} \quad (19)$$

since $J = 1/2$ here, and we calculate $\chi_{\parallel}^{hf}$ and $\chi_{\perp}^{hf}$ as dimensionless quantities. If we use cgs units, for which the Bohr magneton μ_B is -0.927×10^{-20} erg/Oe, and express $|\alpha\lambda|$ in cm^{-1} and T in degrees, eq 19 becomes

$$D = 1.44 \times 10^{-25}\left[\frac{g_{\parallel}^2 - g_{\perp}^2}{(T/1.44)} + \frac{\chi_{\parallel}^{hf} - \chi_{\perp}^{hf}}{|\alpha\lambda|}\right] \text{cm}^3 \quad (20)$$

For the moment, we have been considering the signs of the first and second terms of (20). We have argued that c and d are probably of opposite sign, and showed that $g_{\parallel}^2 - g_{\perp}^2$ is roughly $-53c - 13d$, and $\chi_{\parallel}^{hf} - \chi_{\perp}^{hf}$ roughly $-7c -$

$2.9d$. With the values suggested earlier for $K = Ds/Dt$ (1.42) and $\alpha\lambda$ (1.4 $\times$ 180 cm^{-1}), we find $d = -0.0047Dt$ and $c = 0.00067Dt$ with Dt expressed in cm^{-1}. Then $g_{\parallel}^2 - g_{\perp}^2 \sim 0.029Dt$ and $\chi_{\parallel}^{hf} - \chi_{\perp}^{hf} \sim 0.0094Dt$, i.e., both anisotropies are of the same sign. This means that there is no positive temperature T for which the dipole field factor D vanishes. Thus, if the pseudocontact shifts for cis and trans methanol protons were plotted against reciprocal temperature, they would *not* cross at any positive temperature. However, we have assumed population of only one Kramers' doublet, which is valid only at low temperatures.

For $\lambda = -180$ and $\alpha\lambda$ about -250 cm^{-1}, the energy difference between ground and first excited state is $-(3/2)\alpha\lambda \sim 380$ cm^{-1}. The Boltzmann factor at 200°K would be 0.066 and at 300°K it would be 0.16. Thus the importance of excited states is not negligible, since $|\lambda|$ is probably smaller than 180 cm^{-1} for the complexed ion (it is 150 cm^{-1} for tetrahedral Co^{2+} complexes) and $g_{\parallel}^2 - g_{\perp}^2$ can be much larger than 1.5 for the excited states.

V. Effect of Temperature

The effects of thermal population are considered in this section, as we study the variation of D with temperature. After working out several limiting cases, we show how the experimental results for the γ-picoline complex are explained by the crystal field calculation. In all the calculations, we consider only the lowest 12 states, formed by coupling the two lowest-lying orbital levels, one of which is doubly degenerate, with the spin quartet. Thermal population of other levels is negligible, while their contribution to χ^{hf} is only a few percent of the contribution of the lowest 12 states, as discussed in section I.

Experimental results from which one can determine D as a function of T are available for several systems.[4] We derive D from the shifts of the cis and trans methanol protons of the pentakis(methanol) complex by formulas given in our previous article.[3,34] Over the temperature range studied, the shifts, plotted against T^{-1}, are fit to within experimental error by straight lines. In Table II we give the coefficients a and b in the formula,

$$D = a + bT^{-1} \quad (21)$$

as determined by least-squares fits of the cis and trans shifts. Since a and b have opposite signs, extrapolation of the straight line would lead to a value of T for which D vanishes (see Table II).[35]

In fact, calculations (see below) show that such an extrapolation is not meaningful because the straight-line character of the D vs. T^{-1} plot is only apparent, due to the limited temperature range. This is shown already by simple calculations in the limiting cases corresponding to small spin–orbit coupling, which we perform first. Small values of the spin–orbit coupling constant λ mean that d becomes large compared to c, so this may also by referred to as the high d limit. For the case treated[25] by Abragam and Pryce, $Co(NH_4)_2(SO_4)_2 \cdot 6H_2O$ in the crystal, the values $c = 0.3334$ and $d = -5.373$ are suggested, so that $d/c \sim -16$ and the high d limit should be applicable. Our interest in this limit at present is that it allows explicit formulas for the temperature dependence.

When $|d|$ is large compared to c, we may ignore matrix elements in the secular equations which couple states for which the diagonal elements differ by d, since all these matrix elements are proportional to c. This means that the

TABLE II: Experimentally Determined Dipole Strengths as a Function of Temperature (see Eq 21) for $Co(CH_3OH)_5X^{2+}$ Complexes

Ligand X	Dt (est), cm^{-1}	Temp range, °C	$10^{28}b$	$10^{28}a$	D at 222°K	Crossing, °K
Pyridine	−60	−98 to −10	−7667	19.05	$−15.5 \times 10^{-28}$	402
γ-Picoline	−57	−81 to −40	−7014	19.30	$−12.3 \times 10^{-23}$	363
H_2O	−4	−85 to −1	3640	−9.24	7.2×10^{-23}	394

matrices are effectively diagonal. We must consider separately what happens for positive d and for negative d.

In the latter case, the eigenenergies, in order of increasing energy, are 3/2, 1/2, −1/2, −3/2, d, d (remember that energies are in units of the negative quantity $\alpha\lambda$), with corresponding eigenstates $|\pm 1 \mp 3/2\rangle, |\pm 1 \mp 1/2\rangle, |\pm 1 \pm 1/2\rangle, |\pm 1 \pm 3/2\rangle, |0 \pm 3/2\rangle, |0 \pm 1/2\rangle$. Since we consider d to be large, we can neglect the populations of the last two states. Their contribution to the high-frequency terms in the susceptibilities will also be ignored, because of the large energy denominators. The value[36] of $g_\perp$ (see eq 9) is zero for the other four states because $L_x + 2S_x$ can couple only states differing by unity in either m or m_s. Because the matrix of $L_z + 2S_z$ over these states is diagonal, $\chi_\parallel^{hf}$ is identically zero for all four states.

If only the ground state is considered, $g_\parallel^2 - g_\perp^2$ and $\chi_\parallel^{hf} - \chi_\perp^{hf}$ have opposite signs, and a crossing ($D = 0$) occurs in plots of cis and trans pseudocontact shifts vs. $1/T$. The full expression for D involves calculating $\chi_\parallel - \chi_\perp$ for each of the four states and weighting each with a Boltzmann factor. This yields

$$D = \frac{(\alpha + 3)^2 + (\alpha + 1)^2 P + (\alpha - 1)^2 P^2 + (\alpha - 3)^2 P^3}{3kT(1 + P + P^2 + P^3)} +$$
$$\frac{6 + 2P - 2P^2 - 6P^3}{3\alpha\lambda(1 + P + P^2 + P^3)} \quad (22)$$

where $P = \exp(\alpha\lambda/kT)$. D of eq 22 never becomes zero. Since the plot of D vs. T^{-1} goes through the origin but has an increasing slope with increasing T^{-1}, extrapolation of any portion, after fitting to a straight line, will give an apparent crossing.

If d is large and negative, there are two low-lying doublets, and the other four doublets, with energies lying above these by d, should be dropped from consideration. However, the two states have the same energy, namely, $d\alpha\lambda$, in the limit. We thus must consider mixing of other states to split the degeneracy. According to perturbation theory, the state $|0 \pm 1/2\rangle$ now has an energy in units of $\alpha\lambda$ of $d + 3/2(c + 1)^2/d + 2(c + 1)^2/d$, and the state $|0 \pm 3/2\rangle$ has an energy of $d + 3/2(c + 1)^2/d$. With the abbreviation $u = 2(c + 1)^2\alpha\lambda/dkT$, we calculate

$$D = \frac{-12 + 36e^u}{12(1 + e^u)kT} + \frac{-6 + 6e^u}{3(1 + e^u)ukT}$$

which becomes $(4 + u)/2kT$ for sufficiently small u. Apparently, a plot at high temperatures would not be of the familiar form $a + bT^{-1}$, but rather $aT^{-2} + bT^{-1}$. The T^{-2} term arises from the near degeneracy.[9] Now suppose $c \sim 0$, $\alpha\lambda \sim 250$ cm^{-1}, and $d = 10$; then $u = -72/T$ (degrees). For temperatures of 100, 150, 200, and 250°, the values of D are 0.0127, 0.0101, 0.0082, and 0.0068, respectively, in units of μ_B^2/k. Plotting these against T^{-1}, one obtains reasonable "straight lines" which can be extrapolated to $D = 0$ at about 500°. In fact, the lines are not straight, and direct calculation shows that D never vanishes. Actually, the $a +$
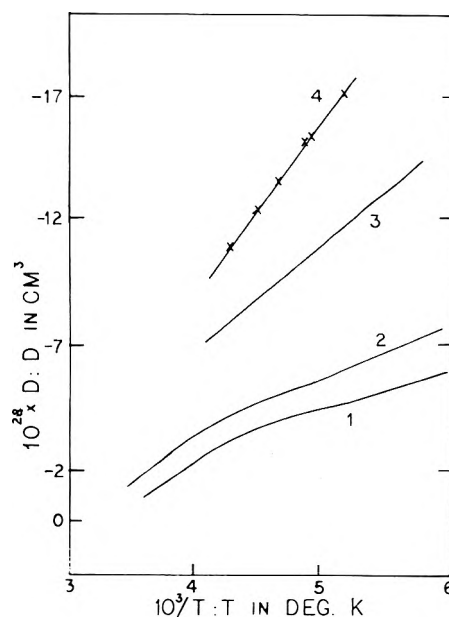

Figure 1. Dipole strength factor (D in $cm^3 \times 10^{28}$) for λ-picoline as a function of temperature ($10^3/T$, T in degrees Kelvin). Curve 1 is calculated with $Dq = 900$ cm^{-1}, $Dt = -57$ cm^{-1}, $Ds = -81$ cm^{-1}, $B = 825$ cm^{-1}. Curve 2 results when λ is changed from −180 cm^{-1} (curve 1) to −150 cm^{-1}. Curve 3 results on changing Dt to −100 cm^{-1}, maintaining the Ds/Dt ratio. Curve 4 is a straight-line fit to the experimental points, shown as X's.

b/T dependence due to the contribution of a single state to D is probably masked by Boltzmann factors, and the crossings of cis and trans pseudocontact shifts as extrapolated from plots vs. T^{-1}, have no real significance.

We have carried out extended calculations of D values, starting from assumed values for Ds and Dt, generating α, α', and Δ, and thence calculating g values and susceptibilities. It is possible to fit the measured values of D as well as their temperature dependence, using reasonable values of the parameters Ds, Dt, and λ. This is not too surprising, perhaps, but it shows that one can discuss and explain observed Co^{2+} pseudocontact shifts in the framework of the crystal field model.

For example, we give the results of complete calculations for a single case, λ-picoline, to show the nature of the temperature dependence and how it is fit by our calculations. The parameters used first are: $\alpha = 1.4355$, $\alpha' = 1.3849$, and $d = 0.2554$ (corresponding to $\lambda = -180$ cm^{-1}). In each case, population of three states is taken into account. A second set of calculations was made using the more reasonable value of −150 cm^{-1} for λ. Results of the two are shown in Figure 1. A high value of $g_\parallel^2 - g_\perp^2$ for the first excited state (with $m' = 3/2$ and thus $g_\perp = 0$) meant that, even with a small population, it gave an important contribution to the g factor term. The value of D is obtained in cm^3 from the numerical value of our expression by multiplication by $(1/3)\nu_0\mu_B^2/k$, where k is the Boltzmann constant, μ_B the

Bohr magneton (0.927×10^{-20} erg/Oe), and ν_0 the NMR frequency (100 MHz in our case).

The experimental values (which are obtained from measured frequencies using a geometrical factor which may be inaccurate due to errors in the assumed geometries) are also plotted (curve 4). Several observations may be made. First, both results give D values of the right sign and having the right temperature dependence. Over the temperature range of the experimental data, the calculated points give a satisfactory straight line on a plot vs. reciprocal temperature. However it would be a grave error to assume that D was of the $a + b/T$ form and extrapolate to the point for which $d = 0$. Thermal population of excited states is actually extremely important.

Another calculation, in which Dt was changed from -57 to -100 cm^{-1}, but $\lambda = -150°$ and $Ds/Dt = 1.4$ were maintained, gave much improved results (see Figure 1, curve 3). The magnitude of D and the slope of the D vs. T^{-1} plot are both significantly increased. The change of 43 cm^{-1} in Dt corresponds to a change of 150 cm^{-1} in the difference of Dq values for methanol and λ-picoline. Since each Dq is about 1000 cm^{-1}, such a change is within the range of our ignorance. Finally, we experimented with changing the Ds to Dt ratio. As our analysis of section II showed, the parameters d and c and hence our results depend strongly on this ratio and a change of a few tenths from the value of 1.4 can move our calculated points above the experimental ones. It is clear from these experiments that, with a reasonable choice of parameters, our model can fit observed data for D of λ-picoline.

Similar numerical experiments have convinced us that fits are similarly obtainable for other systems. Given the inaccuracies of the model and the uncertainty in the value of the parameters, it does not seem valuable to present such results and attempt to choose "correct" values of Ds, Dt, and λ. Only if one of these parameters were independently measured, would it become worthwhile to find the values of the other two required by the experimental results.

Our theoretical work shows that the crystal field model can be used to reproduce and explain pseudocontact shifts and their temperature dependence for the $Co(CH_3OH)_5X^{2+}$ systems and, by implication, for other tetragonal high-spin Co(II) systems. However, our results warn against naive interpretations of the apparent linearity of shifts when plotted against T^{-1}, or extrapolation to a point for which D vanishes. A theory for these shifts must include thermal population of low-lying states, and straight lines on plots of shifts vs. T^{-1} are not be be expected.

The correlation of shifts with crystal field parameters, and particularly with the sign of Dt, is dangerous as well. Such correlations require that Ds/Dt be neither too large nor negative. For all cases of interest to us, simple expressions are now available giving the anisotropy of the low-lying states, as expressed by c and d in terms of the crystal field parameters. Calculation of D in terms of c, d, λ, and the temperature requires more involved calculations.

Supplementary Material Available. The matrices of the effective hamiltonian, $L_z + 2S_z$, and $L_x + 2S_x$, transformed to the basis of Table I will appear following these pages in the microfilm edition of this volume of the journal. Photocopies of the supplementary material from this paper only or microfiche (105×148 mm, 24× reduction, negatives) containing all of the supplementary material for the papers in this issue may be obtained from the Journals Department, American Chemical Society, 1155 16th St., N.W., Washington, D.C. 20036. Remit check or money order for $4.00 for photocopy or $2.50 for microfiche, referring to code number JPC-75-1206.

References and Notes

(1) D. R. Eaton and W. D. Phillips, *Adv. Magn. Resonance*, **1**, 103 (1965); E. deBoer and H. Van Willigen, *Prog. Nucl. Magn. Resonance Spectr.*, **2**, 111 (1967); R. H. Holm, *Acct. Chem. Res.*, **2**, 307 (1969); H. J. Keller, in "NMR: Basic Principles and Progress", Vol. 2, Diehl, Fluck, and Kosfeld, Ed., Springer-Verlag, Berlin, 1970; G. A. Webb, *Ann. Rep. NMR Spectr.*, **3**, 211 (1970); A. F. Cockerill, G. L. O. Davies, R. C. Harden, and D. M. Rackham, *Chem. Rev.*, **73**, 553 (1973); R. von Ammon and D. Fischer, *Angew. Chem. Intl. Ed. Engl.*, **11**, 675 (1972).

(2) J. R. Vriesenga, *Inorg. Chem.*, **11**, 2724 (1972); J. R. Vriesenga, and R. Gronner, *ibid.*, **12**, 1112 (1973); J. R. Vriesenga, submitted for publication.

(3) J. R. Vriesenga and J. Goodisman, *J. Magn. Resonance*, submitted for publication.

(4) K. Plotkin, J. Copes, and J. R. Vriesenga, *Inorg. Chem.*, **12**, 1494 (1973); J. R. Vriesenga and R. Gronner, *ibid.*, **12**, 1112 (1973); J. Copes and J. R. Vriesenga, private communications.

(5) D. Forster, *Inorg. Chem. Acta*, **5**, 465 (1971).

(6) M. Gerloch and D. J. Mackey, *J. Chem. Soc. A*, 3030, 3040 (1970).

(7) M. Gerloch and D. J. Mackey, *J. Chem. Soc. A* 2605, 2612, 3372 (1971); *J. Chem. Soc., Dalton Trans.*, 37, 42, 410, 415 (1972).

(8) R. M. Golding and P. Pyykko *Mol. Phys.*, **26**, 1389 (1973).

(9) B. Bleaney, *J. Magn. Resonance*, **8**, 91 (1972).

(10) L. M. Engelhardt and M. Green, *J. Chem. Soc., Dalton Trans.*, 724 (1972).

(11) R. J. Kurland and B. R. McGarvey, *J. Magn. Resonance*, **2**, 286 (1970).

(12) B. R. McGarvey, *J. Chem. Phys.*, **53**, 86 (1970).

(13) J. P. Jesson, *J. Chem. Phys.*, **45**, 1049 (1966)

(14) G. N. LaMar, J. P. Jesson, and P. Meakin, *J. Am. Chem. Soc.*, **93**, 1286 (1971); G. N. LaMar and F. A. Walker, *ibid.*, **95**, 1782, 1790 (1973); H. A. O. Hill, P. J. Sadler, and R. J. P. Williams, *J. Chem. Soc., Dalton Trans.*, 1663 (1973).

(15) C. Beautè, S. Cornuel, D. Lalandais, N. Thoai, and Z. W. Wolkowski, *Tetrahedron Lett.*, 1099 (1972).

(16) W. D. Perry and R. S. Drago, *J. Am. Chem. Soc.*, **93**, 2183 (1971).

(17) J. P. Jesson, *J. Chem. Phys.*, **47**, 582 (1967).

(18) W. DeW. Horrocks and E. S. Greenberg, *Inorg. Chem.*, **10**, 2190 (1971); W. DeW. Horrocks and D. DeW. Hall, **10**, 2368 (1971); R. Fitzgerald and G. R. Brubaker, *ibid.*, **10**, 1324 (1971).

(19) H. M. McConnell and R. E. Robertson, *J. Chem. Phys.*, **27**, 1361 (1958).

(20) G. N. LaMar, *J. Chem. Phys.*, **43**, 1085 (1965).

(21) J. P. Jesson, *J. Chem. Phys.*, **47**, 579 (1967).

(22) W. DeW. Horrocks, Jr., R. H. Fischer, J. R. Hutchinson, and G. N. LaMar, *J. Am. Chem. Soc.*, **88**, 2436 (1966).

(23) A. D. Buckingham and P. J. Stiles, *Mol. Phys.*, **24**, 99 (1972).

(24) J. M. Briggs, G. P. Moss, E. W. Randall, and K. D. Sales, *Chem. Commun.*, 1180 (1972).

(25) A. Abragam and M. H. L. Pryce, *Proc. Roy. Soc., Ser. A*, **206**, 173 (1951).

(26) A. B. P. Lever, "Inorganic Electronic Spectroscopy", Elsevier, Amsterdam, 1968.

(27) J. R. Perumareddi, *J. Phys. Chem.*, **71**, 3155 (1967); A. B. P. Lever, *Coord. Chem. Rev.*, **3**, 119 (1968).

(28) J. Goodisman, unpublished.

(29) M. Keaton, B. Fa-Chien Chou, and A. B. P. Lever, *Can. J. Chem.*, **49**, 192 (1971); L. Dubicki, M. A. Hitchman, and P. Day, *Inorg. Chem.*, **9**, 188 (1970); T. S. Davis, J. P. Fackler, and M. J. Weeks, *ibid.*, 7, 1994 (1968); A. B. P. Lever, *Coord. Chem. Rev.*, **3**, 119 (1968), Tables 4–6; C. R. Sperati, Thesis, Ohio State University, 1973.

(30) D. R. Eaton and K. Zaw, *Coord. Chem. Rev.*, **7**, 197 (1971); J. P. Jesson, *J. Chem. Phys.*, **45**, 1049 (1966).

(31) T. S. Davis, J. P. Fackler, and M. J. Weeks, *Inorg. Chem.*, **7**, 1994 (1968).

(32) Values for Dq for H_2O and DMSO in Co(II) complexes are available in ref 26, but not for other ligands. Such Dq values are given for Ni(II) tetragonal complexes. We estimate their values for the Co(II) complexes by multiplying the Ni(II) values by 1.09, which is the ratio of Co to Ni Dq values for H_2O and DMSO.

(33) See paragraph at end of text regarding supplementary material.

(34) The definition of D used in the present work, eq 1, conforms more closely to current practice than that of ref 3. The values of D given in ref 3 include a factor of ν_0, and should therefore be divided by 10^8 to yield the values in this paper. Note that we are now using ångstroms for units of length.

(35) Corresponding results have been obtained for other systems (J. Vriesenga, private communication), for which X = α-picoline, β-picoline, 3-chloropyridine, 3-cyanopyridine, acetonitrile, dimethyl sulfoxide, etc.

(36) The g values and high-frequency susceptibilities are given in the microfilm edition of this volume of the journal. See paragraph at end of text for details.

Phosphorus-31 Nuclear Magnetic Resonance Studies on Condensed Phosphates.[1,2] III. Polyphosphate Spectra

Thomas Glonek, Anthony J. R. Costello, Terrell C. Myers, and John R. Van Wazer*

Research Resources Laboratory and Department of Biochemistry, University of Illinois at the Medical Center, Chicago, Illinois 60612 and Department of Chemistry, Vanderbilt University, Nashville, Tennessee 37235 (Received October 24, 1974)

Straight-chain phosphates exhibiting up to 10 phosphorus atoms per chain have been prepared in pure form by column chromatography of a suitable sodium phosphate glass. The ^{31}P NMR spectra of the resulting sodium polyphosphates, $Na_{n+2}P_nO_{3n+1}$ for $n < 9$, have been obtained and the spectra for $n < 8$ have been fully analyzed for their respective shielding parameters and coupling constants. The trends in these values are discussed with emphasis on the curious variation with chain length of the middle-group chemical shifts.

Introduction

The existence of a series of polyphosphates was postulated[3] over a century ago, and the smallest and next larger molecule (the orthophosphate and the pyro- or, alternatively, diphosphate) in this series have been known in crystalline form since alchemical times. The presence of the next two larger species (the tri- and tetrapolyphosphates) has been demonstrated[4,5] in phase-diagram studies only within the last 35 years and the longer-chain phosphates in pure form are still laboratory curiosities. Although naturally occurring mixtures of the longer straight-chain phosphates have been a subject of considerable interest[6,7] for 25 years, there has only been one report[8] of the isolation of the individual members of this series of molecule ions up through the ten-unit chain. The procedure used in that isolation[8] was a difficult and laborious one involving fractional crystallization of the acridinium salts.

In the more recent work on mixtures of polyphosphate molecule ions, ^{31}P nuclear magnetic resonance (NMR) has proved to be an especially powerful analytical tool.[9] However, the fact that chain phosphates having more than three phosphorus atoms per molecule exhibit second-order spectra of considerable complexity has been a great hindrance to the full utilization of this technique in the study of phosphates. Unfortunately, the structure of the spectra are so involved that any systematic spectral analysis usually has been precluded in mixtures which include the longer straight-chain phosphates. Therefore, it seemed desirable to develop an improved method for isolating the longer-chain polyphosphates and to obtain their NMR spectra under optimum conditions. This is the substance of this report.

Experimental Section

Polyphosphate Separations. A separation was effected on a sodium phosphate glass[10] exhibiting a number-average chain length, $\bar{n}$, of 5.5 as determined by end-group titration,[11] as well as by the zinc-oxide gravimetric determination of water[12] coupled with the Na_2O/PO_5 ratio of the reagent mixture from which the glass was made. In order to obtain samples containing as much as 0.2 g of the individual polyphosphate, it was necessary to carry out a two-stage

fractionation. In the first stage a concentrated solution of the glass was applied to the top of a column (80 cm length, 5.0 cm diameter) packed with diethylaminoethyl cellulose in the bicarbonate form.[13] The phosphates were eluted using an 18-l. linear-gradient (0.2 to 1.0 M) triethylammonium bicarbonate solution to give 100-ml cuts which were analyzed for total phosphorus.[14] Upon pooling the appropriate fractions and concentrating in a rotary evaporator at 25°, the bicarbonate-purged triethylammonium phosphates were precipitated from methanol solution by sodium iodide in acetone.[13]

These samples obtained from the crude cuts were further separated by an analogous procedure, using a similarly packed column (240 cm length, 2.5 cm diameter) again with 18 l. of the same eluent. In the initial run with this long, narrow column, 10-ml cuts were employed with an elution rate of 1.0 ml/min. During the elution procedures, it is important always to keep the receiver vials covered, since we have observed that small particles of dust may catalyze the hydrolysis of an individual fraction. Since, under the best conditions, aqueous solutions of phosphates undergo appreciably rapid hydrolysis, the dry sodium salts should be prepared as expeditiously as possible. Each preparation from this procedure yielded NMR spectra showing no unaccountable resonances in the ^{31}P spectrum and also exhibited a clean solitary spot upon thin-layer chromatographic analysis.[15,16] The tetra-n-butylammonium salts were prepared by immediately titrating the solution of the free polyphosphoric acid (obtained by passing the Na salt through a Dowex 50 H^+ column) with tetra-n-butylammonium hydroxide to the desired pH.

NMR Studies. The ^{31}P NMR spectra[17,18] were obtained on a Bruker HFX-5 spectrometer operating at 36.4 MHz for ^{31}P and 90.0 MHz for the ^1H lock. The samples were studied at 25° in freshly prepared aqueous solutions containing 0.1 M of total phosphorus, using 5- or 13-mm spinning sample tubes. The pH was held at 10.2 and the solution was 0.2 M in ethylenediaminetetraacetic acid (EDTA), which was added in order to sequester any trace of multiply charged metal ions since these ions form complexes with the polyphosphates and thereby may cause rather large changes in their ^{31}P NMR parameters. In each run, the scanning speed and observing rf power were carefully adjusted under the signal-averaging conditions employed to ensure that signal saturation was not taking place. All ref-

---

* Address correspondence to this author at the Department of Chemistry, Vanderbilt University, Nashville, Tenn. 37235.

erencing was, of course, carried out with respect to the proton lock signal, but the chemical shifts are formally reported with respect to 85% orthophosphoric acid (externally situated), with positive shifts being upfield.[18]

The spectra were analyzed using a computer package developed by Swalen[19] consisting of three separate programs (NMRIT, NMREN2, and NMRPLT). In this study, it was possible to fit the experimental spectra of the tetra-, penta-, and hexapolyphosphates, using an iterative analytical approach (involving NMREN2 and NMRIT), since the number of observed transitions were not excessively large and were fairly well resolved so that their positions could be assigned with reasonable certainty. Due to the excessive number of transitions involved, the spectra of the hepta- and octapolyphosphates had to be analyzed by cut-and-try methods (using NMRIT and NMRPLT) to obtain a set of NMR parameters which were concordant with those obtained for the shorter-chain phosphates. In order to get a good fit between the calculated and experimental data, 35 separate sets of calculations were needed for the heptapolyphosphate and 13 for the octapolyphosphate molecule ion.

Results and Interpretations

By running a small sample of the original sodium phosphate glass ($\bar{n} = 5.5$) through the 240-cm column employed for the final fractionation of the NMR samples, the elution curve shown in Figure 1 was obtained. Note that this curve approximates the linear elution pattern which should be expected for a regular series of related compounds. The smallest members of the family (the pyro- and tripolyphosphates) deviate from a straight-line curve, as might be anticipated. A similar type of dependence has been observed[13] for the series of cyclic metaphosphates eluted from the same substrate. Evidence that the individual chain lengths noted on the vertical axis of Figure 1 are indeed correct comes from several sources. First, the corresponding polyphosphates from the crystallization of the acridinium salts were shown to fall in the same positions in thin-layer cochromatographic analysis. Secondly, samples of tri- and tetrapolyphosphate run through the 240-cm column elute at the right place, and their NMR patterns corresponded to those given in the literature. Thirdly, the NMR spectra of the eluted samples exhibited the expected ratio of total end, e, to total middle, m, phosphate groups,[20] with no detectable orthophosphate, n, or branch, b, groups (i.e., $n < 0.2\%$ and $b < 1.0\%$ of total P) and no resonances assignable to known cyclic metaphosphates.[13] Furthermore, the applicability of the mathematical analysis[19] of the NMR spectra discussed in this paper is also support for the singularity of each sample.

The spectra of the penta- and hexapolyphosphates, shown in Figure 2, exemplify the quality of fits obtained between the experimental (NMR) and theoretical (computer-simulated) ^{31}P spectra from each member of the series of polyphosphate compounds of this study. The pentapolyphosphate spectrum has the most complicated appearance of any of those obtained from the family of condensed phosphates; however, the number of transitions is not excessively high because of the limited number of interacting nuclei, and the spectrum can be computed with a high degree of certainty. For the chain phosphates, the number of resolvable transitions decreases as the molecular size increases from that of pentapolyphosphate because of the crowding of individual transitions, so that the spectrum appears more simple. The theoretical complexity, however,
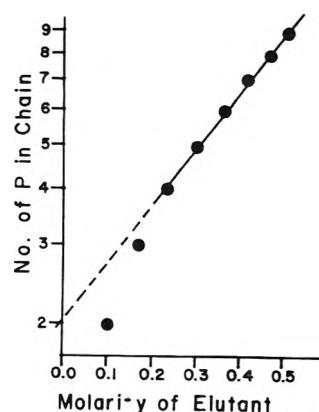

Figure 1. The elution pattern of the chain polyphosphates from the 240-cm column of diethylaminoethyl cellulose, using an 18-l. linear salt gradient of triethylammonium bicarbonate.
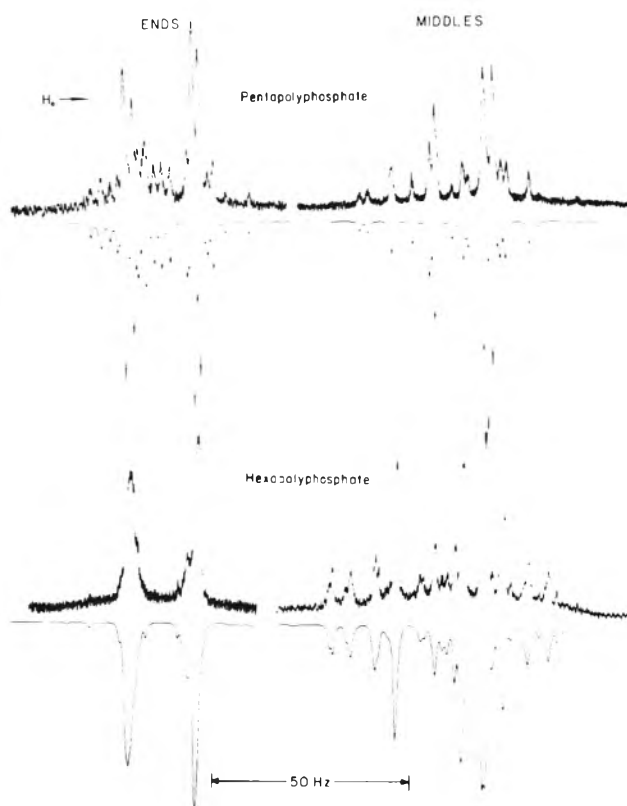

Figure 2. Experimental and simulated (inverted) ^{31}P NMR spectra of sodium penta- and hexapolyphosphate, each at pH 10.2. The signal width at half-height in the calculated spectra was 1.2 Hz.

must increase with increasing molecular size. Thus, for phosphates larger than the pentapolyphosphate, the errors inherent in the calculated values of the chemical shifts and coupling constants increase with the size of the phosphate so that calculations on the nona- and higher polyphosphates, should they be performed, would be of limited accuracy.

Fortunately, as the molecular size increases, the ^{31}P spectrum simplifies. The nona- and decapolyphosphates essentially exhibit a "simple" doublet in the end-group spectral region and a single broad envelop in the middle-group region. For chain lengths greater than ca. 150 phosphorus atoms, the end group (when detectable) is a sharp doublet while the middle-group envelope appears as a sharp singlet. For a carefully prepared solution of Kurrol's

TABLE I: ^{31}P NMR Parameters for Solutions (0.1 M in P) of the Pure Sodium Polyphosphates at pH 10.2

n in Na_{n+2} P_nO_{3n+1}	Chemical shifts,[a] Hz				Coupling constants,[b] Hz			
	End e	Middle groups			$J_{1,2}$	$J_{2,3}$	$J_{3,4}$	$J_{4,5}$
		em	emm	$emmm$				
2	264.1							
3	251.4	743.0			20.6			
4	228.1	748.0			20.2	15.0		
5	207.6	753.7	766.5		19.2	15.5		
6	198.2	732.6	758.6		18.1	16.0	16.0	
7	197.4	757.1	774.6	775.0	17.7	16.2	16.3	
8	197.2	756.2	778.4	778.8	17.6	16.3	16.3	16.3
9	197.2	767.5[c]	778.4[c]	778.8	17.6[c]			
∞	197.2[d]	768.0[c]		778.8[d,e]	17.4[d]			

[a] The chemical shifts measured from the hydrogen lock are referenced to "external" 85% H_3PO_4, with positive shifts being upfield and 1 ppm = 36.4 Hz. The symbol e refers to the phosphate end group and, for example, emm refers to the phosphate middle group which is based on the third phosphorus from the end of the chain. [b] $J_{i,(i+1)}$ is the coupling constant between the pair of neighboring phosphorus atoms in position i and $(i+1)$ where i is the number of the phosphorus atom when counting from the end of the chain. [c] Estimated by extrapolation. [d] Directly measured on several long-chain polyphosphate compositions. [e] This middle-group chemical shift corresponds to phosphorus atoms so far from the ends of the chains as to be unaffected by them.
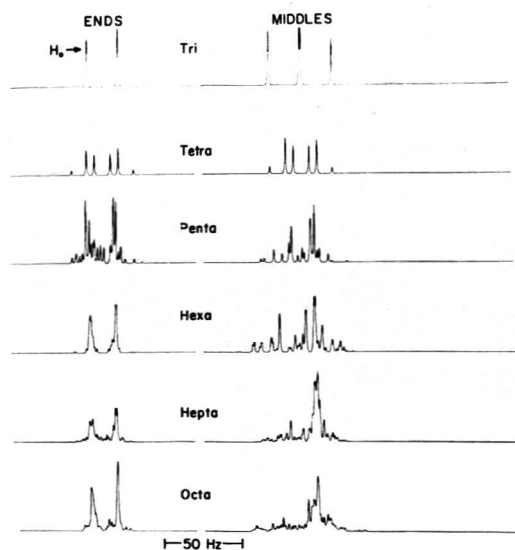
Figure 3. Simulated ^{31}P NMR spectra of the sodium tri- through octapolyphosphates. The amplitude of each multiplet was chosen to correspond to that of the experimental spectrum to which it was fitted and, therefore, the relative areas of the end and middle groups are not comparable. The signal width at half-height used in the simulation was 0.5 Hz. The spectra correspond to those of the sodium polyphosphates at pH 10.2 (solutions 0.1 M in phosphorus and 0.2 M in EDTA).

salt, exhibiting a chain length of ca. 10,000 phosphorus atoms, the middle-group line width was measured to be less than 0.2 Hz, the resolution limit of the spectrometer at that time.

Figure 3 shows the calculated NMR spectra obtained for the tri- through the octapolyphosphate. For illustrative purposes, these spectra are presented instead of the experimental NMR spectra because spectral noise in the experimental records often hides the fine points of multiplet structure. The signal width at half-height was chosen to be 0.5 Hz which corresponds to the best resolution that was obtained for this series of phosphates. The best-fit parameters that were used in simulating the spectra are given in Table I.

The spectra for the pyrophosphate (a singlet in the end-group spectral region) and tripolyphosphate (an end-group doublet and middle-group triplet) have been reported many times elsewhere.[9] Note that the center resonance of the tripoly middle-group triplet is composed of two closely spaced transitions; under optimum scan conditions, this multiplicity can be detected in experimental spectra. Also note that, consistent with the behavior of pseudo first-order NMR spectra, the intensities of the inner signals of each multiplet are greater than that of their outer counterparts. This phenomenon, which is also apparent in the spectrum of the tetrapolyphosphate, is observed experimentally.

The apparent complexity of the end-group multiplet goes from a simple doublet for the tripolyphosphate to a complicated second-order pattern for the tetrapolyphosphate. Although the end-group multiplet structure of the pentapolyphosphate is still quite complicated, the overall envelop is that of a doublet. On proceeding to the longer-chain polyphosphates, the simple-doublet appearance of the end-group multiplet becomes more pronounced.

A similar change in superficial appearance is observed for the middle-group region of the spectrum where the apparent triplet of the tripolyphosphate turns into more complicated patterns for the tetra- through hexapolyphosphates, with the overall shape of the envelop becoming simpler with increase in chain length until finally, for very long chains, a single resonance signal exhibiting a very narrow line width[2] at half-height is observed. Because of its unique symmetry as an aa'xx' molecule, the pattern in the end-group region of the tetrapolyphosphate ion is the mirror image of that in the middle-group region.

The theoretical spectra, which were plotted in Figure 3 assuming a spectral resolution of 0.5 Hz, give no indication of the great complexity of the transition patterns from which they result. For the linear array of spins involved in going from the di- through the octapolyphosphate, the number of transitions are 4, 8, 24, 66, 157, 432, and ca. 2000, respectively, for $Na_4P_2O_7$ through $Na_{10}P_8O_{25}$.

It should be emphasized here that the spectra shown in Figure 3 and the corresponding NMR parameters of Table I refer solely to the polyphosphate anions in aqueous solu-
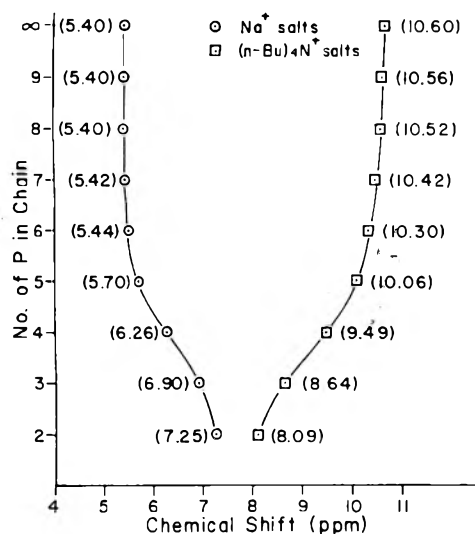
Figure 4. Chemical shifts of the end groups of the sodium and tetra-n-butylammonium polyphosphates at pH 10.2 (i.e., no associated protons, except for pyrophosphate). The numbers in parentheses give the precise values of the chemical shifts in ppm and ∞ symbolizes a polyphosphate glass of $\bar{n}$ = 100.8.
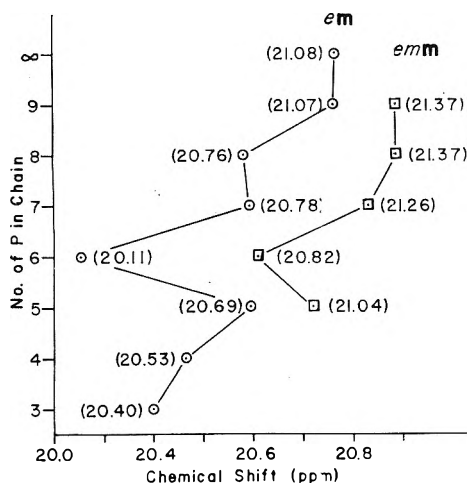

Figure 5. Chemical shifts of the middle groups of the sodium polyphosphates at pH 10.2. The numbers in parentheses give the precise values of the chemical shifts in ppm and ∞ symbolizes a polyphosphate glass of $\bar{n}$ = 100.8. Only the shifts of the second and third phosphorus atoms from the ends of the chains are plotted (em and emm, respectively).

tion at pH 10.2 in the presence of only sodium as the cation. Miscellaneous experiments with highly purified ortho-, pyro-, and trimetaphosphates have led us to believe that the presence of the EDTA in the solutions studied here has essentially no effect on the phosphate ^{31}P NMR parameters other than that of rendering a high degree of precision to the measurements; the reported chemical shifts are not moved by more than 0.1–0.2 Hz. The dramatic effect of changing the counterion while holding the pH constant is shown in Figure 4 in which the findings for the end groups of the sodium salts of the di- through the octapolyphosphate may be compared with those for the respective tetra-n-butylammonium salts. Analogous data have been presented for the cyclic metaphosphates.[13] Note in Figure 4 that the difference in chemical shift upon changing the cation becomes greater with increasing chain length and finally achieves constancy for the larger chain lengths.
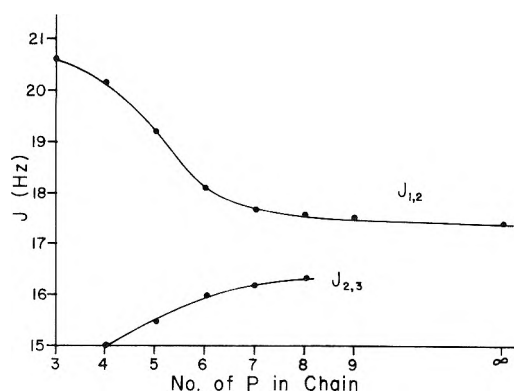

Figure 6. Variation of the coupling constants $J_{1,2}$ and $J_{2,3}$ with phosphate chain length, where phosphorus atom 1 is in an end group.

The change in the middle-group chemical shifts with increasing chain length is shown for the sodium polyphosphates in Figure 5. From comparison of the lower-field curve of Figure 4 with the curves of Figure 5, it can be seen that, for sodium as the cation, the chemical shift of the end groups changes more rapidly and in the opposite sense (downfield vs. upfield) with increasing chain length as compared to the chemical shifts of the middle groups. Also the middle-group variations are not smoothly regular as are those of the end groups. Other studies in these laboratories have shown that, for the tetra-n-butylammonium cation, there is very little change in the chemical shifts of the middle group with increasing polyphosphate chain length (such as that observed for the sodium cation) and that the middle-group and end-group chemical shifts change in the same direction (upfield) with increasing chain length. Moreover, the chemical-shift differences between the em (the middle groups immediately adjacent to the chain end groups) and the interior chain middles observed for the quaternary ammonium polyphosphates are much less (about 10 Hz) than those observed for the sodium polyphosphates. This results in pronounced crowding of the individual transitions, rendering impractical a rigorous computer-simulation analysis of all but the shorter members of the family.

Discussion

As shown in Figures 4 and 6, there is a smooth variation with increasing polyphosphate chain length of the end-group ^{31}P chemical shift as well as a smooth variation of the P–O–P coupling constants between the end and its neighboring middle group ($J_{1,2}$) and between this middle group and its neighboring middle group ($J_{2,3}$). However, in Figure 5, the middle-group chemical shifts vary irregularly with increasing chain length, with the most pronounced deviation from a smooth change occurring in the case of the hexapolyphosphate ion. Note in Figure 5 that the chemical shifts of the middle-group phosphorus atoms immediately adjacent to the end groups are upfield for the chains having an odd number of phosphorus atoms, as compared to the shifts of the neighboring even-numbered chains. Since none of this irregular behavior is found when the sodium counterions are replaced by noncomplexing tetraalkylammonium cations, it appears that these observations are related to the overall conformational ordering of the inherently flexible polyphosphate chains in relationship to the sodium ions with which they are complexed and/or associ-

ated. We are quite certain that the irregularity of the plots given in Figure 5 is a physically real phenomenon since these sets of points have been checked by using entirely different phosphate preparations and carrying through the full experimental and theoretical analysis. Furthermore, attempts at using points from various smooth curves drawn through the data from Figure 5 have consistently led to calculated spectra which simply did not fit the experimental observations. Extension of this study to pH 7 (where all end groups are partially protonated) led to the same situation in which the middle-group chemical shifts gave rise to virtually the same irregularities while the other NMR parameters again exhibited smooth variations with increasing chain length.

When the NMR spectrometer is well adjusted, the line width at half-height at pH 10.2 for the pyrophosphate ion is about 4 Hz; for the tripolyphosphate, about 1 Hz; and for the tetra- through the decapolyphosphate, about 0.5 Hz. As previously noted, phosphate chains exhibiting more than ca. 150 phosphorus atoms exhibits a line width approaching that of cyclic trimetaphosphate, a value which is essentially at the resolution limit of our spectrometer (ca. 0.2 Hz) at the time of these measurements. We conclude from these findings that the middle groups making up the long-chain phosphates are all in the same chemical environment so that in aqueous solution the macromolecular polyphosphate chains exhibit a regular configuration. In a previous publication, we have postulated that, for sodium as the countercation in aqueous solution, this configuration is a helix having three phosphorus atoms per turn.[13]

References and Notes

(1) T. Glonek, R. A. Kleps, E. J. Griffith, and T. C. Myers, *Phosphorus*, in press.
(2) T. Glonek, R. A. Kleps, E. J. Griffith, and T. C. Myers, *Phosphorus*, in press.
(3) T. Fleitmann and W. Henneberg, *Annalen*, 45, 304, 387 (1845).
(4) E. P. Partridge, V. Hicks, and G. V. Smith, *J. Am. Chem. Soc.*, 63, 454 (1941).
(5) R. K. Osterheld and R. P. Langguth, *J. Phys. Chem.*, 59, 76 (1955); R. P. Langguth, R. K. Osterheld, and E. F. Karl-Kroupa, *ibid.*, 60, 1335 (1956); also see R. P. Langguth, M.S. Thesis, Cornell University, Ithaca, N.Y., 1952; and M. Amadori, *Atti. R. Ist. Veneto Sci. Lett. Arti*, 76, 419 (1916).
(6) J. R. Van Wazer and K. A. Holst, *J. Am. Chem. Soc.*, 72, 639 (1950).
(7) J. R. Van Wazer, *J. Am. Chem. Soc.*, 72, 644 (1950).
(8) E. J. Griffith and R. L. Buxton, *J. Am. Chem. Soc.*, 89, 2884 (1967).
(9) M. M. Crutchfield, C. H. Dungan, J. H. Letcher, V. Mark, and J. R. Van Wazer, "P³¹ Nuclear Magnetic Resonance", in M. Grayson and E. J. Griffith, Ed., "Topics in Phosphorus Chemistry", Vol. 5, Wiley-Interscience, New York, N.Y., 1967.
(10) J. R. Van Wazer, *J. Am. Chem. Soc.*, 72, 647 (1950).
(11) J. R. Van Wazer, E. J. Griffith, and J. F. McCullough, *Anal. Chem.*, 26, 1755 (1954).
(12) E. J. Griffith and C. F. Callis, *J. Am. Chem. Soc.*, 81, 833 (1959).
(13) T. Glonek, J. R. Van Wazer, M. Mudgett, and T. C. Myers, *Inorg. Chem.*, 11, 567 (1972).
(14) P. S. Chen, T. Y. Toribara, and H. Warner, *Anal. Chem.*, 28, 1756 (1956).
(15) T. Glonek, J. R. Van Wazer, and T. C. Myers, *Bioinorg. Chem.*, 1, 1 (1971).
(16) J. M. Tanzer, M. I. Krichevsky, and B. Chassy, *J. Chromatogr.*, 38, 526 (1968).
(17) T. O. Henderson, T. Glonek, R. L. Hilderbrand, and T. C. Myers, *Arch. Biochem. Biophys.*, 149, 484 (1972).
(18) T. Glonek, T. O. Henderson, R. L. Hiderbrand, and T. C. Myers, *Science*, 169, 192 (1970).
(19) J. D. Swalen, Programs 33, 35, and 36 in the Quantum-Chemistry Program-Exchange Catalog, Chemistry Department, Indiana University, Bloomington, Ind., 1973.
(20) D. W. Matula, L. C. D. Groenweghe, and J. R. Van Wazer, *J. Chem. Phys.*, 41, 3105 (1964).

A Method for Quantitative Determination of a Small Difference between Diffusion Coefficients

L. Miller

National Chemical Research Laboratory, Pretoria 0001, Republic of South Africa *(Received September 18, 1974; Revised Manuscript Received January 27, 1975)*

Small differences between diffusion coefficients are determined by separative diffusion in the transient state. The method compares experimental results for cylindrical diffusion with computer results. As an example the isotope effect in the diffusion of uranyl nitrate in agar gel was investigated.

Introduction

It is impossible to determine the difference in the diffusion coefficients of two species A and B, $\Delta D = D_A - D_B$ by direct methods when the error in the experimental determination of D_A or D_B is $>\Delta D$. As the experimental accuracy is ~1%, this will always be the case when $\Delta D/D_{A,B} < 1\%$.

Separative diffusion of A and B through a barrier can then be used. For steady-state diffusion the separation factor is defined as the quotient of the concentration ratios c_B/c_A and c_B'/c_A' in front of and behind the barrier

$$S = \frac{c_B'}{c_A'} \Big/ \frac{c_B}{c_A} \tag{1a}$$
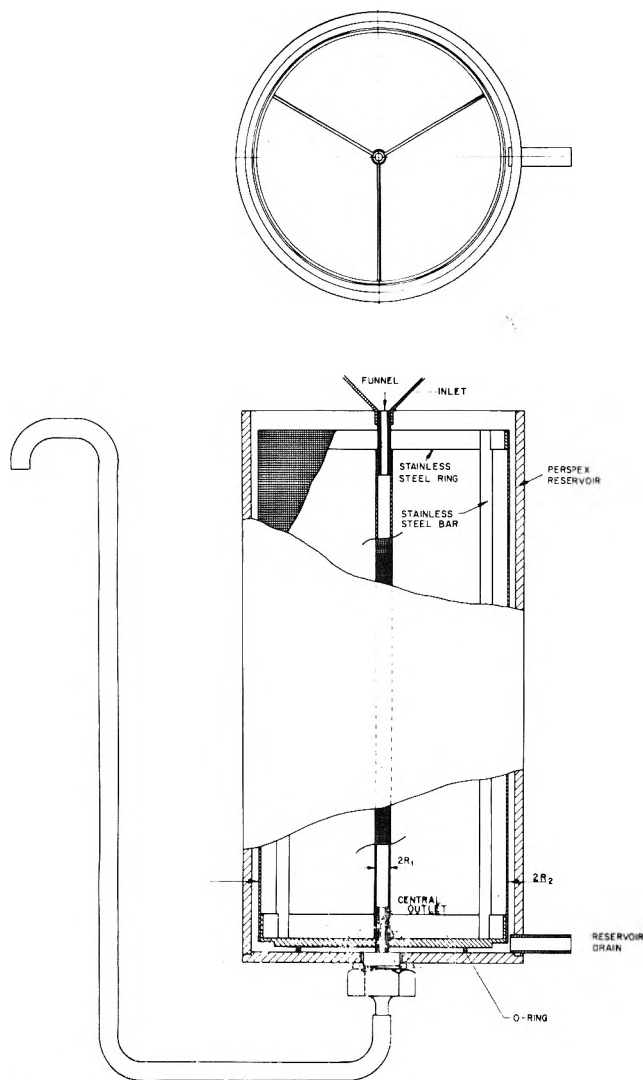
Figure 1. Concentration field in the cylinder. Parameters indicate Dt/R_2^2: St, steady-state curve for $R_2/R_1 = 9.4$; St', steady-state curve for $R_2/R_1 = 20$. The c values indicate fractions of the reservoir concentration (eq 2).

Figure 2. Integrated fluxes increasing with time. The dimension of Q depends on the kind of c (moles/cm^3 or g/cm^3) chosen in eq 2.

Figure 3. Separation factors curing the transient state. Calculations were made for $R_2/R_1 = 9.4$. In the experiment $R_2/R_1 = 20$. Influence on result is negligible in our case.

At steady state[1]

$$S = D_B/D_A \qquad (1b)$$

This equation can be used for the determination of ΔD but for isotopes the separation effect at steady state may still be so small as to be within the error limits of the mass spectrometric results.

The transient state, however, offers a substantially higher separation effect which can be used for accurate determination of ΔD. Equation 1b does not hold in the transient state and the concentration ratio at the output side, c_B'/c_A' in (1a), becomes time dependent. The experimental determination of c_B'/c_A' as a function of time would be very difficult. The concentrations due to the differential fluxes were thus replaced by the integrated fluxes $Q_1^{A,B}$ which will be defined later.

The separation factor for the transient state is

$$S^* = \frac{Q_1^B}{Q_1^A} \Big/ \frac{c_B}{c_A} \qquad (1c)$$

This paper compares experimental results for transient cylindrical diffusion with calculated results.

The Cylindrical Diffusion Problem

We consider a solid cylinder with outer mantle radius R_2 and length L. The end sections are impermeable. A coaxial channel has the radius R_1. The concentrations at the mantle are kept constant

$$c_A = c_B = 0.1 \qquad (2)$$

at R_2 at any time t. At the beginning of the diffusion the concentration inside the cylinder is zero

$$c_A = c_B = 0 \qquad (3)$$

at $t = 0$ for any r when $R_1 < r < R_2$. The material arriving at R_1 is removed by a stream of pure solvent. Thus

$$c_A = c_B = 0 \qquad (4)$$

at R_1 for any t. With the boundary conditions (2) and (4)

and the initial condition (3), the solution of the cylindrical diffusion equation for constant D

$$\frac{\partial c}{\partial t} = D\left(\frac{\partial^2 c}{\partial r^2} + \frac{1}{r}\frac{\partial c}{\partial r}\right) \qquad (5)$$

was computed with a finite-difference method. This was done for a standard A and three test substances B, B', and B'' with $D_A = 0.1 \times 10^{-5}$ cm^2/sec, $D_B = 0.1002 \times 10^{-5}$ cm^2/sec, $D_{B'} = 0.1005 \times 10^{-5}$ cm^2/sec, and $D_{B''} = 0.101 \times 10^{-5}$ cm^2/sec. Mutual interference is assumed to be absent during simultaneous diffusion. In the experimental procedure the separation of the substances which were extracted from the central channel up to a given time t was determined. Corresponding computations were made for the integrated fluxes $Q_1^{A,B}$ at $r = R_1$ for unit length, $L = 1$ cm.

$$Q_1^{A,B} = 2\pi R_1 \int_0^t D_{A,B}\frac{dc}{dr}\,dt \qquad (6)$$

Computer Results

An IBM 360/65 computer was used. The concentration field $c_A(r)$ inside the cylinder for a ratio $R_2/R_1 = 9.4$ is

Figure 4. Cylindrical diffusion apparatus.

given in Figure 1. Generalization is obtained by the parameters Dt/R_2^2 which can be considered as dimensionless times. The data were obtained from computations for two sets of $R_{1,2}$: $R_1 = 0.25$ cm, $R_2 = 2.35$ cm; and $R_1' = 0.106383$ cm, $R_2' = 1.000$ cm. This was done to verify the method and satisfactory agreement was obtained. The curve St is the steady-state curve and the broken line St' gives the steady state for $R_2/R_1 = 20$.

The integrated fluxes $Q_1{}^A$(output) and $Q_2{}^A$(input) as a function of $D_A t/R_2^2$ are shown in Figure 2 for $R_1 = 0.106383$; $R_2 = 1$ cm. This curve could be used for experimental determination of D but does not yield an acceptable precision. Figure 3 presents the separation factors $S^* = Q_1{}^B/Q_1{}^A$ (eq 1c and 2) for the different test species B, B', and B''. These curves are used for comparison with experimental results and for the determination of ΔD. This procedure requires a knowledge of the absolute value of D with the usual experimental accuracy. It can be seen from the curves that ΔD can be determined to about 0.1% under these conditions, except in the very early stages. Due to numerical instability, the S values become unreliable for short times, smaller than $Dt/R_2^2 = 0.02$.

Special computations showed that a slight violation of the boundary condition (2) does not affect S. A limited reservoir is therefore acceptable in the experiments.

Experimental Section

Cylindrical diffusion cannot be applied to the liquid phase if convection is not totally suppressed. This was achieved by working in the gel phase. It is known that gel diffusion is still representative for liquid diffusion. Solid agar gel cylinders were cast in situ within the diffusion apparatus as sketched in Figure 4. The gel cylinder ($2R_2 = 12.5$ cm, $L = 22$ cm) was supported by a frame of stainless steel bars and short pipe sections on which sleeves of stainless steel gauze were mounted. A removable glass cylinder around the mantle sleeve was sealed at the bottom of the reservoir by a 1 cm layer of agar gel. A stainless steel rod was introduced through the central sleeve into the central outlet and acted, together with the removable glass cylinder, as a mold.

Agar (3%) was dissolved in stages in boiling water with constant stirring until a clear solution was obtained. Casting was done when the temperature of the solution had dropped to 50° and the reservoir was filled with cold water to prevent melting of the lower sealing layer of agar gel. On the following day this gel layer, the glass cylinder, and the stainless steel rod were removed. A small glass funnel was fixed on top of the central channel where pure rinsing water was introduced dropwise by a peristaltic micropump.

Diffusion was started by filling the reservoir with 532 ml of concentrated solution of uranyl nitrate ($d = 1.233$). As a check on possible leakage the rinsing water was tested 4.5 hr after the start in a Geiger-Müller counter and background activity was found. All rinsing water was collected over a diffusion time of 100.5 hr. After evaporation the residue was recovered and 18 mg of $UO_2(NO_3)_2$ was found. This sample and the undiffused solution were analyzed with a mass spectrometer to give $Q_1{}^B/Q_1{}^A$ and c_B/c_A and thence the separation factor S^*.

Evaluation of ΔD from Figure 3 also requires the determination of D as mentioned above. A determination of D from Figure 2 would require the precise quantitative detection of a small amount of substance $Q_1{}^A$ from a very dilute solution. Furthermore, the absolute value of $Q_1{}^A$ is far more sensitive to changes in the reservoir concentration and the channel radius R_1 than the ratio $Q_1{}^B/Q_1{}^A$. D was therefore determined by the method of Freise[2] which is essentially a limited reservoir method.

Results

As found previously[3] the heavier isotope was slightly enriched after diffusion in the output at R_1. Mass spectrometric analysis of the diffused sample and of the undiffused solution (blank) gave the following results (U^{235}/U^{238}): blank, 0.007285 ± 0.000018; diffused sample, 0.007208 ± 0.000022.

The result for the diffusion coefficient of uranyl nitrate in 2% agar gel at 20° was $D = 0.716 \pm 0.176 \times 10^{-5}$ cm^2/sec (six measurements). With $t = 361,800$ sec and $R_2 = 6.25$ cm we get $Dt/R_2^2 = 0.0663$. At this abscissa $S = 0.007285/0.007208 = 1.0107$ is entered in Figure 3. Interpolation gives $\Delta D/D_A = 0.0025 \pm 0.0005$. The standard deviation reflects the large experimental scatter of D while the mass spectrometric scatter of S is ignored. This shows that the

method does not require a high accuracy of D. However, a higher sensitivity exists in regard to the experimental scatter of S and a consideration of the possible extreme values of S yields an error bound which is in our case increased by a factor of 3. As an error estimate, however, this would be very pessimistic. The magnitude of ΔD is supported by other experimental results which are not presented here because of minor variations in the experimental technique.

References and Notes

(1) R. A. W. Haul, *Naturwissenschaften*, **255**, 41 (1954).
(2) V. Freise, *Z. Phys. Chem.*, **4**, -29 (1955).
(3) L. Miller, *Ber. Bunsenges. Phy Chem.*, **75**, 206 (1971); *Nature (London)*, **243**, 32 (1973).

Ultrahigh Frequency and Microwave Relaxation of Lithium Perchlorate in Tetrahydrofuran

Herman Farber and Sergio Petrucci*

Departments of Electrical Engineering/Electrophysics and Chemistry, Polytechnic Institute of New York, Brooklyn, New York 11201
(Received May 16, 1974; Revised Manuscript Received January 22, 1975)

The complex permittivity of 0.05 M LiClO$_4$ in tetrahydrofuran (THF) at 25° in the frequency range 0.3–8.5 GHz has been measured. An admittance bridge was used in the frequency range 0.3–1.5 GHz and a power reflection method in the range 2–8.5 GHz. The real and imaginary parts of the permittivity follow a Cole–Davidson distribution of relaxation times with an average relaxation frequency f_R = 1.5 GHz and a distribution parameter β = 0.8. Including data reported in the literature the relaxation amplitude $\epsilon_0 - \epsilon_\infty$ of the solute is found to be a linear function of the concentration of ion pairs. The Cole–Davidson distribution parameter, β, is calculated by a modified Glarum theory which postulates that the diffusion-controlled collision between ion-pair dipoles couples with the diffusional rotational relaxation. The calculated value of β approximates the experimental distribution parameters including those for LiClO$_4$–THF–benzene mixtures.

Introduction

Electrolyte solutions have been investigated using dielectric spectrometry by several workers, notably by Hasted[1] in water and by Davis[2] in media of very low dielectric constants. The interpretation of the former systems was given in terms of the solvation of the ions and the subtraction of free rotating solvent molecules by the solvation in the coordination sphere of the ions. The work of Davis[2] showed in many instances an onset of a distribution of relaxation times. The interpretation was limited to the qualitative assignment of these complexities to the various dipolar species existing in solution as a result of ionic aggregations.

However, for 2:2 electrolytes in water, Pottel[3] succeeded in relating the dielectric spectrum to the relaxation of the diffusional rotation of different solvated ion pairs in addition to the water relaxation. This was based on the Eigen and Tamm theory[4] and the measurements[5] of ultrasonic spectra for the metal (II) sulfates in water with the hypothesis of the multistep solvent substitution mechanism by the ligand. The association constants of 2:2 electrolytes had been determined[6] by classical electrical conductance measurements. To apply the same sequence to other systems, the electrical conductance and the ultrasonic relaxation times were measured[7] for the system LiClO$_4$ in THF between −30 and 25°. Both, ion pairs and triple ions, existed in the concentration range of 10^{-5} to 10^{-1} M, and the for-

mation constants for the two species were determined. Ultrasonic data were interpreted as the equilibrium between ion pairs and triple ions. The rate constants and the activation energy indicated that the process was diffusion controlled.

The uhf and microwave data reported in this work are used to develop a microscopic interpretation of the dielectric spectra. The current data for 0.05 M LiClO$_4$ solutions adds to the available data for 0.25–0.6 M solutions at 30°.[8] It was important to have data for the same system in a broad concentration range, both to check on the reliability of the results and for the interpretation.

Experimental Section

Preparation of Materials. Every precaution was taken to ensure the purity of the chemicals and to eliminate traces of water. The tetrahydrofuran (THF, Matheson Coleman) was distilled in a dry nitrogen atmosphere over a K–Na (60% K) alloy in a 3-ft Vigreaux column. Anhydrous reagent LiClO$_4$ (Smith, Cleveland, Ohio) was kept for 24 hr at 60° and 1 Torr. No appreciable loss of weight was noticed with respect to the starting material. Some of the samples of salt were kept at 190° and at atmospheric pressure for 1–2 days with no change. Solutions were prepared by dissolving a dried weighed sample of LiClO$_4$ in freshly distilled THF in volumetric flasks. These operations were

performed in a dry N_2 filled drybox. Contact with the atmosphere was never longer than 30–60 sec when filling the dielectric cell. To check the reproducibility of the data, the dielectric measurements were repeated for two–three different, freshly prepared solutions over a period of 1 year.

Uhf Measurements. The complex permittivities of THF and of the solutions of $LiClO_4$ were measured in the frequency range of 0.3–1.5 GHz using a General Radio uhf admittance bridge, Model 1602B. The details for making this measurement are given by Mopsick[9] and Glarum.[10]

The Dielectric Cell. A GR874 (D20L) tuning stub was modified by a set of flanges which were used as mounts for a Teflon window. A water jacket also was added to maintain constant cell temperature. The completed dielectric cell and the admittance bridge were mounted on a rigid reference frame and on a sliding platform, respectively.

Procedure. The distance between the bridge and the window of the empty dielectric cell was adjusted so that the equivalent electrical position of the dielectric window was at the bridge center. After filling the cell, the cell length was varied and the cell lengths for conductance minima were noted. These values were reproducible to ±0.003 in. and ±0.2 mmhos the latest as read on the conductance scale of the bridge.

The number of minima that can be determined accurately decreases with increasing loss tangents of the liquid dielectric.[9]

Calculation of the Complex Dielectric Constant. The normalized admittance of the dielectric filled cell for these conditions is

$$Y = \frac{G}{G_0} = \frac{\lambda_0}{4\pi l} \left\{ \frac{b \sinh a - a \sin b}{\cosh a - \cos b} \right\}$$

or

$$Y_n = \frac{G_n}{G_0} = \frac{\lambda_0}{\lambda} \frac{1}{n\pi} C_n(a, b)$$

where G_0, the characteristic transmission line conductance, is equal to 20 mmhos; G is the conductance as measured on the bridge; $a = 2\alpha l$; $b = 2\beta l$; l is the length of the dielectric cell; λ_0 = free space wavelength; λ = wavelength in dielectric medium; and $\gamma = \alpha + j\beta$, the complex propagation constant of the dielectric filled line.

The values of G_n are the bridge readings at the bridge balances (absolute minima), $l = (n\lambda/4)$ where $n = 1, 3, 5$ . . . .

The least-squares plot of l vs. n gives as a slope $dl/dn = \lambda/4$.

The function, $C_n(a,b)$, has been tabulated by Mopsik[9] for $n = 1, 3$, and 5. A computer program has been set up for larger values of n up to $n = 11$ giving the values of $a^2 - b^2$ and $2ab$.

The real and imaginary parts of the complex dielectric constant $\epsilon = \epsilon' + j\epsilon''$ may then be calculated from the following equations:

$$\epsilon' = \left(\frac{\lambda_0 \beta}{2\pi}\right)^2 \left\{1 - \left(\frac{\alpha}{\beta}\right)^2\right\} = \left(\frac{\lambda_0}{\lambda}\right)^2 \left[1 - \left(\frac{\alpha\lambda}{2\pi}\right)^2\right]$$

$$\epsilon'' = \left(\frac{\lambda_0 \beta}{2\pi}\right)^2 \frac{2\alpha}{\beta} = \left(\frac{\lambda_0}{\lambda}\right)^2 \frac{\alpha\lambda}{\pi}$$

These calculations may be simplified as follows: for low loss dielectrics $C_n(a,b) \approx n\pi a/2$. For the conditions $a \ll b$ and $\alpha \ll \beta$ then $\epsilon' \approx (\lambda_0/\lambda)^2$ and $\epsilon'' \approx \epsilon'^{1/2}(4Y/n\pi)$.

Microwave Frequency Measurements. At microwave frequencies (2–4 and 8–10 GHz) the power reflected from

the dielectric cell was measured as a function of cell length. The analysis was similar to the one described by Cutnell.[11]

Equipment. A modified reflectometer set up was used to make the measurements in both frequency ranges. The liquid dielectric cells were similar to the ones used for the uhf measurements.

Procedure. The reflected power from the dielectric cell was measured continuously as the cell length was varied until a final length was reached when the power no longer varied (Figure 1). The maximum useable cell length is dependent on the loss tangent. For high loss tangents the total microwave power is almost completely absorbed in a short dielectric cell and the measured reflected power comes from the dielectric–window–air interfaces.

Data Reduction to Calculate ϵ' and ϵ''. The reflected power periodically goes through maxima and minima and the periodicity of each of these is equal to $\lambda/2$. Cutnell[11] has shown that the maximum points (n odd)

$$e^{-(\alpha/\beta)(n\pi - R)} = \frac{\Gamma - \Gamma_\infty}{1 - \Gamma_\infty \Gamma}$$

and for the minimum points (n even)

$$e^{-(\alpha/\beta)(n\pi - R)} = \frac{\Gamma_\infty \mp \Gamma}{1 \mp \Gamma_\infty \Gamma}$$

where α is the attenuation constant, β is the phase constant $= 2\pi/\lambda$, R is the phase change of the reflected wave $= \pi$ for an ideal short circuit, Γ is the voltage reflection coefficient, and Γ_∞ is the voltage reflection coefficient for a dielectric cell which is electrically infinitely long. The plus sign is chosen when $\Gamma_\infty < e^{-(\alpha/\beta)(n\pi - R)}$ for n even.

A convenient reference power level is the reflected power when the electrical length of the dielectric cell is infinite (Γ_∞).

A semilog plot of $(\Gamma - \Gamma_\infty)/(1 - \Gamma_\infty\Gamma)$ vs. n for n odd or $(\Gamma_\infty \mp \Gamma)/(1 \mp \Gamma_\infty\Gamma)$ vs. n for n even will have a slope of $-\alpha\pi/\beta = -\alpha\lambda/2$ and an intercept of $(\alpha/\beta)R$. (See Figure 2.)

Small deviations of the value of the intercept are the result of a nonideal window and window support, and a nonideal sliding short circuit.[11]

The same equations for calculating the complex permittivity from α, β, and λ_0 in the uhf case also apply in the microwave frequency range.

Calculations and Results

The overall measurement procedure was checked by measuring the complex permittivity of the solvent (THF) at 25°. In the frequency range of 0.3–3 GHz the measured value of $\epsilon' = 7.40 \pm 0.02$ is within experimental error of the value at radio frequencies, $\epsilon' = 7.39$,[12] and the recent value by Lestrade, $\epsilon' = 7.36 \pm 0.03$,[13] in the same frequency range. The imaginary part of the permitivity, ϵ'', agreed within ±0.02 units with published values at 30[8] and 25° [13] in the complete frequency range of 0.3–8.5 GHz.

The measured values of the permittivity of THF and of 0.05 M $LiClO_4$ in THF at 25° are presented in Table I.

The reduced Cole–Cole plot of ϵ_R'' vs. ϵ_R' is shown in Figure 3a where $\epsilon_R'' = \epsilon_d''/(\epsilon_0 - \epsilon_\infty)$ and $\epsilon_R' = (\epsilon_d' - \epsilon_\infty)/(\epsilon_\infty - \epsilon_0)$. ϵ_0 and ϵ_∞ are the low- and high-frequency values of the permittivity with respect to the solute relaxation.

The quantities ϵ_d' and ϵ_d'' refer to a relaxation process not observable in the pure solvent. They are related to ϵ' and ϵ'' by the following equations:[14]

$$\epsilon_d'(\omega) = \epsilon'(\omega) + [\epsilon_s' - \epsilon_s'(\omega)]$$

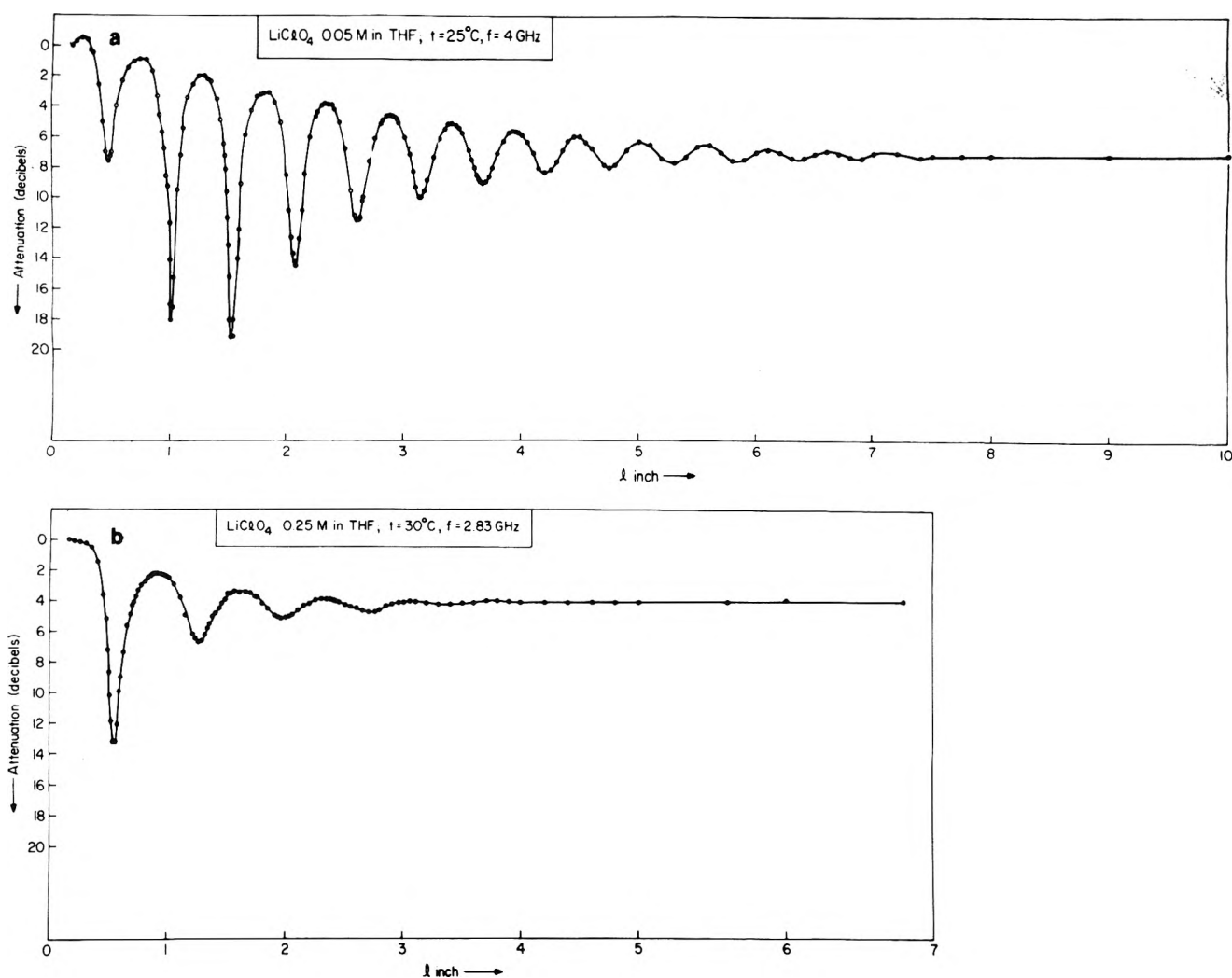$$\epsilon_d''(\omega) = \epsilon''(\omega) - \epsilon_x'' - \epsilon_s''(\omega)$$

Figure 1. Power profiles of the reflected wave of (a) LiClO₄ 0.05 M in THF at 25° and f = 4.0 GHz and (b) LiClO₄ 0.25 M in THF at 30° and f = 2.83 GHz.
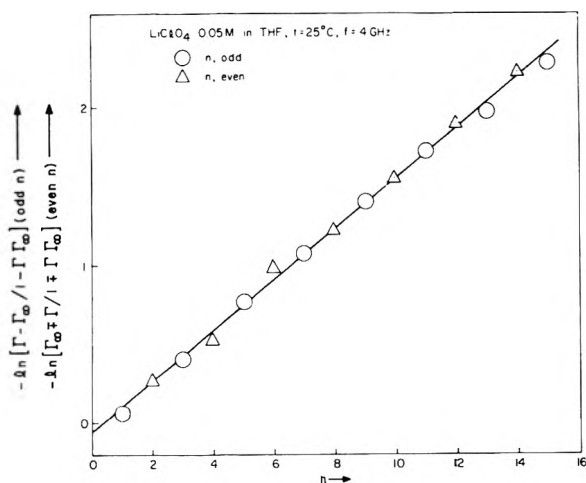

Figure 2. Sample of the functions $-\ln[(\Gamma - \Gamma_\infty)/(1 - \Gamma_\infty\Gamma)]$ vs. odd n's and of $-\ln[(\Gamma_\infty \mp \Gamma)/(1 \mp \Gamma\Gamma_\infty)]$ vs. even n's. LiClO₄ 0.05 M in THF; t = 25°, f = 4.0 GHz.

The correction factor $\epsilon_s' - \epsilon_s'(\omega)$, due to the solvent relaxation at the angular frequency $(\omega = 2\pi f)$, is significant only for f = 4 and 8.5 GHz for the reported system. The corrections are 0.04 and 0.31 units at 4 and 8.5 GHz, re-

spectively. ϵ_x'' is the dc conductance contribution to ϵ'' and $\epsilon_x'' = 1.8 \times 10^{12}\ x/f$ where x is the specific conductivity of 0.05 M LiClO₄ in THf at 25°.

The approximation of $\epsilon_s \approx \epsilon_\infty$ for the solute relaxation is within experimental error for the 0.05 M solutions studied in this work. (The measurements,[8] made at higher concentrations, gave specifically for c = 0.6 M, $(\epsilon_s - \epsilon_\infty)$ = 7.24 − 6.0 = 1.24, for c = 0.25 M, $(\epsilon_s - \epsilon_\infty)$ = 7.24 − 7.09 = 0.15. From these data one can estimate that for c = 0.05 M, $(\epsilon_s - \epsilon_\infty)$ = 0.03 − 0.05. These latter values are on the order of the experimental errors in the measurement of ϵ'.)

The solid line in Figure 3a is the Cole–Davidson function for an asymmetric distribution of relaxation times referred to the solute relaxation. The fit has been obtained with ϵ_0 = 8.35, β = 0.8, and $\epsilon_\infty = \epsilon_s = 7.4$. The dotted line is the Debye semicircle corresponding to a single relaxation function.

The approximations that were used to evaluate the above results have been discussed in the literature. The use of the specific conductance x evaluated at audiofrequencies[7] in the microwave frequency range implies[1,8] that the Falkenhagen effect of the frequency dependence of conduction was disregarded.

Similarly, the use of the correction terms $[\epsilon_s' - \epsilon_s'(\omega)]$ and ϵ_s'' implies that the relaxation of the solvent is not af-

TABLE I: Complex Permittivity of THF and LiClO$_4$ 0.05 M in THF at 25.0°

Fre-quency, GHz	THF		LiClO$_4$ in THF, C = 0.05 M	
	ϵ'	ϵ''	ϵ'	ϵ''
0.30	7.42	0.043	8.32 ± 0.02	0.32 ± 0.02
0.50	7.42	0.063	8.31 ± 0.03	0.33 ± 0.01
0.60	7.42	0.074	8.29 ± 0.04	0.37 ± 0.02
0.90	7.38	0.091	8.18 ± 0.01	0.44 ± 0.02
1.20	7.38	0.110	8.09 ± 0.03	0.50 ± 0.01
1.50	7.38	0.13	7.96 ± 0.05	0.59 ± 0.02
2.00[a]			7.91 ± 0.03	0.61 ± 0.06
3.00	7.39	0.29	7.72 ± 0.03	0.67 ± 0.04
4.00	7.36	0.37	7.58 ± 0.02	0.72 ± 0.08
8.5$_2$	7.09	0.74	7.14	0.87

[a] The reflection technique applied to pure THF gave poor results at this frequency since the attenuation was too small. Similarly the highest frequency for the uhf bridge is f = 1.5 GHz.
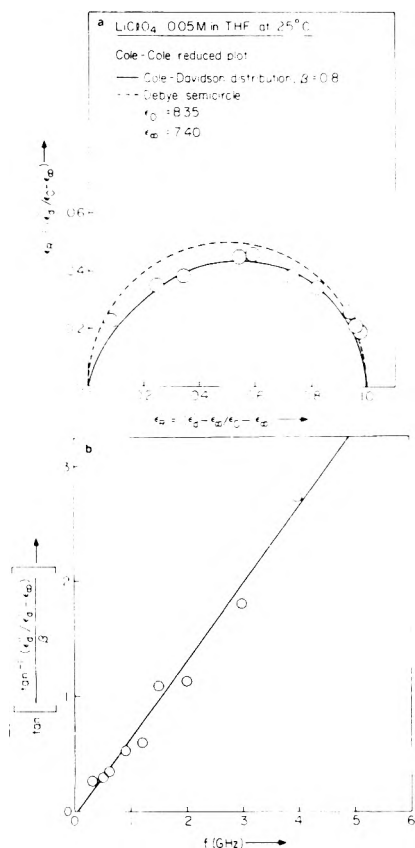
Figure 3. Relaxation behavior for LiClO$_4$ 0.05 M in THF at t = 25°. (a) Cole–Cole plot: ϵ_R'' vs. ϵ_R'. (b) Plot of the function tan $\{[\tan^{-1}(\epsilon_d''/\epsilon_d' - \epsilon_\infty)]/\beta\}$ vs. f. $\epsilon_\infty = \epsilon_s = 7.4$, $\beta = 0.80$.

fected by the solute.[14] Lestrade[8] avoided this approximation using a computer analysis of all of the relaxation spectra, including an additional datum at 35 GHz, namely, including the solvent relaxation in the analysis. However, even in this analysis[8] the value of $\epsilon_{\infty 2}$ for the pure solvent was retained because of the lack of data for frequencies higher than 34.7 GHz.

The complex permittivity is related to the Cole–Davidson distribution parameter β and the loss angle δ by the relationship:[15]

Figure 4. (a) ϵ_d' vs. f. (b) ϵ_d'' vs. f.
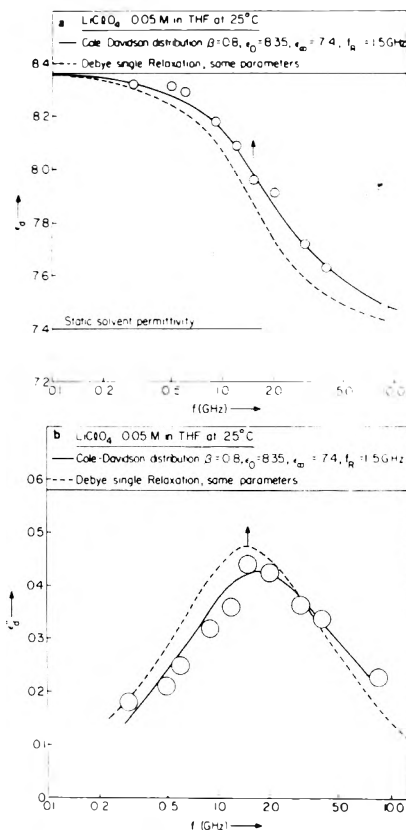
$$\epsilon_R' + j\epsilon_R'' = \cos^3 \delta \cos 3\delta + j \cos^3 \delta \sin 3\delta$$

Therefore a plot of tan $[\tan^{-1}(\epsilon_d''/\epsilon_d' - \epsilon_\infty)/\beta]$ vs. f, shown in Figure 3b, gives a straight line with a slope $1/f_R$. The slope gives f_R = 1.5 GHz.

As a further check on these parameters, ϵ_0, β, and f_R, a plot of ϵ_d' vs. f and ϵ_d'' vs. f are shown in Figure 4a and 4b. The solid lines are the calculated Cole–Davidson distribution functions and the dashed lines are the corresponding Debye functions by retention of the same ϵ_0 and f_R. The final results indicate that a Cole–Davidson distribution function with β = 0.8 can fit the data. Similar conclusions were reached by Lestrade et al.[8] at higher concentrations of LiClO$_4$ with corresponding values of β.

Discussion

Previous theories and results are reviewed briefly to develop a quantitative microscopic interpretation of the dielectric relaxation spectra of LiClO$_4$ in THF. The first[2] viewpoint is that the relaxational behavior is a result of dipolar rotation. The dipolar rotation is a result of all species such as ion pairs, complexes, and other species with a net dipole moment different from zero which exist with a lifetime long enough to interact with the microwave field.[14]

Recently, concepts from irreversible statistical thermodynamics concerning induced dipoles produced by ionic collisions and the general mechanism of the relaxation of transport of charges have been used.[8,16] Particularly, the autocorrelation functions and their applicability to dielectric properties as outlined by Kubo[17] have been used by various authors to calculate the distribution parameters of Cole–Davidson which, in some cases,[8] describe the dielectric behavior of a locus plot of ϵ'' vs. ϵ'.

The following discussion is an evaluation of the relative merits of the two approaches.

(1) Relaxation processes other than those of the solvent are absent for 1:1 electrolytes in water and in all polar solvents of intermediate permittivity[18] where association is absent. Only a depression in the static permittivity occurs which increases with electrolyte concentration.[1,18] This is interpreted as a solvation effect as a result of a depletion of some solvent dipoles which coordinate around the ions. Therefore *if the transport of charge was the only source of the observed dielectric relaxation process it is not apparent why the relaxation should be absent when the electrolyte is completely ionized and more ions are present per unit concentration.*

(2) Relaxation processes, separate from the one of the solvent, are present generally when ionic association is present. Examples of such systems are Bu₄NBr in acetone,[14] tributylammonium picrate and tributylammonium iodide in acetone, in 1,2-dichloroethane, in CHCl₃, and in THF.[19] These show association and a Debye relaxation behavior which was interpreted[14,19] as a diffusional dipolar rotation relaxation.

(3) In very low dielectric constant media the relaxation spectrum becomes very complex and generally non-Debye type. This may be due to overlapping of the relaxation spectra of several dipolar species[2] such as ion pairs, quadrupoles, etc.[2] Electrical conductance studies had indicated the presence of such species.[20] However, no current theory gives a quantitative evaluation of the formation constants using conductance data, except for ion pairs and triplets.

(4) Comparisons of solutions of the same electrolyte in media of progressively lower permittivity, e.g., Bu₄NBr in acetone,[14] pentan-3-one,[16] and 1,2-dichloroethane,[16] show that whereas the former system exhibits a Debye relaxation, the latter two systems exhibit a non-Debye behavior with a Cole–Cole distribution parameter different from zero. A plot of the reported equivalent conductances,[16] Λ, vs. concentration shows no minimum which demonstrates the absence of triple ions. Unfortunately, conductance data cannot distinguish the presence of neutral aggregates larger than ion pairs. Such aggregates are detectable only if triple ions are present as an intermediate species between ion pairs and larger aggregates.

The dielectric relaxation spectra of LiClO₄ in THF is analyzed taking into account the above discussion, published results,[7] and the results of the current investigation. Detailed audiofrequency conductance and ultrasonic measurements[7] have shown that for a LiClO₄–THF system the electrolyte is largely associated into ion pairs. Analysis of the conductance data up to 0.1 M indicated that some triplets and relatively few free ions are also present. The formation constants at 25° for ion pairs and for triplets are $K_A = 4.84 \times 10^7 \, M^{-1}$ and $K_T = 153 \, M^{-1}$, respectively.

Table II shows that (assuming these two species are the only ones present in the concentration range studied) the major portion of the electrolyte is in the form of ion pairs. Thus it is probable that these species should be involved in the observed relaxation process. Previous analysis[8,13] only had assumed collision-induced dipoles due to linear Brownian diffusion of free ions. This was due to the lack of knowledge[8,13] of the species in solution.

If ion pairs are involved in the dielectric phenomenon, it should be reflected in the relaxation amplitude ($\epsilon_0 - \epsilon_\infty$) as is demonstrated in Figure 5.

This quantity (at $C = 0.05 \, M^7$ and from Lestrade[8] at $C = 0.25, 0.40,$ and $0.60 \, M$ at 30°) is plotted against the con-

TABLE II: Concentrations of the Various Species for LiClO₄ in THF

C, M	$[A^+] = [B^-]$	$[A\,B]$	$[A\,B_2] = [A_2\,B]$
0.05[a]	3.2×10^{-5}	0.049	2.5×10^{-4}
0.25[b]	7.3×10^{-5}	0.242	$2.7_5 \times 10^{-3}$
0.40[b]	9.1×10^{-5}	0.383	5.6×10^{-3}
0.60[b]	11.2×10^{-5}	0.569	1.0×10^{-2}

[a] $t = 25°$. [b] $t = 30°$. The difference in K_A and K_T between 25 and 30° has been neglected.
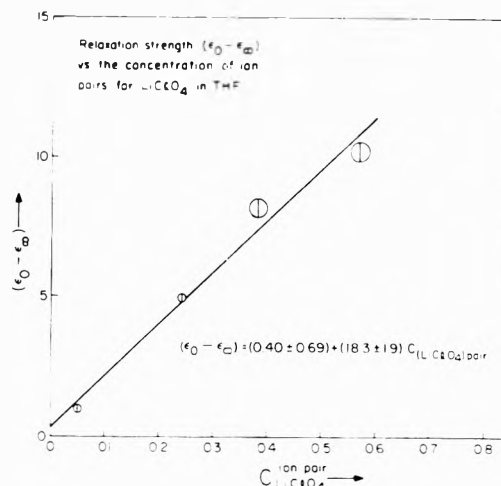
Figure 5. Plot of the quantity ($\epsilon_0 - \epsilon_\infty$) vs. the concentration of ion pairs C_{AB} for LiClO₄ in THF. The solid line is the calculated function by linear least-squares analysis.

centration of the ion pairs $C_{LiClO_4} = C(1 - \alpha - 3\alpha_T)$, with α and α_T the respective degree of dissociation of the two species. Figure 5 shows an approximate linear relationship which would be anticipated on the hypothesis that the rotation of the ion pairs produces the increased permittivity with respect to ϵ_∞ for the solute relaxation. As previously noted, ϵ_∞ for the solute relaxation is generally lower than ϵ_s for high concentrations of electrolyte.

Similar results were noted for tributylammonium picrate and tributylammonium iodide in various solvents when $K_A = 10^5$ to $10^{20} \, M^{-1}$ and where the major portion of the electrolyte exists as ion pairs.[19] However, two considerations are to be taken into account before accepting that ion pair rotation contributes to the difference $\epsilon_0 - \epsilon_\infty$.

The first point to be considered is the lifetime of the ion pairs with respect to the dielectric relaxation time, of the order of 10^{-10} sec. The forward rate constant for diffusion controlled approach of two ions to form an ion pair, following the Debye–Smoluchowski theories,[21] is

$$k_D = \frac{8LkT}{3000\eta} \frac{-b}{e^{-b} - 1}$$

with $b = |Z_1Z_2|e^2/aDkT$. Assuming the interatomic distances within the solvated ion pair to be[7] $a \approx 4 \times 10^{-8}$ cm and $D = 7.4, b = 18.94$ then $k_D \approx 2.72 \times 10^{11} \, M^{-1}$ sec^{-1}.

Assuming a one-step process the reverse rate of diffusion is $k_R = k_D/K_A = 5.44 \times 10^3$. The half-time for the first-order dissociation reaction should be $t_{1/2} = \ln 2/k_R = 1.3 \times 10^{-4}$ sec, which is the half-time of the existence of the ion pairs. This period is much longer than the dielectric relaxation time. Compared to the period of the microwave signal

(10^{-9} to 10^{-10} sec) the ion pairs may be considered as permanent dipoles, even if the association to an ion pair is a two-step process, with $K_A = K_0(1 + K_1)$ where K_0 is the outer-sphere formation constant. K_0 as given by the Fuoss theory,[22] modified by Jagodzinski,[7] is equal to 1.64×10^5 M^{-1} for $a = 4 \times 10^{-8}$ cm, thus $t_{1/2} = 4.2 \times 10^{-5}$ sec.

The second point to be considered is whether only "contact" ion pairs contribute to the difference $\epsilon_0 - \epsilon_\infty$ as is implicit in the above development. According to Bjerrum, ion pairs exist up to the distance of $q = |Z_+Z_-|e^2/2DkT = 38 \times 10^{-8}$ cm for a 1:1 electrolyte in a medium of permittivity $D = 7.4$ at $T = 298.15°K$. Then an inversion of position of two oppositely charged ions as far apart as 38×10^{-8} cm could still increase the permittivity. However, the distribution of ions with distance must be considered. According to the Bjerrum distribution function, the probability of finding an ion within the distance r to $r + dr$ from a reference ion is given by

$$dP = 4\pi r^2 \exp\frac{|Z_+Z_-|e^2}{rDkT} n\, dr$$

where n = number of ions per unit volume.

The ratio of the probabilities of finding an ion at the distance q with respect to the distance a $(4 \times 10^{-8}$ cm), for a unit range dr is given by

$$\frac{dP_1}{dP_2} = \frac{q^2}{a^2}\frac{\exp(|Z_+Z_-|e^2/qDkT)}{\exp(|Z_+Z_-|e^2/aDkT)} = \frac{q^2}{a^2}\frac{\exp 2}{\exp b} = 4 \times 10^{-6}$$

Stated in other terms, the average distance of an ion pair will be given by the relation[7]

$$\langle r \rangle = \frac{\displaystyle\int_a^q 4\pi r^3 \exp(|Z_+Z_-|e^2/rDkT)n\, dr}{\displaystyle\int_a^q 4\pi r^2 \exp(|Z_+Z_-|e^2/rDkT)n\, dr} \approx$$

$$a\left(1 + \frac{1}{b}\right) \approx a$$

for large values of b. Therefore at low dielectric constants, the overwhelming majority of ion pairs will be at the contact distance a.

Values of a between 2.0 and 3.74 Å, depending on the theory used for the association constant K_A, were obtained by conductance data.[7] The above figures are in reasonable accord with the value calculated using dielectric constant data ($\epsilon_0 - \epsilon_\infty$) for $LiClO_4$ in the THF.

If one assumes the quantity ($\epsilon_0 - \epsilon_\infty$), associated to the solute relaxation, to be due to the rotation of ion pairs, from the Böttcher theory as modified by Knight,[19] one has

$$(\epsilon_0 - \epsilon_\infty) = 4\pi\frac{10^{-3}Lc}{(1 - \alpha f)^2}\frac{\mu^2}{3kT}\frac{3\epsilon_0}{2\epsilon_0 + 1}$$

where $f = (2\epsilon_0 - 2)/(2\epsilon_0 + 1)a^3$, is the reaction field factory, a is the cavity radius, and α is the polarizability of the dipole having moment μ located at the center of the cavity.

Assume $\alpha = 5.4 \times 10^{-24}$ cm³ as calculated from refraction data.[23] By retaining $a = 4 \times 10^{-8}$ cm and $\epsilon_0 = 8.35$ as found above for 0.05 M $LiClO_4$, $f = 1.29 \times 10^{22}$ cm⁻³ and $\alpha f = 0.0695$ which gives $(1 - \alpha f)^2 = 0.865$. Neglecting this correction factor and using the average value ($\epsilon_0 - \epsilon_\infty$)/$C = 18.3$ as calculated above using least squares, one has $\mu = 14.5 \times 10^{-18}$ esu cm. Taking $\mu = ae$, then $a = 3.0 \times 10^{-8}$ cm, which is the same order of magnitude as the value calculated[7] from the conductance association constant K_A.

However if the relaxation process observed from $LiClO_4$ in THF is due only to the *independent* rotation of ion

pairs, then a pure Debye relaxation should have been observed. Instead, a Cole–Davidson distribution is observed. Moreover there is a broadening, with concentration, of the Cole–Davidson distribution of relaxation times. In fact, we have reported $\beta = 0.8$ at $c = 0.05$ M, whereas Lestrade et al.[8] reported $\beta = 0.65$ at $c = 0.6$ M.

Several molecular mechanisms may be responsible for the appearance of a Cole–Davidson distribution. The presence of two overlapping Debye processes having different statistical weight (different relaxation amplitude) would be the more obvious cause of a Cole–Davidson distribution. "Outer-sphere" and "contact" ion pairs having different dipole moments may have a different rotational relaxation time (this would include the discrete molecular nature of the solvent at variance with the distribution calculation shown above). However, such arguments would remain speculative rationalizations because of the lack of experimental evidence of the simultaneous presence of these species for $LiClO_4$. We prefer a hypothesis based on the decrease of independence of the free rotation of ion pairs with increasing concentration. The fact that, as shown below, by this environmental effect, we are able to reproduce the experimental Cole–Davidson distribution parameter β fairly well, gives credence to the validity of the hypothesis.

Schwartz[24] has dealt with dipolar orientation processes in competition with chemical reactions. However a theory similar to the one developed by Glarum[25] may be more directly applicable. Accordingly defects in molecular liquids cause instantaneous relaxation of the rotation of the dipoles upon encounter. This is a result of the zero viscosity in the cavity of the defects. A one-dimensional diffusion walk approach for the cavity[25] shows that a distribution function extremely close to a Cole–Davidson one is predicted whenever the relaxation time of the linear diffusion process is comparable to the rotational diffusional relaxation time. In other terms the dielectric process becomes cooperative. The functional form for β predicted by the theory is[25]

$$\beta = \frac{(\tau_{dif}/\tau_D)^{1/2}}{1 + (\tau_{dif}/\tau_D)^{1/2}} \tag{I}$$

where τ_{dif} is the relaxation time for the diffusion process and $\tau_{dif} = l_0^2/D$; l_0 is the average distance of diffusion and D is the diffusion coefficient of the cavity. In particular for $\tau_{dif} = \tau_D$, $\beta = 0.5$. Glarum's theory[25] may be applied to the $LiClO_4$–THF system by identifying the diffusing defects as the ion pairs themselves colliding with other ion pairs (while rotating under the influence of the external field) because of mutual diffusion. As a result of a collision the two ion pairs may "lose" the field because of a new dipole moment and moment of inertia of the momentary quadrupole.[25]

Previous analysis of conductance[7] data in the concentration range 10^{-5} to 0.1 M did not demonstrate the presence of such species. However, we are dealing here with dielectric data in the concentration range 0.05–0.6 M and the presence of these aggregates cannot be excluded. Hemmes[27] has shown for $LiNO_3$ in THF that the slope of the Λ vs. c plot may be affected by quadrupoles. Indeed an inflection in the Λ–c plot (log–log) was noticed[7] for $LiClO_4$ in THF at concentrations larger than 0.1 M.

To evaluate $\tau_{diff} = l_0^2/D$ the diffusion coefficient D of the ion pairs may be evaluated from the Stokes–Einstein relation $D = kT/6\pi\eta r$; for the ion pair distance,[7] $r = 3.74 \times 10^{-8}$ cm, $D = 1.3 \times 10^{-5}$ cm² sec⁻¹. $2l_0$ is the distance between the next-neighbor cavities in the Glarum theory,[25]

TABLE III: Calculation of the Cole–Davidson Distribution Function β for LiClO$_4$ in THF by the Glarum Theory

C, M	l_0, cm	τ_{dif}, sec^a	τ_D, sec^a	β_{calcd}	β_{expt}	Ref
0.05	20.3×10^{-8}	3.15×10^{-9}	0.9×10^{-10}	0.86	0.80	b
0.25	11.8×10^{-8}	1.08×10^{-9}	1.28×10^{-10}	0.74	0.79 ± 0.06	c
0.40	10.1×10^{-8}	7.88×10^{-10}	1.92×10^{-10}	0.67	0.53 ± 0.04	c
0.50	8.85×10^{-8}	6.02×10^{-10}	1.68×10^{-10}	0.65	0.65 ± 0.05	c

^{a} $\tau_{dif} = l_0^2/D$. τ_D = dielectric relaxation time. ^{b} This work. ^{c} Reference 8.

hence l_0 is the average distance a dipole must diffuse in each direction to meet a cavity. This distance $2l_0$ in our case is the average distance between half the ion pairs taken as randomly distributed. Therefore

$$2l_0 = \left[\frac{1}{\frac{1}{2}c_{pair} \times 10^{-3}L}\right]^{1/3} \simeq \left[\frac{1}{\frac{1}{2}c \times 10^{-3}L}\right]^{1/3}$$

where c_{pair} is the concentration of ion pairs (mole/liter), approximated to the stoichiometric concentration because $K_A = 4.8 \times 10^7\ M^{-1} \gg K_T > K_{quadrupole}$.[27] L is the Avogadro number; the factor $\frac{1}{2}$ accounts for the fact that the ion pair is considered alternatively cavity and rotating dipole. The values of l_0 and of τ_D for $c = 0.05\ M$ at 25° measured in this study and at $c = 0.25$–0.40 and $0.60\ M$ at 30°[8] are reported in Table III together with the calculated values of β from eq I. The calculated and the experimental values of β are in agreement with the exception of the value of $c = 0.4\ M$[8] where the experimental results show also an inversion in the trend of ϵ_∞ with concentration. Also as the concentration increases τ_{dif} becomes shorter and closer to the value of τ_D. The process becomes cooperative and β tends toward 0.5 as predicted by the Glarum theory.[25]

In fact, recently Lestrade et al.[28] have published data for LiClO$_4$ in benzene added to THF as to make the molar ratio (THF/LiClO$_4$) = 3. The electrolyte concentration was $c = 0.8\ M$. By setting ϵ_∞ for the LiClO$_4$ solution equal to the pure solvent ($\epsilon_\infty = 2.38$) these authors give $\tau_D = 5.10 \times 10^{-10}$ sec, $\beta = 0.51$. Setting $\epsilon_\infty = 2.274$, the permittivity of pure benzene, it gave $\tau_D = 5.20 \times 10^{-10}$ sec and $\beta = 0.50$. Using the modified Glarum theory we obtain $l_0 = 8.04 \times 10^{-8}$ cm and $\tau_{dif} = 4.97 \times 10^{-10}$ sec, which in turn gives for $\tau_D = 5.1 \times 10^{-10}$ sec β_{calcd} 0.50 and for $\tau_D = 5.2 \times 10^{-10}$ sec, $\beta = 0.49$.

References and Notes

(1) J. B. Hasted and G. W. Roderick, J. Chem. Phys., **29**, 17 (1958).

(2) M. Davis and G. Johansson, Acta Chem. Scand., **18**, 1171 (1964), and previous literature quoted therein.

(3) R. Pottel, "Chemical Physics of Ionic Solutions", B. E. Conway and R. G. Barradas, Ed., Wiley, New York, N.Y., 1966, p 581.

(4) M. Eigen and K. Tamm, Z. Electrochem., **66**, 93 (1962).

(5) K. Tamm, G. Kurtze, and R. Kaiser, Acustica, **4**, 380 (1954); G. Kurtze and K. Tamm, ibid., **3**, 33 (1954).

(6) G. Davies, "Ion Association", Butterworths, London, 1962, pp 168–172.

(7) P. Jagodzinski and S. Petrucci, J. Phys. Chem., **78**, 917 (1974).

(8) J. P. Badiali, H. Cachet, and J. C. Lestrade, C. R. Acad. Sci., Paris, **271**, 705 (1970); J. P. Badiali, H. Cachet, and J. C. Lestrade, Ber. Bunsenges. Phys. Chem., **75**, 297 (1971).

(9) F. I. Mopsik, Ph.D. Thesis, Brown University, 1964; F. I. Mopsik and R. H. Cole, J. Chem. Phys., **44**, 1015 (1966).

(10) S. H. Glarum, Rev. Sci. Instrum., **29**, 1016 (1958).

(11) J. D. Cutnell, Ph.D. Thesis, University of Wisconsin, 1967; J. D. Cutnell, D. E. Kranbuehl, E. M. Turner, and W. E. Vaughan, Rev. Sci. Instrum., **40**, 908 (1969).

(12) D. J. Metz and A. Glines, J. Phys. Chem., **71**, 1158 (1967); E. Kuss, Z. Angew. Phys., **7**, 376 (1955).

(13) J. P. Badiali, H. Cachet, A. Cyrot, and J. C. Lestrade, J. Chem. Soc., Faraday Trans. 2, **69**, 1339 (1973).

(14) E. A. S. Cavell, Trans. Faraday Soc., **61**, 1578 (1965); E. A. S. Cavell, P. C. Knight, and M. A. Sheikh, ibid., **67**, 584 (1971).

(15) N. Hill, W. E. Vaughan, A. H. Price, and M. Davies, "Dielectric Properties and Molecular Behaviour", Van Nostrand, London, 1969, pp 55, 244.

(16) E. A. S. Cavell and P. C. Knight, J. Chem. Soc., Faraday Trans. 2, **68**, 765 (1972).

(17) R. Kubo, J. Phys. Soc., **12**, 570 (1957): "Lectures in Theoretical Physics", Vol. I, Interscience, New York, N.Y., 1958, Chapter IV.

(18) J. Barthel, H. Behret, and F. Schmithals, Ber. Bunsenges. Phys. Chem., **75**, 305 (1971).

(19) E. A. S. Cavell, P. C. Knight, and M. A. Sheik, Trans. Faraday Soc., **67**, 2225 (1971).

(20) C. A. Kraus, et. al., J. Am. Chem. Soc., **72**, 166 (1950); **55**, 21, 3614 (1933).

(21) M. von Smoluchowski, Z. Phys. Chem. (Frankfurt am Main), **92**, 179 (1917); P. Debye, Trans. Elect. Soc., **82**, 265 (1942).

(22) R. M. Fuoss, J. Am. Chem. Soc., **80**, 5059 (1958).

(23) The present data of molar refraction taken at the sodium D line wavelength are $R_D(Li^+) = 0.20$ cm^3, $R_D(ClO_4^-) = 13.32$ cm^3 (from C. P. Smyth "Dielectric Constant and Molecular Structure", Chemical Catalog, New York, N.Y., 1931).

(24) G. Schwartz, J. Phys. Chem., **71**, 4021 (1967); **74**, 654 (1970); G. Williams, Adv. Mol. Relaxation Processes, **1**, 409 (1970); W. Scheider, J. Phys. Chem., **74**, 4296 (1970).

(25) S. H. Glarum, J. Chem. Phys., **33**, 639 (1960).

(26) The rotational relaxation time is proportional to the square root of the moment of inertia [E. Bauer, Can. Phys., **20**, 1 (1944)].

(27) H. C. Wang and P. Hemmes, J. Am. Chem. Soc., **95**, 5119 (1973).

(28) J. P. Badiali, H. Cachet, P. Canard, A. Cyrot, and J. C. Lestrade, C. R. Acad. Sci., Paris, **273**, 199 (1971).

COMMUNICATIONS TO THE EDITOR

Comment on the Paper "Ionic Solvation Numbers from Compressibilities and Ionic Vibration Potentials Measurements", by J. O'M. Bockris and P. P. S. Saluja

Sir: In a paper in this journal, Bockris and Saluja[1] have attempted to use ionic vibration potentials (IVP) together with compressibility data to calculate ionic hydration numbers and their concentration dependence. Some assumptions involved in their approach, however, raise substantial questions concerning the significance of the hydration numbers so evaluated.

1. Nature of Ionic Vibration Potentials. IVP's are a measure of the apparent mass (W_i) of the solvated ion, i.e., the mass of each solvated ion minus the mass of the free displaced solvent.[2] Thus

$$W_i = (M_s)_i - (V_s)_i \rho_0 = M_i + n_i M_0 - (V_s)_i \rho_0 \quad (1)$$

where $(M_s)_i$ is the molar mass of the ith solvated ion, $(V_s)_i$ is the volume of the solvated ion, and the other symbols coincide with those in ref 1. The question of what constitutes the solvated ion requires consideration of the basic differential equation for the forces acting on the ith ion in the theoretical treatment of IVP.[3] Neglecting terms which are small for dilute solutions, this equation has the form

$$e_i X - f_i(v_i - v_0) + V_i \rho_0 \frac{dv_0}{dt} = m_i \frac{dv_i}{dt} \quad (2)$$

where e_i is the charge of the ith ion, f_i the frictional coefficient, v_i the velocity, m_i the mass, V_i the volume, X the electric field intensity, v_0 the solvent velocity, and t the time. Implicit to this equation is a model consisting of the core ion surrounded by solvent molecules bound to it with all other solvent in the system behaving as pure bulk solvent and no rapid exchange of this bound solvent with bulk solvent. This model is questionable even as an approximation. Significant momentum transfer occurs between the solvated ion and bulk solvent through the rapid exchange of the solvent in the solvation sheath with bulk solvent. For ions such as the alkali metal cations and halide anions, the lifetime of a water molecule in even the primary hydration sheath is many orders of magnitude shorter than the period of the ultrasonic waves used for the experimental studies. What constitutes bound solvent is therefore very much in doubt. Furthermore, unless the model for the solvated ion is such as to include all solvent whose density is perturbed by the ion, both the frictional and pressure gradient terms in the sound field are incorrect because the local environment does not have the velocity v_0 of bulk solvent. The amplitude and phase of the motion of any region in the solution within the sound field depends on its density.

Fortunately there is compensation of some of these difficulties in the IVP treatment based on eq 2. The final

equations obtained for the IVP are expressed as a function of the apparent mass W_i (given by eq 1) and the transference number (t_i). By using transference data, the effects of the momentum transfer associated with the solvent exchange are taken into account without the introduction of new errors provided the solutions are dilute. Further, the value of W_i and hence the IVP are *not* dependent on how large the volume $(V_s)_i$ of the solvated ion and hence the solvation number n_i in eq 1 are taken to be, *provided* the values of these quantities are at least large enough to encompass all solvent whose density is perturbed by the ion. If the size of the solvated ion is taken to be greater than this minimum value, both the mass and the buoyancy terms increase by the same amount in eq 1 and do not influence W_i or the values of IVP calculated from them. Thus the value of n_i in the Bockris–Saluja paper depends on how $(V_s)_i$ is fixed and does not correspond to any simple concept of bound water.

IVP may also be viewed as an ac acceleration potential and treated in terms of the thermodynamics of flow in an acceleration field[4] since the mass relaxation frequencies of the solvated ions are many orders of magnitude higher than the ultrasonic measurement frequencies.[2] Thus for an acceleration field under isothermal conditions, the electric potential gradient is[4]

$$\nabla \psi = -\frac{1}{F} \sum_i \frac{t_i}{z_i} [\nabla \mu_i + W_i \nabla \phi] \quad (3)$$

where ϕ is the acceleration field potential, F is the Faraday constant, μ_i is the chemical potential, and the apparent mass W_i is *thermodynamically* specified as

$$W_i = M_i - \rho \bar{V}_i \quad (4)$$

where $\bar{V}_i$ is the ionic partial molal volume and ρ is the solution density. The isothermal assumption is reasonable for the propagation of sound in water although probably not for other solvent systems with much larger specific heat ratios. If the assumption is made that the $\nabla \mu_i$ terms in eq 3 are small compared to the $W_i \nabla \phi$ terms, then the expression obtained for IVP from eq 3 is the same as obtained from the dynamic reaction approach using eq 2 except that W_i is defined by eq 4 rather than eq 1. [Note that the electrodes used to measure IVP are only capacitively coupled to the solution through the interfacial capacitance and sense only the ac potential differences between regions with two different accelerations.]

Equations 1 and 4 became equivalent expressions when the size of the solvated ion is taken sufficiently large so as to encompass all solvent whose density has been perturbed by the ion. This can be demonstrated as follows. Combining eq 1 and 4 yields

$$\bar{V}_i = [(V_s)_i - n_i(M_0/\rho_0)](\rho_0/\rho) \quad (5)$$

For moderately dilute solutions $(\leq 10^{-1} M)$, $\rho = \rho_0$ to a good approximation and

$$\bar{V}_i = (V_s)_i - n_i V_0 \qquad (6)$$

and the partial molal volume of the electrolyte as a whole is

$$\bar{V}_2 = \sum_i \bar{V}_i = \sum_i [(V_s)_i - n_i V_i] \qquad (7)$$

This equation is valid only if $(V_s)_i$ and n_i include all of the solvent whose volume differs from that of pure solvent but is still correct even if $(V_s)_i$ and n_i include additional solvent whose volume is not perturbed by the ions.

The term "ionic vibration potentials" may be somewhat misleading since it tends to conjure up thoughts of vibrating solvated ions and simple mass inertia effects involving solvated ions. The ultrasonic frequencies (10^5–10^6 Hz) at which IVP's are measured, however, are far below (by a factor of $\sim 10^6$) those at which inertia effects would cause any appreciable phase lag. The ultrasonic waves give only a very slight periodic bias to the random movement of the ions under the influence of the thermal energy within the liquid.

2. Nature of the Hydration Numbers Involved in Ionic Vibration Potential. Bockris and Saluja used values of $(V_s)_i$ in eq 1, calculated from the corrected Stokes' law radii of the hydrated ions given by Nightingale.[5] The n_i values involved in this part of their work are really the corrected Stokes' law radius–partial molal volume values. This can be seen from eq 6, which in rearranged form is

$$n_i = [(V_s)_i - \bar{V}_i]/V_0 \qquad (8)$$

where V_0 is the molar volume of pure water. The subtraction of $\bar{V}_i$ (rather than just the central ion volume) from $(V_s)_i$ includes a correction for the difference in volume of the hydration water and bulk water. This correction is quite accurate for dilute and even moderately concentrated solutions, *provided* the volumes $(V_s)_i$ calculated from the corrected Stokes' law radii include all the water molecules surrounding each ion with effective volumes differing appreciably from that of bulk solvent. The values of $\bar{V}_i$ are directly related to the apparent masses W_i by eq 4 and in turn the IVP's are a measure of W_i and hence $\bar{V}_i$. Thus, the two terms on the right-hand side of eq 7 in ref 1 can be expressed in the forms

$$\frac{\psi_0/a_0}{2.79} = \frac{1}{M_0}\left[\frac{t_+}{z_+}(M_+ - \bar{V}_+\rho_0) - \frac{t_-}{z_-}(M_- - \bar{V}_-\rho_0)\right] \qquad (9a)$$

$$A = -\frac{1}{M_0}\left\{\frac{t_+}{z_+}[M_+ - (V_s)_+\rho_0] - \frac{t_-}{z_-}[M_- - (V_s)_-\rho_0]\right\} \qquad (9b)$$

The principal reason for involving IVP's in the evaluation of the hydration numbers is that the IVP's depend on difference terms rather than sum terms for the cations and anions and, when combined with sum data for n_i's, permit the evaluation of individual ionic values. The two types of data, however, must involve the same kinds of hydration numbers. In the work of Bockris and Saluja, it is doubtful that the corrected Stokes' law radius–partial molal volume hydration numbers involved with the IVP's are the same as obtained from compressibility data using the Passynskii equation. The combination of the corrected Stokes' law radius–IVP data with partial molal volume data for the electrolytes would appear more consistent and logical since this essentially eliminates any question as to both types of data involving the same kind of hydration numbers at least up to moderate concentrations.

The equivalent calculation may be readily carried out with eq 8 using the individual ionic partial molal volumes obtained earlier from IVP data[2] and the Stokes' law radii as corrected by Nightingale[5] for deviations from Stokes' law. The values so caclulated are essentially the same as listed in Table V of ref 1 under the heading "values of ionic solvation numbers from partial molal volume and Stokes' law radii data".

At first consideration, it may appear that the combination of the corrected Stokes' law radius–IVP data with sum data for n_i permits the evaluation of individual ionic hydration numbers without assuming the hydration number of any one ion to be zero. Unfortunately such is not completely true. Bockris and Saluja incorporated the assumption that the hydration numbers of the tetraalkylammonium ions larger than $(CH_3)_4N^+$ are zero when they made use of the corrected Stokes' law radii of Nightingale[5] in calculating the A term in eq 7 of ref 1 for the majority of the ions for which they list n_i values. The value of the hydration numbers so calculated are strongly influenced by the assumptions made by Nightingale in obtaining the effective radii of hydrated ions, particularly for the smaller ions. Stokes' law fails for ions which are not large compared to the dimensions of the solvent molecules. To correct for such, Nightingale used a calibration curve somewhat similar to that proposed by Robinson and Stokes.[6] A plot of the hydrated ionic radius vs. the measured Stokes' law radius was prepared by assuming all of the tetraalkylammonium ions with Stokes' law radii > 2.5 Å to be unhydrated and then using as calibration points their crystallographic radii vs. their measured Stokes' law radii. This procedure is equivalent to fixing the hydration numbers of these tetraalkylammonium ions as $n_i = 0$. The tetraalkylammonium ions provided calibration points down to measured Stokes' law radii of 2.5 Å. To complete the calibration curve, Nightingale assumed that the curve was linear below 2.5 Å and that the corrected hydrated ionic radius approaches a finite limit diameter of a water molecule as the measured Stokes' law radius approaches zero. For ions such as the halides, with measured Stokes' law radii well below 2.5 Å, these assumptions have much influence on the hydration numbers calculated from IVP's.

All things considered, we find it difficult to associate any special advantage with hydration numbers evaluated from IVP–corrected Stokes' law radius data together with either partial molal volume or compressibility data relative to some other kinds of hydration numbers. Unfortunately all of the various types of hydration numbers so far proposed either involve questionable assumptions and/or are very restricted in their definitions. One of the merits of the paper of Bockris and Saluja is that it attempts to distinguish between solvational and nonsolvational water molecules within the hydration shell on a kinetic basis.

3. Concentration Dependence of IVP's and the Corrected Stokes' Law Radii. The equations ((4) and (7) in ref 1) used to calculate the ionic hydration numbers from IVP's are questionable at concentrations up to 5 M. Charged ion aggregates can cause substantial errors, particularly with asymmetric electrolytes for which the ion pairs have a net charge. It is not necessary for these aggregates to be inner coordinate sphere complexes to contribute to the observed IVP's. Further, even the apparent masses of the ions are no longer properly given by eq 1 above or eq 5 in ref 1 since the pressure-gradient term in the equation[3] for the forces acting on the ions can no longer be approximated as a simple function of the density of pure solvent.

At concentrations from 10^{-2} to 1 M, IVP's have been

found to change relatively little with concentration for most electrolytes.[1,2] Above 1 M, the only published experimental IVP data appear to be those in ref 1 for $CaCl_2$ and $SrCl_2$ at 5 M. For these two electrolytes, the IVP's decrease by approximately 30% between 10^{-1} and 5 M. For all of the other values in ref 1, the values at 5 M have been extrapolated from the value at 0.05–1 M. For 12 out of 16 electrolytes, the IVP's at 5 M have been taken to be the same as at 1 M. We believe that this is a very dubious procedure.

In using the IVP and compressibility data at various concentrations up to 5 M, Bockris and Saluja did not appear to have corrected the Nightingale hydrated ionic radii for their change with changing hydration at high concentrations, assuming for the moment that the hydration numbers decrease at high concentrations in the manner reported by these authors. It appears that concentration-independent A values were used in eq 7 of ref 1 for both asymmetric as well as symmetric electrolytes despite the dependence of this term on transference numbers as well as $(V_s)_i$. Pending some vigorous defending of these additional assumptions, the quantitative conclusions reached in ref 1 concerning the concentration dependence of the hydration numbers do not seem justified.

References and Notes

(1) J. O'M. Bockris and P. P. S. Saluja, J. Phys. Chem., 76, 2140 (1972).
(2) R. Zana and E. Yeager, J. Phys. Chem., 71, 521 (1967).
(3) J. Bugosh, E. Yeager, and F. Hovorka, J. Chem. Phys. 15, 592 (1947).
(4) See, e.g., H. S. Harned and B. B. Owen, "Physical Chemistry of Electrolyte Solutions", Reinhold, New York, N.Y., 1958, pp 39–41, 279–280.
(5) E. R. Nightingale, J. Phys. Chem., 63, 1381 (1959).
(6) R. A. Robinson and R. H. Stokes, "Electrolyte Solutions", Academic Press, New York, N.Y., 1955, p 118.

Chemistry Department   Ernest Yeager*
Case Western Reserve University
Cleveland, Ohio 44106

C.N.R.S., C.R.M.   Raoul Zana
67083 Strasbourg-Cedex, France

Reply to the Comments of Yeager and Zana on the Paper "Ionic Solvation Numbers from Compressibilities and Ionic Vibration Potential Measurements"

Sir: Yeager and Zana (Y–Z)[1] have questioned the reliability of ionic solvation numbers and their concentration dependence, which were evaluated from the combination of compressibility and ionic vibration potentials (IVP) measurements.[2] We discuss the points of Y–Z in order.

(1) Are the two methods, compressibility and IVP, measuring the same kind of solvation (hydration) numbers? We examined this in section IV (1a and 1b) in our paper[2] (pp 2146–2149).

According to Y–Z, the solvent molecules of the solvated ions undergo a large number of exchanges with the bulk solvent during the period of the ultrasonic waves (10^5–10^6)

while measuring IVP. In considering ionic solvation number, one is concerned with the state of individual ions. These ions are in random motion irrespective of whether the system is in equilibrium or not. Thus, the compressibility method, which involves measurements of the solution at equilibrium, nevertheless concerns ions in a state of dynamic movement and should measure the same kind of solvation numbers as one would expect from a measurement method made when the ions are drifting under nonequilibrium conditions (e.g., under an ultrasonic or electric field). The deviation of movement, then, is tiny from that indicated in random motion.

Considering the individual state of ions in solution: on a time average, the solvent molecules in the vicinity of ions undergo exchanges with the bulk solvent in both measurements—compressibility and IVP—used in our work.[2] The solvation numbers measured by these methods are those solvated water molecules *strongly* (see p 2150 of ref 2 for the discussion of the magnitude of such strong interactions) bound to the ion, termed by us "solvationally coordinated water". We showed by calculation in section IV (1a and 1b) in our paper[2] that the water molecules *loosely* bound to the ion, termed by us "nonsolvationally coordinated water", behave approximately like bulk solvent molecules in respect to their compressibility and their interactions with ions moving in an ultrasonic field. These molecules coordinated to the ion in the first coordination shell are consistent with numbers indicated by X-ray[3,4] studies on coordination numbers of ions in aqueous solutions.

The *solvation* number—the number of water molecules attaching to the ion *during movement*—is the number reacted to both by the compressibility (nonsolvated, but coordinated, water compressible) and by the IVP, for this is concerned with relative *motion* and, hence, *drag* on the ion *during* that motion.

(2) (a) Concerning a buoyancy term (last term in eq 1 of Y–Z[2]),[5] we have already raised a question ourselves[6] whether this term should be used for the motion of an ion in the direction of an ultrasonic field. We return to this theme below.

(b) The use of a corrected Stokes' law radii, V_s, contains an implicit assumption that the solvation number of tetraalkylammonium ions with radii equal to or greater than 2.5 Å is zero. According to Y–Z, the ionic solvation numbers obtained by us involving the use of V_s may not be absolute. However, Y–Z themselves argue that this assumption is reasonable[7,8] because the electrostriction term is small due to a low charge size ratio for such ions.

Further, extrapolation of a plot of our ionic solvation numbers for cations and anions against the reciprocal of ionic radii predicts an interesting result; i.e., solvation numbers for the ions with radii greater than 2.7 Å are zero (see Figures 4 and 5 of ref 2). This does suggest that sufficiently large ions are unhydrated and is not importantly deviant from the 2.5 Å involved in our assumption about tetraalkylammonium ions. Within a thus indicated degree of approximation, the values of ionic solvation numbers in our paper should be considered absolute.

This assumption—that there are zero *oriented* coordination water molecules attached to sufficiently large ions—has nothing to do with structure-breaking effects, which are, of course, also caused by tetraalkylammonium ions.

(c) Are the calculated values of ionic solvation numbers sensitive to the use of extrapolated values of V_s for ions with radii below 2.5 Å from the plot of a corrected Stokes'

TABLE I: Effect of 20% Uncertainty in the Volume of the Moving Ion on the Bockris–Saluja Method and that Using Stokes' Law Directly

| | n_s ($\pm 20\%$ V_s) | |
Ion	Bockris and Saluja	Direct method
Li$^+$	4.5 ± 0.02	4.7 ± 1.0
Na$^+$	4.5 ± 0.05	3.7 ± 0.8
K$^+$	3.8 ± 0.01	2.7 ± 0.6
Rb$^+$	3.0 ± 0.04	2.5 ± 0.6
Cs$^+$	2.5 ± 0.07	2.3 ± 0.6
F$^-$	4.0 ± 0.02	3.3 ± 0.7
Cl$^-$	2.2 ± 0.05	2.3 ± 0.6
Br$^-$	1.8 ± 0.05	2.0 ± 0.6
I$^-$	1.5 ± 0.05	1.6 ± 0.6

law radii against ionic radii? We have shown[6] that the ionic solvation number, being the difference of two terms $[(t_+/z_+)(V_s)_+ - (t_-/z_-)(V_s)_-]$, is not sensitive to uncertainty in values of V_s, because a systematic error in V_s will tend to cancel. For a 20% uncertainty in V_s, the solvation numbers change by less than 0.1, whereas if one uses a modified Stokes' equation directly, any error depends directly on the degree of validity of (i.e., error in) this form of Stokes' law and for an uncertainty of 20% in V_s, solvation numbers change by more than 1 unit (see Table I).

The assumption of linearity in the calibration curve of Nightingale[5] for the values of V_s for ions with radii less than that for ions with negligible hydration will thus not be a *sensitive* assumption within the structure of equations in IVP. Thus, the determinations of the difference of solvation numbers of ions from IVP involves the *difference* of two quantities $[(t_+/z_+)(V_s)_+ - (t_-/z_-)(V_s)_-]$, which are nearly equal for most electrolytes (Table II of ref 2).

(d) Last, Yeager and Zana's comment that "the combination of corrected Stokes' law radius–IVP data with partial molal volume data for the electrolyte would appear more consistent . . . since this eliminates any question as to both types of data involving the same kind of hydration at least up to moderate concentrations", is answered as follows. We considered this point in our work[2] (see Table V of ref 2) and our calculations indicated that the values of ionic solvation numbers obtained by use of this alternative method are about 2 units higher than those obtained by the method we used. Discussion suggests it is a less clearly arguable method. Do the density measurements for the evaluation of the partial molal volume of the electrolyte concern the same packing, and therefore local density (or electrostriction), as that which occurs during IVP measurements? How is the partial molal volume of the electrolyte broken up? One would have to enter a detailed examination of the validity of this method, perhaps along the lines in section IV (1a) in our work[2] on the validity of the compressibility method, before its significance could be evaluated to the degree which we have evaluated that of the method we used.

(e) It may well be argued that the buoyancy term should arise only when we are considering vertical (downward or upward) motion of the ions in solution, because then only the Archimedean upthrust arises. Since we are considering the acceleration in the x direction in the presence of ultrasonic field, any Archimedean upthrust should not affect the acceleration in the x direction. The origin of the Archi-

medean term in Debye's theory lies in a private communication of Debye to Hermans. Hermans opined that, when the density of the solute and solvent is equal, we should not observe any IVP. The introduction of the buoyancy terms was essential to satisfy this condition.

If one examines the magnitude of buoyancy terms (see the second term on the right-hand side of eq 6 in ref 2), from the parameters in Table II of ref 2, one finds the value to be −0.004 to −0.3. Substitution shows that the maximum effect of the buoyancy term will be 0.2 in the solvation number. The degree of consistency of primary solvation number measurements among various methods is c + 1.

(3) This comment refers to concentration dependence of the IVP, corrected Stokes' law radii, or volume V_s and the transference number of the ions on the values of ionic solvation numbers evaluated from eq 7 of ref 2.

(a) One should indeed use concentration-dependent values of V_s, but the advance of using this higher form of the approximate correction will be nugatory for the arguments presented in section 2c: the difference between solvation number of cations and anions is not sensitive to the variation in V_s, even to the extent of 20% (see column 2 of Table I).

(b) The effect of the formation of ion-pair and higher aggregates, and also of hydrolysis, was examined for concentrated solutions (see ref 2, p 2144). For the electrolytes and the concentration range studied in our work,[2] these effects were found to have a numerically negligible effect on the calculated ionic solvation number.

(c) The effect of concentration variation on the transference numbers t_+ and t_- was also examined in our work (see ref 2, bottom of p 2144 and first paragraph on p 2145). In the case of NaCl, the effect of the concentration on t_{Na^+} changed the solvation number of Na$^+$ by less than 0.2. When the transference numbers of cation and anion are equal at infinite dilution (as in KCl), the concentration dependence on t is found negligible (<0.1 change in solvation number), and so the effect of the concentration dependence of transference numbers on ionic solvation numbers was found negligible in general.

(d) Last, corrections due to a concentration dependence of IVP on the ionic solvation numbers are examined in view of the available data[2,9] on IVP. The concentration dependence of IVP, obtained by Zana and Yeager,[9] indicates that the experimental values of the IVP's were constant for 26 of the 32 electrolytes within ±0.1 μV over the range of concentration 0.003–0.1 N. In our work,[2] the IVP was found to change little for most of the electrolytes over the concentration range 0.01–1.0 N. Thus, a combination of the data of Zana and Yeager[9] and our data[2] on the concentration dependence of IVP indicates that IVP changes negligibly (measured by the criterion of effect on the calculated solvation number) over the concentration range 0.003–1.0 N. However, the experimental values of IVP at higher concentration of 5 N were determined for three electrolytes.[2] Table II of our paper[2] shows that, here, the values of IVP change in going from 1 to 5 N by 0.2–0.3 μV (20%). The error will be given by the first term on the right-hand side of eq 7 in ref 2, i.e., 0.25/2.79 or 0.1. The associated error due to extrapolation to 5 N, the data for IVP against concentration over the range 0.003–1.0 N, will thus be 0.1 in the ionic solvation numbers.

In the work of Bockris and Saluja,[2] individual solvation numbers have been obtained for the first time by a new ex-

perimental approach.[10] In the theoretical approach,[13] we distinguished between coordination of the ion in aqueous solution and the number of water molecules temporarily attached to the ion during its random movement in the solution. We submit that our method is a new, clear, and independent way to examine the problem of the environment around an ion in aqueous solution.

References and Notes

(1) E. Yeager and R. Zana. *J. Phys. Chem.*, preceding paper, this issue.
(2) J. O'M. Bockris and P. P. S. Saluja, *J. Phys. Chem.*, **76**, 2140 (1972).
(3) R. M. Lawrence and R. F. Kruh, *J. Chem. Phys.*, **47**, 4758 (1967).
(4) H. G. Hertz, *Angew. Chem., Int. Ed. Engl.*, **9**, 124 (1970).
(5) E. R. Nightingale, *J. Phys. Chem.*, **63**, 1381 (1959).
(6) Reply to R. H. Stokes, private communication, June 1973.
(7) R. Zana and E. Yeager, *J. Phys. Chem.*, **71**, 4241 (1967).
(8) L. Hepler, *J. Phys. Chem.*, **61**, 1426 (1957).
(9) R. Zana and E. Yeager, *J. Phys. Chem.*, **71**, 521 (1967).
(10) Although we are confident of the correctness of our approach, and its

reasoning, there are much greater errors than we had anticipated involved in the neglect of the partial molar volume term connecting compressibility to solvation number. We had based our neglect of it on the advice given in the well-known book of Stokes and Robinson.[11] We owe an increased awareness of the need for the correction term even in dilute solutions to R. H. Stokes.[12]

(11) R. H. Stokes and P. A. Robinson. "Electrolytic Solutions", Wiley, New York, N.Y., 1952.
(12) R. H. Stokes, private communication, May 1973.
(13) J. O'M. Bockris and P. P. S. Saluja, *J. Phys. Chem.*, **76**, 2298 (1972).

School of Physical Sciences   **J. O'M. Bockris***
The Flinders University of South Australia
Bedford Park, South Australia, 5042
Australia

Department of Chemistry   **P. P. S. Saluja**
Banaras Hindu University
Varanasi-221005
India